Site M0027[1]

Expedition 313 Scientists[2]

Chapter contents

Operations

Mobilization of the *L/B Kayd*

Mobilization of the *L/B Kayd* began with shipping the European Consortium for Ocean Research Drilling (ECORD) Science Operator (ESO) laboratory, database, and office containers from ESO partner institutes in Europe. Once all the equipment and containers had cleared customs, they were delivered to the U.S. Coast Guard Station in Atlantic City, New Jersey (USA).

On 24 April 2009, the *L/B Kayd* arrived ahead of schedule at the Coast Guard Station in Atlantic City. Mobilization was started immediately by the drilling contractor, Drilling, Observation and Sampling of the Earth's Continental Crust (DOSECC), who loaded the drilling and ESO containers onto the platform. ESO staff from the British Geological Survey (BGS) arrived at the *L/B Kayd* on 28 April to prepare the containers for operations, including installing a shipboard computer network. Because of the nature of transiting in a lift boat, with water spilling over the deck, power could not be fully installed in the containers until the first hole was reached.

Mobilization continued for 6 days. The wireline logging equipment was transferred to the *L/B Kayd* out of Miller's Launch, Staten Island, New York (USA), on 1 May, with the first supply boat and crew change.

Transit to Hole M0027A

At 1030 h Universal Time Coordinated (UTC) on 30 April 2009, the *L/B Kayd* set sail from Atlantic City and headed for the first coring site (Integrated Ocean Drilling Program [IODP] Hole M0027A). A brief stop was made on the way to Hole M0027A to modify the flooring of the cantilevered drilling platform, which was being forced up by waves breaking on the *L/B Kayd*'s bow. At 2345 h, the *L/B Kayd* arrived on site and prepared to position above Hole M0027A.

Hole M0027A

At 0003 h on 1 May 2009, the *L/B Kayd* was positioned above Hole M0027A and the legs were lowered to tag the seabed. Once the seabed was tagged, the preload procedure began by gradually increasing the load on the seabed. The preload procedure was interrupted to reposition the *L/B Kayd* so that the communication

[1] Expedition 313 Scientists, 2010. Site M0027. *In* Mountain, G., Proust, J.-N., McInroy, D., Cotterill, C., and the Expedition 313 Scientists, *Proc. IODP,* 313: Tokyo (Integrated Ocean Drilling Program Management International, Inc.). doi:10.2204/iodp.proc.313.103.2010
[2] Expedition 313 Scientists' addresses.

doi:10.2204/iodp.proc.313.103.2010

satellites were not eclipsed by the legs. The preload and settlement procedure continued until 1053 h, when the *L/B Kayd* was jacked-up to ~30 ft above the water. Normal access to the working deck was granted, and all teams prepared to begin coring. At 1215 h, the supply vessel *Rana Miller* arrived at the platform and delivered equipment and personnel, which included the wireline logging tools and the remaining scientific staff. At 1640 h, the drill rig was started, the mast was raised, and the conductor pipe was run to the seabed, tagging it at 2134 h. The core barrel was lowered to just above the seabed, and the first hydraulic piston corer (HPC) core was fired at 2350 h (Table **T1**).

The first core arrived on deck at 0010 h on 2 May. Coring continued using the HPC, and the hole was advanced by recovery. Sixteen HPC attempts resulted in two nonfires and a penetration of 28 m in just under 20 h. Three core runs showed signs of caving, with the amount of caving fill between 0.33 and 0.72 m. Once the base of the sand layer had been established, coring was stopped. At 2035 h, the drill string was tripped, and the conductor pipe was extended into the seabed to act as casing.

At 0130 h on 3 May, the conductor pipe was set at 17.6 m drilling depth below seafloor (DSF). The hole was conditioned, and the PQ drill string was run to the base of the hole, where HPC coring commenced. After two HPC attempts, the coring tool was switched to the extended nose corer (EXN) because of a hard lithology preventing HPC recovery. However, recovery was still poor. The coring method was switched back to the HPC, after which 6 m of cavings was encountered. In an attempt to stabilize the hole, the mud was changed and the hole was reamed with a full-face bit in a standard rotary corer (ALN) barrel. Hole stability problems continued, and the full-face bit was found to have no cutting surface left when retrieved at 1830 h. The string was tripped back to the surface to inspect the outer bit; however, no damage was observed. The string was rerun to the base of the hole, and coring continued with the HPC, which, when retrieved, contained a few pebbles and had a dented nose. The ALN was run to clear the hole shortly before midnight.

During the rerun of the ALN corer, the bit blocked again. A second ALN corer was run at 0100 h on 4 May, which on the second attempt advanced the full 3 m but recovered no core. At 0353 h, HPC coring advanced the hole but ended when the drill string became stuck in the hole. After the drill string was freed, it was recovered to the deck and checked for damage. The string was lowered back into the hole to within 9 m of the base, where it was stopped by infill material. It was also suspected that pieces of the previously broken full-face bit had been encountered, and the hole was reamed out with the ALN corer to save the PQ string bit. Coring recommenced using the EXN tool. At 1620 h, it was decided that the depth of casing in the hole should be increased. After pulling the PQ string, the casing could not be moved in the hole, so the hole was reentered using the PQ string and the hole was advanced using the EXN tool. The EXN was used in favor of the HPC, as the HPC seemed to increase hole collapse.

By 0400 h on 5 May, Hole M0027A was good, clean, and free-running with circulation at the base. EXN coring continued throughout the day with mixed recovery, although infill was encountered with most new core runs. The core barrel handling procedure was modified so that two EXN core barrels were always operational, which reduced the time the hole was left vulnerable to cave-ins. This, coupled with using the EXN, dramatically improved the coring. From 2000 h, an increasingly hard lithology caused core runs to become blocked, and a liner was crushed at the shoe.

At 2355 h on 5 May, operations were halted because of a thunderstorm.

Coring restarted at 0255 h on 6 May using the ALN, but problems with crushed liners blocking the bit persisted throughout the first half of the day. At 1500 h, the mud mix was altered slightly, and the ALN corer was switched to the HPC tool, which improved recovery slightly. At 1830 h, a meeting was convened to discuss how to best advance the hole, as progress to date had been slow. All agreed to HPC spot core in maximum 60 ft increments (6 × 10 ft pipe lengths, ~18 m), or sooner if a variation in drilling parameters was encountered that suggested a change in lithology. This was done to ~180 m DSF, where continuous coring resumed. The first open-hole interval commenced at 2140 h and continued past midnight.

Rapid progress was made at the beginning of 7 May using the strategy of HPC spot coring every 60 ft or less. Seven HPC attempts over 64 m were made in 20 h, with a slight setback occurring when the HPC tool became stuck in the bottom-hole assembly (BHA) and the wireline wire broke during an attempt to pull the tool free. The result of this was that the PQ string had to be pulled out of the hole, which was a wet pipe trip because of the HPC sealing the BHA. The wireline was not fished, as there was no way to circulate the mud during fishing, which would have increased the risk of hole collapse.

The wireline wire, which had broken ~80 ft above the BHA, was replaced early in the morning of 8 May, as was a worn bit on the BHA. The drill string

was tripped back in the hole with the noncoring bit inserted. The string reached the base of the hole 20 m higher than expected because of infill, which was subsequently drilled out. The noncoring barrel got stuck 3 m above the base of the hole when it was unlatched from the BHA. This necessitated another drill string trip. After 14 h, HPC coring resumed at 1325 h. The liner collapsed in several runs because of very stiff clay, which limited core recovery and caused several core barrels to become stuck in the BHA.

Problems with the HPC tool getting stuck in the BHA continued for the first 3 h of 9 May. After partly tripping the drill string, the HPC became free and was returned to the deck. From 0330 h, EXN and HPC coring were alternately conducted, with the EXN tool eventually chosen in favor of the HPC tool. Seven runs with the EXN tool collected very good core before chattering on the drill string, and a lack of penetration indicated a change back to sand.

To tackle this lithology, the ALN corer was prepared, and early on 10 May coring resumed with the ALN in what appeared to be a gravel layer. There was no recovery in this layer. A mud backflow occurred, and large bubbles were observed rising up the drill string. No H_2S or abnormal smell was recorded by the DOSECC or ESO instruments, and it was assumed that the gravel layer was hosting a freshwater flow. The next core did have an abnormal smell, and tests using the ESO gas analyzer measured 7.7 ppm H_2S and no flammables. A later core tested positive (1%) for flammables near a thin very dark layer. Excellent coring conditions prevailed into 11 May through alternating hard clays and hard fine sands.

Progress slowed slightly when the lithology became more sandy until the hole collapsed and the drill string became stuck at 1150 h on 12 May. Upon freeing the string, 9 m of infill blocked the hole and an increase in rotational torque was observed. To reduce this pressure on the string, thought to be from the clay formation above, the string was pulled back a total of 26 m to ream the hole. Progress continued through very loose, clean sand for the rest of the day, with surprisingly excellent core recovery. On 13 May, very good progress continued using the ALN corer, reaching 451.06 m DSF at midnight.

By 0430 h on 14 May, it became apparent that the BHA stabilizer rings were worn and needed replacement. The string was tripped in order to replace both rings. The trip was completed by 0800 h, the rings replaced, and the pipe run back into the hole. The bottom of the hole was tagged at 335 m DSF because of a bridge that had formed, at which depth open holing commenced to clear it. A zone of high-pressure water was encountered, which continued until 345 m DSF. Below this, the backpressure decreased to normal, and the string broke through the blockage. Infill was encountered after another 8–10 m air gap beneath the bridge. Approximately 100 m of fill was drilled out to reach the bottom of the hole. Coring recommenced using the ALN corer at 1910 h.

Progress slowed on 15 May, although core recovery was generally good with near 100% for many of the runs. However, some sections of some cores were undersized. The ALN corer was replaced by the EXN corer for one run to see if it gave better results. The lithology proved to be unsuitable for EXN coring with little penetration, high backpressure, and torque, so the ALN corer was used for the rest of the day. In the evening, the core barrel got stuck in the BHA at 509 m DSF. It was eventually freed, but after this event, core recovery was poor and there were ongoing problems with core barrel latching and retrieval. By the end of the day, the depth of the hole was 515 m DSF.

Steady progress was made on 16 May with the ALN corer. Core slippage occurred on some core runs, but the core was usually retrieved on the next run. Good progress was made on 17 May, with most cores having 100% recovery. Repairs to the wireline and bit refurbishment caused some delays in the afternoon and early evening.

On 18 May, 11 core runs were made with >30 m penetration using the ALN corer. Recovery was more variable than in recent days (85%). In some cases this was due to core slippage, although slipped material was often recovered in the next run. The rate of penetration slowed because of a combination of the formation becoming harder and the round trip of the core barrel taking longer with increasing depth in the hole. There were reports of a "petroleum smell" from the drillers in the early morning. However, there was no reading on the gas monitors. A slight increase in torque was noticed in the evening.

Shortly before midnight on 18 May, the core barrel was recovered to deck with no core. It was suspected that the core barrel had not latched into the BHA. Another barrel was deployed and became jammed in the upper section of the drill string. This was discovered when the overshot latched onto the barrel at approximately the waterline. After removing 11 double stands of pipe, the overshot with the latch head was unable to pass through, although the overshot alone could. The core barrel was deployed with the latching indicator ball installed and successfully latched into the BHA. After adding pipe (0410 h, 19 May) to return the string to the base of the hole, increased torque, backlash during rotation, and backpressure on the mud gauge was noted. When the string was broken to add further lengths, frothing and an overflow of mud occurred. On lowering the

overshot, slack on the wireline indicated it was being temporarily stopped in the drill string. The overshot latched on as normal, but on recovery, the assembly became jammed at ~25 m below deck level. After two attempts to release the core barrel, it was recovered to deck. Scratches and spiral polishing were noted on the outside of the barrel.

At 0600 h on 19 May, the coring operation in Hole M0027A was stopped (base of last core; 631 m DSF) and preparations made to start the logging program. Because of the instability in the upper part of the hole, the decision was made to log the open hole in three sections. Through-pipe total gamma ray (TGR) was acquired along almost the full length of the hole. Open-hole resistivity, magnetic susceptibility, sonic velocity, and spectral gamma ray were acquired for the bottom section from 421 to 631 m DSF. Acoustic images were acquired in the top half of this lowermost interval. The pipe was then pulled to 195 m DSF, beginning at 1455 h on 20 May, and resistivity, magnetic susceptibility, spectral gamma ray, sonic velocity, and acoustic image logs were acquired between 195 and 342 m DSF. A bridge that had formed at 342 m DSF prevented logging of the section between 342 and 421 m DSF.

At dawn on 21 May, preparations were made to begin a vertical seismic profile (VSP), beginning with a marine mammal watch at 0513 h. Air gun firing began at 0548 h, and the VSP tool was inserted into the pipe at 0600 h. VSP work continued throughout the day until ~1900 h. Open-hole VSP data were acquired from 323 to 195 m DSF with through-pipe VSP data from 195 m DSF to seafloor. Marine mammal observations ceased at 1930 h.

Preparations were made to pull the pipe up to the top of the next open-hole logging section. However, a fault developed with the drilling rig motor before pipe pulling commenced. Repairs required a spare part that was not on the platform. Efforts to make a temporary repair on board to keep the system operational for the remainder of the logging program were attempted but were unsuccessful. Late in the evening, operations ceased while waiting for the part (and additional spare) to be delivered by supply boat on 22 May.

The rig was operational by 0830 h on 22 May. Two double stands were tripped with the aim of opening the hole to 97 m DSF. However, the pipe became stuck, and despite applying five times the usual torque, the pipe would not rotate in the hole and could not be pulled further. The decision was made to abandon the hole and move to Hole M0028A to begin coring operations. The pipe was cut just above the core barrel and tripped. The casing was retrieved, and the deck, drilling rig, and containers were secured for the rig move.

Lithostratigraphy

Figure F1 provides a key to colors and symbols used for figures in this section.

Hole M0027A was drilled in the shallow shelf to sample a thick early Miocene succession. The hole also sampled relatively thin and incomplete Pleistocene, late to middle Miocene, early Oligocene, and late Eocene sediments. No Pliocene sediments were found.

The succession is divided into eight lithostratigraphic units (Table T2; Fig. F2). Basal Unit VIII (631.15–625.60 meters below seafloor [mbsf]; Eocene) comprises clay deposited in a deep offshore environment. The overlying Unit VII (625.60–488.75 mbsf; late early Oligocene to early Miocene [early Aquitanian]) shows large-scale uphole coarsening from silt through very fine sand to poorly sorted glauconite-rich coarse sand deposited as debrites and turbidites. Cyclic changes in average grain size and glauconite content occur upcore on the scale of 5–10 m, but sedimentary structures are rare, possibly because of bioturbation. The succession is interpreted as the progradation of a clinoform slope succession over deep (>200 m?) apron deposits located seaward of the toe-of-clinoform slope. Unit VI (488.75–355.72 mbsf; late Aquitanian–early Burdigalian) marks the progradation of a thick storm-dominated river-influenced delta (offshore through shoreface–offshore transition to shoreface) over a toe-of-slope apron. A thick shoreface succession (Subunit VIA; ~57 m thick) comprises clean quartz sand. The overlying Unit V (355.72–335.93 mbsf; early–middle Burdigalian) marks an abrupt change in sedimentary facies and mineralogy to poorly sorted glauconite-rich sand with quartz and lithic granules and a poorly constrained environment of deposition in a clinoform rollover position. Unit IV (335.93–295.01 mbsf; middle Burdigalian) comprises an overall deepening-upward succession of shoreface–offshore transition to offshore facies. Units III and IV are separated by an erosion surface that is overlain by 1.5 m of very coarse glauconitic sand interpreted as a transgressive lag deposit. Unit III (295.01–236.16 mbsf; late Burdigalian–early Langhian) comprises deepening- and shallowing-upward packages of silty offshore and shoreface–offshore transition environments with a major storm influence. Unit II (236.16–167.74; Langhian) is a series of deepening-upward sedimentary cycles deposited in environments evolving from shoreface through shoreface–offshore transition to

offshore. These cycles are interpreted as incomplete depositional sequences lacking regressive facies successions because of subsequent erosion. The upper part of Unit II is a clay-rich offshore succession. Unit I (167.74–0 mbsf; late Miocene[?]–late Pleistocene, with no evident Pliocene) comprises sand and gravel deposited in a range of fluvial, coastal plain, estuarine, and shoreface environments, with incised valley fills identified. See **"Chronology"** for refined ages, **"Paleontology"** for paleodepth estimates, and **"Stratigraphic correlation"** for comparison of key stratigraphic surfaces identified in cores, well logs, and seismic reflection profiles.

Lithologic descriptions are given according to the order of core numbering, from the top to the base of each lithostratigraphic unit or subunit, whereas interpretations are given in chronologic order, from the base of each unit or subunit uphole. Figure **F3** summarizes Units I–III and their constituent subunits, described in detail below. Figure **F4** summarizes Units IV–VII. Table **T3** describes thin sections that aided in core descriptions.

Unit I

Interval: 313-M0027A-1H-1, 0 cm, to 57H-2, 48 cm
Depth: 0–167.74 mbsf
Age: late Pleistocene to late Miocene (?)

Unit I is predominantly sand. Core recovery was good only for the uppermost 32 m, and units below this level are poorly characterized.

Subunit IA

Interval: 313-M0027A-1H, 0 cm, to 14H-1, 71 cm
Depth: 0–26.29 mbsf

This subunit comprises mainly gray-brown, quartz-rich coarse and very coarse sand (Fig. **F5**) with thick interbeds of gray clay. Shell fragments are abundant in the sand. The subunit is coarse to very coarse at the top, grading down to clay at ~18 m and gravel at the base.

Interpretation

The succession is interpreted as a transgressive–regressive facies cycle composed mostly of shallow marine (shoreface to shoreface–offshore transition zone) and estuarine sediments.

Subunit IB

Interval: 313-M0027A-14H-1, 71 cm, to 34X-1, 0 cm
Depth: 26.29–70.92 mbsf

This subunit is poorly recovered medium to coarse sand with granules. Three further divisions are possible. Subdivision A (Cores 313-M0027A-15H through 19H; 26.29–32.77 mbsf) comprises clean, well-sorted sand with rare gravel beds and no shells (Fig. **F6**). This upper succession may represent a beach or foreshore environment. Subdivision B (Cores 313-M0027A-20H through 26X; 32.77–46.52 mbsf) was very poorly recovered and is composed of poorly sorted sand with abundant subangular granules. Poor recovery makes environmental interpretation impossible. Subdivision C (Cores 313-M0027A-27X through 34X; 46.52–77.92 mbsf) is stratified and poorly sorted with subangular sand and granules (Fig. **F7**), with some burrows filled with dark organic material (organic matter is otherwise rare). Locally, well-developed cross-bedding occurs, indicating unidirectional currents.

Interpretation

The lowest succession (Subdivision C) is interpreted as fluvial. Seismic lines and well logs support the interpretation that Core 313-M0027A-27X may have been drilled into an incised valley and the sediments captured here reflect the transgressive fill of the valley.

Subunit IC

Interval: 313-M0027A-34X-1, 0 cm, to 49H-1, 66 cm
Depth: 70.92–92.93 mbsf

This lithologically variable unit comprises thin interbeds and interlaminae of sand and clay. Sediments in this poorly recovered interval show abrupt downcore facies changes. Plant debris and large fragments of wood are common (e.g., interval 313-M0027A-38X-1, 59–97 cm; 77.61–77.99 mbsf).

Interpretation

This interval may represent estuarine environments.

Subunit ID

Interval: 313-M0027A-49H-1, 66 cm, to 57H-2, 48 cm
Depth: 92.93–167.74 mbsf

This subunit is very poorly recovered. Two cores near the top (Cores 313-M0027A-50H and 51H; 95.32–110.83 mbsf) are nonmarine and exhibit paleosol fabrics (Fig. **F8**). Below the paleosol fabrics, sand (Cores 313-M0027A-53H through 56H; 134.97–162.49 mbsf) is generally poorly sorted coarse to very coarse quartz with small-pebble conglomerate. Large gaps in recovery separate cores (e.g., between Cores 313-M0027A-50H and 51H, 51H and 53H, and 54H and 56H; 96.12–110.57, 110.83–134.97, and 139.24–162.37 mbsf, respectively).

Interpretation

These sediments likely represent fluvial environments, with possibly some shoreface deposits at the base of Core 313-M0027A-57H.

Unit II

Interval: 313-M0027A-57H-2, 48 cm, to 83R-2, 126 cm
Depth: 167.74–236.16 mbsf
Age: middle Miocene (Langhian)

Recovery of this unit was good overall (70%), except for the top 23 m, where it was poor (16%). Broadly, the unit comprises clay and silt, with beds of sand and granules occurring prominently in the lowest 20 m. Well-sorted fine and very fine sand also occur at the top of the unit (e.g., interval 313-M0027A-58H-2, 0–118 cm; 175.19–176.35 mbsf). The underlying clay is interbedded with 1–2 cm thick silt beds and laminae of alternating dark and pale gray (e.g., Core 313-M0027A-65X; 192.11–193.61 mbsf). Sporadic very fine sand laminae occur (Fig. **F9**). Below this level (Core 313-M0027A-65X; 193.61 mbsf), the sediment is relatively homogeneous clay with only weak and rare color banding. Pale and medium gray-brown color-banded clay recurs in the underlying thickly interbedded clay and bioturbated silty clay (Cores 313-M0027A-67X through 69X; 197.91–207.06 mbsf). Burrows are present throughout the clay-dominated section; these are millimeter scale and dominantly horizontal where color banding is preserved and centimeter scale where color banding is disrupted. Bedding is contorted at a range of scales through the interval (Cores 313-M0027A-65X through 69X; 192.11–207.06 mbsf) (e.g., small-scale soft-sediment folding at 201.49 mbsf; Section 313-M0027A-68X-1, 53 cm) (Fig. **F10**). Homogeneous silty clay with common shell layers (bivalve and gastropods), foraminifers, and diatoms occurs below (Cores 313-M0027A-70X through 75X; 207.06–219.26 mbsf).

The lowest part of this lithologic unit comprises a series of at least four ~5–10 m thick sedimentary cycles bounded sharply at their bases by beds of very coarse sand and/or granules. Examples are Sections 313-M0027A-75X-2, 50 cm (218.21 mbsf); 80R-1, 10 cm (225.46 mbsf) (Fig. **F11**); 82R-1, 1 cm (231.47 mbsf); and, at the base of the unit, 83R-2, 26 cm (236.16 mbsf). Burrows commonly pipe coarse sediments down into underlying fine sediments (Fig. **F12**). Each cycle coarsens downhole, and the lower two cycles are glauconitic at the base. Successive cycles become notably thinner downhole.

Interpretation

At the base of the unit, fining-upward sedimentary cycles are interpreted as having been deposited in transgressive shoreface evolving through shoreface–offshore transition to offshore environments. These cycles are interpreted as incomplete depositional sequences in which regressive facies successions are missing and, presumably, subsequently eroded. The highest part of the unit represents shoreface–offshore transition and offshore environments subject proximally to episodic influx of sand due to storm events and distally to episodic input of mud, also possibly a result of storm-related processes. The thick clay-prone succession is interpreted as an offshore environment in a topset position. Soft-sediment folding indicates postdepositional disruption of the succession. This could be caused by downslope sediment transport, although an alternative interpretation is deformation while in a cohesive state, perhaps related to overpressure in the underlying sands (see **"Unit II"** in **"Lithostratigraphy"** in the "Site M0028" chapter). Fine sand at the top of the unit (Cores 313-M0027A-58H and 59H) is interpreted as shoreface–offshore transition and shoreface and signifies shallowing.

Unit III

Interval: 313-M0027A-83R-2, 126 cm, to 102R-2, 105 cm
Depth: 236.16–295.01 mbsf
Age: early middle to late early Miocene (early Langhian to late Burdigalian)

Recovery of this interval was excellent (~99%). The top of the unit (Sections 313-M0027A-83R-2, 126 cm, to 87R-2, 156 cm; 236.16–249.76 mbsf) comprises medium gray to dark gray-brown clay with faint laminations defined by weak concentrations of plant debris. A thin sharp-based horizon comprising calcilutite occurs in interval 313-M0027A-84R-3, 76.5–80 cm (244.375–244.41 mbsf) (Fig. **F13**). The clay passes down into a lithologically more varied succession of sandy mud and silty sand and gravel in Cores 313-M0027A-88R through 96R (249.76–274.21 mbsf). Sandy mud gradually coarsens downhole to a sharp basal contact separating granule-rich sandy silt above from silt (containing complete turritellid gastropods) below (Section 313-M0027A-89R-1, 40 cm; 253.21 mbsf) (Fig. **F14**). The silt succession sharply overlies glauconitic shelly and silty sand across a surface marked by fragmented shells (Section 313-M0027A-89R-2, 85 cm; 255.16 mbsf) (Fig. **F15**). A further abrupt and weakly bioturbated surface separates coarse glauconite-rich sand with granules and

sandy silt above from silt below (Section 313-M0027A-90R-1, 33 cm; 256.09 mbsf). The underlying silt has discrete beds of clayey silt and sandy silt with parallel to subparallel lamination and little evidence of bioturbation (Sections 313-M0027A-90R-1, 33 cm, to 95R-1, 14 cm; 256.09–271.25 mbsf). This part of the succession is initially dominantly silt, with shell-lined burrows and rare shell-hash layers (Cores 313-M0027A-91R and 92R; 258.91–265.01 mbsf), but coarsens downhole with an increasing number and thickness of silty very fine to fine sand beds with shell fragments. Beneath a marked surface, the succession changes to coarse sand with granules, pebbles, and woody debris (Section 313-M0027A-95R-1, 14 cm; 271.25 mbsf).

Below a 1 m coring gap, the succession is sandy silt and silty sand containing normally graded sand beds with concave-downward lamination and low-angle truncation surfaces (e.g., Sections 313-M0027A-96R-1, 22 cm, to 96R-1, 39 cm; 274.38–274.55 mbsf) (Fig. F16). Overall, the succession continues to fine downhole and is principally dark brown clay with thin interbeds of very fine sand, silt, or shells. Sand and shell beds thin downhole from thin beds to thick laminae. Where undisturbed by drilling, they are sharp based and graded normally. Core 313-M0027A-100R (286.36–289.41 mbsf) represents overall the finest grain size in this sediment package. The base of the unit occurs in Section 313-M0027A-102R-2, 105 cm (295.01 mbsf), where ~1.5 m of coarse to very coarse poorly sorted glauconitic (2%) sand with plant debris and angular quartz sits sharply on a prominent burrow-galleried erosion surface cut into the silt of Unit IV (Fig. F17).

Interpretation

The major erosion surface at the base of the subunit in Section 313-M0027A-102R-2, 105 cm (295.01 mbsf) is overlain by ~1.5 m of very coarse glauconitic sand interpreted as a transgressive lag deposited in a shoreface environment. This sand grades abruptly uphole into the weakly laminated brown clays with thin beds of silt and shells that represent a shoreface–offshore transition environment characterized by deposition of thin storm beds under low-oxygen conditions, reaching a maximum water depth and a maximum flooding at ~288 mbsf (Core 313-M0027A-100R). Above this level, the succession contains more frequent interbeds of very fine sand and is interpreted as a regressive shoreface–offshore transition zone. Further coarsening-upward into sediments with discrete very fine sand beds containing hummocky cross stratification indicates a storm-dominated shoreface–offshore transition setting. The storm beds become increasingly amalgamated, and the coarse sand in interval 313-M0027A-95R-1, 14–68 cm (271.25–271.79 m), suggests a shoreface environment. The coarse sand is overlain by a prominent surface. The surface is interpreted as a flooding surface, without a transgressive lag (Section 313-M0027A-95R-1, 14 cm; 271.25 mbsf).

The overlying well-stratified silt-rich succession (~15 m thick) with discrete shell-rich layers, commonly in life position, indicates a generally low-energy offshore environment, with individual beds interpreted as deposits of distal storm events. An interval with less sand or silt may be the deepest environment in this setting (Section 313-M0027A-92R-2; ~263 mbsf) and may represent the maximum flooding surface (MFS). Above this level, the uphole trend is shallowing with greater influence of storm activity to an abrupt contact with glauconitic coarse sand with thick-shelled bivalves (Section 313-M0027A-90R-1, 33 cm; 256.19 mbsf), indicating a high-energy shoreface environment. This contact is interpreted as a sequence boundary between shoreface–offshore transition deposits below and shoreface deposits above (see **"Stratigraphic correlation"**). This thin unit fines slightly uphole and then coarsens uphole to an abrupt flooding surface 0.93 m higher, which may indicate preservation of sea level lowstand deposits. A 2 m thick silt succession, rich in gastropod shells, is abruptly overlain by a dark brown sandy mud that has a fining, deepening-upward trend to another abrupt contact (Section 313-M0027A-88R-1, 68 cm; 250.44 mbsf), above which a clayey silt to silty clay also shows a weak deepening-upward trend in an offshore setting. The overall significance of these contacts at the top of meter-scale fining-upward silt-prone units (shoreface–offshore transition zone to offshore) is not clear (i.e., parasequence or sequence versus autogenic). Clays and silts at the top of the unit (236.16–249.76 mbsf) are interpreted as offshore with very minor reworking of silt and very fine sand from updip.

The following Units IV–VIII are summarized in Figure F4 and described hereafter.

Unit IV

Interval: 313-M0027A-102R-2, 105 cm, to 116R-1, 77 cm

Depth: 295.01–335.93 mbsf

Age: middle early Miocene (mid-Burdigalian)

Core recovery for this unit was excellent (98%). The unit comprises mostly medium gray to gray-brown silt, more or less rich in very fine sand, with abundant macroscopic dispersed plant debris and mica grains and scattered gastropod and bivalve shells. The succession is strongly bioturbated. Rare thin

beds of parallel-laminated fine sand represent discrete depositional events (e.g., in intervals 313-M0027A-107R-2, 24–29 cm [Fig. F18], and 110R-2, 80–83 cm; 309.45–309.50 and 319.16–319.19 mbsf). A normally graded interval of sandy silt to shelly very fine to fine sand has an abrupt basal contact modified by burrows (*Thalassinoides*) that penetrate the underlying silt to 39 cm (Section 313-M0027A-114R-2, 133 cm) (Fig. F19). Very fine sandy silt continues down to an abrupt contact with the underlying unit (Section 313-M0027A-116R-1, 91 cm; 336.07 mbsf).

Interpretation

The succession is interpreted as having been deposited mostly in deepening-upward packages of river-influenced shoreface–offshore transition to offshore setting (prodelta), with graded shell beds (storms) and high silt and plant debris content (rivers). The thick graded sandy interval overlying an abrupt surface at 331.85 mbsf (Section 313-M0027A-114R-2, 133 cm) (Fig. F19) is interpreted to represent abrupt shallowing from an offshore silt below to shoreface sand above and may be a sequence boundary.

Unit V

Interval: 313-M0027A-116R-1, 77 cm, to 125R-CC, 12 cm
Depth: 335.93–355.72 mbsf
Age: middle early Miocene (early–middle Burdigalian)

This unit is poorly recovered (64%). The lithology is typically very poorly sorted glauconite-rich (typically 3%–10%) coarse to very coarse sand. The maximum observed glauconite concentration in this unit occurs in Core 313-M0027A-120R (~342 m), where it is estimated at ~20% (Fig. F20). K/Th ratios in the spectral gamma ray log indicate a significant change to lower glauconite concentration at about the middle of the unit; this likely corresponds to Section 313-M0027A-121R-1, 110 cm (345.40 mbsf), where glauconite sand content decreases downhole from ~20% above to ~5% below Section 313-M0027A-122R-1, 28 cm (347.64 mbsf). Downhole, carbonate-cemented laminae and rare burrows are present, and soft mud is less prevalent. An abrupt contact with a ~15 cm thick carbonate-cemented bed lies at the base of the unit (interval 313-M0027A-125R-1, 132–147 cm; ~355.45–355.49 mbsf) (Fig. F21).

Interpretation

The environment of deposition of the coarse to very coarse glauconitic sand succession with carbonate cement concentrated at the base is poorly constrained. One interpretation is that sand is reworked by physical and biological processes in a transgressive shoreface to offshore setting. Seismic reflection data indicate a clinoform rollover position, and alternative environment of deposition interpretations include gulley fills or small deltas. Maximum condensation may correspond to the most glauconite rich interval (~342 mbsf).

Unit VI

Interval: 313-M0027A-125R-CC, 12 cm, to 170R-1, 109 cm
Depth: 355.72–488.75 mbsf
Age: middle early Miocene (late Aquitanian to early Burdigalian)

Subunit VIA

Interval: 313-M0027A-125R-CC, 12 cm, to 145R-2, 120 cm
Depth: 355.72–414.11 mbsf

Overall, 66% of this subunit was recovered. The unit was recovered least effectively where the lithology, as determined from downhole log signatures, is most variable: in the uppermost 10 m and the lowermost 20 m. The subunit comprises mostly gray quartz-rich coarse–medium sand with ~3% black nonorganic detrital grains (Fig. F22), wood debris, and shell debris. There is a general downhole decrease in grain size from coarse to medium sand and an increase in bioturbation. *Cylindricnus* (distinctive concentrically backfilled burrows) occurs near the top of the subunit (e.g., interval 313-M0027A-127R-1, 60–95 cm; 360.16–360.51 mbsf). Sorting is moderately good, although granules occur throughout some intervals (e.g., interval 313-M0027A-129R-1, 60–100 cm; 366.26–366.66 mbsf). Thick beds exhibiting sets of low-angle inclined stratification alternate with more homogeneous bioturbated intervals (Fig. F22). Near the base of the subunit, silt laminae are present (e.g., interval 313-M0027A-144R-1, 119–121 cm; 409.55–409.57 mbsf) (Fig. F23).

Interpretation

The lower, slightly muddy sands are interpreted as (lower) shoreface deposits at the base of cleaner (upper) shoreface deposits. Low-angle cross-lamination, burrows, and shell fragments support an upper shoreface to foreshore environment sustained over >30 m, which may indicate that sediment supply kept pace with relative sea level rise.

Subunit VIB

Interval: 313-M0027A-145R-2, 120 cm, to 170R-1, 109 cm
Depth: 414.11–488.75 mbsf

About 95% of this unit was recovered. The uppermost 40 cm comprises brown very fine sand and sandy silt (Sections 313-M0027A-145R-2, 120 cm, to 145R-CC, 10 cm; 414.11–414.51 mbsf). The bulk of the subunit is composed mostly of dark brown silt and clayey silt with common mica flakes and abundant dispersed plant debris (Fig. F24). Thin-shelled bivalves, commonly intact, occur throughout. Well-defined thin beds of very fine sand occur sporadically in the top 25 m and show strong parallel lamination or climbing-ripple cross-lamination (e.g., Sections 313-M0027A-148R-1, 421 mbsf [Fig. F25], and 149R-2, 425 mbsf). The succession is well bioturbated at the top but is more weakly bioturbated in the middle, with weak parallel fine lamination and streaky fabric predominant in Sections 313-M0027A-152R-1 (434 mbsf) through 164R-2 (472 mbsf). A trace of glauconite grains occurs in Core 313-M0027A-161R. Diatoms are present in smear slides.

Below ~468 mbsf (Core 313-M0027A-163R), corresponding to a prominent seismic reflector (see "Stratigraphic correlation") and a downhole decrease in density, the succession gradually becomes more coarse grained, with sediment grading from dark brown silt into brown fine sandy silt and eventually to greenish gray fine glauconitic sand with rare burrows (Core 313-M0027A-167R; 478 mbsf). Below this level, glauconite sand becomes progressively more abundant, and bioturbation and shell content increases to an abrupt change across a bioturbated surface to coarse, poorly sorted glauconitic sand in Section 313-M0027A-168R-2, 55 cm (483.64 mbsf) (Fig. F26), that continues to the base of the subunit.

Interpretation

The lower part of the subunit is interpreted as having been deposited in relatively deep water by the reworking and transport of materials derived from the top and slope of the previously deposited clinothem via sediment gravity flows into a toe-of-clinoform-slope apron setting. The upper part of the succession, characterized by high amounts of plant debris and mica, low intensity of bioturbation, and common thin-shelled bivalves, is interpreted as having been deposited in a poorly oxygenated, silt-dominated, river-influenced offshore (prodelta) setting. Thin beds of very fine sand with planar and climbing-ripple cross-lamination are interpreted as deposits of river flood events.

Unit VII

Interval: 313-M0027A-170R-1, 109 cm, to 223R-1, 69 cm
Depth: 488.75–625.60 mbsf
Age: early Miocene (early Aquitanian) to late early Oligocene

Subunit VIIA

Interval: 313-M0027A-170R-1, 109 cm, to 175R-3, 10 cm
Depth: 488.75–499.91 mbsf

This thin subunit is characterized by coarse grain sizes and strong glauconite enrichment. Lithology ranges from glauconitic quartz sand with coarse quartz granules and clay beds to quartz-rich glauconite sand. Sorting is moderate to poor, and sediments are locally carbonate cemented (intervals 313-M0027A-171R-1, 31–63 cm, and 171R-2, 40–130 cm; 489.70–490.01 and 491.39–492.19 mbsf). Bioturbation is variable, and, where weakly developed, sediment is well bedded and occasionally normally graded (e.g., interval 313-M0027A-174R-1, 110–121 cm; 494.86–494.97 mbsf) (Fig. F27). The maximum glauconite concentration is estimated as ~80%–90% in interval 313-M0027A-172R-1, 31–63 cm (489.70–490.01 mbsf). At several levels, pale brown clay with nannofossils occurs in thin beds and as burrow fills, including *Chondrites*. Bedding is predominantly horizontal, but locally the clay and sand interbeds are inclined to ~15° (apparent dip) (interval 313-M0027A-171R-2, 66–105 cm; 491.55–494.91 mbsf) (Fig. F28), possibly representing migration of a dune-scale bedform. The transition to the underlying subunit at Section 313-M0027A-175R-3, 10 cm, is subtle.

Interpretation

The coarse, poorly sorted glauconite sand at the base of the unit is interpreted as a relatively deep shelf (~100 m water depth) sediment-starved deposit with abundant in situ deepwater glauconite. This becomes mixed with increasingly coarse quartz sand and granules uphole to the abrupt facies change in Section 313-M0027A-170R-1, 109 cm (488.75 m), which marks the top of the unit. Graded beds with angular quartz and rounded glauconite in inclined beds and the well-stratified succession with nannofossils in clay laminae suggest a sediment supply via sediment gravity flows (turbidity currents and debris flows) in a deepwater apron environment (i.e., seaward of the toe-of-clinoform break in slope). Sediment was likely sourced from a clinoform rollover location that may either have been exposed or flooded. These deposits may have a channelized context.

Subunit VIIB

Interval: 313-M0027A-175R-3, 10 cm, to 223R-1, 69 cm
Depth: 499.91–625.60 mbsf

This thick subunit (125.69 m thick) is characterized by strong glauconite sand enrichment in fine sand or a matrix of silt. Gradual cyclic changes in average grain size and glauconite content occur downcore on the scale of 5–10 m, but there is also a large-scale downhole trend from very fine sand at the top to silt near the base. Glauconite sand content locally reaches as high as 60% (e.g., Core 313-M0027A-188R) but is generally in the range of 5%–20%. Quartz granules occur rarely (e.g., at a sharp contact between very fine sand and clayey silt in Core 313-M0027A-201R). Trace mica occurs throughout. The sediment fabric is structureless overall and presumed to be intensely bioturbated; locally, muddy laminae are observed (e.g., Core 313-M0027A-200R). An interval of glauconite-rich well-sorted fine sand with ripple-scale cross-lamination occurs in Cores 313-M0027A-191R and 192R. Ripple cross-lamination also occurs in other sand-rich intervals (e.g., Cores 313-M0027A-202R and 205R). Further downsection, primary parallel lamination is developed (Cores 313-M0027A-215R through 217R). Thin-shelled bivalves (e.g., Core 313-M0027A-207R) and benthic foraminifers are common (e.g., 3% in Core 313-M0027A-192R) throughout Cores 313-M0027A-188R through 198R and 210R through 217R. Woody debris (e.g., Core 313-M0027A-191R) is common at several levels, and distinct burrow forms are also recorded (e.g., *Diplocraterion* in Cores 313-M0027A-186R and 198R, ?*Teichichnus* in Cores 190R and 198R, *Chondrites* in Core 221R, and possible *Zoophycos* in Core 223R). Pyrite is common as a diagenetic mineral, observed to have replaced shell material, in Cores 313-M0027A-218R through 222R. The base of the unit is marked by a highly bioturbated contact between silty sand above and silty clay below.

Interpretation

The basal strata of the unit comprise sandy silt coarsening down to silty sand on an abrupt and highly bioturbated (*Thalassinoides*) contact with pale green silty clay from the underlying unit. Bottom water oxygen content is interpreted as reduced in the lower ~20 m of the succession based on burrow type and sulfide mineral precipitation. Glauconite sand is interpreted as a mixture of in situ grains and grains reworked from shallower water. The environment of deposition of the overlying strata is interpreted as coalesced fans beyond the toe-of-clinoform slope with sediment deposited from density flows.

Unit VIII

Interval: 313-M0027A-223R-1, 69 cm, to 224R-3, 19 cm

Depth: 625.60–631.15 mbsf

Age: late Eocene?

This unit represents only the top part of a likely much thicker unit that was not drilled. Gray-brown bioturbated silty clay with trace mica and scattered glauconite sand is moderately well bioturbated with identifiable *Chrondrites* and *Planolites* (Fig. **F29**). Rare thin-shelled bivalves and foraminifers are present. Disseminated pyrite is present, locally replacing burrows. The top of the section has burrows piping down glauconitic sand ~30 cm from the overlying unit (Fig. **F30**).

Interpretation

The environment of deposition is interpreted as deep offshore with dysoxic bottom waters.

Computed tomography scans

Computed tomography (CT) was used on 38 whole-core samples from Hole M0027A to acquire two-dimensional (2-D) and three-dimensional (3-D) images. An example scan from Section 313-M0027A-69X-1 (204.01–205.51 mbsf) is illustrated in Figure **F31,** together with the line-scan image of the split core, magnetic susceptibility and density data from the multisensor core logger (MSCL), and an acoustic image from the borehole. This comparison enables better definition of sediment characteristics, structures, and lithologic boundaries. CT images shown were acquired in two perpendicular planes (see **"Lithostratigraphy"** in the "Methods" chapter).

Hole M0027A lithostratigraphic summary

Late Eocene deep offshore silty clay (Unit VIII) is abruptly overlain by late early Oligocene to early Miocene glauconitic clastics (Unit VII) that overall coarsen from silts to sands but comprise smaller scale cyclicity in grain size and glauconite content (Fig. **F32**). These are interpreted to be deepwater apron deposits seaward of the lower clinoform break in slope that are overstepped by less glauconitic toe-of-slope and clinoform slope deposits (Subunit VIIA). Unit VI marks the progradation of a storm-dominated river-influenced delta, which is abruptly capped by poorly sorted coarse-grained deposits in a clinoform rollover position. The overlying succession (Units IV and III) comprises a series of deepening-upward packages, with less common shallowing-upward packages in storm-dominated shoreface, shoreface–offshore transition, and offshore settings in clinothem topset position. Unit II, which comprises a series of top-truncated deepening-upward sequences from shoreface through shoreface–offshore transition to offshore settings, overall fines uphole to a thick clay-prone succession. Unit I comprises a

range of fluvial, coastal plain, estuarine, and shoreface environments.

Paleontology

Biostratigraphic age assignments in Hole M0027A were determined from integrated calcareous nannofossil, planktonic foraminifer, and dinocyst zonations (Fig. **F33**). Paleobathymetry and paleoenvironments were determined from benthic foraminifers, dinocysts, and terrigenous palynomorphs. Palynomorph studies allowed for interpretation of both marine and terrestrial paleoenvironments. Calcareous microfossil occurrences ranged from absent to abundant, and preservation ranged from poor to excellent, with the best preserved, most abundant specimens and most diverse assemblages often occurring in the finer grained sediments. In general, organic microfossils were abundant and well preserved in fine-grained sediments. Reworking of all microfossil groups was found in some samples and was distinguished from in situ assemblages.

Pleistocene, Miocene, Oligocene, and possible uppermost Eocene sections were identified and integrated with Sr isotope stratigraphy to establish a chronostratigraphic framework for Hole M0027A (Fig. **F34**). The use of multiple planktonic microfossil zonations allowed ages to be refined, as the boundaries between nannofossil, planktonic foraminifer, and dinocyst zones tend to be offset. For example, planktonic foraminifer Zone M1/N4 overlaps with calcareous nannofossil Zone NN1 and dinocyst Zone DN1 only between 23.2 and 23.8 Ma, confirming that lowermost Aquitanian sediments were recovered in Hole M0027A. Similarly, the boundary between the early and middle Miocene, which falls within calcareous nannofossil Zone NN4 and dinocyst Zone DN4, was identified using the boundary between planktonic foraminifer Zones N7 and N8 (or M4 and M5).

Paleodepths varied throughout Hole M0027A, ranging from inner neritic (0–50 m) to outer neritic (100–200 m). In several sequences, paleobathymetric fluctuations indicated shallowing-upward successions that occurred within a sequence stratigraphic framework. In general, good correlation was found between sedimentary facies and benthic foraminifer biofacies. Similarly, benthic foraminifer water depth estimates and palynological estimates of proximity to shoreline were consistent. Palynological data support previous reconstructions of a warm, humid early Neogene climate.

Biostratigraphy

Calcareous nannofossils

A total of 86 samples from Hole M0027A were examined for calcareous nannofossil biostratigraphy. Sample spacing was generally one sample every three cores (approximately every 10 m), although fewer samples were taken within sandy units. Additional samples were also examined near sequence boundaries and when initial analysis indicated an unconformity. The total abundance of calcareous nannofossils within samples ranged from barren to very abundant. Preservation also varied significantly throughout the hole, ranging from poor to good, with the best preservation in the uppermost part of the hole. Members of the Noelaerhabdaceae family dominate assemblages throughout the hole. Reworked Paleogene material is also prevalent throughout.

Horizons recovered in Hole M0027A contain Pleistocene, Miocene, and Oligocene assemblages (Table **T4;** Fig. **F35**). Sediments from Cores 313-M0027A-1H through 13H (0–23.79 mbsf) are assigned to Martini's (1971) Zone NN21 based on the presence of *Emiliania huxleyi,* which first occurred at 0.25 Ma. This section can be further divided based on the zonation of Hine and Weaver (1998). Sediments from the top of the hole through Sample 313-M0027A-5H-CC (0–11.14 mbsf) contain common *E. huxleyi* and are tentatively assigned to the *Emiliania huxleyi* Acme Zone (<90 ka). Samples 313-M0027A-8H-1, 79 cm, to 13H-1, 111 cm (16.05–23.79 mbsf), contain assemblages with fewer *E. huxleyi* but common small *Gephyrocapsa* spp. and are therefore assigned to either the Transitional Zone or the *Gephyrocapsa aperta* Acme Zone, which together span 90–250 ka. A single sample from Core 313-M0027A-15H (27.42 mbsf) is tentatively assigned to Zone NN19 (0.41–1.97 Ma) based on the presence of a single *Pseudoemiliania ovata*. Samples from Cores 313-M0027A-17H through 51H (28.21–110.66 mbsf) are barren of nannofossils and are unzoned. Below the barren interval, samples from Cores 313-M0027A-59H through 69X (176.81–207.44 mbsf) contain poorly preserved calcareous nannofossils with no definitive age-diagnostic taxa, so that interval is also unzoned.

Two samples from Cores 313-M0027A-72H and 73X (210.67–212.13 mbsf) are assigned to undifferentiated Zone NN6/NN7 based on the last occurrence (LO) of *Coccolithus miopelagicus* (11.0 Ma). No other biostratigraphic events are found in the cores above the LO of *Sphenolithus heteromorphus,* making it impossible to further refine the zonal assignment at this time. This interval is characterized by the occurrence of a *Catinaster*-like species (possibly a broken

Discoaster) that makes zoning difficult without the presence of other index taxa.

The LO of *S. heteromorphus* is found in Sample 313-M0027A-75X-1, 100 cm (217.21 mbsf), although this may not be the actual extinction (13.6 Ma) of this species. The interval from this sample to Sample 313-M0027A-83R-3, 12 cm (236.52 mbsf), is assigned to Zone NN5 (13.6–15.6 Ma) based on the presence of *S. heteromorphus* and the absence of *Helicosphaera ampliaperta*. The LO of the latter species occurs in Sample 313-M0027A-86R-2, 130 cm (246.46 mbsf). There is no evidence of a hiatus above this sample, so this likely represents the extinction of *H. ampliaperta,* which occurred at 15.6 Ma. The section from Core 313-M0027A-86R to Sample 313-M0027A-116R-1, 40 cm (335.56 mbsf), is assigned to Zone NN4 (15.6–18.3 Ma) based on the co-occurrence of *H. ampliaperta* and *S. heteromorphus* and the absence of *Sphenolithus belemnos*. The next core (313-M0027A-117R; 339.21 mbsf) contains a sparse assemblage of nannofossils that are not age diagnostic. The interval including Cores 313-M0027A-122R through 127R (347.46–360.94 mbsf) is barren of nannofossils. Cores 313-M0027A-139R and 142R (393.90–402.41 mbsf) also contain a sparse nannofossil assemblage that is not age diagnostic; therefore, the interval including Cores 313-M0027A-117R through 142R (339.21–402.41 mbsf) is unzoned.

A diverse nannofossil assemblage is present again beginning in Sample 313-M0027A-144R-1, 120 cm (409.56 mbsf). Characteristic lower Miocene marker taxa are rare or absent in sediments from Hole M0027A; therefore, the age assignment of this interval is based primarily on the absence of species, as well as the general assemblage. The assemblage in this sample is older than the first occurrences (FOs) of *S. heteromorphus* (18.2 Ma) and *H. ampliaperta* (~21.0 Ma), although the age of the latter datum is not well constrained. *Triquetrorhabdulus carinatus,* the LO of which marks the base of Zone NN3 (19.6 Ma), is sporadically present below this horizon, indicating Zone NN2 or older. Furthermore, the interval from Sample 313-M0027A-144R-1, 120 cm, to 174R-1, 123 cm (409.56–494.99 mbsf), is above two secondary events: the last common occurrence of *T. carinatus* (22.9 Ma), which is near the base of Zone NN2, and the crossover in abundance of *Helicosphaera euphratis* with *Helicosphaera carteri,* which is tentatively dated to 21.5 Ma. This interval also contains consistently present *Cyclicargolithus floridanus,* as well as more frequent occurrences of *Discoaster deflandrei*. Thus, samples from Cores 313-M0027A-144R through 174R (409.56–494.99 mbsf) are assigned to Zone NN2 and most likely the middle part of the zone, ~21–21.5 Ma. A single sample from Core 313-M0027A-177R (504.78 mbsf) contains few calcareous nannofossils that are not age diagnostic.

A significant change in assemblage occurs in Sample 313-M0027A-179R-2, 10 cm (508.24 mbsf). This sample contains common *C. floridanus,* as well as frequent *H. euphratis* and *T. carinatus*. This sample also contains *Helicosphaera recta,* which was once used as a marker for the boundary between Zones NP25 and NN1, which approximates the Oligocene/Miocene boundary. This species is now known to occur within the lower Miocene (Perch-Nielsen, 1985), but the combination of assemblage change and occurrence of *H. recta* suggests that samples from Cores 313-M0027A-179R through 183R (508.24–515.14 mbsf) can be assigned to the lowermost portion of Zone NN1, very near the Oligocene/Miocene boundary. The LO of *Sphenolithus ciperoensis* (24.75 Ma), which marks the top of Zone NP25 and approximates the top of the Oligocene, occurs in Sample 313-M0027A-186R-1, 34 cm (521.55 mbsf). There is no evidence of a hiatus between the samples assigned to lowermost Zone NN1 and Zone NP25.

The LO of *Sphenolithus distentus* (27.5 Ma), which marks the base of Zone NP25, is somewhat problematic in this hole. Sphenoliths are not very abundant in these sediments, and moderate preservation makes it difficult to distinguish between *S. distentus* and *S. ciperoensis*. A questionable specimen of *S. distentus* occurs in Sample 313-M0027A-192R-1, 37 cm (539.88 mbsf), whereas *S. distentus* is definitely present in Sample 313-M0027A-199R-1, 18 cm (554.94 mbsf). Thus, the interval including Cores 313-M0027A-192R through 196R (539.88–549.03 mbsf) is assigned to undifferentiated Zone NP24/NP25. Sediments from Samples 313-M0027A-199R-1, 18 cm, through 218R-2, 103–106 cm (554.94–615.24 mbsf), are assigned to Zone NP24 based on the sporadic co-occurrence of *S. distentus* and *S. ciperoensis*. The FO of the latter species marks the base of Zone NP24 at 29.9 Ma.

Below Core 313-M0027A-218R (615.24 mbsf), there appear to be several hiatuses separated by sediments of different ages. These sediments could represent stacked condensed sections formed during periods of low sedimentation rate. Samples from Cores 313-M0027A-220R and 221R (620.80–624.77 mbsf) contain a lower Zone NP23 assemblage based on the absences of *S. distentus* (FO 30.4 Ma) and *Reticulofenestra umbilicus* (LO 32.3 Ma). The LO of the latter occurs in Sample 313-M0027A-222R-CC (624.97 mbsf). The presence of a few specimens of *R. umbilicus,* together with frequent *Isthmolithus recurvus* (LO 32.46 Ma), suggests that the upper portion of Zone NP22 is missing in this hole. Thus, sediments from Samples 313-M0027A-222R-CC to 223R-1, 26 cm

(624.97–625.17 mbsf), are assigned to lower Zone NP22.

The LO of *Ericsonia formosa* (32.8 Ma), which marks the base of Zone NP22, is found in Sample 313-M0027A-223R-1, 146 cm (626.37 mbsf). Because this species is found in frequent numbers in this sample, the upper portion of Zone NP21 is likely missing in Hole M0027A. A sample from the base of the hole, within Core 313-M0027A-224R (631.09 mbsf), contains a very abundant assemblage characteristic of the Eocene–Oligocene transition (EOT). *E. formosa, R. umbilicus,* and *I. recurvus* are much more abundant in this assemblage. The base of Zone NP21 is marked by the LO of *Discoaster saipanensis,* the last of the rosette Paleogene discoasters. This species does not occur in the sediments of Hole M0027A, although the LO of *D. saipanensis* (34.2 Ma) occurs a few hundred thousand years prior to the Eocene/Oligocene boundary (33.7 Ma) (Coccioni et al., 2008). Thus, the oldest sediments from this hole are assigned to lower Zone NP21, which spans the Eocene/Oligocene boundary. These sediments could be uppermost Eocene or lowermost Oligocene; further biostratigraphic analyses of calcareous nannofossils and planktonic foraminifers are necessary to further refine this age estimate.

Planktonic foraminifers

A total of 79 samples from Cores 313-M0027A-6H through 224R (13.75–631.15 mbsf) were examined in this study; only samples containing planktonic foraminifers are shown in Figure **F36** and Table **T5.** Primarily core catcher samples obtained during drilling and processed prior to the Onshore Sampling Party (OSP) were picked for planktonic foraminifers, although some additional samples from split cores were washed and picked during the OSP. Planktonic foraminifers indicate that the Miocene section in Hole M0027A extends from at least 213.14 to ~509.19 mbsf between Samples 313-M0027A-73X-CC, 0–3 cm, and 179R-CC, 2–4 cm. The Oligocene occurs between Samples 313-M0027A-179R-CC, 13–15 cm, and 214R-CC, 12–14 cm (509.30–602.01 mbsf). Eocene sediments may occur in the deepest Sample 313-M0027A-224R-CC (631.15 mbsf). Key marker species for identifying the Oligocene/Eocene boundary (e.g., *Hantkenina* and the *Turborotalia cerroazulensis* lineage) are absent, so further work is needed to confirm the presence of uppermost Eocene strata.

Planktonic foraminifers are present in low abundances but are well preserved in Hole M0027A. Typical middle Miocene assemblages are present between Samples 313-M0027A-80R-CC and 98R-1, 141–145 cm. The LO of *Paragloborotalia mayeri* occurs in Sample 313-M0027A-80R-CC, 0–15 cm (227.65 mbsf). This event marks the base of Zone M12/N15 at 11.4 Ma, indicating this sample is at least that old. Sample 313-M0027A-89R-CC, 0–2 cm (255.90 mbsf), contains well-preserved species of *Praeorbulina sicana.* The LO of this species is at 14.8 Ma and approximates the base of Zone M7/N10. This species continues downcore through Sample 313-M0027A-98R-1, 141–145 cm (281.67 mbsf). The FO of *P. sicana* marks the base of Zone M5/N8 (16.4 Ma). Another key species is *Praeorbulina curva,* which is present in Sample 313-M0027A- 89R-CC, 0–2 cm (255.90 mbsf).

The lower Miocene extends from Sample 313-M0027A-101R-3, 34–38 cm (292.76 mbsf), through 179R-CC, 2–4 cm (509.19 mbsf). This interval is characterized by *Catapsydrax dissimilis, Fohsella peripheroronda, Globoquadrina baroemoenensis, Catapsydrax unicavus, Globorotalia praescitula, Globigerina angulisuturalis,* and *Globigerinoides primordius.* The LO of *C. dissimilis* (17.3 Ma) marks the base of Zone M4a/N7 and occurs in Sample 313-M0027A-101R-3, 34–38 cm (292.76 mbsf). A single *G. praescitula* is found in Sample 313-M0027A-151R-1, 155–160 cm (431.26 mbsf). The FO of this species falls within Zone M3/N6 at 18.5 Ma. *G. angulisuturalis* is found within Sample 313-M0027A-154R-2, 72–77 cm (441.08 mbsf). The LO of this species occurs at 21.6 Ma, within Zone M1/N4. *Paragloborotalia kugleri,* a species confined to Zone M1/N4, occurs in Sample 313-M0027A-179R-CC, 2–4 cm (509.19 mbsf). The FO of this species is at 23.8 Ma, indicating that the interval from 441.08 to 509.19 mbsf is dated to 21.6–23.8 Ma.

The FO of *G. primordius* (26.7 Ma) is found in Sample 313-M0027A-179R-CC, 13–15 cm (509.30 mbsf). This event falls within Zone O6/P22. This sample is also characterized by *Paragloborotalia opima nana,* a species with a range that extends into the basal Miocene; thus, these sediments are tentatively assigned to the uppermost Oligocene but could range into the lowermost Miocene. Definite Oligocene sediments are found below this sample based on the absence of *G. primordius*. *Paragloborotalia* cf. *opima opima* occurs in Sample 313-M0027A-195R-2, 9–11 cm (549.60 mbsf). No definite specimens of *Paragloborotalia opima opima,* the LO of which marks the base of Zone O6/P22 at 27.1 Ma, were observed at Site M0027; however, the presence of similar forms suggests this sample may be older than 27.1 Ma. The next biostratigraphically useful taxon found is *Globigerina ampliapertura* (LO 30.3 Ma), which marks the base of Zone O3/P20. The LO of this species occurs in Sample 313-M0027A-209R-3, 33–36 cm (588.51 mbsf), indicating Zone O2/P19. The interval between Samples 313-M0027A-217R-3, 10–12 cm, and

223R-CC, 18–20 cm (612.76–627.56 mbsf), is barren of planktonic foraminifers.

The LO of *Pseudohastigerina* spp. (32.0 Ma) marks the base of Zone O2/P19. The last sample examined (Sample 313-M0027A-224R-CC; 631.15 mbsf) contains *Pseudohastigerina micra*, indicating that the base of the hole is at least lowermost Oligocene Zone O1/P18. The Eocene/Oligocene boundary is correlated using the LO of the genus *Hantkenina* (33.8 Ma). A secondary marker for this event is the FO of *Cassigerinella chipolensis*. These species were not observed in Hole M0027A, suggesting that the oldest sediment recovered is lowermost Oligocene. The presence of large, flattened Eocene subbotinids (*Subbotina eocaena* and *Subbotina cryptomphala*) could suggest the section is Eocene, although these species could range into the Oligocene. A single Sr isotope age of ~34 Ma suggests an Eocene correlation (see **"Chronology"**). Analysis of additional samples from the base of the hole is necessary to determine if the section is uppermost Eocene or lowermost Oligocene.

Dinocysts

A total of 47 samples between Samples 313-M0027A-9H-CC and 223R-CC (19.59–627.58 mbsf) were examined for dinocysts (Fig. **F37;** Table **T6**). Sample 313-M0027A-9H-CC (19.59 mbsf) is assigned to the Pleistocene on the basis of sparse dinocyst assemblages dominated by *Bitectatodinium tepikiense* together with *Brigantedinium* spp., *Tectatodinium pellitum*, and *Selenopemphix nephroides*. Sample 313-M0027A-50H-CC (96.12 mbsf) was barren of palynomorphs. The presence of *Habibacysta tectata, Labyrinthodinium truncatum modicum, Labyrinthodinium truncatum truncatum, Paleocystodinium golzowense, Trinovantedinium papulum*, and *Hystrichosphaeropsis obscura* constrains the age of Samples 313-M0027A-65X-CC through 67X-CC (195.53–201.22 mbsf) to dinocyst Zones DN5–DN8. Sample 313-M0027A-69X-CC (207.44 mbsf) is assigned an age of late Serravalian to early Tortonian (Zones DN7–DN8; 12.8–8.6 Ma) based on the occurrence of *Erymnodinium delectabile* together with *T. papulum*, as well as common *Batiacasphaera sphaerica*. The occurrence of *Apteodinium tectatum, Unipontedinium aquaeductum, Systematophora placacantha, L. truncatum truncatum*, and *L. truncatum modicum* constrains the age of Sample 313-M0027A-91R-CC (262.05 mbsf) to the lower part of Zone DN5 (~15.2–14.2 Ma), around the Langhian/Serravalian boundary.

Sample 313-M0027A-101R-CC (292.91 mbsf) is assigned to Zone DN3 (late Burdigalian; ~18.6–16.8 Ma) based on the occurrence of *Lingulodinium multivirgatum, Distatodinium paradoxum, Cousteaudinium aubryae*, and *Cerebrocysta poulsenii*. A sparse assemblage in a terrigenous-dominated slide allows a minimum age of 15.2 Ma (top of Zone DN4) for Samples 313-M0027A-105R-CC and 146R-CC (304.95 and 417.57 mbsf) based on the presence of *A. tectatum, C. aubryae*, and *Pentadinium laticinctum*. These samples are thus tentatively assigned to Zone DN3, given the well-constrained age of overlying Sample 313-M0027A-101R-CC (292.91 mbsf). Samples 313-M0027A-149R-CC through 177R-CC (426.71–505.33 mbsf) are assigned to Zone DN2, which spans 22.2–19.1 Ma (late Aquitanian–early Burdigalian) based on the common presence of dinocysts typical of the lower Miocene (e.g., *L. multivirgatum, Tityrosphaeridium cantharellum, Cribroperidinium tenuitabulatum*, and *Cerebrocysta satchelliae*). Following de Verteuil and Norris (1996), the presence of *Exochosphaeridium insigne* suggests an early Burdigalian rather than late Aquitanian age over most of this interval (Samples 313-M0027A-155R-CC through 167R-CC; 445.17–481.60 mbsf), although others have found *E. insigne* lower in the Burdigalian.

Samples 313-M0027A-185R-CC through 191R-CC (520.96–539.19 mbsf) are assigned to Zone DN1 (latest Chattian–Aquitanian; ~22.2–25.2 Ma), the lower boundary age of SNSM1 from Munsterman and Brinkhuis (2004). Common dinocysts in sediments assigned to Zone DN1 in Hole M0027A are *Chiropteridium galea, Deflandrea phosphoritica, Dinopterygium cladoides, Homotryblium floripes, Homotryblium vallum, Glaphrocysta* spp., and *C. satchelliae*. Samples 313-M0027A-192R-CC through 193R-CC (542.48–545.61 mbsf) are assigned to the uppermost Oligocene (Chattian) based on the presence of *C. galea* and *Glaphrocysta* spp. together with *Distatodinium biffii*, as well as *Apteodinium australiense, Polysphaeridium zoharyi*, and *S. placacantha*. The presence of genera that do not extend into the Chattian (e.g., *Phthanoperidinium, Areosphaeridium, Diphyes, Charlesdowniea*, and *Rhombodinium*) allows Samples 313-M0027A-204R-CC through 220R-CC (573.01–620.83 mbsf) to be assigned to the Rupelian. Based on the absence of Oligocene markers and the presence of *Svalbardella cooksonia*, Sample 313-M0027A-223R-CC (627.58 mbsf) is tentatively assigned a middle–late Eocene age.

Paleoenvironment

Benthic foraminifers

Benthic foraminifers were examined from 77 (primarily core catcher) samples from Hole M0027A: Samples 313-M0027A-6H-1, 145–150 cm (12.99 mbsf), through 223R-CC (627.96 mbsf). Benthic foraminifer abundances ranged from absent to abundant, and preservation ranged from poor to excellent. Poorly preserved specimens are likely to have

been reworked and were not used in paleodepth estimates. The long-term change in paleodepth from the Eocene(?)–Oligocene to the modern seafloor is reflected in the overall shallowing from the outer neritic zone (100–200 m) to the inner neritic zone (0–50 m), with the present water depth at 33.5 m (Fig. F38; Table T7). Benthic foraminifer biofacies changes within this section indicate additional, higher resolution paleodepth variations superimposed on the long-term trend. Barren intervals occur throughout the section and may indicate nearshore/nonmarine environments, substantial downslope transport, or dissolution. It should be noted that the low-resolution shipboard sampling interval did not bracket all lithologic changes and that the sampling interval varied throughout the hole.

Stratigraphic biofacies distributions may be related to substrate (finer grained versus sandier sediments), changes in sediment input, and/or organics/dysoxia, which often correspond to bathymetry. Comparisons in Hole M0027A show good correspondence between sedimentary facies and biofacies, with shallower water biofacies (<50 m) occurring in the sandier intervals of the shoreface–offshore transition (between storm wave base and fair-weather wave base) and deeper water biofacies (50–80 m) occurring in the siltier intervals of the offshore sedimentary facies (deeper than storm wave base). In addition, preliminary results presented here suggest that benthic foraminifer biofacies changes in Hole M0027A indicate that paleobathymetric fluctuations occur within a sequence stratigraphic framework, with several sequences showing a shallowing-upward succession. Detailed higher resolution postcruise studies will elaborate on this.

Samples above Sample 313-M0027A-70X-CC (208.92 mbsf) were barren or contained only one or two specimens of foraminifers; no paleodepth could be determined for these samples (Fig. F38). In and below this (Miocene Samples 313-M0027A-70X-CC, 0–2 cm, to 98R-1, 144–145 cm; 208.92–281.70 mbsf), paleowater depths varied within the inner neritic zone from ~15 to 50 m. These samples are dominated by *Nonionella pizarrensis/Nonionella miocenica stella, Hanzawaia concentrica/Hanzawaia hughesi,* and *Lenticulina* spp. (including *Lenticulina americana*). Samples characterized by abundant *H. concentrica/H. hughesi* (in the absence of *Nonionella*) indicate depths of ~10–25 m, whereas samples dominated by *N. pizarrensis/N. miocenica stella* indicate somewhat greater depths of ~25–50 m. Occasional specimens (typically rare to few) of *Bolivina* spp., *Bulimina mexicana, Buliminella gracilis, Cancris sagra, Cibicides lobatulus, Cibicidoides* spp., *Fissurina* spp., *Lagena* spp., *Pararotalia bassleri, Plectofrondicularia morneyae, Rectuvigerina lamelata, Uvigerina juncea,* polymorphinids, and agglutinated benthic foraminifers are found in these samples.

Benthic foraminifer faunas indicate that paleowater depths varied from ~25–50 to ~75–100 m in Miocene Samples 313-M0027A-101R-3, 34–38 cm (292.76 mbsf), through 165R-CC, 5–7 cm (475.81 mbsf) (Fig. F38). Key depth-indicator taxa (*Hanzawaia* and *Nonionella*) for the inner neritic zone are discussed above. For the middle neritic zone (50–100 m), *B. gracilis* and *U. juncea* are excellent depth indicators and are found throughout this section (Table T7). Samples containing more abundant *B. gracilis* indicate slightly shallower paleodepths (50–80 m) than samples containing more abundant *U. juncea* (75–100 m), based on faunal studies from New Jersey coastal plain boreholes (Miller et al., 1997). Other rare to common species found in these *Buliminella/Uvigerina*–dominated faunas typically include *Bolivina* spp., *Cibicidoides* spp., *H. concentrica/H. hughesi, Lenticulina* spp., *Plectofrondicularia* spp., *Stilostomella* spp., and miliolids.

The deepest water benthic foraminifer associations (outer neritic; 100–200 m) were identified below reflector m6 in the Eocene(?)–Oligocene section (Samples 313-M0027A-179R-CC, 13–15 cm, through 223R-CC; 509.30–627.58 mbsf); however, there was significant within-sequence shallowing indicated by faunal changes (Fig. F38). In general, deeper water assemblages are more diverse with more abundant specimens and include taxa such as *Anomalinoides* spp., *Cassidulina* spp., *Cibicidoides pachyderma, Cibicidoides primulus, Coryphostoma georgiana, Globobulimina auriculata, Gyroidinoides* spp., *Hanzawaia mantaensis, Melonis barleeanum, Melonis pompilioides, Oridorsalis* sp., *Plectofrondicularia* spp., *Pullenia salisburyi, R. lamelata, Siphonina danvellensis, Sphaeroidina bulloides, Trifarina wilcoxensis,* polymorphinids, and agglutinated benthic foraminifers. Outer neritic faunas typically include shallower water benthic foraminifer taxa that either range to greater depths or were transported.

Terrestrial palynomorphs and palynofacies

Thirty-one samples from Hole M0027A were analyzed for palynomorphs. Sample spacing was fairly consistent for the lower Miocene and Oligocene sections (approximately one sample every three cores beginning at Core 313-M0027A-146R; 417.57 mbsf). Sample spacing was somewhat greater for the middle Miocene section, with seven samples examined between Samples 313-M0027A-65X-CC and 105R-CC (195.53–304.95 mbsf). Only one sample was examined for Pleistocene sediments. All samples contain numerous pollen grains and other palynomorphs

with generally good preservation, with the exception of one sandy sample. In some samples, pollen grains are filled with pyrite, hampering identification and assignment to herbal or arboreal taxa.

Results are discussed according to the age of the sediments: Pleistocene, middle Miocene, early Miocene, Oligocene, and the EOT. Age estimations are based on the Sr-based age model and biostratigraphic results. Percentages of palynomorphs are given with respect to the number of nonsaccate pollen (combined nonsaccate pollen is always 100%).

Pleistocene

One sample (313-M0027A-9H-CC; ~19.59 mbsf) from the Pleistocene was palynologically analyzed. The palynomorph assemblage is characterized by high bisaccate pollen content compared to nonsaccate pollen (Figs. **F39, F40**). Among the nonsaccate pollen, pollen of deciduous trees is most abundant. Grass, sedge, and herb pollen are also abundant (>15% grass and sedge pollen and >20% herb pollen) (Fig. **F40**). The sample is also characterized by high percentages of trilete spores, probably of the genus *Sphagnum*.

Dinocysts are rare in relation to nonsaccate pollen (~17%). Furthermore, the assemblages are dominated by only one cyst type (probably *B. tepikiense,* generally described as a freshwater and/or meltwater indicator. The amount of foraminifer test linings is very low (<2%). These findings imply that Hole M0027A was probably proximate to the coast during this interval, as higher abundances of foraminifer test linings would be expected in a more distal setting. This is in accordance with the benthic foraminifer–based water-depth reconstruction.

Pollen data imply that deciduous trees (probably deciduous oaks and birches) dominated the New Jersey hinterland during the interval represented by Sample 313-M0027A-9H-CC; however, conifers were widespread and probably also settled in the lowlands and on exposed shelf regions (Fig. **F39**). These findings indicate that the sample represents an interval of drier and/or cooler conditions compared to samples from the Miocene (see below). This is suggested by the comparatively high percentages of grass, sedge, and herb pollen, indicating vegetation similar to the modern onshore New Jersey coastal plain, which is dominated by mixed pine-oak forests and open vegetation sphagnum bogs/swamps. One sample between 19.59 and 195.53 mbsf was examined and found to be barren of pollen.

Middle Miocene (Serravallian and Langhian)

Four core catcher samples (313-M0027A-65X-CC, 67X-CC, 69X-CC, and 91R-CC; 195.53–262.05 mbsf) were analyzed for palynology and interpreted as middle Miocene (Serravallian and Langhian) based on pollen and dinocysts (Fig. **F39**). The lowermost sample is placed just below the lower/middle Miocene boundary based on the age-depth plot (see **"Chronology"**). Bisaccate pollen percentages are very low (~3% for the Serravallian and ~4%–13% for the Langhian) (Fig. **F40**). Nonsaccate pollen of arboreal taxa—mainly oak pollen—is most frequent and may indicate more extensive oak forests in the New Jersey hinterland. Hickory was probably also very frequent. Grass and herb pollen are rare in middle Miocene sediments, indicating a predominance of forests in the source region. Low percentages of the generally overrepresented bisaccate pollen may indicate that conifers (mainly pines) were only present in areas distant from the sea, probably in mountainous areas (Fig. **F39**). Climate conditions during the middle Miocene were probably warm and humid. Very low percentages of dinocysts (3%–8%) (Fig. **F40**) and foraminifer test linings suggest a shorter distance between Hole M0027A and the coastline.

Early Miocene (Burdigalian–Aquitanian)

Eighteen core catcher samples analyzed for palynology (Samples 313-M0027A-101R-CC through 191R-CC; 292.91–539.19 mbsf) (Table **T8;** Fig. **F39**) are interpreted as early Miocene (Burdigalian–Aquitanian) based on pollen and dinocysts (Fig. **F39**). This differs from the placement of the Oligocene/Miocene boundary at ~500 mbsf based on the age-depth plot (Fig. **F34**) but reflects the fact that the o.5 sequence from 494.87 to 539.5 mbsf straddles the Oligocene–Miocene transition. The uppermost samples from the upper Burdigalian (Fig. **F39**) are similar to the samples from the Langhian in terms of palynomorph assemblages; however, they show slightly higher percentages of dinocysts and bisaccate pollen, which points to a greater distance between Hole M0027A and the coastline at this time (Fig. **F39**). Furthermore, conifers were probably still constrained to mountainous areas because, despite the general overrepresentation of bisaccate pollen in the marine record, percentages do not exceed 50% (Fig. **F40**). The lowlands were probably dominated by hickory-oak forests, as indicated by comparatively high amounts of oak and hickory pollen.

The interval from the lower upper Burdigalian to the lower Aquitanian (~420 to ~540 mbsf) shows strong variations in organic-walled dinocysts and bisaccate pollen, but both palynomorph types increase from younger to older sediments. In light of this, the Aquitanian was probably an interval of greater distance between Hole M0027A and the coastline compared to the Burdigalian and especially the Langhian. The late Aquitanian was further characterized

by the presence of different hemlock species, probably indicating moister conditions during this interval. During the lowermost Aquitanian, linden pollen shows high percentages. The vegetation reconstructions described above imply that the climate during the early Miocene was probably warm and humid.

Oligocene

Six samples (313-M0027A-193R-CC through 220R-CC; 545.61–620.83 mbsf) analyzed for pollen were assigned to Oligocene sediments based on pollen and dinocysts, with the lowermost sample close to the EOT (Sample 313-M0027A-220R-CC). Oligocene sediments show an increasing number of hickory and linden-like plant pollen. Bisaccate pollen grains exhibit high percentages (>100%), especially during the Chattian. This could be caused by an increasing distance between Hole M0027A and the shoreline because bisaccate pollen has a very high aeolian transport potential and thus tends to be more overrepresented under more distal conditions. However, it is equally probable that during the middle Oligocene, decreasing temperatures and/or humidity led to a spread of pines and other conifers (Figs. **F39, F40**). High percentages of herbal taxa (mainly members of *Brassicaceae;* 5%–22%) suggest decreasing humidity.

Most samples from the Oligocene show relatively low contents of foraminifer test linings compared to the lower Miocene and the ?Eocene (see below). The lowermost two samples show high abundances of dinocysts; however, during the upper Rupelian and the lower Chattian, dinocyst percentages decreased. These findings may point to relatively shallow water depths and a shorter distance between Hole M0027A and the coastline during the middle Oligocene and slightly greater depths and increased distance at the onset of the Oligocene.

?Eocene

The ?Eocene is reflected by only one sample (313-M0027A-223R-CC; 627.58 mbsf) in Hole M0027A. This sample is close to the EOT based on other fossil groups and Sr isotopes, although it could be uppermost Eocene or lowermost Oligocene (see **"Chronology"** and **"Planktonic foraminifers"**). The sample is characterized by very high percentages of dinocysts and foraminifer test linings, indicating relatively deep water.

Although percentages of bisaccate pollen are almost equal with percentages of nonsaccate pollen (Figs. **F39, F40**), considering the overrepresentation of bisaccate pollen in marine pollen records, conifers with bisaccate pollen were probably either rare or grew in distant, mountainous areas (Fig. **F39**). They were still more abundant than during the Miocene. The New Jersey hinterland was probably dominated by deciduous trees and shrubs. Furthermore, the presence of herb taxa indicates the presence of small open areas or, alternatively, the presence of herb populations (mainly members of *Brassicaceae*) close to the shoreline. Oaks were probably the most frequent trees/shrubs; however, compared to the Miocene, the percentages of oak pollen are lower. Hickory pollen—although very frequent in samples from the Oligocene—was not found in the ?Eocene sample. Cypress-like taxa, on the other hand, seem to have been more frequent than during the following intervals. Pollen assemblages point to a generally warm and humid climate at that time.

Geochemistry

Interstitial water

The salient characteristics of interstitial water from Hole M0027A are how fresh it is and how frequently and abruptly it alternates from fresh to salty downhole. Chloride concentrations vary from 41 to 530 mM, compared to 524 mM in the shallowest pore water sample (from 0.5 mbsf) that likely reflects ambient bottom water (Table **T9;** Fig. **F41**). The average chloride concentration over the 631 m sampled for pore water, weighted by depth interval, is 273 mM, and only 52% of that is in the shallowest sample; in other words, nearly half of the water in the drilled interval is fresh. We sampled at least five distinct layers of freshwater, some thin and some thick, at ~29, 79, 87, 183–341, and 419 mbsf. Backflow was observed in the drill pipe at 225 mbsf, within the thickest layer of freshwater, suggesting that an aquifer had been penetrated. These fresh layers alternate with salty layers at ~0–15, 47–71, 80–83, 96–167, and 351–410 mbsf that reach chloride concentrations of at least 434–529 mM chloride, 83%–101% of that in bottom seawater. Even with our average sampling interval of 7.3 m (87 pore water samples over 631 m sampled), it is clear that downhole gradients in the salinity of pore water are frequent and sharp. A central task in interpreting the pore water chemistry is to explain how these sharp chemical gradients are maintained in the face of chemical diffusion, which tends to soften such gradients and then, in time, to erase them altogether.

Beneath the lowest freshwater layer at 419 mbsf, the chloride concentration increases linearly with depth to 488 mM, 93% of that in bottom seawater, at 621 mbsf, near the bottom of the hole. Comparison of this profile with those from Holes M0028A and M0029A suggests that this increase continues with depth below the drilled interval and probably

achieves concentrations well in excess of that in seawater. This linear increase below 419 mbsf is much more gradual than every other fresh to salty transition in Hole M0027A and suggests there are no more freshwater layers in this hole below that depth. This suggestion is reinforced by other aspects of the pore water chemistry discussed below. Three small peaks in this otherwise linear gradient, at 493, 507, and 549 mbsf, correlate with other chemical species and need to be investigated further.

Most of the major and minor ions in the seawater mimic the depth profile for chloride quite closely (Fig. **F41**), indicating that the interlayering of freshwater and seawater dominates the chemical profiles rather than reaction with sediment. These ions include Br, Na, K, Mg, Ca, and Sr. In discerning the effects of chemical reaction and differences in the chemistry of the various freshwater layers, therefore, ratios of these elements to chloride (Fig. **F41**) are more useful than concentrations. Sulfate (Fig. **F42**) mimics chloride except for the deepest interval, below 419 mbsf; over this interval, chloride increases linearly whereas sulfate stays at low concentrations, mostly <1 mM. Over the same deep interval, pH decreases and alkalinity increases tenfold, from the 2.3 mM typical of seawater (but in the freshwater layer) to a maximum of 26 mM at 549 mbsf (Fig. **F42**). Ammonium also increases greatly over this depth interval, mimicking alkalinity. These chemical changes are the characteristic signature of microbial oxidation of organic matter in anoxic sediments, utilizing sulfur in sulfate as an electron acceptor:

$$SO_4^{2-} + 2CH_2O = H_2S + 2HCO_3^-,$$

where CH_2O represents generic organic matter. In this reaction, N in organic matter is liberated as ammonium and sulfate is reduced to H_2S, which then typically precipitates as Fe sulfides, which eventually recrystallize to become pyrite. We detected an H_2S odor in the cores only rarely during Expedition 313 (the only depth at which we detected it in Hole M0027A was at 236 mbsf), so this process is not likely to be very active at present over this depth interval. We did, however, observe frothing and bubbling of the cored mud at 565 and 577 mbsf, suggesting that microbes may be generating methane within this sulfate-depleted interval. Note also that the sulfur content of the sediments is relatively high below ~420 mbsf, reaching 2.7 wt% at 440 mbsf (Fig. **F43**).

Carbonate alkalinity generated by the above reaction causes the measured rise in the pore water but also drives precipitation of $CaCO_3$ as follows:

$$Ca^{2+} + 2HCO_3^- = CaCO_3 + H_2O + CO_2.$$

$CaCO_3$ precipitation dominates near the alkalinity peak at 549 mbsf, as the ratio of Ca to chloride reaches a minimum over this same depth interval, at 538–555 mbsf. The highest concentration of carbonate C in the sediment was also measured near this interval, at 534 mbsf (although measurements over this depth range are sparse) (Fig. **F43**). Alkalinity then generally falls off with increasing depth because of less organic matter oxidation and/or continued precipitation of $CaCO_3$ as Ca rises along with overall salinity. Although Ca concentration increases with depth over this interval, Ca/Cl does not, as a result of carbonate precipitation.

Over this same interval from 419 to 631 mbsf, relative to the steep increase in chloride, Na, K, and B decrease; Mg increases by 60%; Li and Sr nearly double; and Br, like Ca, shows no large net change, as illustrated by the ratios of each of these species to chloride (Fig. **F41;** Li/Cl, B/Cl, and Sr/Cl are not shown). Also increasing greatly over this interval is Ba (although Ba/Cl is more complicated), because of dissolution of barite from the sediment in response to microbial sulfate reduction and the resulting decrease in dissolved sulfate.

Freshwater and saltwater layers above 419 mbsf have distinct chemistries. These differ not only between fresh and salty but also between individual fresh or salty layers. The three freshwater layers within the upper 100 mbsf, for example, have Na/Cl ratios that are lower and Mg/Cl ratios that are higher than those in the adjacent salty layers and seawater, whereas in the 158 m thick layer of freshwater at 183–341 mbsf and the deepest layer at 419 mbsf, these ratios vary in the opposite sense. These differences presumably reflect the different origins and histories of the various freshwater layers. By contrast, the five salty layers above 419 mbsf, as well as the water with seawater chloride concentration from near the bottom of the hole, all have Na/Cl ratios near that of seawater (with the exception of a single sample from 394 mbsf, which is discussed in detail below). The five freshwater layers generally have higher K/Cl, Ca/Cl, and Br/Cl ratios than in the adjacent salty layers and in seawater and also higher alkalinity, especially in the thick layer of freshwater at 183–341 mbsf. This thick fresh layer also has exceptionally high Si and B/Cl and low sulfate, ≤1 mM, which is much lower than would be expected from its chloride content, suggesting that microbial sulfate reduction has occurred within this interval as well, consistent with its higher alkalinity. Ba is high, too, in response to the low sulfate and resulting barite dissolution from the sediment.

Underlying the thick freshwater layer at 183–341 mbsf is a thick salty layer at 351–410 mbsf that is

bounded on its upper side by a thin layer of highly cemented sand and on its lower by the deepest freshwater layer at 419 mbsf. This salty layer contains seawater that is more altered than any shallower in the hole but not as altered as that found below 419 mbsf. Its chloride concentration reaches 491 mM, 94% of the seawater value, its Na/Cl and sulfate are similar to values in seawater, but it has lost some K and Mg and gained Ca, Sr, and P. These are typical changes for a low-temperature reaction with igneous material, from which Ca is leached in exchange for Mg and K is taken up into secondary clay minerals and/or zeolites. The highest peak in ammonium in Hole M0027A occurs at the lower boundary of this salty layer, with a second large peak at its upper boundary. Between these two peaks, ammonium falls to a low concentration. This pattern is likely microbial in origin. One microbial community appears to be producing ammonium by exploiting the chemical gradients between fresh and salty water at the upper and lower boundaries of the salty layer, whereas a second process that may also be microbial is consuming ammonium in between. It may not be coincidental that dissolved phosphorus is high at these intervening depths. Note, however, that sediment within this interval at 351–410 mbsf contains almost no organic carbon, carbonate, or sulfur (Fig. **F43**).

Mn and Fe are both sensitive to redox conditions within the sediment, as both elements form extremely insoluble oxide and hydroxide minerals. Fe, in fact, is often lost from pore water prior to its recovery by squeezing; it is also easy to contaminate with at low concentrations. Mn data from pore water are generally much more reliable. The multiple peaks in these elements (Fig. **F42**) suggest discrete zones of reduction. Five of these zones show peaks in both Mn and Fe and are the most likely to reflect real processes in the sediment. The upper four, at 15–18, 75, 96, and 175 mbsf, all occur within the narrow and sharp transitions from fresh to salty water. Their presence within these transitions suggests they may be microbial in origin, as microbes are masters at exploiting chemical gradients. Further investigation of these zones is certainly warranted. Note that organic carbon is generally quite low in the sediment above ~170 mbsf except near the three layers of freshwater (Fig. **F43**).

The fifth and deepest peak, which lies at 394 mbsf within the salty layer discussed above, represents the single largest and most problematic chemical anomaly in the pore waters from Hole M0027A. It is defined by a single sample from the core catcher from Core 313-M0027A-139R. This sample has exceptionally high Mn, Fe, Li, B, K, Si, Ca, and Sr and low Na/Cl. For Si, Ca, and Sr, these are the highest concentrations and for Na/Cl the lowest value measured in Hole M0027A, and they are nearly so for Fe, B, and K. Whether this anomaly represents contamination of some sort we are still debating, but an identical anomaly occurs in Holes M0028A and M0029A from multiple samples that are less obviously disturbed. Its cause does not appear to be simple contamination by drilling mud. Drilling fluid is enriched relative to seawater in Si, Ca, and Sr (Table **T9**) but to nowhere near the concentrations measured in the pore water sample from 394 mbsf. Drilling fluid is also enriched in ammonium, Ba, Al, P, and, for the fluids used in Holes M0028A and M0029A (but not Hole M0027A), in Mn and Fe. It does not appear to be enriched in Li, B, and K, nor does it have low Na/Cl. The composition of drilling fluid is therefore a poor match for that of the pore water from 394 mbsf and for the similarly anomalous samples from Holes M0028A and M0029A.

Sediment

Sediment samples were analyzed for total carbon (TC), total organic carbon (TOC), and total sulfur (TS) concentrations. Total inorganic carbon (TIC) was calculated as the difference between TC and TOC (Table **T10**). Bulk sample X-ray diffraction (XRD) data were produced for the same samples (Table **T11**).

Total carbon, total organic carbon, and total sulfur

TOC and TS are relatively abundant in all five layers occupied by freshwater in Hole M0027A and are nearly absent in the salty layers, except for the deepest salty layer below 420 mbsf to the bottom of the hole (Fig. **F43**). This is because the five salty layers above 420 mbsf are all extremely quartz rich, based on XRD analyses, whereas the freshwater layers all reside in quartz-poor sediment that is rich in detrital and authigenic minerals, including pyroxene, epidote, chlorite, magnetite, goethite, and the clay minerals kaolinite, glauconite, and mica + illite, along with mixed-layered clays (Figs. **F44, F45**). Pyrite is also abundant in three of the five freshwater layers; its relative abundance as determined by XRD correlates extremely well with TS (Fig. **F43**). These minerals are all present at low abundance or not at all in the salty layers, based on XRD. All but the uppermost salty layer at 0–15 mbsf also lack calcite, plagioclase, and K-feldspar. TOC and TS are especially abundant in the two deepest freshwater layers; within the thickest of these, at 183–341 mbsf, concentrations reach 7.4 wt% TOC and 4.0 wt% S.

These observations are consistent with the lack of evidence for sulfate reduction within the salty layers,

except below 420 mbsf; as noted above, pore water sulfate profiles mimic chloride above 420 mbsf, and the sulfate/chloride ratio is constant at the seawater value within these salty layers (Fig. F43). Within the freshwater layers, by contrast, the presence of organic carbon allows for microbial sulfate reduction, so at least some of the sulfur, present as pyrite in the sediment, is likely authigenic in origin. Within the salty layer below 420 mbsf, where pore water sulfate has clearly been reduced, some or all of the pyrite is certainly authigenic.

TIC, or carbonate carbon, is highest at 0–22 mbsf within the uppermost salty layer and its transition to freshwater, where it is present mainly as calcite and high-Mg calcite, based on XRD analyses (Fig. F44); near the transition from freshwater to saltwater at ~90–110 mbsf, where it is present mainly as high-Mg calcite and dolomite; within the thick freshwater layer from 183 to 341 mbsf, where it is present as both calcite and dolomite; and within the transition to saltwater as the bottom of the hole is approached, at ~420–600 mbsf, where it is present as calcite, high-Mg calcite, and dolomite. Large intervals in Hole M0027A, particularly within layers occupied by saltwater, are essentially carbonate free. As noted in the discussion of pore water chemistry above, the highest concentration of TIC measured in Hole M0027A was 3.2 wt% at 534 mbsf, within the deep salty layer where sulfate reduction has occurred, producing carbonate alkalinity and inducing $CaCO_3$ precipitation. This highest TIC concentration correlates with a similarly large XRD peak in high-Mg calcite.

As noted in the above discussion of pore water, the thick salty layer at 351–410 mbsf has exceptionally high concentrations of ammonium at its upper and lower boundaries, where it adjoins freshwater. Within the salty layer, ammonium concentrations are much lower, whereas dissolved phorphorus is much higher. Apatite content as determined by XRD is likewise low within this salty layer but higher along its boundaries; in fact, apatite concentrations are higher along several of the freshwater/saltwater boundaries in Hole M0027A than elsewhere, suggesting that it may be authigenic (Fig. F43).

Mineralogy by X-ray diffraction

The semiquantitative abundance of a number of minerals has been determined by XRD from the ratio of the intensity of a peak for a single mineral divided by the sum of the integrated intensities for all peaks in a scan (Table T11). The mineralogy of Hole M0027A is heavily dominated by quartz, which accounts for 6%–86% of the signal for a given sample (mean = 62%). Other minerals with maximum signals above 6% are, in order from highest concentration to lowest, kaolinite, plagioclase, chlorite, K-feldspar, Mg calcite, calcite, clays, siderite, micas and illite, mixed-layer clays, pyroxene, pyrite, and glauconite. As noted above, the depth profile for pyrite abundance correlates extremely well with that for TS measured chemically on the same sample (Fig. F43). The abundance of carbonate minerals also correlates well with the chemical measurement of carbonate carbon (TIC), but only when all carbonate minerals are considered; XRD data can thus be used to estimate the relative proportions of calcite, high-Mg calcite, dolomite + ankerite, and possibly rhodochrosite (Fig. F44) and siderite (Fig. F45).

Many of these minerals show similar abundance patterns with depth in Hole M0027A and thus correlate with one another. The strongest correlations are found between dolomite + ankerite and rhodochrosite; pyroxene, epidote, and amphibole; siderite and apatite (Fig. F44); kaolinite, chlorite, magnetite, goethite, glauconite, and, to a lesser extent, pyrite and gibbsite, all of which are anticorrelated with quartz; and clays, mica + illite, mixed-layered clays, and, to a lesser extent, smectite (Fig. F45).

The distribution of these minerals with depth in Hole M0027A correlates well with the distribution of freshwater and saltwater layers, which thus appears to be determined largely by lithology. The five salty layers above 420 mbsf contain abundant quartz and not much else, whereas the five freshwater layers contain abundant detrital and authigenic minerals, including pyroxene, epidote, chlorite, magnetite, goethite, and the clay minerals kaolinite, glauconite, and mica/illite, along with mixed-layered clays (Figs. F44, F45). Pyrite is also abundant in three of the five freshwater layers, whereas it is present at very low concentration or not at all in the salty layers. Plagioclase and K-feldspar are especially abundant within the uppermost 22 mbsf.

Physical properties

The primary aim of this section is to provide a description of the petrophysical data sets collected on cores from Hole M0027A, including their significant characteristics and variations. The secondary aim is to discuss in more detail a number of interesting aspects. Some measurements display variation primarily associated with depositional sedimentological changes, whereas other measurements are controlled by more postdepositional factors, such as the degree of cementation and the type of interstitial water. In addition, combined integration of core and logging petrophysical data sets allows calibration of core data

with in situ borehole properties and provides an assessment of the precise depth from which core was collected in the borehole.

Whole-core measurements were acquired on a MSCL: gamma ray density, *P*-wave velocity, noncontact electrical resistivity, and magnetic susceptibility (see **"Physical properties"** in the "Methods" chapter). Thermal conductivity and natural gamma radiation (NGR) measurements were taken on whole cores prior to the commencement of the OSP. Density, porosity, and *P*-wave velocity were measured and calculated from, on average, one discrete sample in every core section. Figure **F46** provides an overview of the data acquired.

Density and porosity

Gamma density and wet bulk density

Gamma density varies from 1.55 to 2.4 g/cm^3 in cores from Hole M0027A (Fig. **F47**). Wet bulk density calculated from wet and dry weight and dry volume of samples from cores varies between 1.55 and 2.5 g/cm^3. In general, there is good correspondence between gamma density and wet bulk density, with a slight tendency for higher estimates of density from gamma density (Fig. **F48**). Based on repeat measurements, it is estimated that wet bulk density of sands is overestimated by 5%.

Density varies downhole with intervals of lower densities (~1.85 g/cm^3) and higher densities (~2.05 g/cm^3) (Fig. **F47**). These variations broadly correspond to different lithologies: respectively, clay- to silt-rich intervals and sand, glauconite, or cemented intervals. This correspondence to lithologies is particularly clear when investigated in combination with porosity (see **"Combined density and porosity as a stratigraphic tool"**).

Calculated porosity

Calculated porosity, here referred to as porosity, is derived from the difference between the wet and dry weights and the dry volume of selected sediment samples (see **"Physical properties"** in the "Methods" chapter). Some core liners had little drill fluid in them. As a result, sediments with high permeability may have been drained of water during storage and handling. Porosity, particularly that of sands, may therefore be underestimated. Based on repeat measurements, we estimate that porosity of sands was probably underestimated by up to 19%. Clays and silt sediments have relatively little permeability and are not expected to have drained as much. Calculated porosity values vary from 20% to 65%.

Stratigraphically, porosity varies, with intervals of low porosity (~35%) and intervals of high porosity (~50%–60%) corresponding to lithology variations (Fig. **F47**). Clay- to silt-rich sediments in general have high porosities, and sand, glauconitic, or cemented sediments have low porosities. Such differences are in contrast to deeply buried sediments in general (Bahr et al., 2001).

The top 200 m of Hole M0027A is characterized by reduced sediment porosities. Coring techniques in these less consolidated intervals included hydraulic piston coring and extended nose coring (see **"Operations"**). This may have resulted in dewatering and thus reduced calculated porosity. Also, loose sands may have drained more during storage and handling, resulting in artificially low porosities.

Below ~200 mbsf the porosity of the clay and silt intervals decreases with depth. The same tendency is observed for sand-rich intervals. This porosity reduction is a result of compaction caused by the lithostatic load. Porosity reductions broadly follow the exponential decrease in porosity of sands, silts, and clays that have been observed from a number of passive margins and derived analytically (Sclater and Christi, 1980; Bahr et al., 2001). At depths shallower than ~700 mbsf, the exponential porosity reduction is nearly linear (Bahr et al., 2001).

Combined density and porosity as a stratigraphic tool

When viewed in conjunction, wireline logs of density and porosity are very useful for detecting different lithologies in deeply buried sedimentary successions (Rider, 2006). Even at shallow depths in Hole M0027A there is a significant inverse variation between porosity and density of the samples (Fig. **F49**). The different lithologies of Hole M0027A fall close to a mixing line between rock and saltwater. Rock has zero porosity and a density of 2.7 g/cm^3. Saltwater has 100% porosity and a density of 1.024 g/cm^3. Sand, glauconite sediments, and the majority of clay and silt samples plot above or close to the line. A significant portion of the silt and clay samples plot below the line with reduced densities. This could result from the presence of organic matter that causes the density to be reduced comparatively more than if the decrease was only caused by a porosity increase (Rider, 2006).

Downhole, the separation between density and porosity curves varies from intervals with lower density and higher porosity to zones with higher density and lower porosity (Fig. **F50A, F50B, F50C, F50D**). These variations correspond to the main lithology variation in the hole, as shown in the crossplot (Fig. **F49**). In this context, it is worth noting that at these shallow depths the porosity of clay and silt is still relatively higher than that of sands. As a result, the

"separation" of porosity and density curves are not fully expressed, as in deeply buried shale and sand successions (cf. Rider, 2006).

In a sequence stratigraphic context, as determined by sedimentology, transgressive and maximum flooding intervals seem to be characterized by a rapid reduction in density and an increase in porosity (Fig. F50C). Intervals with abundant organic phytoclasts seem to have densities reduced relative to porosity. Overall, density increases and porosity decreases in coarsening-upward prograding successions (Fig. F50).

P-wave velocity

Velocity measurements on whole cores can be correlated well with density measurements for the majority of Hole M0027A, although in places there is considerable scatter in the velocity data due to the variable liner fill and saturation of cores (see "Physical properties" in the "Methods" chapter). Major trends in *P*-wave velocity also correlate with major trends in the sonic log. There are some offsets observed in the MSCL data that are absent in the downhole log, often between successive sections or cores. Some of these offsets may relate to the degree of liner fill and the suitability of some of the whole cores for measurement (see "Physical properties" in the "Methods" chapter). Velocity trends are described more extensively in "Downhole measurements."

It was not possible to measure any discrete samples for velocity in the upper part of the hole above 195 mbsf or between 325 and 415 mbsf because of the unconsolidated nature of the core. In the clays between 195 and 208 mbsf, velocities are consistent and low. More variable values are present in the more variable grain-sized sands and silts in Units II–V. In Unit IV, there are fewer velocities attained on the MSCL because of more variable liner fill. In the sandstone around 315 mbsf, velocity measured on discrete samples is higher than that of the downhole sonic log. Higher values in both MSCL velocities and discrete velocities are apparent at the cemented levels at the Unit V/VI boundary. On average, velocity increases slightly with depth for both discrete samples and whole-core measurements. MSCL velocities increase at the Unit II/III boundary (236 mbsf), consistent with the increase observed in the downhole sonic log. Velocities on discrete samples were measurable again from 415 mbsf in the silts and display some variation with grain size.

Downhole from ~468 mbsf, velocities increase in both discrete samples and MSCL measurements as the succession becomes a glauconitic sand in Units V and VI. Velocities remain high and vary with cementation from here to the base of the hole.

Magnetic susceptibility

Magnetic susceptibility was measured at 1 cm intervals and illustrates high-resolution changes in lithology related to variations in the magnetic minerals and/or their sizes. Core measurements and log measurements correlate extremely well, although absolute values are different. Hole M0027A trends associated with lithological units are more extensively described in "Downhole measurements."

Electrical resistivity

Resistivity is affected by lithology and cementation but also pore fluid and pore water salinity, as well as core liner saturation. In general, there appeared to be a decrease in the amount of drill fluid in core liners down a recovered core. As a result, the last section of every core, generally a short section, artificially has very high resistivity and was removed from analysis. Most very short sections have low core liner saturation. Removal of this effect has been attempted by high-pass filtering (Fig. F47). Resistivity values are low in some poorly recovered sands. Despite the uncertainties, resistivity measurements downhole have interesting variations related to changes in salinity of formation water and lithology, minerals, and organic matter.

Resistivity is highly variable from low values of 0.2 Ωm to high values of 16 Ωm. Notable high resistivity occurs at 21–29, 176–189, 265–267, 413–425, and, less certainly, 354–355 mbsf. The lowest resistivity is registered at 32–49 mbsf, sporadically between 94 and 164 mbsf, and between 600 and 623 mbsf. Values are low (0.8 Ωm) between 344 and 410 mbsf with a short interval of intermediate values at 353–361.5 mbsf.

The high resistivity of silts at 413–425 mbsf overlain by low-resistivity sands is an interesting feature, with the upper limit of silts corresponding to the transition from low to high chlorinity (see further description for the rest of the hole in "Conductivity logs").

At centimeter-scale resolution, the correlation between lithology and the high-pass filtered resistivity is variable and is related to variable amounts of low-resistivity minerals, high-resistivity lignite, and the degree of cementation (Fig. F50A, F50B).

Digital linescans and color reflectance

All cores from Hole M0027A were imaged using an X-ray fluorescence (XRF) digital linescan system equipped with a charge-coupled device (CCD) camera using 3 × 2048 pixels with a beam-splitter and a manually controlled Pentax 50 mm lens. Data were recorded at a resolution of 0.068 mm as both images and red-green-blue (RGB) values. All suitable cores

were also scanned for color reflectance. These data may reflect changes in glauconite content (green wavelengths) or iron content (seen in a*/b* ratios). The varying suitability of the core section for color reflectance measurements was observed to have a significant effect on the scatter present within the data set (see **"Physical properties"** in the "Methods" chapter). Some effort was made to correlate color reflectance changes as measured by the Minolta with other measurements and observations, but detailed filtering and comparisons were deemed to fall within the domain of postexpedition research.

Thermal conductivity

Thermal conductivity data vary downhole and can be divided loosely into four intervals. In the upper ~150 m of the hole, there is considerable variation in thermal conductivity in the unconsolidated sands, although values are generally high, with a departure to a lower value around 80 mbsf. Between ~175 and ~375 mbsf, thermal conductivity decreases quite sharply to a low around 275 mbsf before increasing again. From 375 to 425 mbsf is another decrease. At ~425 mbsf, conductivity varies but generally stays low to the base of the hole. There is a correlation between thermal conductivity and chlorinity. However, the transition from low to high values tends to be sharper in the geochemical data than in the thermal conductivity data, possibly because of some diffusion processes occurring in the core between drilling and measurement subsequent to transportation and storage. This may have resulted in some mixing of fluid from upper and lower levels prior to thermal conductivity measurement, whereas geochemical data were derived from pore water extracted immediately after coring. For most of Hole M0027A, thermal conductivity and pore water chlorinity trends are parallel (see **"Downhole measurements"**). The highest values are between 353 and 412 mbsf in a saline interval. Values here may be linked to higher values in the quartz-rich sands.

Natural gamma radiation and core-log correlation

All cores were measured for NGR with the primary purpose of core-log correlation (see below). Data collected are equivalent to the TGR downhole log. Although absolute values are different, trends are the same. Gamma ray trends and characteristics are extensively described in **"Downhole measurements."** In general, correlation between core and log data sets is excellent, with only minor (<1 m and usually <0.6 m) vertical offsets in any interval (e.g., Fig. **F51**). The correlation data set is a most straightforward match where there is both good core recovery and distinctive peaks in both data sets.

Correlation between core and logging data is evaluated primarily using NGR, but several petrophysical data sets can be used. Toward the top of the hole, the correlation process enabled a systematic error in top core depth to be identified and corrected in Cores 313-M0027A-25R through 58R (see **"Stratigraphic correlation"**).

Paleomagnetism

Sediments from Hole M0027A generally possess a weak or unstable natural remanent magnetization (NRM). Alternating-field (AF) demagnetization up to 15–30 mT, depending on lithology, typically removes a low-coercivity overprint with normal polarity, sometimes revealing a higher coercivity stable component. During AF demagnetization, a few samples acquired what was identified as gyroremanent magnetization (GRM). The effect of GRM was removed by applying an antigyroremanent demagnetization procedure. Two reversal boundaries were successfully identified in the clay sequence in upper lithologic Unit II that could be assigned to either Chron C5ACn or C5ADn according to the time constraints of Sr analyses and biohorizons.

Discrete sample measurements

A total of 744 samples from Hole M0027A were measured in the pass-through magnetometer. In addition to the standard one sample per section, Cores 313-M0027A-65R through 70R, 110R through 116R, 155R through 166R, 175R through 193R, and 209R through 224R were sampled at a denser resolution, ranging from one sample every 50 cm to one sample every 10 cm. NRM and remanence after sequential AF demagnetization up to 60 or 100 mT was measured for all samples.

Remanent magnetization

The primary magnetization in Hole M0027A is mostly carried by a low-coercivity component, but demagnetization also indicates the presence of a high-coercivity magnetic mineral. The initial NRM moment of the sediments is typically weak, on the order of 10^{-10} to 10^{-8} Am^2 (Fig. **F52**). Clay sediments in Cores 313-M0027A-61R through 70R (~183–209 mbsf) exhibit stronger magnetic moments on the order of 10^{-7} to 10^{-6} Am^2, coinciding with a peak in magnetic susceptibility (Fig. **F52**). Finer grained sequences further downcore exhibit significantly lower NRM magnetic moments, perhaps indicating regional dissolution of the primary magnetic mineral.

Inclination data show prevailing normal polarity, suggesting a viscous overprint. In general, data are too noisy to distinguish any polarity zones except for Cores 313-M0027A-61R through 70R (183–209 mbsf), which exhibit stronger NRM magnetic moments. These cores are located in the high–magnetic susceptibility clays of Unit II.

The cores were recovered using the HPC, EXN, and ALN. Weak and unstable NRM magnetization was generally observed in unconsolidated layers recovered by the ALN, indicating magnetic grain rotation and/or structural deformation.

Demagnetization behavior varies considerably depending on lithology. Typically, the NRM of sediments exhibits a normal polarity overprint, which in some cases makes it hard to distinguish the primary component (Fig. **F53A**). AF demagnetization of some samples typically shows a double-bulge shape feature, which is interpreted as the successive removal of two overlapping low- and high-coercivity components (Fig. **F53B**). The characteristic remanent magnetization (ChRM) of samples exhibiting GRM behavior during demagnetization was successfully isolated using the anti-GRM technique (Fig. **F53C, F53D**). We could only isolate a stable ChRM within intervals with high magnetic susceptibility, implying to some degree dissolution of the primary magnetic carriers within intervals with low magnetic susceptibility. In thin sections, iron sulfide and iron carbonate are commonly observed as diagenetic phases in the sediment matrix (see Fig. **F46** in the "Site M0028" chapter). These minerals are most likely secondary features, as the minerals form framboids or aggregates along preexisting fabrics, grains, or fossils. Nevertheless, hematite and some other opaque grains are observed as detrital grains, which may carry a primary magnetization.

Magnetostratigraphy

Because of the generally weak and unstable NRM of the sediments, we were only able to establish a polarity magnetostratigraphy for Cores 313-M0027A-61R through 70R (183–209 mbsf) (Fig. **F54**). Preliminary magnetostratigraphic age-depth tie points are given in Table **T12.** Polarity interpretations are based on principal component analysis (PCA) for samples from 208.39 to 201.31 mbsf, which were demagnetized using the antigyroremanence procedure. Based on these results, the 30 mT demagnetization step was identified as the most representative of the ChRM and was therefore used, together with studies of individual orthogonal Zijderveld plots, to establish the polarity for samples from 201.21 to 182.52 mbsf.

Magnetostratigraphic interpretation of inclination data from Cores 313-M0027A-61R through 70R is dependent on the placement of the m4.1 surface (currently placed at ~195 mbsf), which, according to the seismic study, could represent an unconformity in Hole M0027A. In this section, we present two alternative interpretations (Table **T12**) for each reversal boundary based on the constraints given by Sr isotope ages from the core catcher of Core 313-M0027A-70R (13.7 ± 1.17 Ma) and the identification of upper dinocyst Zone DN5 (14.2–13.6 Ma) in the sediments from the core catcher of Core 313-M0027A-65R.

The reversal boundary (from reversed to normal polarity [R/N]) between 206.94 and 206.74 mbsf is identified as the onset of either Chron C5ACn or C5ADn. The next reversal boundary (from normal to reversed polarity [N/R]) between 196.09 and 195.79 mbsf is identified as the onset of either Chron C5ABr or C5ACr. Cores 313-M0027A-61R through 63R (183–189 mbsf) (arrows in Fig. **F54** show the intended core length) suffered from poor sediment recovery. The actual position of the recovered sediments within the cores is unknown, and we are therefore only able to narrow down the reversal boundary (R/N) to a relatively large depth range, 191.96–189.03 mbsf. The reversal boundary is tentatively identified as the onset of either Chron C5AAn or C5ABn, taking into account the possible hiatus below the reflector m4.1 surface.

Magnetic susceptibility

MSCL magnetic susceptibility data from the midpart of the Oligocene section in Hole M0027A display high values and large (~60×10^{-5} SI units) variations (Fig. **F55**). There appear to be ~20–25 magnetic susceptibility cycles in this 45 m section (1.8–2.25 m/cycle = 0.44–0.55 cycles/m). Magnetic susceptibility cyclicity is likely due to variations in abundance of glauconite and associated minerals (Miller et al., 1996; Metzger et al., 1997) and should be evaluated through compositional and gray-scale studies. In general, magnetic susceptibility of sediments strongly depends on the amount of mainly ferrimagnetic and partly paramagnetic minerals. Based on microscopic observation and rock magnetic work, ferrimagnetism mainly resides in greigite grains and paramagnetism resides in glauconite and pyrite grains in the section. Most greigite is authigenic and may be linked to astronomical-pace-forcing with climate proxies. High susceptibility values in sequence o1 (539.5–596.3 mbsf) appear to be derived from greigite (ferrimagnetic minerals), as well as glauconite pellets and pyrite framboids (paramagnetic minerals).

One possible cause for cyclicity in glauconite abundance is variations in downslope transport on the off-apron toe-of-slope setting (see **"Lithostratigraphy"**). Such variations may reflect astronomical-scale eustatic changes.

Shipboard age constraints hint at astronomical control by precession and eccentricity. The sequence between 494.97 and 539.5 mbsf is dubbed sequence o1. It can be dated as ~28.5–29.0 Ma based on Sr isotopic stratigraphy and biostratigraphy (Fig. **F34**). Thus, these roughly 0.5 m thick cycles appear to be precessional in scale. The general increasing trend from 530 to 565 mbsf and the decreasing trend from 565 to 595 mbsf may reflect modulation by the long eccentricity cycles. Further work should test these speculative correlations to astronomical forcing and evaluate the cause. Further discussion of magnetic susceptibility variations can be found in **"Downhole measurements."**

Downhole measurements

The focus in this section is to provide a description of the wireline data sets collected in Hole M0027A and their downhole characteristics and variations. A few detailed examples are given, interpreting interesting aspects of the log trends. Trends in MSCL core measurements and equivalent borehole measurements are also discussed in this section. Some measurements display variation primarily with depositional sedimentary composition, whereas others are controlled more by postdepositional factors such as the degree of cementation and the type of interstitial formation water. Integration of core and logging data sets allows calibration of core data with in situ borehole properties and provides an assessment of the precise depth from which cores were collected. These correlations are described briefly in **"Physical properties."** At the end of the section, a synthesis of petrophysical data and downhole logs and derived quantities is presented for each stratigraphic unit.

Downhole measurements in Hole M0027A

In Hole M0027A, 2297 m of wireline logs was acquired, along with VSP measurements. Spectral gamma ray logs were acquired through steel drill pipe down to 603 m wireline log depth below seafloor (WSF), thus providing coverage in all except the bottommost section of the hole (see Table **T7** in the "Methods" chapter). An open-hole run of the same probe from 410 to 621 m WSF provided an additional 18 m of coverage at the base of the hole.

Two sections of open hole were logged with other tools in Hole M0027A, from 192 to 342 m WSF (middle section) and from 418 to 623 m WSF (lower section). The base of the middle interval became shallower with each successive run because of the formation of a bridge and infilling from 342 m WSF. This prevented the section between 342 and 418 m WSF from being logged. In the lower section, the acoustic log was completed at 575 m WSF because of the timing of further wireline operations planned for this site.

Open-hole measurements were acquired for magnetic susceptibility, spectral gamma ray, acoustic imaging, conductivity, and sonic velocity. VSP measurements were acquired in the middle section in open hole and through pipe in the upper section (see Table **T8** in the "Methods" chapter). Figure **F56** provides an overview of all slimline downhole measurements taken in Hole M0027A.

In all figures, downhole geophysical data and images are plotted in meters below present-day seafloor based on the wireline scale (WSF) (see **"Downhole measurements"** in the "Methods" chapter). Where appropriate, boundaries between lithologic units (Units I–VII) are indicated to facilitate comparison with other data analyses in this hole and with analyses in other Expedition 313 holes.

Spectral gamma ray logs

Spectral gamma ray logs allow continuous characterization of the entire borehole. Comparison of through-pipe data and the open-hole logs indicates slight attenuation of the through-pipe signal but excellent matching of trends (Fig. **F56**). The TGR signal from the downhole probe and NGR measurements made on whole cores correlate very well, in some cases allowing accurate repositioning of core depth below seafloor (see **"Physical properties"**).

In general, trends in TGR are dominated by the K component of the signal (Fig. **F56**). High amounts of K appear to be related to two main factors: silt/clay with high mica content and the occurrence of glauconitic sands.

Total counts in the upper 168 m (Unit I) are generally low. Through-pipe TGR values of ~20 counts per second (cps) and K amounts of <100 Bq/kg correspond to sandy intervals (3–8, 30–71, and 119–168 m WSF). A few excursions to higher values (>100 cps) correspond to clays, which were the intervals generally recovered. In Units II–IV, values are relatively constant (~150 cps) with small lows. In Unit V, with the exception of a small peak near the top related to high U (probably linked to organic matter described in cores) and high K, gamma counts are very low (<20 cps) to 400 m WSF, where they begin to rise. This interval of low counts is characterized by

low core recovery and nonconsolidated sands. Cave formation around the pipe at these depths may have contributed to an underestimation of NGR emissions. Total counts in the lower part of Unit VI are relatively constant at slightly increased values compared to those observed in Units III and IV. In Unit VII, counts increase significantly to very high values (>500 cps) between 500 and 510 m WSF in an interval rich in U (top of Subunit IIB). Total counts, still high, then decrease progressively to 600 m WSF before gradually rising to the end of the log at 620 m WSF.

Along the hole, Th/K and U/K ratios are quite variable (Fig. **F57**). Around 355 and 430 m WSF, U/K is slightly lower at a cemented level. Transitions between low gamma ray in sandy intervals and high gamma ray in clay intervals can either be sharp (e.g., 77 and 96 m WSF) or progressive (e.g., 12–15 and 405–415 m WSF). In the latter case, Th/K and U/K ratios remain quite stable (Fig. **F57**), suggesting a progressive change in sand/clay ratio with no change in mineralogy.

Below 480 m WSF, high K values are not related to mica-rich clay and silt but to the occurrence of K-rich glauconite in the sediment. The presence of glauconite is also indicated by low Th/K values and correlates with high magnetic susceptibility (Figs. **F56, F57**). The low Th/K value in the middle part of the hole also corresponds with the occurrence of glauconite (between 337 and 355 m WSF). Between 50 and 75 m WSF, the Th/K ratio is also low but the cores appear to be glauconite free; however, core recovery is low.

The highest TGR values are located at 500 m WSF and are related to the combination of high U and high K (Fig. **F56**). The U spike is associated with interesting features just above: from 480 to 490 m WSF, K content increases with glauconitic content, whereas U and Th are depleted. Minimum U and Th contents occur between 490 and 495 m WSF in cemented glauconitic sandstones. Below these cemented rocks, Th values increase to an average of 25 Bq/kg, similar to values found in other parts of the hole, whereas U increases significantly to a maximum of 180 Bq/kg at 504.5 m WSF and then decreases gradually to an average of 50 Bq/kg below 560 m WSF.

The association of low U and Th also occurs when glauconite appears in the sediment from 340 to 355 m WSF. A spike of U at 361 m WSF underlies a cemented sandstone at 355 m WSF, which is accompanied by a progressive decrease in U to 380 m WSF. The pattern at 340–380 m WSF is located between a freshwater aquifer above and a saltier aquifer below (see **"Geochemistry"**). Observed patterns of K and U are interpreted as diffusion processes during diagenesis at the boundary between two aquifers with distinctly different chemical properties (e.g., especially Eh controlling the solubility of U).

Magnetic susceptibility logs

Magnetic susceptibility is often a clear indicator of lithological variations because of its high sensitivity to iron-bearing minerals. Susceptibility is generally anticipated to be higher in clays than in sands and higher where terrestrial input to the sediment is greater. In Unit I and the upper part of Unit II, magnetic susceptibility is high in clay intervals. In all holes, magnetic susceptibility signals from the EM51 downhole probe and MSCL correlate very well, allowing, in some cases, very accurate repositioning of core depth below seafloor.

In Hole M0027A, the highest magnetic susceptibility values are found around 390 m WSF in a clay interval in Unit II, as seen in the MSCL-measured magnetic susceptibility (Figs. **F56, F58**). Although glauconite, which is a mineral with high magnetic susceptibility, was not observed in these clays by the sedimentologists, XRD analyses show a ?glauconite? spike in these upper clay intervals. This suggests that fine-grained glauconite may be the influence on magnetic susceptibility. XRD analyses indicate that a peak in magnetite accompanies the glauconite peaks. This magnetite may be forming around the glauconite grains (see **"Paleomagnetism;"** see Fig. **F46** in the "Site M0028" chapter). For the remainder of the hole below the base of the clay at ~209 m WSF, glauconite is the dominant control on magnetic susceptibility, which correlates with sedimentological observations of this mineral. In some cores, a clear correlation is observed between magnetic susceptibility peaks (both from the MSCL and the EM51) and darker layers containing sulfides, closely related to the formation of magnetic minerals such as greigite (Figs. **F31, F58**). Below this level, the magnetic susceptibility signal is much lower to the top of Unit VII. High values are then observed between 490 and 495 m WSF, followed by a progressive decrease in magnetic susceptibility to 600 m WSF. In Unit VII, the magnetic susceptibility signal correlates with K, and both closely reflect the glauconite content estimated by the sedimentologists (Fig. **F59**). A discussion of the cycles observed within this interval (540–585 mbsf) and their potential relationship to variations of glauconite transport on the off-apron toe-of-slope setting (see **"Lithostratigraphy"**) can be found in **"Paleomagnetism"** (Fig. **F55**). Susceptibility variations commonly correlate with density variations because both parameters are high where glauconite is present.

Acoustic image logs

The ABI40 acoustic image log was run at a resolution of 72 parts per thousand in Hole M0027A. Acoustic amplitude and traveltime images provide an estimate of the borehole diameter and the induration and rugosity of the borehole walls. Softer intervals are characterized by shorter traveltimes and a lower amplitude signal, which can be used to pick out nonconsolidated intervals often related to sandier levels in the cores. The hardest zones are generally characterized by higher traveltimes and higher amplitudes (Figs. **F51, F59**). Centralization of the tool during acquisition affects the accuracy of the acoustic caliper calculated from the traveltime image. A generally large and variable diameter borehole is indicated in softer intervals and a more consistent smaller diameter in more indurated zones (Fig. **F51**). Thus, lithological changes as well as potential impedance contrasts can be identified. In Hole M0027A, sharp changes in the ABI40 signal between 310 and 326 m WSF mark a bridge formation at this depth during logging operations, leading to a sharp decrease in hole diameter and lower quality images because of the presence of particles in the hole.

Sonic velocity logs

On average, sonic velocity in Hole M0027A increases with depth, as would be expected (Fig. **F56**). It changes across most major lithology changes, varying from slight increases or decreases to more significant jumps (Fig. **F56**). Velocity is also affected by the induration of the sediment, and increases are observed in levels where sediment becomes harder or is cemented. As such, these changes tend to correlate with variations in conductivity (Fig. **F56**). Around 205 m there is an increase in velocity that corresponds with a change in lithology from sands to clays. A slight decrease is observed at the interface between Units II and III, when passing from sands (above) to clays (below). The velocity peak just above marks a cemented level. Two distinctive transition increases are apparent, one just above the interface between Units III and IV (295 m WSF) and the other between Units VI and VII (488 m WSF), with a step increase at the latter boundary. Velocity increases over a short interval at the first transition because of the presence of a 40 cm thick cemented horizon passing downhole to clay. This transition is also observed in the conductivity log. The second transition is similarly picked out by a magnetic susceptibility increase and a conductivity decrease. Within Unit VI, at 470 m WSF, a gradual increase in velocity corresponds with an increase in density identified in whole-core logging as the lithology grades from silt to fine sand. Velocities remain high with variation throughout Unit VII.

Conductivity logs

Conductivity in the borehole is influenced by a variety of aspects, including lithology, pore water content, and salinity. In Hole M0027A, conductivity clearly correlates with changes in water chlorinity (Fig. **F60;** see **"Geochemistry"**), emphasizing that conductivity measurements are at a first order driven here by pore water salinity. Note that higher conductivities (and associated chlorinities) mainly correlate with coarse-grained intervals. Conductivity in the middle logged section (195–330 mbsf) indicates, on average, a decrease through the section with few notable peaks to higher values, often associated with a decrease in Th content. An example of this is a peak in conductivity at 224 mbsf (Table **T13**), which likely correlates with the m5.2 surface (see **"Stratigraphic correlation"**). In the lower section, there is an overall increase in conductivity downhole. The lowest measured values are observed at the top of Unit V and within Unit VI, bounding both above and below the sands with high-chlorinity pore water observed between 350 and 405 m WSF (Fig. **F60;** see **"Geochemistry"**). A change in conductivity is also commonly observed at the boundaries of sedimentary units or just above or below a stratigraphic boundary, often associated with cemented intervals and located where conductivity anticorrelates with changes in sonic velocity.

Vertical seismic profiling

VSP data were acquired in open hole from 329 to 204 m WSF and through pipe from 204 m WSF to the seafloor (Fig. **F61**) (see **"Downhole measurements"** in the "Methods" chapter for more detail). Downgoing waves were picked and time-depth relationships calculated. The resultant time-depth curve can be used to calibrate the time to depth of the seismic reflection profile. The time-depth relationship from the VSP survey can be compared with the relationship estimated by processing the seismic survey data (see Fig. **F18A** in the "Methods" chapter). All depths converted from traveltime in seismic profiles at this site were estimated using stacking velocities (see **"Downhole measurements"** and **"Stratigraphic correlation,"** both in the "Methods" chapter).

Example of multilog interpretation

Petrophysical and downhole measurements can provide evidence for sequence boundaries. Figure **F51** is a compilation of several parameters around the m5.3 boundary as defined in **"Stratigraphic correlation."** The boundary is located at the interface between lithologic Units II and III, at an abrupt transition at 236.16 mbsf from clay below to medium, moderately glauconitic sand above. In Figure **F51,** the core and

data measured on the whole core have been shifted 0.50 m downhole to match the wireline signal. The m5.3 boundary is therefore located at 236.66 m WSF. The boundary is marked on the petrophysical data by a slight decrease in *P*-wave velocity and a slight increase in density when passing from clay to sands. These sands are characterized by a decrease in TGR counts and an increase in magnetic susceptibility (both on the EM51 log and the MSCL data), reflecting the presence of glauconite in the sand. On the ABI40 amplitude image, the m5.3 boundary is also characterized by a change in color and texture from light uniform colors in clay below to patchy dark red colors in the sand above. The caliper extracted from the acoustic image shows the hole diameter is larger in the sandy interval. Above this boundary, a cemented interval (235.22–235.63 m WSF) is clearly indicated by an increase in density and *P*-wave velocity. This interval is also visible on the ABI40 images.

Most lithological units and stratigraphic surfaces are often picked out by utilizing several of the wireline logs or petrophysical core data. This is clear on Figures **F56** and **F62** and in the last column of Table **T13,** which lists these surfaces against the petrophysical surfaces, where appropriate.

Downhole log and physical properties integration

This section combines results of logging and physical property measurements with the main characteristics of the lithostratigraphic units. It ends with a brief summary of the links between petrophysical intervals (Table **T13**) and stratigraphic surfaces (Fig. **F62**). All depths in Figure **F62** are given in meters below seafloor and ignore small differences that may exist between core (mbsf) and log (m WSF) depths. Various points shown in Figure **F62** can generally be seen in greater detail in various figures in **"Physical properties"** or **"Downhole measurements."** Numerical data are accessible online; see **"Publisher's notes"** for links to the database.

Lithostratigraphic Unit VIII

The upper part of this thin unit was logged with only some of the tools. Results are of poor quality.

Lithostratigraphic Unit VII

Lithostratigraphic Unit VII shows high K content and high magnetic susceptibility, density, and sonic velocity compared to the units above, reflecting glauconite (Fig. **F62B**). However, there is a high degree of variability in these parameters. Gamma ray from the base of the unit increases to an overall high rich in U at the Subunit VIIA–VIIB transition at 499.5 mbsf. U and Th contents decrease above to the boundary with Unit VI. The density log has a blocky appearance in the lower half of the unit (below 570 mbsf) but more stable density values at the top of the unit. A low at 499.50 mbsf is close to the U rich/poor transition. In this coarse-grained unit, chlorinity is high, reflecting salty pore water (Fig. **F60;** see also **"Geochemistry"**) and conductivity, which slightly decreases uphole, clearly following the chlorinity trend. Lows in conductivity usually tie with sonic peaks and porosity lows, reflecting cemented or more indurated intervals rather than pore water chlorinity changes.

The transition to Unit VI is clearly marked by a decrease in K content, magnetic susceptibility, sonic velocity, electrical conductivity, and impedance. Density has a small peak just below the unit boundary, mirrored by porosity. The Th/K ratio clearly increases when entering into Unit VI.

Lithostratigraphic Unit VI

The data sets in Unit VI clearly evidence the two subunits identified in **"Lithostratigraphy,"** which show very distinct lithologies (Fig. **F62B, F62C**). TGR in Subunit VIB is characterized by a relatively high signal indicative of clayey sediment and becomes more variable at the bottom of the unit below 465 mbsf (silt/sand interbedding with clay layers). Subunit VIB is also characterized by low conductivity compared to the sands above in Subunit VIA. From ~488 mbsf, there is a stepped density decrease (porosity increase) to 465 mbsf, where an MFS has been interpreted. This is also matched by the sonic curve. At the MFS, there is a small peak in the Th/K ratio. From the low at the MFS, density increases stepwise, paralleling small "coarsening"-upward motifs, to just above the Subunit VIA/VIB boundary. Entering the sands of Subunit VIA, TGR decreases gradually to very low values. Toward the top of the unit, a peak in Th a few meters below the Unit V/VI boundary probably characterizes the unconformity correlated with seismic sequence boundary m5.7. Density does not change significantly upsection in Subunit VIA except at the top. In the lower, fine-grained part of Unit VI, chlorinity is lower than in Unit VII but decreases to 418 mbsf. The electrical conductivity curve parallels the chlorinity trend as well as the porosity and density curves, reflecting either changes in water content volume or mineralogy, such as the presence of clay. In the upper coarse-grained sandy part of Unit VI, chlorinity increases drastically to salty pore water in parallel with MSCL conductivity between 412 and 343 mbsf (see further description in **"Physical properties"**).

At the boundary with Unit V, gamma ray increases from very weakly serrated low values in two bell-shaped trends with sharp tops associated with seismic sequence boundaries m5.7 and m5.6. The latter peak in gamma ray is associated with a sharp increase in K and density, mirroring the density that characterizes the Unit V lower boundary.

Lithostratigraphic Unit V

Unit V is glauconite rich, as evidenced by a low Th/K ratio and high magnetic susceptibility. Density in this unit is high, paralleling the K curve and dominated by glauconite, although those correlations do not always fit with the glauconite estimates made by sedimentologists. The TGR curve displays the superposition of bell- and funnel-shaped curves. Highs in TGR correspond to high magnetic susceptibility, K, and density and are interpreted as an increase in glauconite content rather than clays. A density high at the base of the unit correlates with a carbonate cemented bed (see **"Lithostratigraphy"**). At ~350 mbsf, there is a low in density followed by a gradual increase upsection, mirrored in porosity. Conductivity is high in the unit, roughly paralleling the gamma ray trend, which is in adequation with the overall coarse-grained lithology, relatively low porosity, and high chlorinity measured on the cores. The decrease in conductivity at ~340 mbsf matches the decrease in chlorinity and the increase in porosity.

TGR changes at the boundary with Unit IV from a decreasing funnel shape below to a higher but constant and serrated curve above. This change correlates to a sharp increase in conductivity and decreases in density and porosity. In detail, the rate of density decrease is greater just at the boundary with a subsequent brief local high at seismic sequence boundary m5.45.

Lithostratigraphic Unit IV

Unit IV is characterized by a flat, serrated TGR curve typical of largely clayey material with high Th content at the bottom. Approximately the lower half of the unit is marked by a decrease in density mirroring a porosity increase, suggesting a weak fining-upward succession in an overall clayey sediment. Two sharp-topped bell-shaped sonic increases (324–309 and 309–296 mbsf) are anticorrelated but parallel to the conductivity curve. Increases in density with no decrease in porosity possibly indicate increases in heavy mineral content despite the lack of evidence along the magnetic susceptibility curve. In this fine-grained unit, chlorinity is low, slightly increasing uphole, according to the global trend of the conductivity logs.

At the boundary with Unit III, TGR changes from weak serrated intermediate values to boxcar-shaped lower values just above a sharp confined peak in TGR. Sonic velocity increases significantly at the small bed immediately above the boundary with a small low in conductivity and a small peak in U. Density decreases sharply above this bed, and porosity increases because of sharp grain size diminution.

Lithostratigraphic Unit III

Unit III shows TGR values serrated intermediate with boxcar to weak bell shapes characteristic of clays and silts, with a distinct low at 272 mbsf. This latter sand bed correlates to seismic sequence boundary m5.4, characterized by a decrease in density and a peak in the Th/K ratio, sonic velocity, and magnetic susceptibility. Density rapidly decreases and then slowly increases uphole to 272 mbsf (m5.4), mirrored by the porosity curve. Density rapidly decreases to a low at 265 mbsf and then stepwise increases to the top of the unit. At 240 mbsf, clay volume peaks and density increases, possibly related to a high content of heavy minerals (pyrite). Chlorinity is low in Unit III, increasing uphole and correlated with the conductivity curve.

The boundary with Unit II is characterized by a clear increase in sonic velocity, an increase and then decrease in conductivity, an abrupt change from high serrated gamma values to a weak funnel trend, a sharp increase in density, and decreases in porosity.

Lithostratigraphic Unit II

Unit II shows a composite TGR curve with a succession of boxcar trends in the lower part overlain by a tight serrated shape in the upper part. This shape corresponds to the superposition of an alternation of sand and clay motifs at the base with homogeneous clayey sediment at the top. These TGR trends are paralleled by Th, K, and density curves but are anticorrelated with porosity, which confirms the fining-upward clayey trends.

Several peaks in magnetic susceptibility correlate with peaks in conductivity and density, which are possibly correlated with glauconite occurrences at the base of the unit. At the m4.5 unconformity, density decreases sharply and sonic velocity peaks. The sharp change in the overall shape of the TGR trend at 205 mbsf is clearly evidenced on the acoustic images and conductivity curves. The trend shows a drastic increase in magnetic susceptibility due to a high content of ferromagnesian minerals. Chlorinity increases progressively from 188 mbsf uphole to salty water (see Fig. **F60**), in parallel with conductivity (see **"Geochemistry"**). In the units below, high

chlorinities were usually correlated to coarse-grained intervals. In this unit, high chlorinity appears in much clayey sediment. However, peaks in conductivity between 235 and 232 mbsf fit with TGR gamma lows and may reflect the presence of saltier pore water in coarse sediments that have not been sampled for geochemical measurements.

The boundary with Unit I is characterized by a rapid funnel-shaped TGR trend at the transition between weakly serrated high values below and smooth boxcar low values above, indicating a rapid grain size increase from silty muds below to clean sands above. The boundary is underlined by an increase in Th/K ratio.

Lithostratigraphic Unit I

The TGR signature of Unit I is composed of two 50 m thick low-value boxcar-shaped trends interbedded with 20–40 m thick stacks of 10 m thick bell- and funnel-shaped trends with intermediate values. These evolutions are typical of alternation of clean shoreface sands with coastal plain sands, silts, and clays. Trends in TGR are paralleled by Th, K, and U curves. Porosity and density trends are highly variable but very well anticorrelated. The Subunit IC/ID boundary (seismic sequence boundary m1) occurs at the top of a stepped boxcar-shaped interval with increasing gamma values. The Pleistocene surfaces corresponding to marine isotope Chrons (MICs) 4, MIC3c, and MIC3a are characterized by abrupt decreases in TGR values at the top of a thick boxcar trend and at the base of bell and funnel trends, respectively.

Stratigraphic surfaces and correlation with petrophysical intervals

Table T13 summarizes the key petrophysical surfaces and intervals. Most of them correspond to stratigraphic surfaces recognized on the core and on seismic profiles (see penultimate column in Table T13). Small differences in depth are due to the lack of precision in the location of an event (i.e., at the start of an increase in a parameter value or at the peak of the change). Petrophysical surfaces and intervals are defined by combining the full suite of logs and petrophysical parameters at places where more than one property displays a significant change. The m4 surface is imprecisely located because of a lack of data in this interval (see **"Stratigraphic correlation"**). The m3 surface is picked at the largest observed increase in gamma ray, but it falls a few meters above the seismic pick because of low core recovery. Flooding surfaces and transgressive surfaces are, in places, characterized by series of fluctuations in petrophysical parameters like density, magnetic susceptibility, and gamma ray (e.g., between 253 and 256 mbsf). Seven additional surfaces/intervals were picked from petrophysical data that are not obviously related to any seismic pick or major lithological unit/subunit transition. Some of these correspond to cemented horizons (see notes in last column of Table T13), whereas others reflect minor sedimentological changes.

Stratigraphic correlation

Seismic sequence identification

Site Survey *Oceanus* 270 (Oc270) and *Cape Hatteras* 0698 (CH0698) seismic data formed the framework for predicting seismic sequence boundaries in Hole M0027A (see Fig. F7 in the "Expedition 313 summary" chapter). Reflectors interpreted as lower and middle Miocene sequence boundaries (Miller and Mountain, 1994) were traced through the lower resolution *Ewing* 9009 (Ew9009) (~15 m vertical resolution) seismic grid from the outer shelf/slope region across the New Jersey shelf. These surfaces were subsequently correlated to the higher resolution Oc270 and CH0698 grids (Monteverde et al., 2008). Hole M0027A lies within a CH0698 hazard grid at the crossing of dip profile 107 common depth point (CDP) 11165 and strike profile 102 CDP 5704. CH0698 line 107 resampled part of Oc270 line 529. Time-depth correlations are based on semblance velocity data from Oc270 (see **"Stratigraphic correlation"** in the "Methods" chapter).

Targeted horizons in Hole M0027A range from the Pleistocene through the Eocene. The uppermost seismic reflectors intersected in Hole M0027A were Pleistocene surfaces identified on Geopulse data as MIC3a, MIC3c, and MIC4, with predicted depths on Oc270 line 529 at 6, 31, and 46 ms two-way traveltime (TWT) (Sheridan et al., 2000) corresponding to 12, 24, and 36 mbsf, respectively (see **"Chronology"** for age control on Pleistocene surfaces). Corresponding surfaces in the hole were identified as described below.

For Miocene and older sequences, seismic sequence boundaries were identified (see **"Stratigraphic correlation"** in the "Methods" chapter), and TWTs were picked by G.S. Mountain (unpubl. data) on OC270 line 529 and used during drilling operations. Monteverde et al. (2008) and this study (see **"Stratigraphic correlation"** in the "Methods" chapter) reevaluated loop correlations through the Oc270 seismic grid and provide slightly different TWT picks on some surfaces, as discussed below (Table T14). The velocity-depth function thus yielded two slightly different predictions of seismic sequence boundary correla-

tions in Hole M0027A, and a third one was provided based on a post-OSP revised velocity analysis (see **"Stratigraphic correlation"** in the "Methods" chapter). The three estimates provided close agreement, except for differences noted below. Corresponding surfaces in the hole were identified as described below.

Tracking Miocene seismic sequence boundaries m1, m3, and m4 to the Expedition 313 sites is tenuous because of the distance to ODP Leg 150 drill sites and the nature of chaotic seismic facies in the vicinity of Hole M0027A. Depth predictions of these seismic surfaces are similar between seismic interpretations. Five new surfaces have been identified between m4 and m5 seaward of Hole M0027A, but only two, m4.1 and m4.5, track into the drill site. Here, surface m4.1 is a merged reflector of surfaces m4.1, m4.2, m4.3, and m4.4, from youngest to oldest. Surface m4.5 merges with middle Miocene seismic sequence boundary m5 <1 km seaward (east) of Hole M0027A at CDP 6995 (Fig. **F63**) on line 529. Surface m4.2 is defined as a seismic sequence boundary, whereas surfaces m4.3 and m4.4 are reflector terminations that are suggestive of MFSs. Surface m4.5 has some weak indications as a possible sequence boundary on the limited number of dip lines within the Oc270 and CH0698 seismic grids. Lower and middle Miocene seismic surfaces m5.4, m5.3, and m5.2 are more clearly defined as moderate- to high-amplitude continuous reflectors and are imaged clearly. Hole M0027A intersects these surfaces landward of their corresponding rollover (clinoform inflection) positions. A new surface was defined at the base of well-defined downlapping reflectors between CDPs 5411 and 4934 on line 529 across Hole M0028A (Figs. **F63, F64**). This surface, lying between m5.4 and m5.3 and named m5.32, was traced following a moderate- to high-amplitude, discontinuous, slightly undulating reflector into Hole M0027A. No rollover/inflection point is associated with seismic surface m5.45 along line 529. However, surface m5.45 correlates to a seismic sequence boundary within the CH0698 grid to the south (Monteverde et al., 2008; Monteverde, 2008).

The nature of the next deepest seismic sequence boundary, m5.47, is more complex. Boundary m5.47 correlates to a highly bisected surface between Holes M0027A and M0028A (CDPs 7033–5386 on Oc270 line 529). This surface truncates seismic surface m5.6 at CDP 7133 on line 529 immediately east of Hole M0027A. The eastern continuation of surface m5.6 emerges from the erosional truncation immediately west of Hole M0028A at CDP 5516 on line 529. Surface m5.7 was sampled in Hole M0027A ~100–200 m landward of its rollover/inflection point. This surface is a high-amplitude continuous reflector along the seaward-dipping clinoform front. Near its rollover/inflection point, however, it becomes a low- to moderate-amplitude discontinuous reflector. Immediately above and below the m5.7 rollover/inflection point are low- to moderate-amplitude hummocky reflectors. This seismic facies continues from 449 to 525 ms TWT below seafloor at the drill site, and below that, the facies changes to low- to moderate-amplitude, parallel to subparallel seismic facies to 566 ms TWT. A sharp high-amplitude continuous reflector separates the previous seismic facies above from a thin zone (20 ms) of well-imaged high-amplitude reflectors that show both downlap and onlap seismic terminations. Seismic surface m5.8 forms the base of this seismic unit. Hole M0027A is downdip (seaward) of the m5.8 rollover/inflection point. Reflector m5.8 is placed in the core at 489.4 mbsf, slightly below its predicted depth (470–480 mbsf). Post-OSP revision of the time-depth correlation has reduced this disagreement between depths calculated from TWT and presumed surface in the core (see **"Stratigraphic correlation"** in the "Methods" chapter).

Surface m6 underlies m5.8 as a moderate-amplitude, discontinuous, undulating reflector. It traces to a sigmoidal structure with a rollover at CDP 9395 on line 529. A new surface identified as o.5 (G.S. Mountain, unpubl. data) is a moderate- to high-amplitude discontinuous reflector that traces westward to a major downlap surface near CDP 7500 on line 529; this was originally identified as reflector m6 (see Table **T10** in the "Methods" chapter), but loop correlations now indicate that it is older than reflector m6. Surface o.5 approximates the Miocene/Oligocene boundary (see **"Chronology"** for age control). The deepest predicted seismic surface encountered in Hole M0027A is surface o1, imaged as a moderate- to high-amplitude continuous reflector. Mountain et al. (1994) dated surface o1 as the Oligocene/Eocene boundary; however, in Hole M0027A it is clearly middle Oligocene (see **"Chronology"** for age control). The lack of Oligocene reflections between o.5 and o1 is due to the relative thinness. Numerous Oligocene sequence boundaries cored onshore (e.g., Pekar et al., 2000) are below seismic resolution.

Core-seismic sequence boundary integration

Core-seismic sequence boundary correlations are shown in Figures **F65, F66, F67, F68,** and **F69.** They are based on the integration of seismic and lithostratigraphy, log analysis, and age datings.

Pleistocene

A surface at Section 313-M0027A-5R-1, 11 cm (10.41 mbsf), marks the base of a coarsening-upward section, assigned an age of <90 ka based on nannofossils (Fig. F70). We interpret this surface as sequence boundary MIC3a (Sheridan et al., 2000). Gravel at the bottom of Core 313-M0027A-14R (26.38 mbsf) is dated at 125–250 ka based on nannofossils (Fig. F71). We interpret this as a sequence boundary predicted to be MIC3c (Sheridan et al., 2000). The section below this is older Pleistocene (NN19 with Sr isotope age estimates averaging 1.35 Ma in Section 313-M0027A-15R-CC). The base of this sequence is predicted at ~36 mbsf (Sheridan et al., 2000); it is poorly defined in cores because of poor recovery. It is tentatively placed at the gravel at Section 313-M0027A-19R-1, 39 cm (31.9 mbsf), though the position of this core is uncertain (Fig. F65).

Miocene

Reflectors m1–m4 are not well located relative to cores. Seismic reflector m1 is predicted (87–91 mbsf) in a poorly recovered zone, though we place it at 96 m log depth at a distinct decrease downsection in gamma ray values. Section 313-M0027A-50R-1 (97.12 mbsf) recovered a paleosol (Fig. F72) associated with moderate gamma values that decrease farther downsection and may mark the top of the underlying sequence m3. Reflector m3 was not cored but is placed near its predicted depth (105–109 mbsf) at the base of a downhole shift in gamma log values at 115 mbsf. Reflector m4 is predicted at 138–142 mbsf in an uncored interval, with little log expression (Fig. F73).

Reflector m4.1 marks a concatenated surface (at seismic resolution of ~5 m) of reflectors m4.1, m4.2, m4.3, and m4.4. Despite this probable condensed section or actual erosion, there is no apparent lithostratigraphic surface or change in log character at its predicted depth of 196 mbsf.

Reflector m5 is merged with reflector m4.5 at the site. This composite reflector m4.5/m5 (predicted depth of 210–215 mbsf) is tentatively placed at Section 313-M0027A-75R-2, 68 cm (218.39 mbsf), at the base of a granuliferous sandy silt over silty clay (Fig. F74). It is marked by a distinct impedance contrast caused by an increase in velocity and density measured by the MSCL (Fig. F66). It is interpreted as a candidate sequence boundary based on core observation (see "Lithostratigraphy"). The seismic placement is slightly above this depth, and this interval requires further study.

Reflector m5.2 (predicted depth of 225–230 m) was placed at Section 313-M0027A-80R-1, 10 cm, at the base of granuliferous very coarse sand over silty clay and corresponds to the base of a gamma log minimum (Fig. F66). There appear to be high MSCL density values at this level as well, although the recovery and data quality are too poor to be certain that this is an impedance contrast. It is interpreted as a candidate sequence boundary based on core observation (see "Lithostratigraphy").

A surface noted at the top of Section 313-M0027A-82R-1 (231.46 mbsf) has no obvious seismic expression. It consists of coarse sand in burrows at the top of the section and very fine sand below. The section above this (Section 313-M0027A-81R-2) changes downsection from clay to glauconite sand, consistent with its status as a candidate sequence boundary (see "Lithostratigraphy"). A downsection increase in MSCL density values is consistent with this section being a minor impedance contrast (Fig. F66).

Reflector m5.3 (235–240 mbsf predicted depth) is placed at Section 313-M0027A-83R-2, 127 cm (236.17 mbsf), at a contact between sand above and tight clay below (Fig. F75). There is a relatively large downhole decrease in MSCL density values across this surface that yields an impedance contrast (Fig. F66). It is interpreted as a candidate sequence boundary based on core observation (see "Lithostratigraphy").

A newly identified surface, m5.32 (predicted depth of 258–260 mbsf), appears to be a sequence boundary expressed as a surface at Section 313-M0027A-90R-1, 33 cm (256.19 mbsf). The surface juxtaposes granuliferous shelly silty sand over sandy silt (Fig. F76) and is interpreted as a candidate sequence boundary based on core observation (see "Lithostratigraphy").

Seismic sequence boundary m5.4 (predicted depth of 278–284 mbsf) appears to have an expression at Section 313-M0027A-95R-1, 10 cm (271.21 mbsf), at a sharp sedimentary facies change from laminated clayey silt above to sand below (Fig. F77). Core observation suggests this may be a transgressive surface, with the candidate sequence boundary immediately below (Fig. F66; see "Lithostratigraphy").

A surface noted at Section 313-M0027A-102R-2, 105 cm (295.01 mbsf), has no obvious seismic expression but is interpreted as a candidate sequence boundary based on core observations (see "Lithostratigraphy") (Fig. F78). It consists of very poorly sorted slightly glauconitic shelly sand deposited in shoreface–offshore transition environments overlying clayey silt deposited in offshore environments.

Seismic sequence boundary m5.45 (predicted depth of 325–330 mbsf) correlates with a surface at Section 313-M0027A-114R-2, 135.5 cm (331.9 mbsf), with a

shelly, silty very fine sand overlying a sharp, irregular surface with heavy bioturbation that overlies sandy silt deposited in offshore environments (Fig. F79). There is a slight increase in MSCL density and velocity at this level. This level corresponds to a bioturbated surface and is interpreted as a candidate sequence boundary based on core observation (see "Lithostratigraphy").

Seismic sequence boundary m5.47 (predicted depth of 335–340 mbsf) correlates with a surface at Section 313-M0027A-116R-1, 90 cm (336.06 mbsf). This is a sharp, heavily bioturbated erosion surface separating clayey very fine sandy silt deposited in offshore environments from underlying silty, poorly sorted fine–very fine glauconitic sand with granules and pebbles deposited as a transgressive lag deposit (Fig. F63). The bioturbation extends from 72 to 101 cm. This surface is interpreted as a candidate sequence boundary based on core observation (see "Lithostratigraphy").

Seismic sequence m5.5 is truncated at this site, but seismic sequence m5.6 (predicted depth of 345–350 mbsf) appears to correlate with Section 313-M0027A-125R-1, 140 cm (355.53 mbsf). This zone is indurated, with shelly glauconite sand from a poorly recovered zone of indurated quartz sands below (Fig. F80). This zone shows a major downhole increase in core density and NGR (Fig. F67) and is interpreted as a candidate sequence boundary based on core observation (see "Lithostratigraphy"). Seismic sequence m5.7 is predicted close to this level (350–360 mbsf), and we tentatively place it in a coring gap below Section 313-M0027A-127R-2, 22 cm (361.28 mbsf), at a major downhole change in gamma log values.

Sequence m5.8 is very thick (~127 m) and contains a strong intrasequence reflection predicted at 450–460 mbsf. This intrasequence surface appears to be the MFS identified in Core 313-M0027A-162R (465 mbsf) based on benthic foraminifer paleobathymetry (see "Paleontology"), though the downhole gamma log may indicate its placement at a peak in Core 313-M0027A-163R (Fig. F68). Core observations place the MFS slightly higher (~458 mbsf; see "Lithostratigraphy"). A gradual increase in MSCL density between 465 and 475 mbsf appears to be the cause of this reflection. Seismic sequence boundary m5.8 is predicted at 470–480 mbsf. It is best placed deeper than predicted; we tentatively place it at the top of cemented glauconite sands in Section 313-M0027A-170R-CC (489.39 mbsf) or the top of Core 171R (489.39 cm), with cemented glauconite sands continuing below.

Seismic sequence boundary m6 was initially predicted at 540–545 mbsf, but this surface was retraced during the OSP as a sequence in the Oligocene (o.5). Based on this revision, the m6 reflection is thus predicted at 475–503 mbsf, which we correlate with Section 313-M0027A-174R-1, 111 cm (494.87), at the base of indurated glauconitic sandstones and the top of silty glauconite sands. This level is a candidate sequence boundary based on core observation (Fig. F69) (see "Lithostratigraphy"). However, at this stage of analysis, this reflector could be placed as low as a large downhole gamma log increase at ~499 mbsf.

Reflector o.5 was predicted at 540–545 mbsf and is tentatively correlated with the top of Core 313-M0027A-192R (539.51 mbsf). The o.5 sequence is uppermost Oligocene to ?lowermost Miocene (see "Chronology"). There is no obvious lithologic expression of this reflection, and it may be in a core gap between Cores 313-M0027A-193R and 195R (545.5–548.66 mbsf) or possibly at the base of a shelly zone in Section 313-M0027A-193R-1, 134 cm (543.90 mbsf) (Fig. F69). However, Section 313-M0027A-192R-CC is dated as older than 28 Ma and has Sr isotope and paleontological ages in congruence with the section below (see "Chronology"), though it is possible that the shells are reworked in the base of the sequence. Post-OSP studies are needed to resolve placement of the reflector and hiatus with respect to the cores.

Reflector o1 was predicted at 585–590 mbsf and is correlated with a surface at Section 313-M0027A-209R-1, 22 cm (585.48 mbsf). At this depth, a heavily bioturbated surface separates muddy glauconitic very fine sand from underlying clayey silts; it is associated with a significant downhole increase in MSCL density values (Fig. F81), suggesting that this is the source of an impedance contrast (Fig. F82). Reflector o1 was dated on the continental slope by Leg 150 and *Alvin* cores as the EOT (Miller et al., 1998); however, o1 here is clearly a younger sequence boundary because it is well dated as middle Oligocene (see "Chronology").

Two Oligocene surfaces identified in cores appeared to be possible sequence boundaries based on lithostratigraphic characteristics but were too subtle and closely spaced to be imaged well with available seismic data at this burial depth. A tentative surface at Section 313-M0027A-212R-2, 30 cm (596.30 mbsf), is a thin bed of shells and foraminifers sandwiched between glauconitic silty clay in an interval of heavy biscuiting, but it is associated with a major gamma kick in logs and cores (Fig. F69).

Calcareous nannofossils indicate a major hiatus between upper Oligocene Zone NP24 in Sample 313-M0027A-218R-2, 103–106 cm, and lower mid-Oligocene Zone NP23 in Sample 313-M0027A-220R-2, 49–52 cm. A faint surface at Section 313-M0027A-219R-

1, 24 cm (617 mbsf), is a candidate for a sequence boundary associated with this hiatus, but we do not recognize a potentially correlative seismic surface.

The EOT is associated with a major erosional surface at Section 313-M0027A-223R-1, 90 cm (628.86 mbsf). Nannofossils in Sample 313-M0027A-223R-1, 26 cm, indicate lower Oligocene Zone NP22, whereas Sample 223R-1, 146 cm, indicates lower Zone NP21 and probable uppermost Eocene. Seismic and core expressions of Oligocene sequences are muted in Hole M0027A, and dating of hiatuses by biostratigraphy and Sr isotopes should provide a means of resolving sequence boundaries.

An acoustic impedance log was computed for Hole M0027A following the OSP to aid in core-seismic integration. The impedance log was constructed in two ways using MSCL bulk densities; velocities were taken from both MSCL velocity logs and downhole sonic logs. The resultant acoustic impedance logs shown on the synthesis figures (Figs. **F65, F66, F67, F68, F69, F73, F82**) allow evaluation of seismic-core correlation made by other means (e.g., the velocity-depth function, matching to core surfaces, downhole log, and MSCL changes). The impedance log in the top 200 m (Figs. **F65, F73**) uses only MSCL data, and core-log seismic integration is hampered by poor recovery. Comparison with the positions of reflections m4.5, m5.2, flooding surface m5.3, m5.32, and m5.4 with the impedance log is compelling: reflections are placed in the core by other criteria precisely at acoustic impedance contrasts except for m5.3, which is <2 m offset (Fig. **F66**). Acoustic log quality is not as high for sections encompassing seismic sequence boundaries m5.45, m5.47, m5.6, and m5.7 (Fig. **F67**) but are generally consistent with the core placement. Acoustic impedance data support placement of sequence boundaries m5.8 and m6 and are generally consistent with o1 but suggest that seismic sequence boundary o.5 may be too deep by ~5 m (Fig. **F67**).

Core-seismic-log synthesis

Figures **F65, F66, F67, F68, F69, F73,** and **F82** summarize the ties between sequence boundaries, sedimentary facies, and chronostratigraphy developed in Hole M0027A and are discussed below, emphasizing the relationships between core sequences, logs, and seismic facies within a lithostratigraphic framework. (These figures are combined in Fig. **F83.**) Correlations include a synthesis of the lithology accompanied by an indication of depositional environments and paleodepth estimated by benthic foraminifer assemblages (see **"Paleontology"**). TGR (downhole logging data), NGR (MSCL measurements), and the relative concentration of isotope decay products (K, U, and Th) are also shown. Chronostratigraphy is established on the basis of biostratigraphic analyses (see **"Paleontology"**), whereas indication of age is given by the Sr dates (see **"Chronology"**). The data set is completed with a preliminary characterization of the seismic facies and with the correlation between the sequence boundaries detected in the cores and the predicted depth range of seismic reflections. Moreover, predicted depths from post-OSP revision to the time-depth function are shown in the figures, but they are not discussed because they were not available during the OSP (Figs. **F65, F66, F67, F68, F69, F73, F82**).

Lithostratigraphic Unit I (0–167.74 mbsf)

Seismic reflector MIC3c (Sheridan et al., 2000), with a predicted depth of 24 mbsf, is associated with a core sequence boundary at 26.29 mbsf (base of Core 313-M0027A-14R) and marks the boundary between lithostratigraphic Subunits IA and IB and the upper versus lower Pleistocene (Fig. **F65**). Seismic reflector MIC4, with a predicted depth of 36 mbsf, is associated with a major gap between the Pleistocene and the Miocene. The predicted depth from Geopulse seismic profiles (Sheridan et al., 2000) and the velocity function used during the OSP (see **"Stratigraphic correlation"** in the "Methods" chapter) is 36 mbsf, slightly deeper than the depth interpreted in the core lithology (Section 313-M0027A-19R-1, 56 cm; 31.9 mbsf). The succession passes downhole to a poorly recovered and barren interval (possibly fluvial deposit infilling a valley incision) of supposed Miocene age that includes lithostratigraphic Subunits IC and IB. The position of reflector m1 is based on well log data (decreasing gamma ray values at ~96 mbsf) and corresponds to the transition between lithostratigraphic Subunits IC and ID. The predicted depth range (89–94 mbsf) for reflector m1 is slightly shallower than the position inferred from gamma ray log values. The transition to possibly coarse-grained sediment is also marked on the seismic profile by the abrupt transition from parallel reflectors to channel-fill seismic facies.

Recovery is very poor down to Core 313-M0027A-58R (176 mbsf; lithostratigraphic Subunit ID). The section mainly corresponds to very low gamma ray values with granules and pebbles at the base, as evidenced in Cores 313-M0027A-55R and 56R. Reflector m3 has been positioned at 115 mbsf by relying on the well-log data, whereas the predicted depth range lies between 89 and 94 mbsf (Fig. **F73**). The log data signature was also used to locate reflector m4, where the predicted depth range based on velocity is 138–143 mbsf. The transition between lithostratigraphic Units I and II is not cored but is evidenced by down-

hole increasing gamma ray values and falls into an interval characterized by chaotic seismic facies.

Lithostratigraphic Unit II (167.74–236.16 mbsf)

The lack of a surface in the core or a change in either log or MSCL character at the predicted depth of reflector m4.1 (196 mbsf) requires further examination. Similarly, more work is needed to understand why the predicted depth for reflector m4.5 (208–211 mbsf) is shallower than the position interpreted in the core (Section 313-M0027A-75R-2, 68 cm; 218.39 mbsf). In contrast, reflectors m5.2 (Section 313-M0027A-80R-1, 10 cm; 225 mbsf) and m5.3 (Section 83R-2, 127 cm; 237.3 mbsf) match fairly well with the predicted depths (225–230 mbsf for m5.2 and 235–242 mbsf for m5.3) as shown in Figure F66. Reflector m5.3 coincides with the transition between lithostratigraphic Units II and III.

Several fining- and deepening-upward intervals (corresponding to transgressive shoreface evolving to shoreface–offshore transition; see "Lithostratigraphy") are identified between the predicted depths of reflectors m4.5, m5, and m5.3 (lithostratigraphic Unit II of middle Miocene age, as indicated by nannofossils). Each succession is truncated at the top, and the basal lag is marked by low values in gamma ray, K, U, and Th. The sequence overlying reflector m4.5 becomes homogeneous toward the top and bears a MFS (195 mbsf) that has no log expression. Nonetheless, it has been estimated on lithological facies (Section 313-M0027A-66R-2) in association with a downhole log gamma peak.

Lithostratigraphic Unit III (236.16–295.01 mbsf)

Lithostratigraphic Unit III (early middle Miocene) is composed of two distinct fining-upward sequences resting on reflectors m5.32 (256.2 mbsf) and m5.4 (271.21 mbsf) (Fig. F66). The predicted depths of the seismic reflectors lie slightly below the surfaces interpreted in the cores (258–260 mbsf for m5.32 and 278–284 mbsf for m5.4). Reflector m5.4 marks a significant change in seismic facies from parallel (above reflector m5.4) to subparallel reflectors.

The base of lithostratigraphic Unit III was positioned at 295 mbsf, corresponding to a major erosion surface (Section 313-M0027A-102R-2; see "Lithostratigraphy"). It corresponds to a peak in NGR-TGR values and a locally sharp increase in impedance derived from the sonic log (Fig. F67), but no seismic expression has yet been identified.

Lithostratigraphic Unit IV (295.01–335.93 mbsf)

Lithostratigraphic Unit IV contains reflectors m5.45 and m5.47 (Fig. F67). Reflector m5.45 is correlated at 331.9 mbsf at the base of the predicted depth interval (328–331 mbsf). It is marked by a peak in NGR values and a bioturbated surface. Reflector m5.47 is positioned at 336 mbsf (base of Unit IV), within the predicted depth range (335–343 mbsf), where a major lithological change is observed (coarse sand–silt transition) at the base of Unit IV (Fig. F84). In general, lithostratigraphic Unit IV is characterized by shallowing-upward successions from silt-prone offshore to shoreface–offshore transition with intercalated storm beds. Changes in the K-gamma log support these observations. Abrupt changes in impedance values (Fig. F67) suggest there ought to be strong seismic reflections in this unit as well. Indeed, there are corresponding reflections between reflectors m5.47 and m5.3, but they have very short lateral continuity (<1 km) on line 529, consistent with a series of retrograde parasequences.

Lithostratigraphic Unit V (335.93–355.72 mbsf)

The predicted depth of reflector m5.6 (346–350 mbsf) is 6–10 m above the preferred location at the base of lithostratigraphic Unit V (355.53 mbsf); hence, this unit is bracketed by reflectors (m5.47 at the top and m5.6 at the base) with no other seismic feature noted in between. Recovery in this unit was comparatively poor, and in general, the cores showed poorly sorted glauconite-rich sand with quartz and lithic granules interpreted as a transgressive shoreface environment. Perhaps this high-energy environment did not preserve the lateral continuity of stratal features that need to be resolved by seismic profiling. A Fresnel radius of ~100 m would be expected with the Oc270 air gun array at this depth, meaning that features on the order of a few tens of meters in lateral extent may not be detectable.

Lithostratigraphic Unit VI (355.72–488.75 mbsf)

Lithostratigraphic Unit VI is bracketed by reflectors m5.6 at its top and m5.8 at its base. It is a thick (~127 m) coarsening-upward succession of prodelta silt becoming clean shoreface quartz sand at top. The gamma log character shows this pattern of values smoothly decreasing uphole, with the exception of a local increase near 363 mbsf (Fig. F65) that corre-

sponds to locally finer sediment in Core 313-M0027A-127R. This depth is close to the range of predicted depths for reflector m5.7 (350–360 mbsf) and is the position chosen for its most likely correlation. However, there is little other supporting evidence to justify this core-seismic correlation. In general, lithostratigraphic Unit VI corresponds to a large clinoform buildup comprising sequence m5.8 plus the poorly recovered ~8 m between reflector m5.7 and the top of Unit VI at reflector m5.6. The seismic facies show a subtle change from crudely parallel but discontinuous in the basal finer grained portion to faintly hummocky, irregular, and even more discontinuous in the coarser sands near the top of Unit VI.

Reflector m5.8 (Fig. F68) is placed in the core at 489.4 mbsf, slightly below its predicted depth (470–480 mbsf); as noted above, we attribute this to a possible overestimate of velocity. Within this sequence, a significant lithological change from medium-coarse grained sand (top) to silt (bottom) is associated with a gradual transition from very low to relatively high gamma ray values (transition between lower Miocene lithostratigraphic Subunits VIA and VIB and corresponding to river-influenced offshore to river-influenced shoreface–offshore transition). There is no seismic reflection associated with this coarsening upsection from silt to sand, but a change of seismic facies can be observed: slightly hummocky reflectors characterize Subunit VIA, and parallel reflectors match Subunit VIB (Fig. F68).

Lithostratigraphic Unit VII (488.75–625.60 mbsf)

A 5 m interval of coarse-grained, carbonate-cemented sand occurs at the top of lithostratigraphic Unit VII and creates large impedance contrasts (Fig. F69). The top of this interval is marked by a sharp downhole increase in impedance and provides a placement for reflector m5.8 within a few meters of its predicted depth. The bottom of this indurated interval creates a sharp downhole decrease in impedance and corresponds to reflector m6, also within a few meters of its predicted depth.

Downhole (between Cores 313-M0027A-176R and 180R), fluctuations of U concentration may indicate variable amounts of organic matter (and/or phosphorite?) in the sediments. These fluctuations are visible through the succession to Reflector o.5 (539.51 mbsf). This surface is predicted to lie between 540 and 545 mbsf, which matches reasonably well with the sedimentological interpretation (1–5 m deeper than the core pick). Surface o.5 spans the Miocene/Oligocene boundary, based mainly on dinoflagellate biostratigraphy at the top of Core 313-M0027A-192R. Below this surface, highly variable K concentrations could be related to glauconite content in the sand, but no evident surface has been identified in the sediment core.

At 585.48 mbsf, Reflector o1 was tied to Section 313-M0027A-209-1R, 22 cm, where it correlates perfectly with its predicted depth (585–590 mbsf).

Lithostratigraphic Unit VIII (625.60–631.15 mbsf)

The very bottom of Hole M0027A consists of deep-water (>100 m) sediments (see "Lithostratigraphy") moderately rich in glauconite. Downhole log data stop at ~600 mbsf, but the high amplitude of NGR measurements are possibly related to the presence of glauconite.

The Oligocene–Eocene transition is detected in Section 313-M0027A-223-1R, 90 cm (628.86 mbsf), with no associated seismic reflection.

The core-seismic-log synthesis (Fig. F70) in Hole M0027A shows fairly good correlation between the seismic surfaces and the log data in lithostratigraphic Unit I. However, the correlation with surfaces in the core is hardly possible in the Miocene succession because of poor recovery. Thus, the correlation is mainly based on downhole logging data. Lithostratigraphic Units II, III, IV, and V are almost totally recovered. An excellent correlation between the surface picked in the cores and reflectors is possible here. Reflectors m4.5, m5.2, m5.3, and m5.4 also match TGR-NGR values.

Lithostratigraphic Unit VI is poorly characterized in terms of sequence boundaries; the position of reflector m5.8 was problematic because of possible overestimation of velocity. The lowermost Miocene reflector (m6 in lithostratigraphic Unit VII) is well evidenced both in lithology and TGR values and correlates well with reflector m6. For positioning Oligocene reflectors o.5 and o1, further studies are necessary because no evident surfaces have been identified in the cores.

Chronology

Chronology is provided for the uppermost Eocene? to Pleistocene section in Hole M0027A by integrating the following on an age-depth diagram (Figs. F34, F85):

1. Biostratigraphy provided by calcareous nannofossil, planktonic foraminifer, and dinocyst data. Zonal durations are plotted using tables provided in "Paleontology."
2. Sr isotopic ages and associated age errors.
3. Placement of sequence boundaries and other stratal surfaces (Table T14).

4. The timescale of Berggren et al. (1995; BKSA95). (Although this timescale is demonstrably incorrect in the earliest Miocene [e.g., correlation of the base of the Miocene as 22.9 ± 0.1 Ma versus 23.8 Ma in Shackleton et al., 2000], Sr isotope regressions and dinocyst zonations have not been calibrated to the GTS2008 [Ogg and Gradstein, 2008.])

Surfaces were picked as seismic sequence boundaries in TWT (Table **T14**), converted to depth, and tied to cores (Table **T14**) using a velocity function (see **"Stratigraphic correlation"** in the "Methods" chapter for discussion of criteria used to define seismic sequence boundaries and the derivation of the time to depth conversion of seismic data). In figures, features are presented as follows:

- If unsampled by cores, the reflector is indicated with a gray shaded zone (e.g., m4 at ~140 m; Fig. **F34**).
- If identified in a core, the surface was plotted as a solid red line for candidate sequence boundaries.
- A few prominent (but not all) features interpreted as MFSs identified in the cores (see figures in **"Stratigraphic correlation"**) are indicated with a green line.
- A visual best fit sedimentation rate line was estimated for each sequence and an age error assigned to each (shaded zones; Fig. **F34**).
- All estimated sedimentation rates do not include estimates of postdepositional compaction, so they are minimum values.

Pleistocene sequences in Hole M0027A were identified on Geopulse seismic profiles and interpreted as representing MIC3a, MIC3c, and MIC4 (Sheridan et al., 2000). Calcareous nannofossils suggest that the top sequence (above 10.41 mbsf) is upper Pleistocene (<90 ka) because it is within the acme zone of *Emiliania huxleyi* (Hine and Weaver, 1998). One or more sequences between 10.41 and 26.38 mbsf are estimated as 90–250 ka between the acme and FO of *E. huxleyi*. A thin Pleistocene (Zone NN19) sequence from 26.4 to 31.9 mbsf appears to be lower Pleistocene based on an Sr isotope age estimate of 1.35 Ma ± 0.35 m.y. We speculate that this may represent MIC30 (~1 Ma). Sedimentation rates are difficult to establish with the age model at this preliminary stage. Pleistocene sedimentation rates appear to be high (>100 m/m.y).

The fluvial–estuarine section above seismic sequence boundary m1 (~96 mbsf) and the poorly sampled section from that depth to 140 mbsf containing seismic sequence boundaries m3 (~115 m) and m4 (~140 mbsf) provide no age constraints at this location. Seismic sequence boundary m2 and all of the sediments that make up the m2 sequence have been removed by erosion. The m1, m3, and m4 seismic sequence boundaries have been dated on the slope as ~11.5, 13.6, and 14.1 Ma, respectively (Miller et al., 1997), which yields minimum sedimentation rates of 50, 25, and 50 m/m.y., respectively, for the sequences in Hole M0027A.

Reflector m4.1 is interpreted as a MFS at this site based on its correlation into the middle of a succession of clay. Seismic reflector m4.1 seismically merges with several older surfaces (m4.2, m4.3, and m4.4 [dated in Hole M0029A]) and must represent a significant hiatus that is not discernable with the available age control. Magnetic susceptibility measurements suggest a break at 195 mbsf in the middle of the clay that may mark this coalesced surface. Seismic sequence boundary m5 apparently merges with the m4.5 surface (218.4 mbsf), and sediments from the overlying sequence(s) are poorly dated. Sr isotope ages of 13.6–13.7 Ma ± 1.2 m.y. in the lower part of the section are consistent with dinocyst assignment to upper Zone DN5 and calcareous nannofossils to Zones NN6–NN7 (~11.2–13.6 Ma).

A series of relatively thin (<25 m) sequences (m5.2, unnamed, m5.3, m5.32, m5.4, and unnamed) span the lower/middle Miocene boundary (16.2 Ma BKSA95 and the 2004 geologic timescale. There are no constraints on the age of seismic sequence boundary m5.2 and the overlying sequence other than superposition. The underlying sequence m5.3 is assigned to Zone NN5 (>15.6 Ma) and Sr isotope age estimates of 15.8 and 16.0 Ma ± 0.6 m.y. (below). The sequence overlying seismic sequence boundary m5.32 records the change from Zone NN5 to NN4 (15.6 Ma) with a basal Sr isotope age of 16.3 Ma ± 0.6 m.y. However, correlations to Holes M0028A and M0029A suggest that the base of Zone NN4 may be depressed in Hole M0027A, as the marker for the base of this zone is predicted to range higher in the sandy sediments in Hole M0027A. Sequence m5.4, an unnamed sequence with a base at 295.0 mbsf, and sequences m5.45 and m5.47 all lie within Zone NN4 (15.6–18.4 Ma), with planktonic foraminifer Zone N6/M3 (17.3–18.8 Ma) in the basal 5.47 sequence. Sr isotopes provide some age constraints on the sequences overlying the following seismic sequence boundaries: 17.0 Ma ± 0.6 m.y. (m5.4), 17.2 and 17.8 Ma ± 0.6 m.y. (unnamed; 295 mbsf), and 18.4 Ma ± 0.6 m.y. (m5.45). Age estimates of basal sequence boundary ages (ranging from ~17.3 to 18.4 Ma; Table **T14**) have fairly large errors because of limited data, and future work should tighten the age estimates. Mean apparent sedimentation rates during deposition of the thin sequence spanning the lower/middle Miocene boundary (sequence m5.2–m5.47) were at least 30–40 m/m.y. Shorebased stud-

ies should improve the age resolution for this interval.

A 36.9 m thick sequence m5.45 (295.01–331.90 mbsf) and a thin (4.2 m) sequence m5.47 (331.90–336.06 mbsf) are estimated as ~18.0 and ~18.3 Ma, respectively, and are reasonably well constrained by *Praeorbulina sicana* and Zone NN4 with ±0.5 m.y. age resolution.

Thin sequences m5.6 and m5.7 (336.1–355.5 and 355.5–361.3 mbsf, respectively; ~18.7–19.6 Ma) have no current age information (barren/non–age diagnostic nannofossils), although they contain shells. Shore-based analyses are expected to produce ages based on dinocysts and Sr isotopes.

A thick (128.1 m) sequence m5.8 (361.3–489.4 mbsf) has a lower seismic sequence boundary dated as 21.1 Ma. Ages in the lower part of the sequence are well constrained by Sr isotopes and foraminifer and dinocyst zones and are assigned to the middle portion of nannofossil Zone NN2. The upper sands of this sequence are poorly dated (20 Ma? by extrapolation of sedimentation rates), although sedimentation rates for this sequence must be high (~120 m/m.y.).

A thin lowermost Miocene sequence m6 (489.4–499.9 mbsf) is dated only by assignment to mid-Zone NN2. Nevertheless, the short duration (<0.5 m.y.) required by the short zone and a thick section assigned to mid-Zone NN2 above suggest a moderate sedimentation rate (>20 m/m.y.).

At least four Oligocene sequences and part of an uppermost Eocene to lowermost Oligocene sequence occur in the bottom of the hole. The Oligocene succession is unusually thick (>129 m) compared to onshore successions (Pekar et al., 1997). A previously unnamed sequence (o.5; 499.8–539.5 mbsf) apparently straddles the Oligocene/Miocene boundary with nannofossil Zone NN1 and a tentative assignment to planktonic foraminifer Zone N4 in the upper part of the sequence and dinocyst Zone DN1 (uppermost Oligocene–lowermost Miocene) throughout. Further work on this boundary interval is needed. A slightly discordant Sr isotope age (25.3 Ma) requires verification. Sedimentation rates can only be roughly estimated as ~40 m/m.y.

The o1 sequence (539.5–585.5 mbsf) is well dated by all fossil groups and Sr isotopes as mid-Oligocene (28.5–29.0 Ma). This sequence has a high sedimentation rate (~92 m/m.y.). The underlying unnamed sequence (585.5–596.3 mbsf) is poorly dated as ~30 Ma. One or more sequences between 596.3 and 628.9 mbsf have conflicting ages, and further study is needed. The base of this interval is assigned to lower Oligocene nannofossil Zone NP22 (Chron C12r). The base of the hole is in lower Zone NP21, suggesting that Chron 13n and some of upper Chron C13r (the Eocene/Oligocene boundary) is represented by a hiatus across a sequence boundary at 628.9 mbsf. This basal Oligocene sequence boundary is most likely equivalent to the global sea level fall associated with isotopic increase Oi1, and further magnetostratigraphic, biostratigraphic, and stable isotopic studies will test the continuity of this section.

References

Bahr, D.B., Hutton, E.W.H., Syvitski, J.P.M., and Pratson, L.F., 2001. Exponential approximations to compacted sediment porosity profiles. *Comp. Geosci.,* 27(6):691–700. **doi:10.1016/S0098-3004(00)00140-0**

Berggren, W.A., Kent, D.V., Swisher, C.C., III, and Aubry, M.-P., 1995. A revised Cenozoic geochronology and chronostratigraphy. *In* Berggren, W.A., Kent, D.V., Aubry, M.-P., and Hardenbol, J. (Eds.), *Geochronology, Time Scales and Global Stratigraphic Correlation.* Spec. Publ.—SEPM (Soc. Sediment. Geol.), 54:129–212.

Berggren, W.A., and Pearson, P.N., 2005. A revised tropical to subtropical Paleogene planktonic foraminiferal zonation. *J. Foraminiferal Res.,* 35(4):279–298. **doi:10.2113/35.4.279**

Cande, S.C., and Kent, D.V., 1995. Revised calibration of the geomagnetic polarity timescale for the Late Cretaceous and Cenozoic. *J. Geophys. Res., [Solid Earth],* 100(B4):6093–6095. **doi:10.1029/94JB03098**

Coccioni, R., Marsili, A., Montanari, A., Bellanca, A., Neri, R., Bice, D.M., Brinkhuis, H., Church, N., Macalady, A., McDaniel, A., Deino, A., Lirer, F., Sprovieri, M., Maiorano, P., Monechi, S., Nini, C., Nocchi, M., Pross, J., Rochette, P., Sagnotti, L., Tateo, F., Touchard, Y., Van Simaeys, S., and Williams, G.L., 2008. Integrated stratigraphy of the Oligocene pelagic sequence in the Umbria-Marche Basin (northeastern Apennines, Italy): a potential Global Stratotype Section and Point (GSSP) for the Rupelian/Chattian boundary. *Geol. Soc. Am. Bull.,* 120(3–4):487–511. **doi:10.1130/B25988.1**

de Verteuil, L., and Norris, G., 1996. Miocene dinoflagellate stratigraphy and systematics of Maryland and Virginia. *Micropaleontology,* 42(Suppl.). **doi:10.2307/1485926**

Hine, N., and Weaver, P.P.E., 1998. Quaternary. *In* Bown P.R. (Ed.), *Calcareous Nannofossil Biostratigraphy:* Dordrecht (Kluwer Academic Publishers), 266–283.

Martini, E., 1971. Standard Tertiary and Quaternary calcareous nannoplankton zonation. *Proc. Int. Conf. Planktonic Microfossils,* 2:739–785.

Metzger, J.M., Flemings, P.B., Christie-Blick, N., Mountain, G.S., Austin, J.A., Jr., and Hesselbo, S.P., 2000. Late Miocene to Pleistocene sequences at the New Jersey outer continental shelf (ODP Leg 174A, Sites 1071 and 1072). *Sediment. Geol.,* 134(1–2):149–180. **doi:10.1016/S0037-0738(00)00018-X**

Miller, K.G., and Mountain, G.S., 1994. Global sea-level change and the New Jersey margin. *In* Mountain, G.S.,

Miller, K.G., Blum, P., et al., *Proc. ODP, Init. Repts.,* 150: College Station, TX (Ocean Drilling Program), 11–20. **doi:10.2973/odp.proc.ir.150.102.1994**

Miller, K.G., Mountain, G.S., Browning, J.V., Kominz, M., Sugarman, P.J., Christie-Blick, N., Katz, M.E., and Wright, J.D., 1998. Cenozoic global sea level, sequences, and the New Jersey transect: results from coastal plain and continental slope drilling. *Rev. Geophys.,* 36(4):569–602. **doi:10.1029/98RG01624**

Miller, K.G., Mountain, G.S., the Leg 150 Shipboard Party, and Members of the New Jersey Coastal Plain Drilling Project, 1996. Drilling and dating New Jersey Oligocene–Miocene sequences: ice volume, global sea level, and Exxon records. *Science,* 271(5252):1092–1095. **doi:10.1126/science.271.5252.1092**

Miller, K.G., Rufolo, S., Sugarman, P.J., Pekar, S.F., Browning, J.V., and Gwynn, D.W., 1997. Early to middle Miocene sequences, systems tracts, and benthic foraminiferal biofacies, New Jersey coastal plain. *In* Miller, K.G., and Snyder, S.W. (Eds.), *Proc. ODP, Sci. Results,* 150X: College Station, TX (Ocean Drilling Program), 169–186. **doi:10.2973/odp.proc.sr.150X.313.1997**

Monteverde, D.H., 2008. Sequence stratigraphic analysis of early and middle Miocene shelf progradation along the New Jersey margin [Ph.D. dissert.]. Rutgers Univ.

Monteverde, D.H., Mountain, G.S., and Miller, K.G., 2008. Early Miocene sequence development across the New Jersey margin. *Basin Res.,* 20(2):249–267. **doi:10.1111/j.1365-2117.2008.00351.x**

Mountain, G.S., Miller, K.G., Blum, P., et al., 1994. *Proc. ODP, Init. Repts.,* 150: College Station, TX (Ocean Drilling Program). **doi:10.2973/odp.proc.ir.150.1994**

Mountain, G.S., Proust, J.-N., and McInroy, D., 2009. New Jersey shallow shelf: shallow-water drilling of the New Jersey continental shelf: global sea level and architecture of passive margin sediments. *IODP Sci. Prosp.,* 313. **doi:10.2204/iodp.sp.313.2009**

Munsterman, D.K., and Brinkhuis, H., 2004. A southern North Sea Miocene dinoflagellate cyst zonation. *Geol. Mijnbouw,* 83(4):267–285. **http://www.njgonline.nl/publish/articles/000060/article.pdf**

Ogg, J.G., Ogg, G., and Gradstein, F.M., 2008. *The Concise Geologic Time Scale*: Cambridge (Cambridge Univ. Press). **http://www.cambridge.org/catalogue/catalogue.asp?isbn=9780521898492**

Pekar, S., Miller, K.G., and Browning, J.V., 1997. New Jersey coastal plain Oligocene sequences. *In* Miller, K.G., and Snyder, S.W. (Eds.), *Proc. ODP, Sci. Results,* 150X: College Station, TX (Ocean Drilling Program), 187–206. **doi:10.2973/odp.proc.sr.150X.314.1997**

Pekar, S.F., Miller, K.G., and Kominz, M.A., 2000. Reconstructing the stratal geometry of latest Eocene to Oligocene sequences in New Jersey: resolving a patchwork distribution into a clear pattern of progradation. *Sediment. Geol.,* 134(1–2):93–109. **doi:10.1016/S0037-0738(00)00015-4**

Perch-Nielsen, K., 1985. Cenozoic calcareous nannofossils. *In* Bolli, H.M., Saunders, J.B., and Perch-Nielsen, K. (Eds.), *Plankton Stratigraphy:* Cambridge (Cambridge Univ. Press), 427–554.

Rider, M., 2006. *The Geological Interpretation of Well Logs* (2nd ed.): Sutherland, Scotland (Whittles).

Sclater, J.G., and Christie, P.A.F., 1980. Continental stretching: an explanation of the post-mid-Cretaceous subsidence of the central North Sea basin. *J. Geophys. Res., [Solid Earth],* 85(B7):3711–3739. **doi:10.1029/JB085iB07p03711**

Shackleton, N.J., Hall, M.A., Raffi, I., Tauxe, L., and Zachos, J., 2000. Astronomical calibration age for the Oligocene–Miocene boundary. *Geology,* 28(5):447–450. **doi:10.1130/0091-7613(2000)28<447:ACAFTO>2.0.CO;2**

Sheridan, R.E., Ashley, G.M., Miller, K.G., Waldner, J.S., Hall, D.W., and Uptegrove, J., 2000. Offshore-onshore correlation of upper Pleistocene strata, New Jersey coastal plain to continental shelf and slope. *Sediment. Geol.,* 134(1–2):197–207. **doi:10.1016/S0037-0738(00)00020-8**

Van Simaeys, S., Munsterman, D., and Brinkhuis, H., 2005. Oligocene dinoflagellate cyst biostratigraphy of the southern North Sea Basin. *Rev. Palaeobot. Palynol.,* 134(1–2):105–128. **doi:10.1016/j.revpalbo.2004.12.003**

Publication: 4 December 2010
MS 313-103

Figure F1. Symbols and colors used in "Lithostratigraphy" and "Stratigraphic correlation" figures for Hole M0027A.

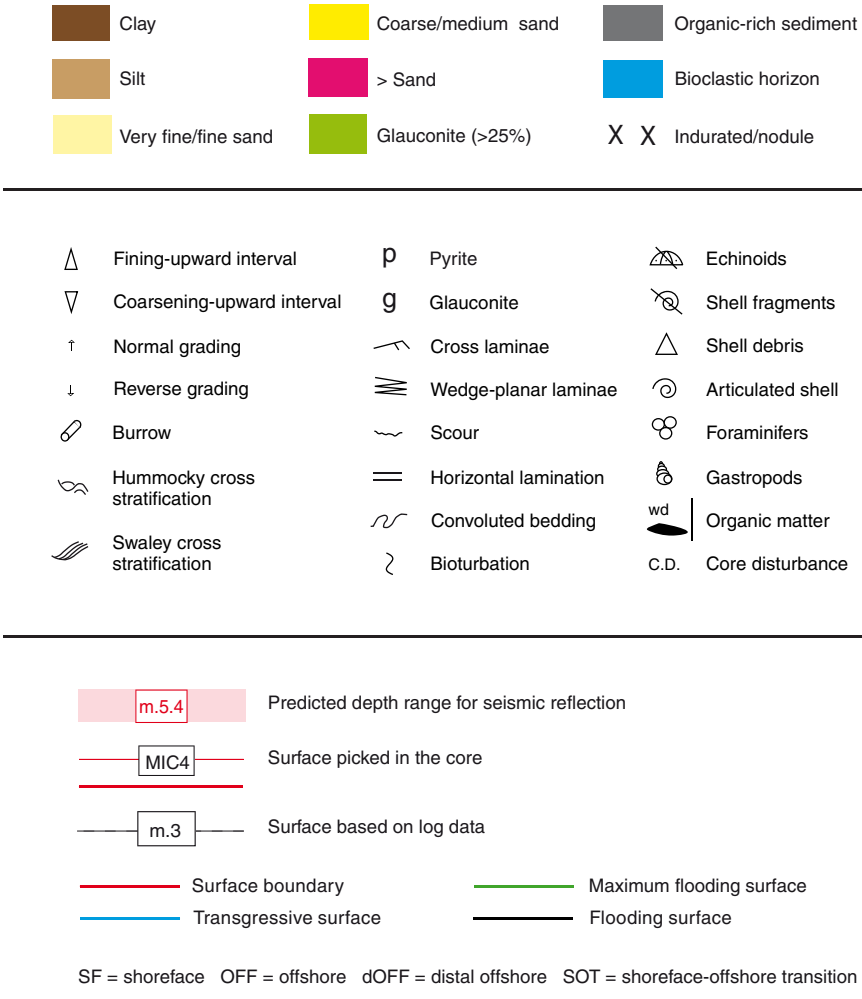

Figure F2. Location of Hole M0027A on seismic line 529, showing lithostratigraphic units in color on a background with seismic reflectors. See Table T2 for depths of seismic units. CDP = common depth point.

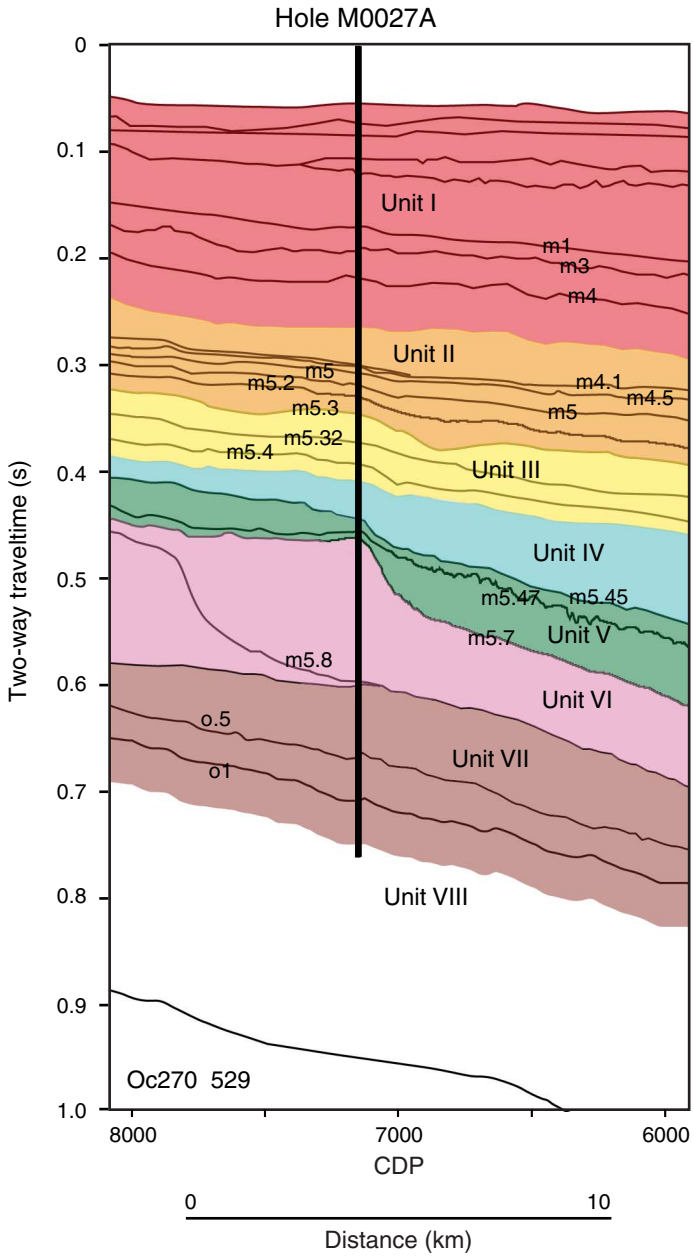

Figure F3. Summary sedimentary logs of lithostratigraphic units and subunits identified in Hole M0027A, from the top of Unit I to the base of Unit III. See Figure F1 for lithology legend. vf = very fine, f = fine, m = medium, c = coarse.

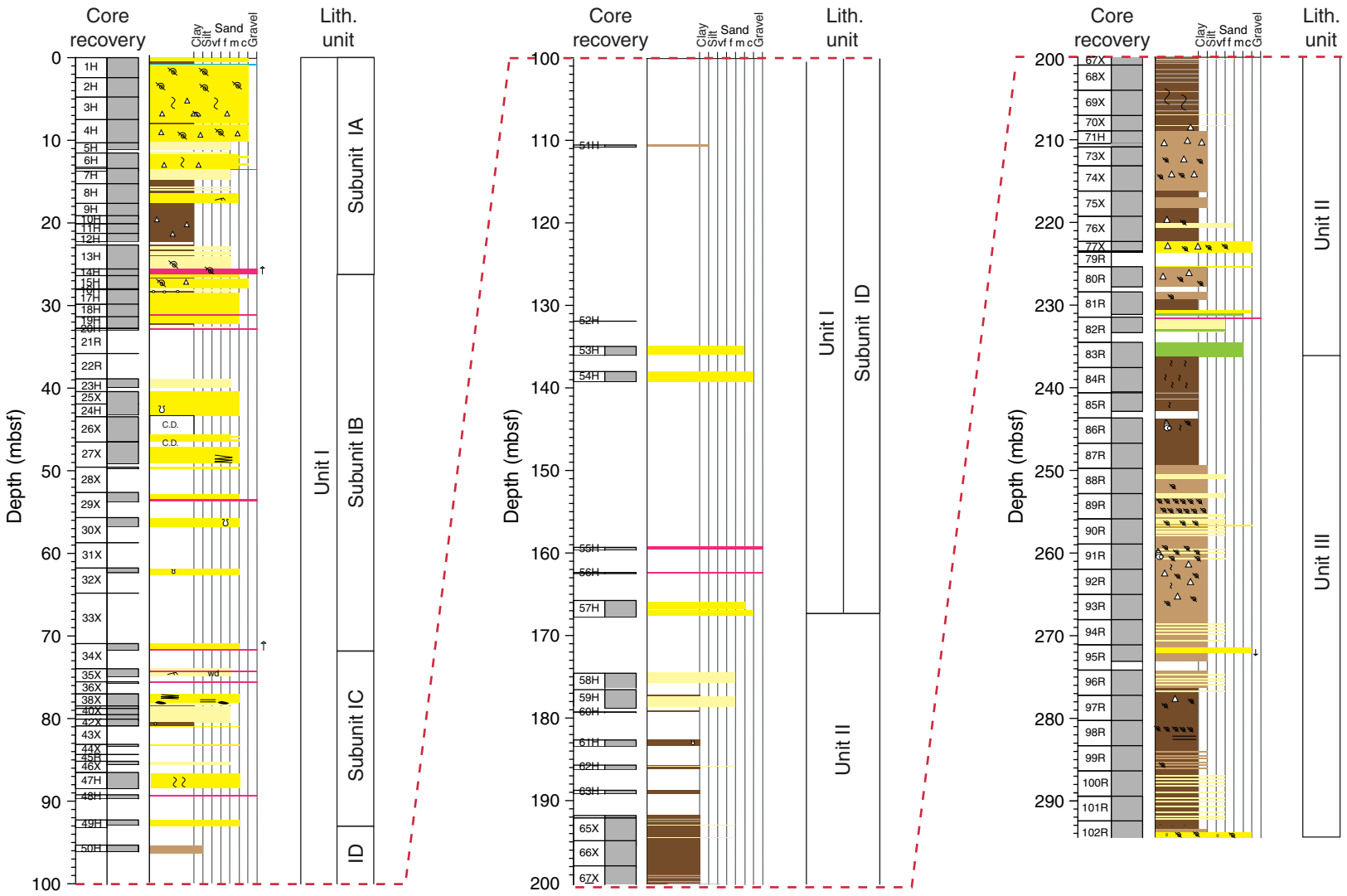

Figure F4. Summary sedimentary logs for Units IV–VIII from Hole M0027A. See Figure F1 for lithology legend. vf = very fine, f = fine, m = medium, c = coarse.

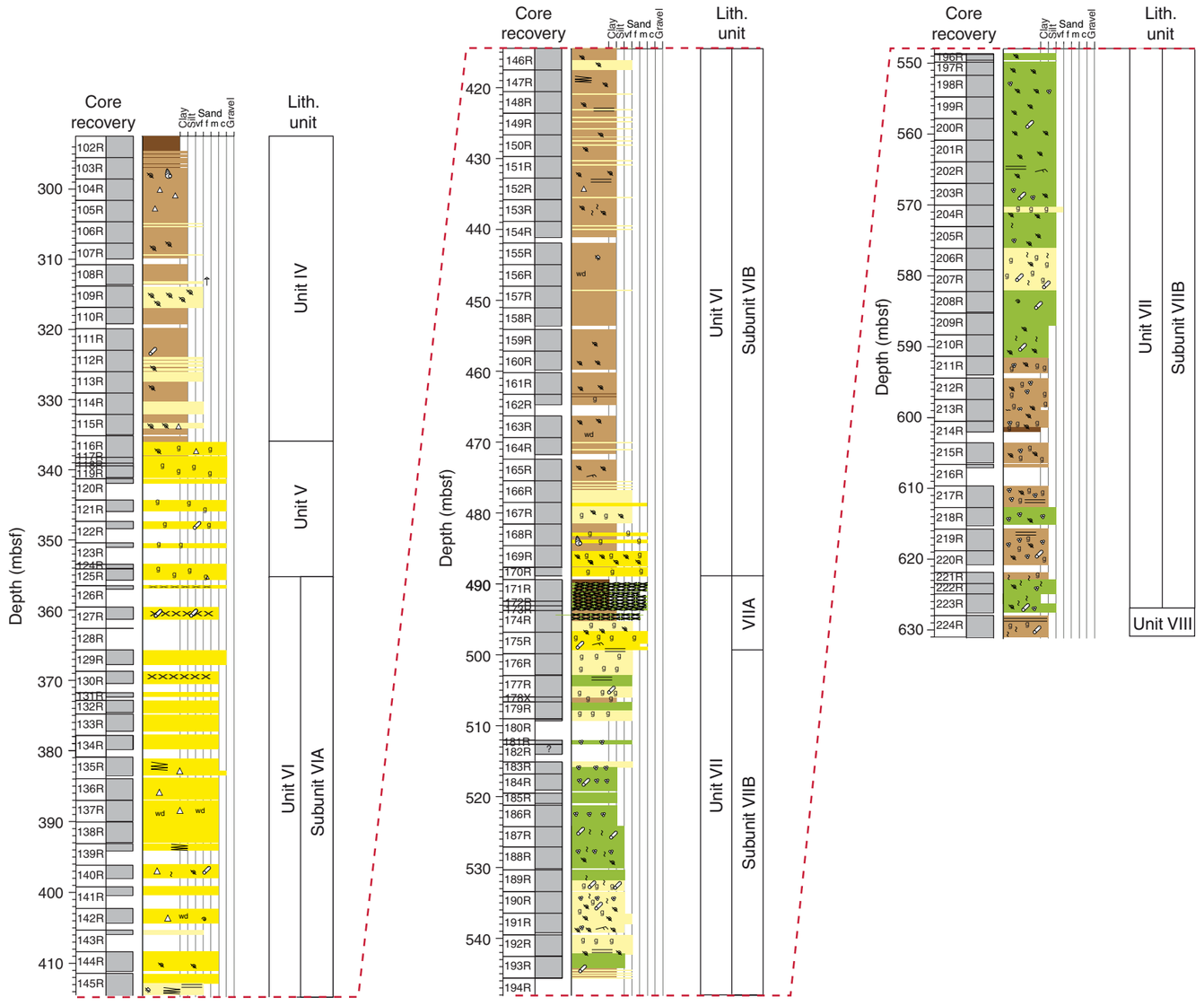

Figure F5. Core photograph of coarse sand with shell and echinoid fragments interpreted as a shoreface deposit (Unit I; interval 313-M0027A-4H-2, 80–90 cm).

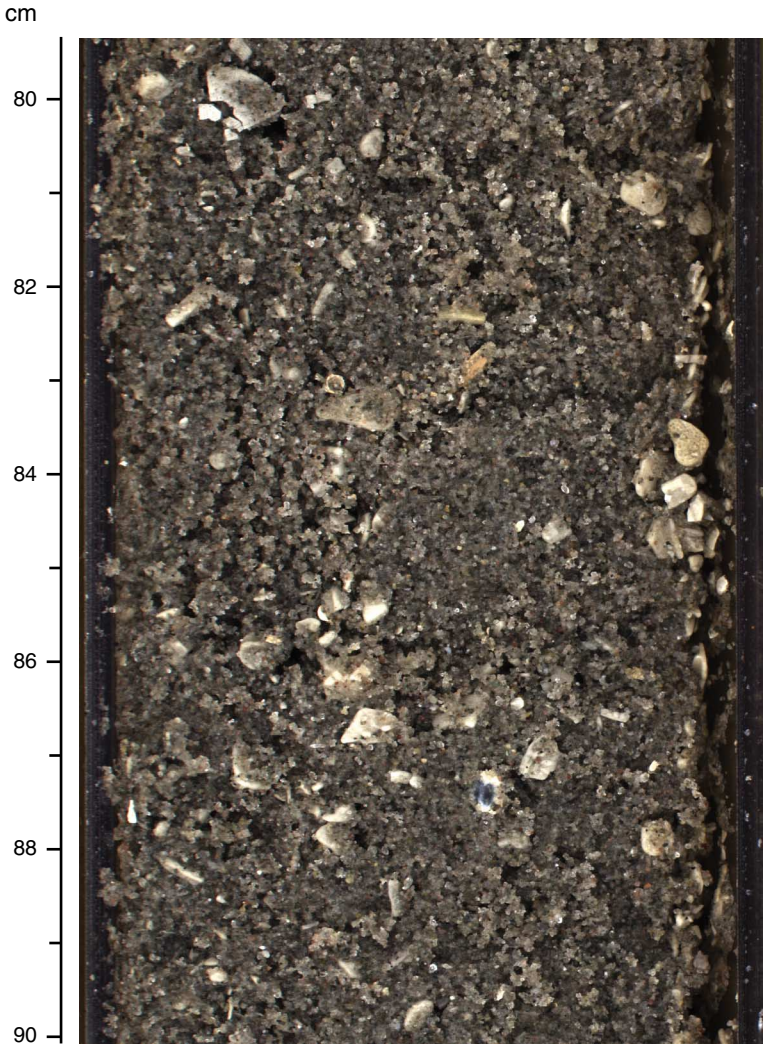

Figure F6. Core photograph of well-sorted medium sand passing down abruptly into gravel with rounded to well-rounded granules of quartz, black minerals, and subangular lithic granules (at 89 cm) (Unit I; interval 313-M0027A-18H-1, 80–100 cm).

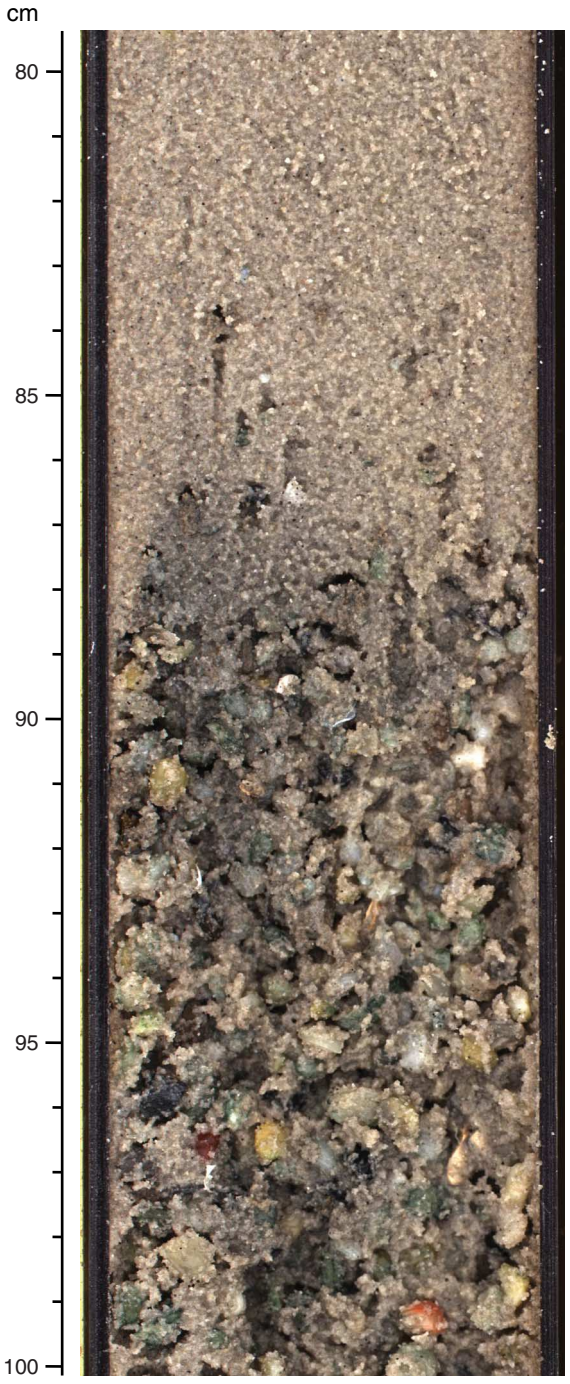

Figure F7. Core photograph of medium sand with grain-size variations highlighting cross-beds that steepen uphole (Unit I; interval 313-M0027A-27X-2, 110–122 cm). These cross-beds are interpreted as indications of the migration of subaqueous dunes or bars in a fluvial environment, possibly within an incised valley setting.

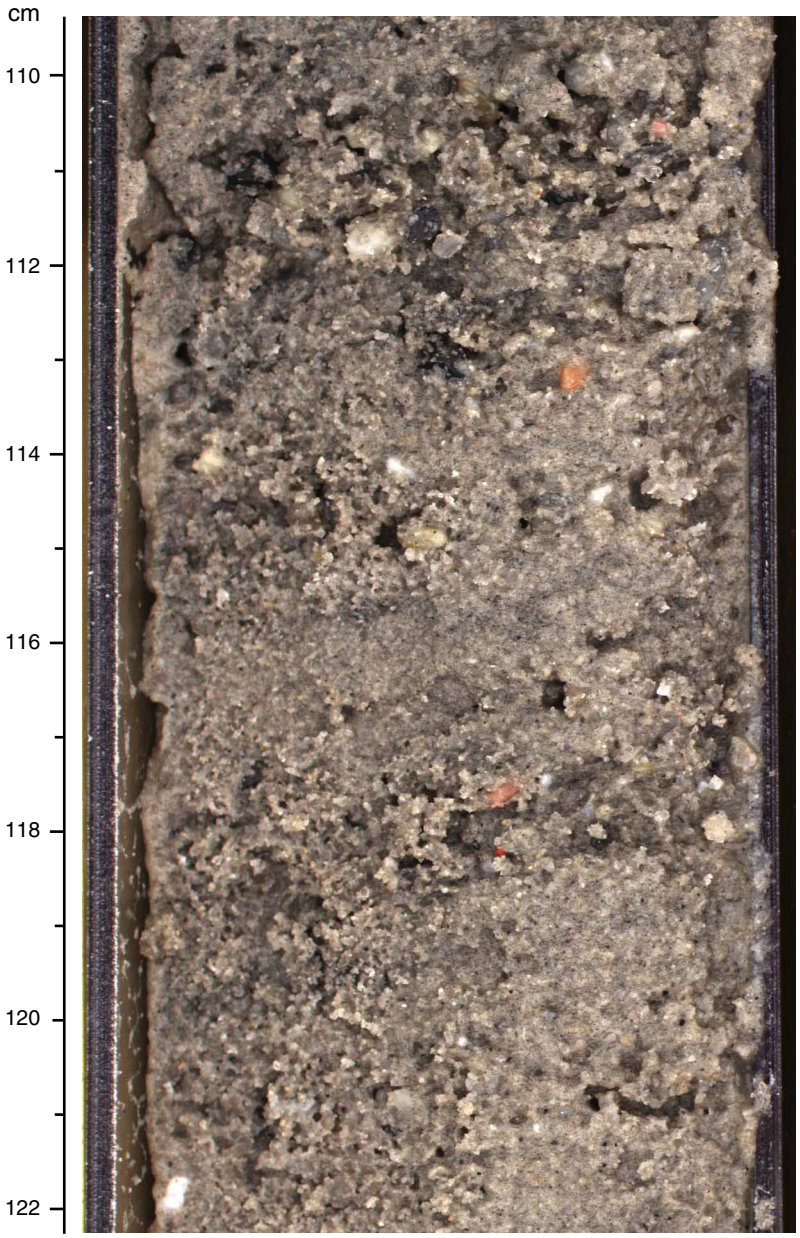

Figure F8. Core photograph of mottled silty clay with a microcalcrete (caliche), interpreted as a paleosol (Unit 1; interval 313-M0027A-50H-1, 1–20 cm).

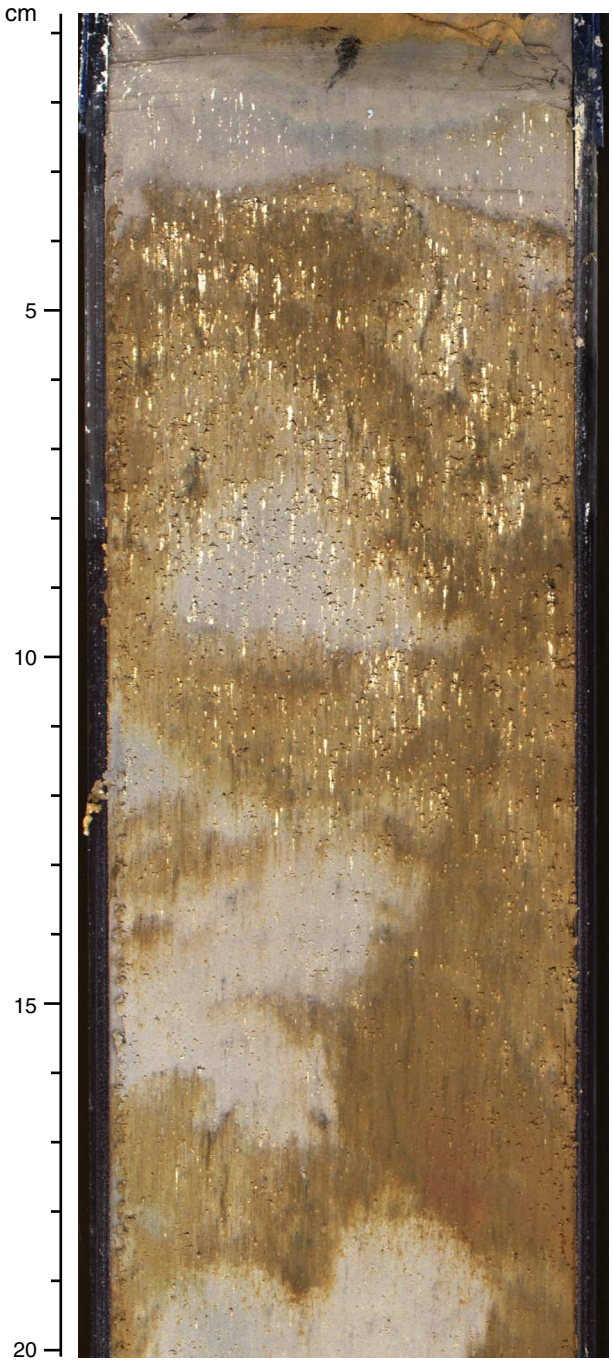

Figure F9. Core photograph of clay with very fine sand laminae at 12 cm with moderate bioturbation (Unit II; 313-M0027A-63H-1, 9–18 cm).

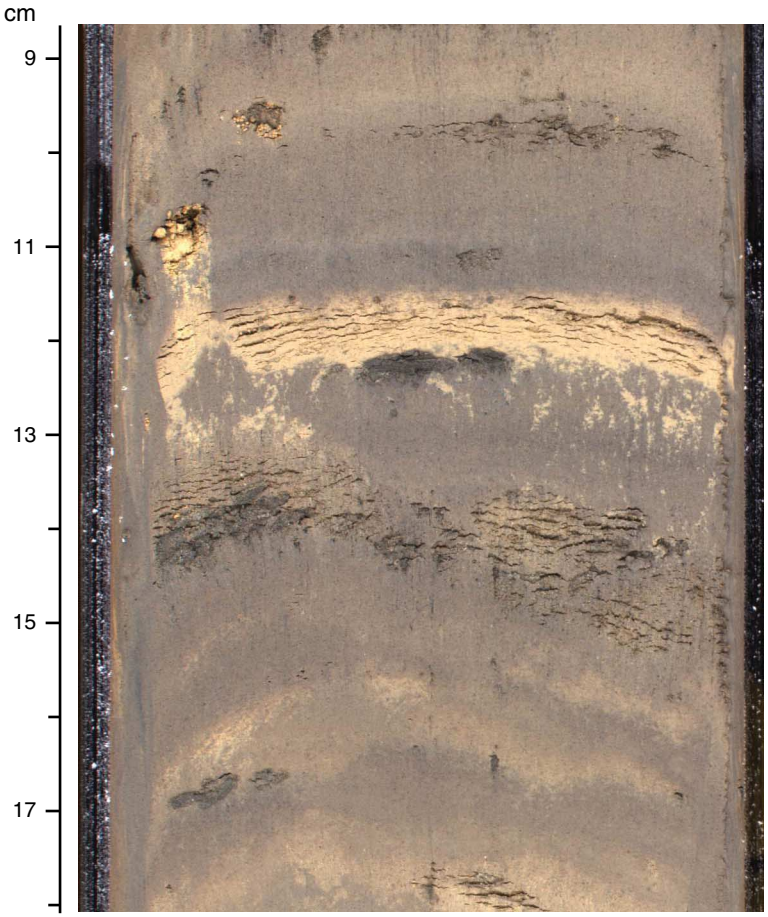

Figure F10. Core photograph of clay with contorted color banding (53 cm) (Unit II; 313-M0027A-68X-1, 45–60 cm). Surrounding parallel color banding indicates clay has been remobilized as a slump and/or slide.

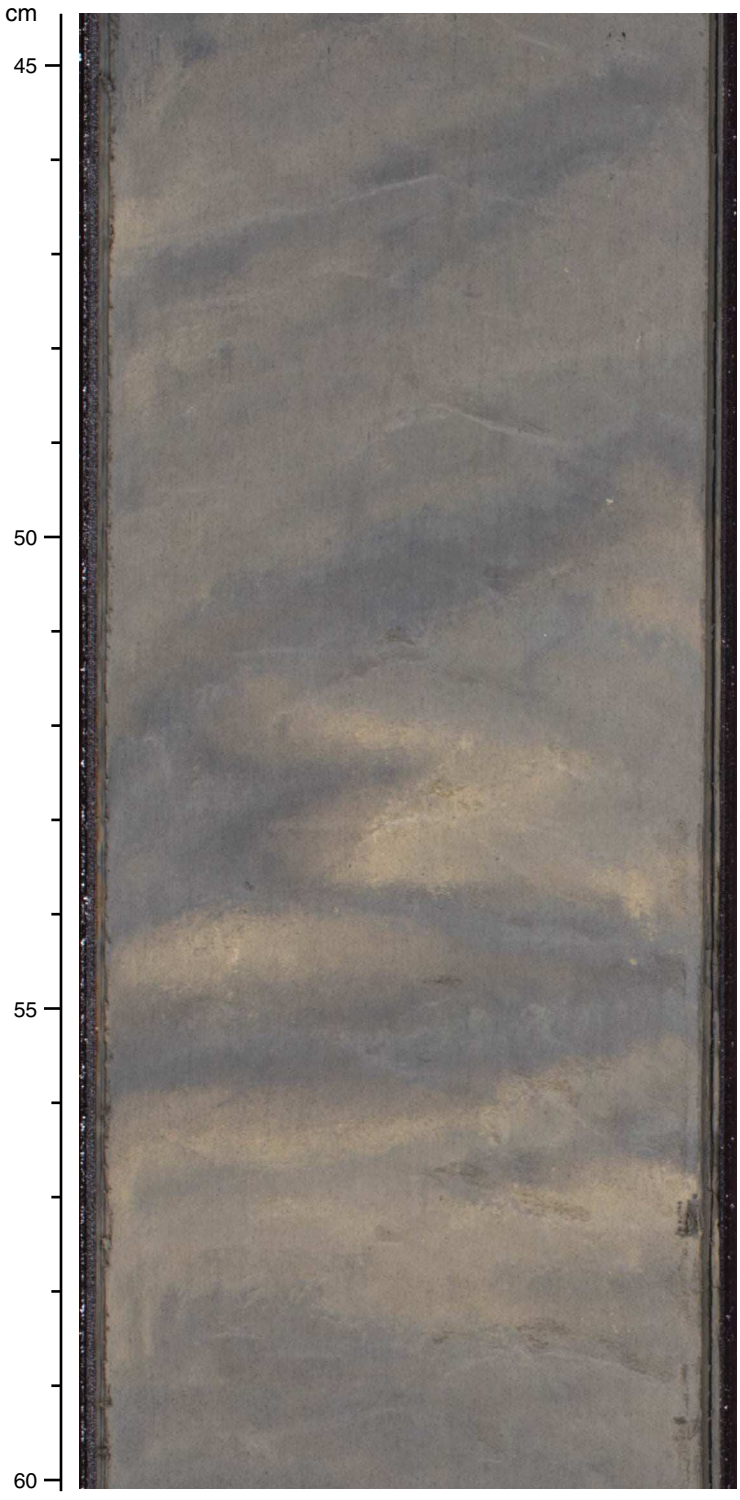

Figure F11. Core photograph of well-sorted very coarse sand abruptly overlying dark silty clay with shell fragments at 10 cm (Unit II; 313-M0027A-80X-1, 0–20 cm).

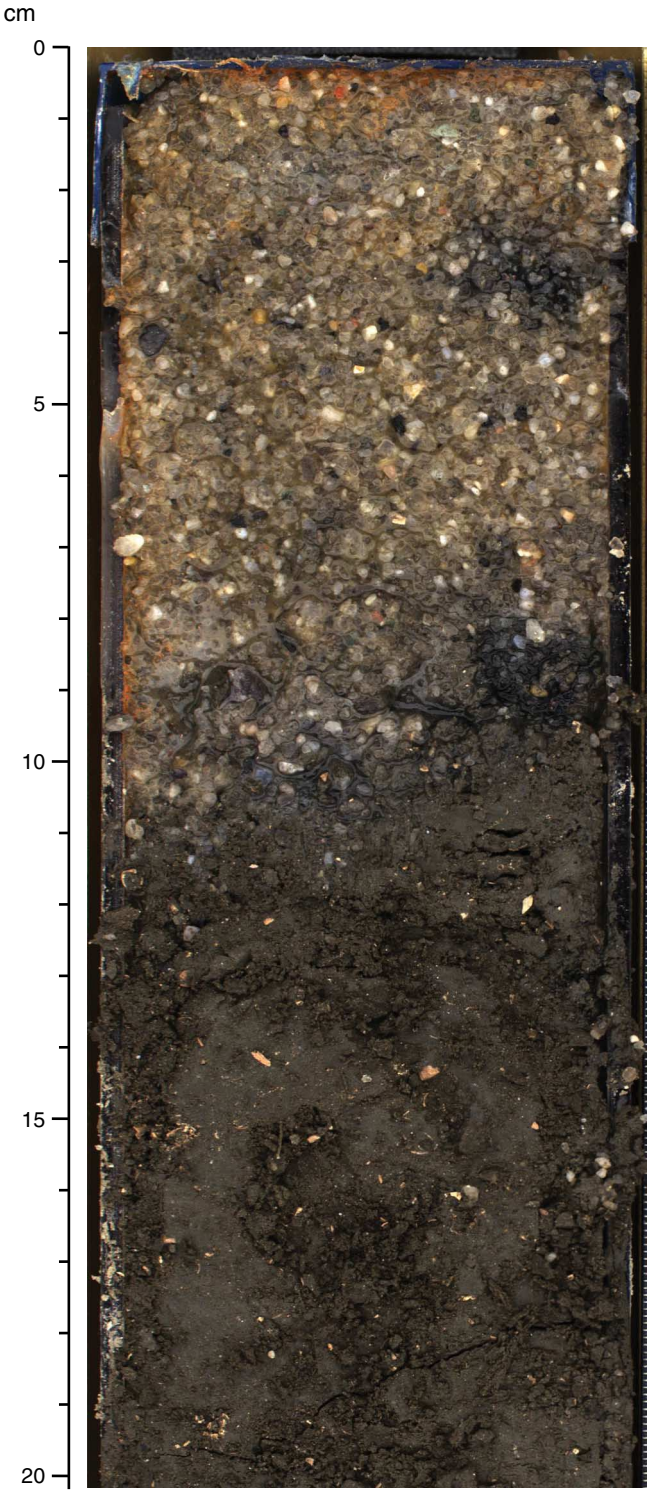

Figure F12. Core photograph of sandy silt with gravels abruptly overlying silty clay with articulated thin-walled shells (76 cm) (Unit II; 313-M0027A-75X-2, 60–80 cm). Contact is bioturbated, with gravel-filled burrows (e.g., 77 cm).

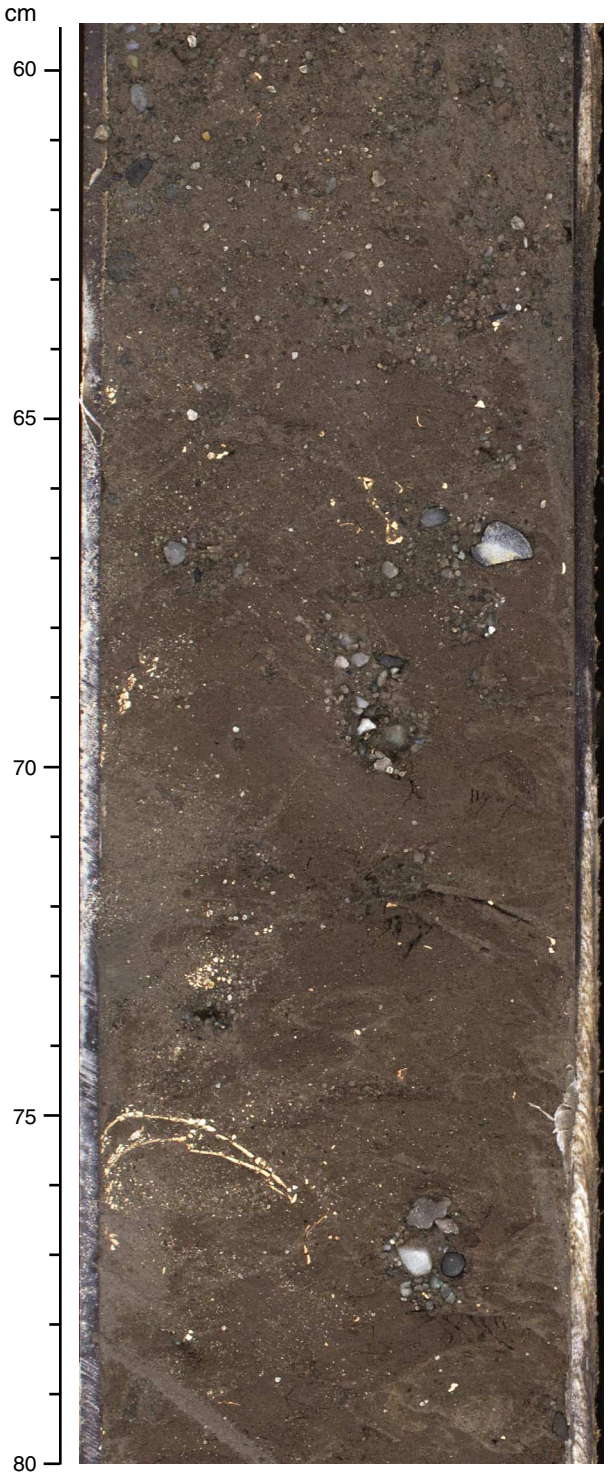

Figure F13. Core photograph of laminated and burrowed clay with dark lignitic laminae gradationally overlying pale calcareous clay (80–76.5 cm) (Unit III; 313-M0027A-84R-3, 62–81 cm). Offshore environment.

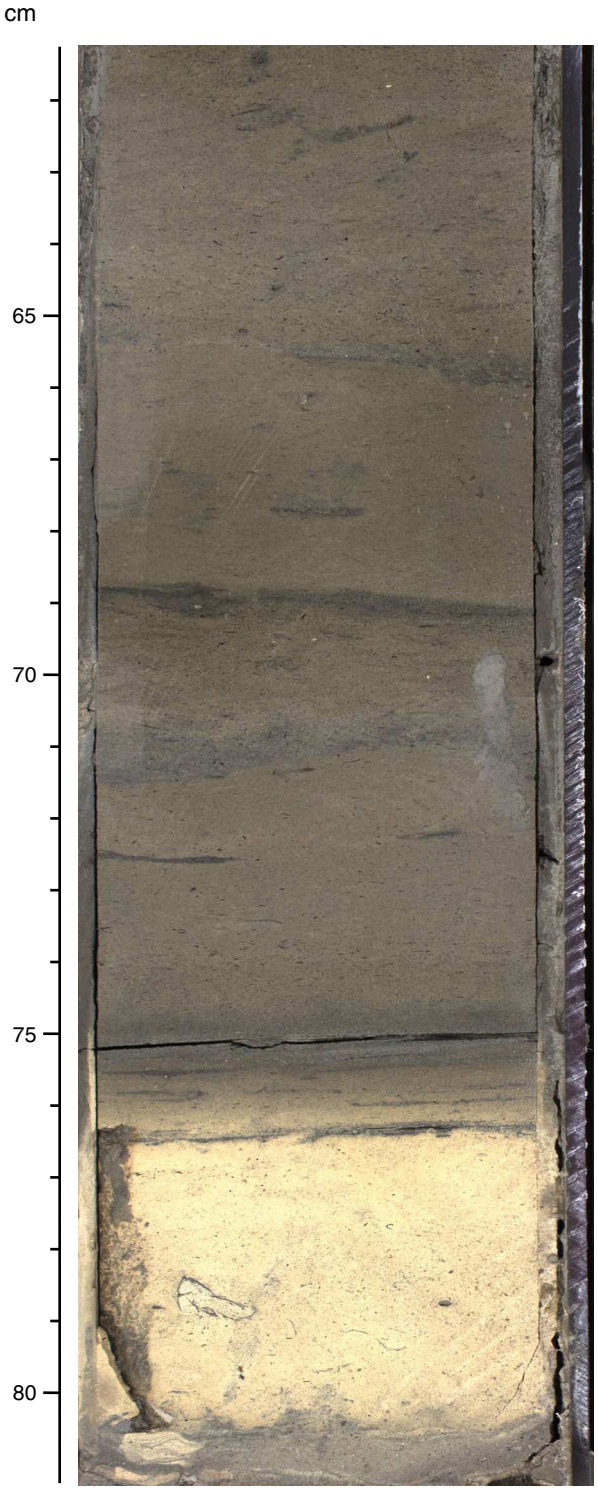

Figure F14. Core photograph of sandy silt with oyster shell fragments and granules concentrated at contact (41 cm) with underlying silt containing large intact macrofauna (e.g., turritellid gastropod) and shell-filled burrows (58 cm) (Unit III; 313-M0027A-89R-1, 31–65 cm).

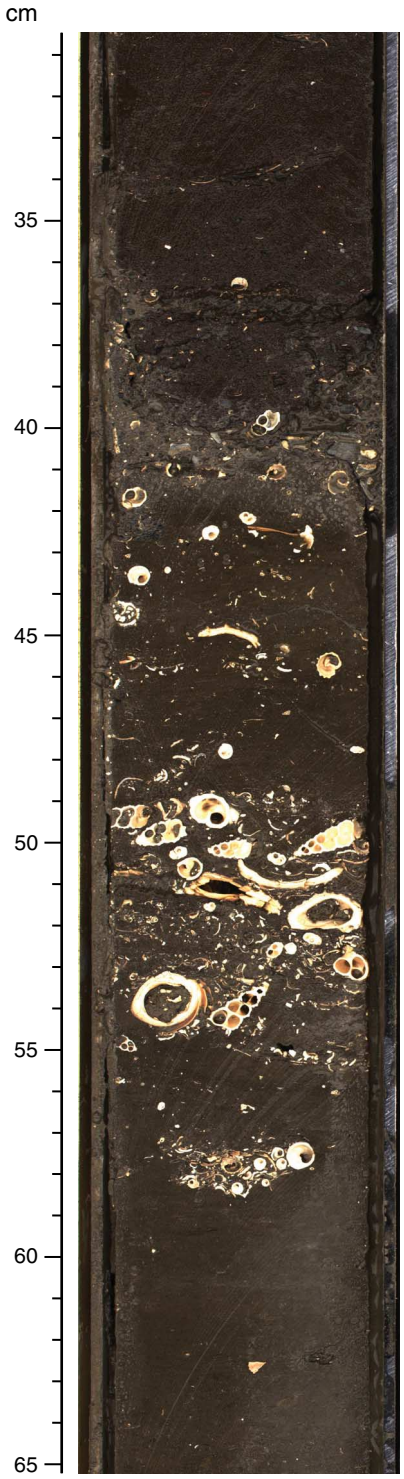

Figure F15. Core photograph of silt with organic matter and thin shells abruptly overlying silty medium sand with common glauconite grains and gastropod shells (85 cm), which in turn overlies chaotically arranged thick shells (Unit III; 313-M0027A-89R-2, 80–102 cm). Contact is interpreted to be a flooding surface, with an offshore setting abruptly overlying a shoreface to shoreface–offshore transition setting.

Figure F16. Core photograph of sharp-based normally graded fine sand beds with low-angle to convex-up lamination interbedded with silty sand (34–38 cm) (Unit III; 313-M0027A-96R-1, 22–39 cm). Facies association is interpreted as storm deposits in a wave/storm–dominated shoreface–offshore transition setting.

Figure F17. Core photograph of abrupt boundary between poorly sorted coarse sand with thick shells above and clayey silt with dispersed terrestrial organic matter below (at 105 cm) (Unit III; 313-M0027A-102R-2, 95–115 cm). Surface is bioturbated with burrows filled by coarse sand and marks an abrupt shallowing from an offshore/prodelta setting to shoreface. Surface separates lithostratigraphic Units III and IV.

Figure F18. Core photograph of ripple cross-laminated fine sand above a scour surface that cuts into brown sandy silt in an interpreted river-influenced shoreface–offshore transition setting (Unit IV; 313-M0027A-107R-2, 22–30 cm).

Figure F19. Core photograph of fine sand that coarsens downhole to medium sand with granules, along with shell fragments abruptly overlying sandy silt (at 133 cm) into which *Thalassinoides* are deeply burrowed and sand filled (Unit IV; 313-M0027A-114R-2, 118–150 cm).

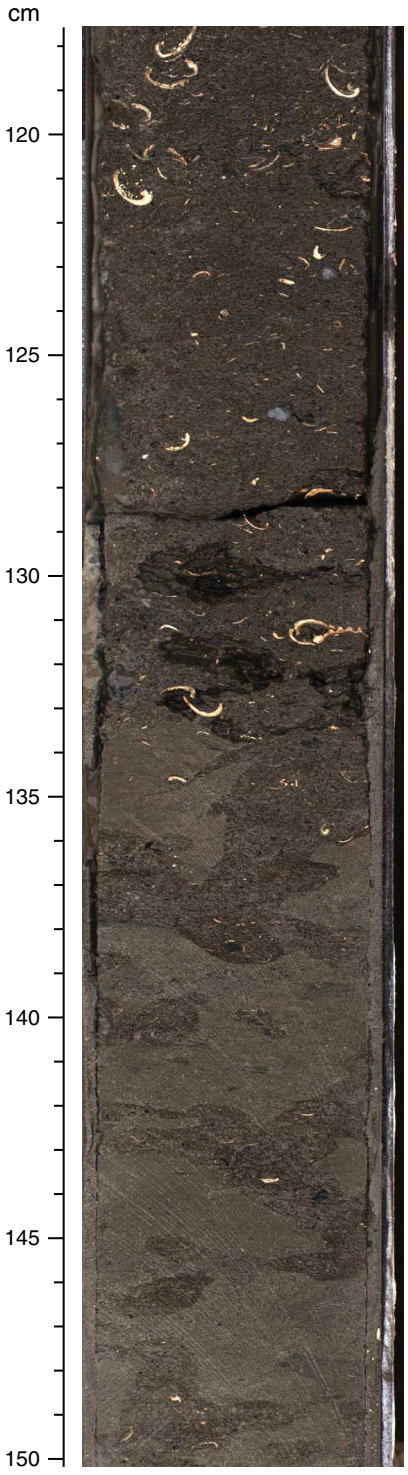

Figure F20. Core photograph of coarse glauconitic sand (Unit V; 313-M0027A-120R-1, 27–38 cm). Glauconite comprises 20%–25% of sediment mineralogy.

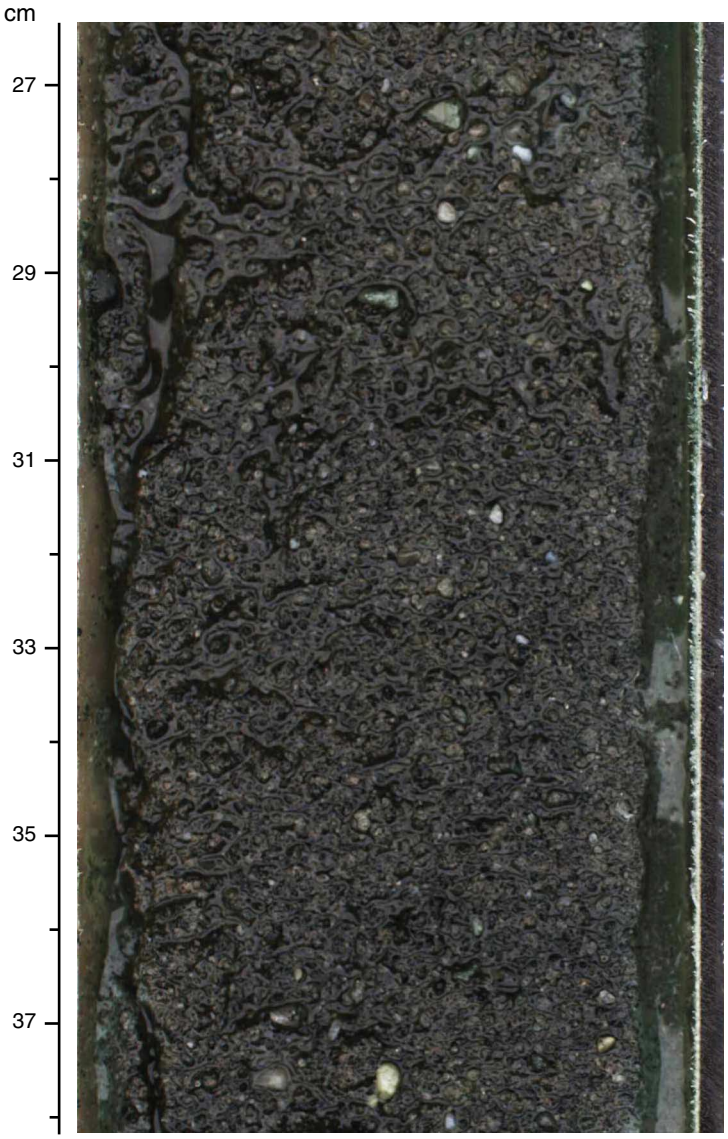

Figure F21. Core photograph of abrupt contact between poorly sorted coarse sand with glauconite and pale brown sandstone with a glauconite-filled burrow (Unit V; 313-M0027A-125R-1, 125–142 cm). Surface at 132 cm separates Units V and VI.

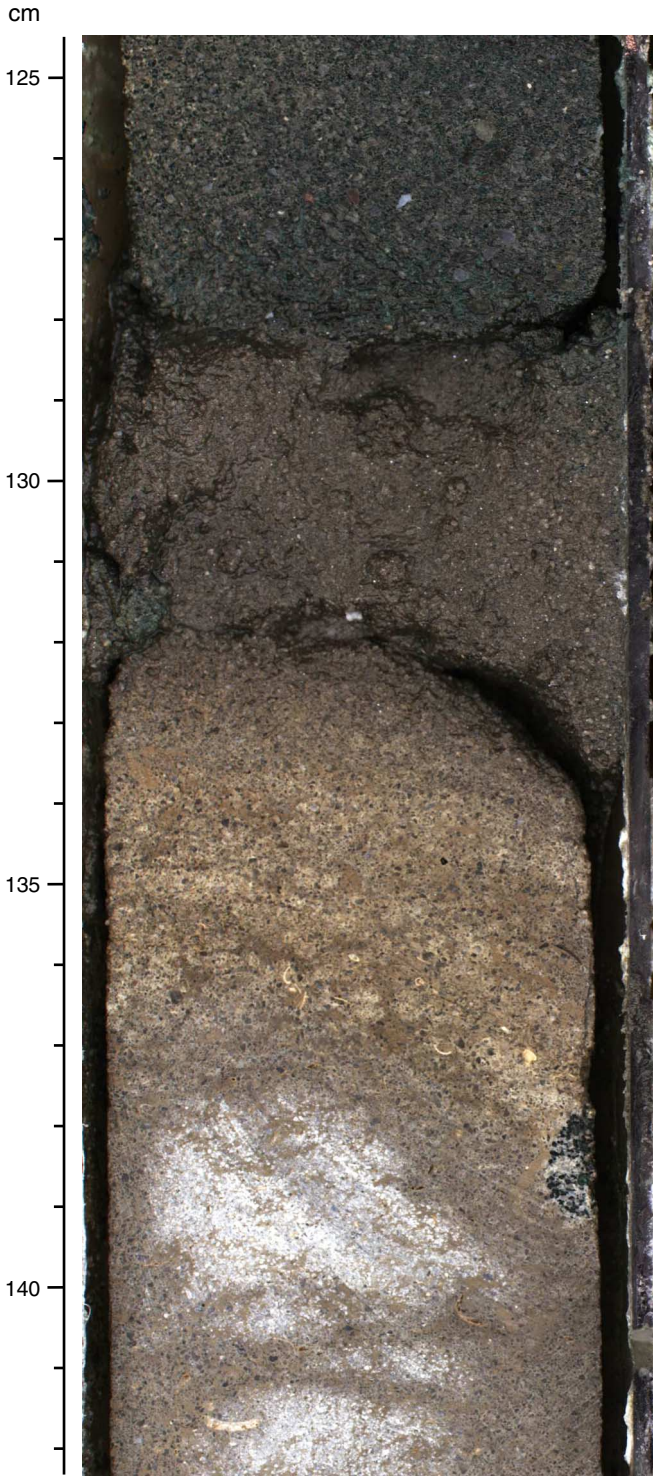

Figure F22. Core photograph of well-sorted medium sand, with cross-stratification highlighted by finer dark grains (Unit VI; 313-M0027A-135R-1, 33–53 cm). Facies is representative of a shoreface to foreshore setting.

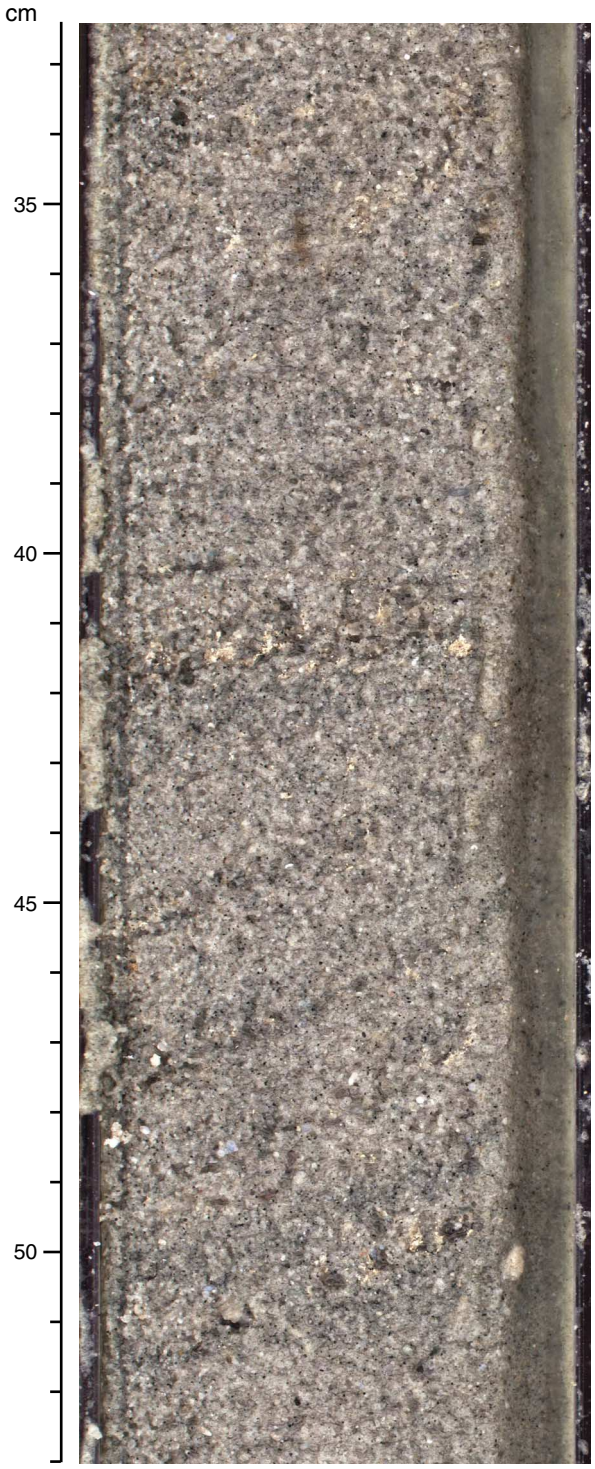

Figure F23. Core photograph of medium sand with articulated shells in a shoreface–offshore transition setting (Unit VI; 313-M0027A-142R-2, 15–44 cm).

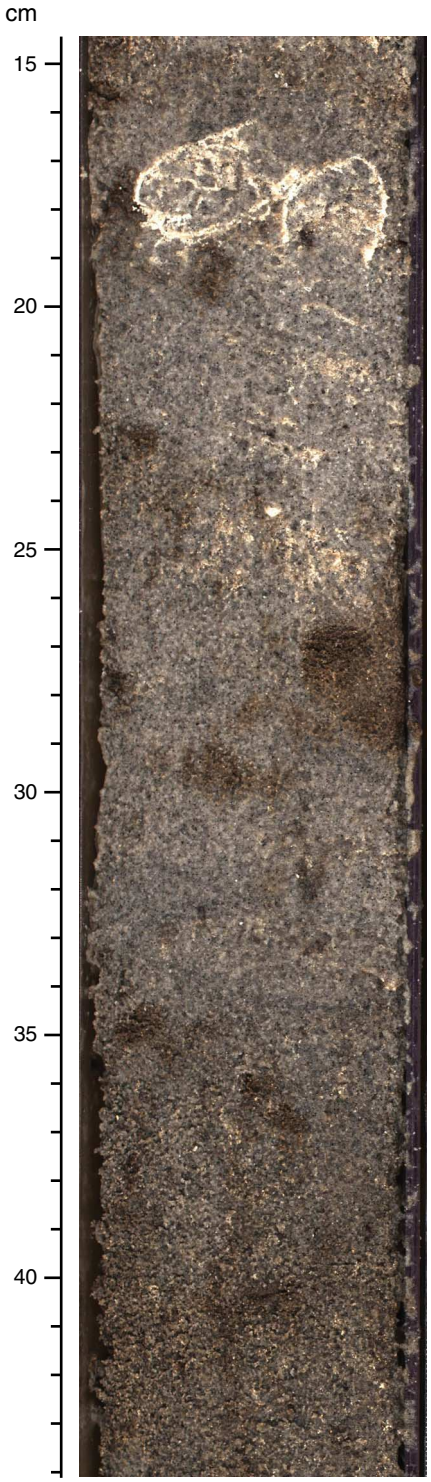

Figure F24. Core photograph of very fine sandy silt with common black organic fragments and thin bivalve and gastropod shells (Unit VI; 313-M0027A-146R-1, 65–75 cm).

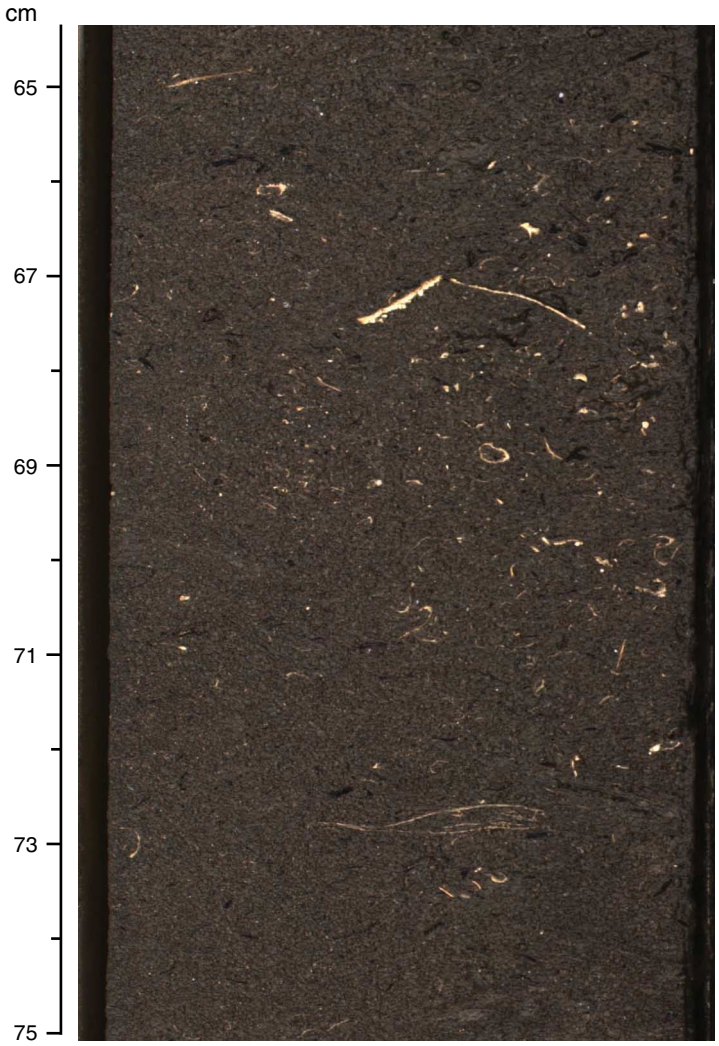

Figure F25. Core photograph of a sharp-based fine sand bed that is reverse then normally graded, which may indicate a river flood event in a prodelta environment (Unit VI; 313-M0027A-148R-1, 130–137 cm).

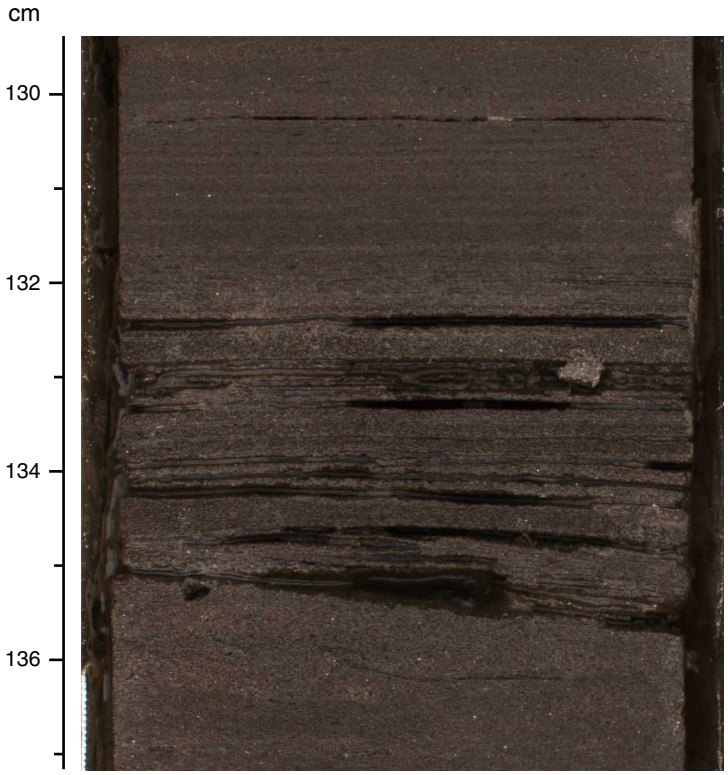

Figure F26. Core photograph of very poorly sorted medium sand with grain size ranging from silt to granules and 10%–15% glauconite (Unit VI; 313-M0027A-168R-2, 40–85 cm).

Figure F27. Core photograph of glauconitic sandstone graded normally from coarse to fine sand (Unit VII; 313-M0027A-174R-1, 111–121 cm).

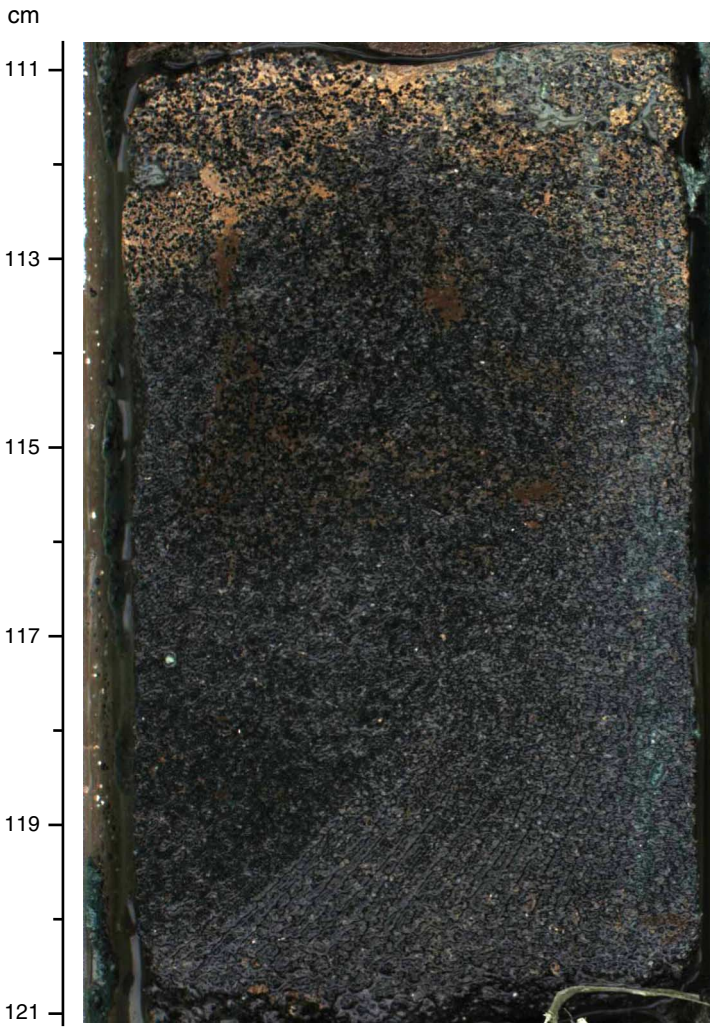

Figure F28. Core photograph of cross-stratified glauconite (80%) sandstone beds interbedded with silty clay laminae (e.g., 98 cm) interpreted as sediment gravity flow deposits (turbidites), with silty clayey beds indicating quiet background environment (Unit VII; 313-M0027A-171R-2, 70–106 cm).

Figure F29. Photomicrograph of glauconitic, silty very fine sand with dark brown organic grains or muddy materials, scattered framboidal pyrite grains, and some opaque minerals (Unit VIIB; Sample 313-M0027A-177R-1, 41 cm). Black small spherule grains of framboidal pyrite are scattered. Different colored glauconite grains may reflect maturity differences. Photo under crossed polars is 0.7 mm (700 µm) wide.

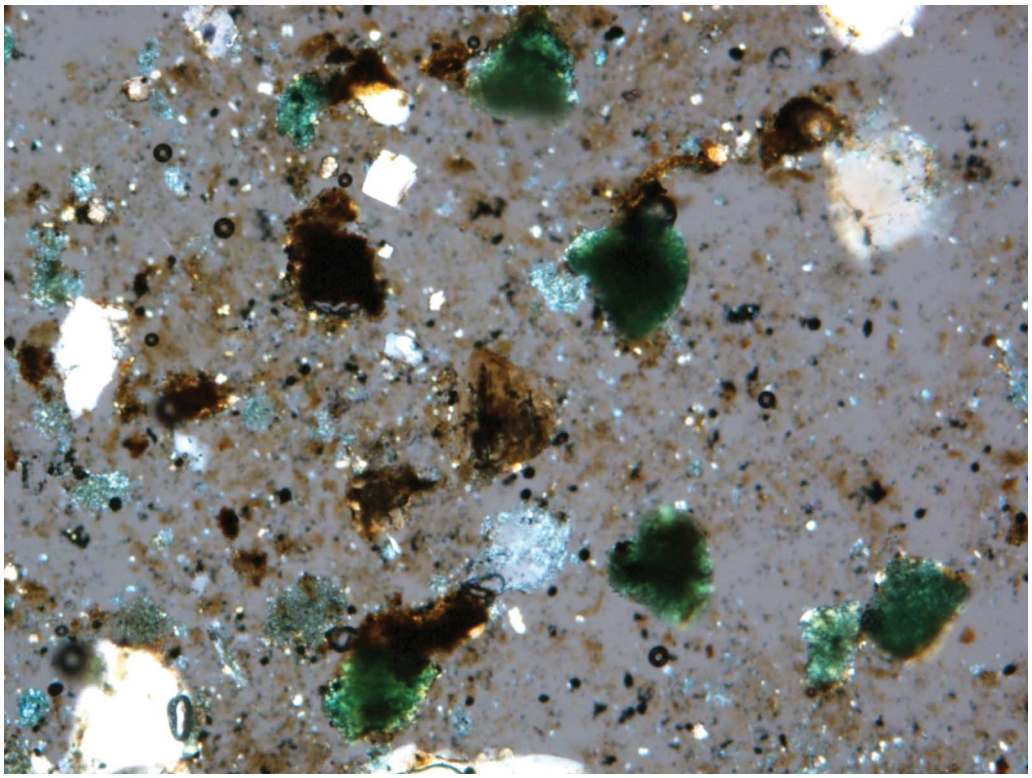

Figure F30. Core photograph of silty very fine sand with glauconitic sand-filled burrows and *Chondrites* (Unit VIII; 313-M0027A-223R-1, 65–105 cm). The transition between Units VII and VIII is placed at the heavily bioturbated surface at 93 cm.

Figure F31. Two-dimensional computed tomography (CT) scan of Section 313-M0027A-69X-1 from Unit II shown with a line-scan image, magnetic susceptibility (red) and density (blue) from multisensor core logger (MSCL) measurements, and an acoustic image from the borehole. H = horizontal scan, V = vertical scan (see **"Lithostratigraphy"** in the "Methods" chapter). The lithology is predominantly clay, and laminae and thin beds are clearly expressed as a color contrast likely related to organic matter content. 0–50 cm: alternation of faint light and dark laminae, intensely bioturbated, expressed as relatively constant values in all data sets. 50–100 cm: millimeter-scale laminae are well expressed through density contrast in the CT image and also in oscillating values of bulk density from MSCL. Maxima of density occur in the dark beds found at 70.5 and 89 cm, which are very bright on the CT images and correspond to a high coefficient of attenuation. These layers may be defined by accumulation of heavy minerals. 100–150 cm: an abrupt contact is evident from the acoustic image around 100 cm in the core, with much paler color indicating a different sediment texture. vf = very fine, f = fine, m = medium, c = coarse. See Figure **F1** for lithology legend. (**Figure shown on next page.**)

Figure F31 (continued). (Caption shown on previous page.)

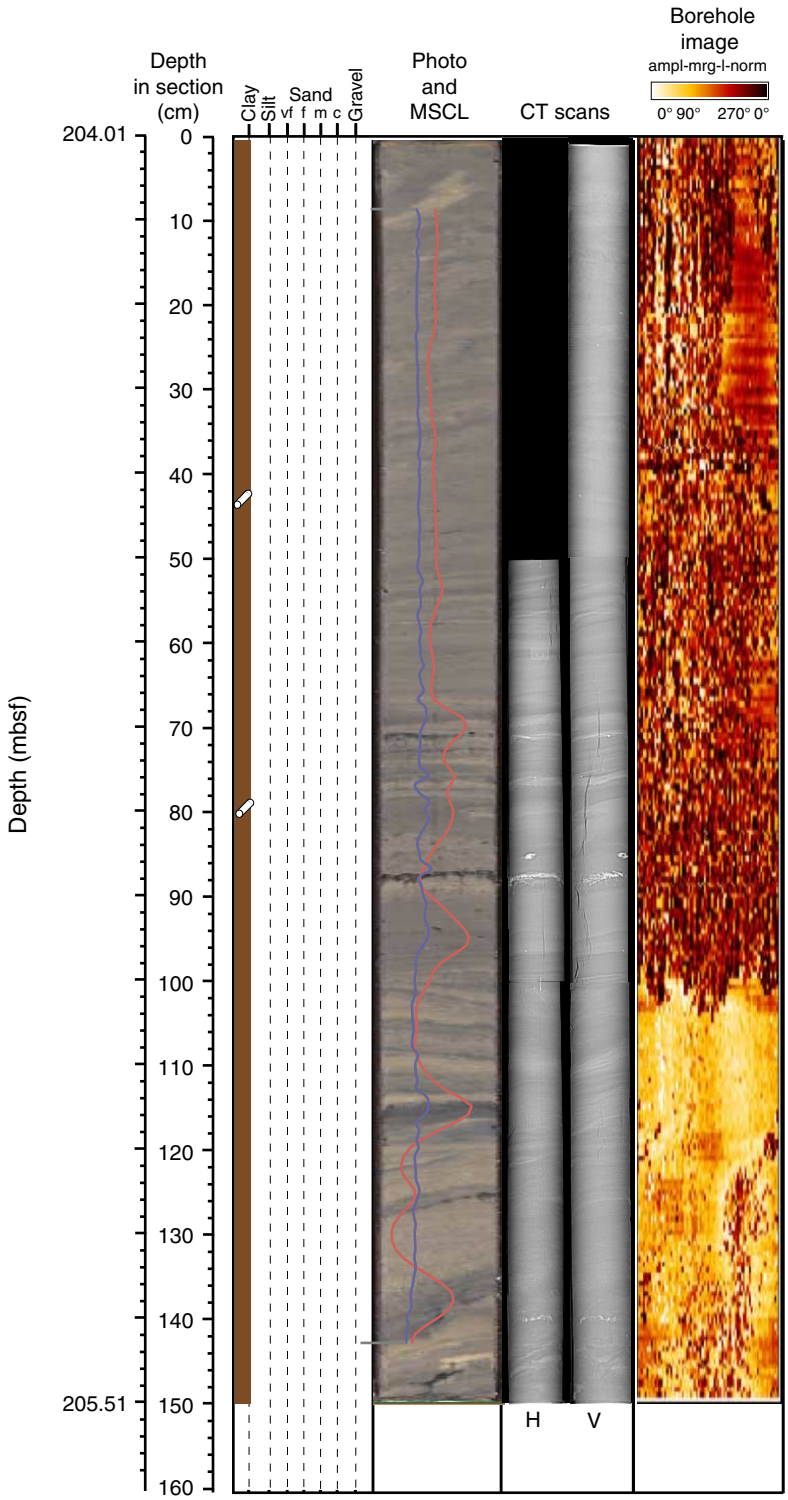

Figure F32. Percentages of sand, silt, and clay based on smear slides from Hole M0027A. See "Lithostratigraphy" in the "Methods" chapter for more information.

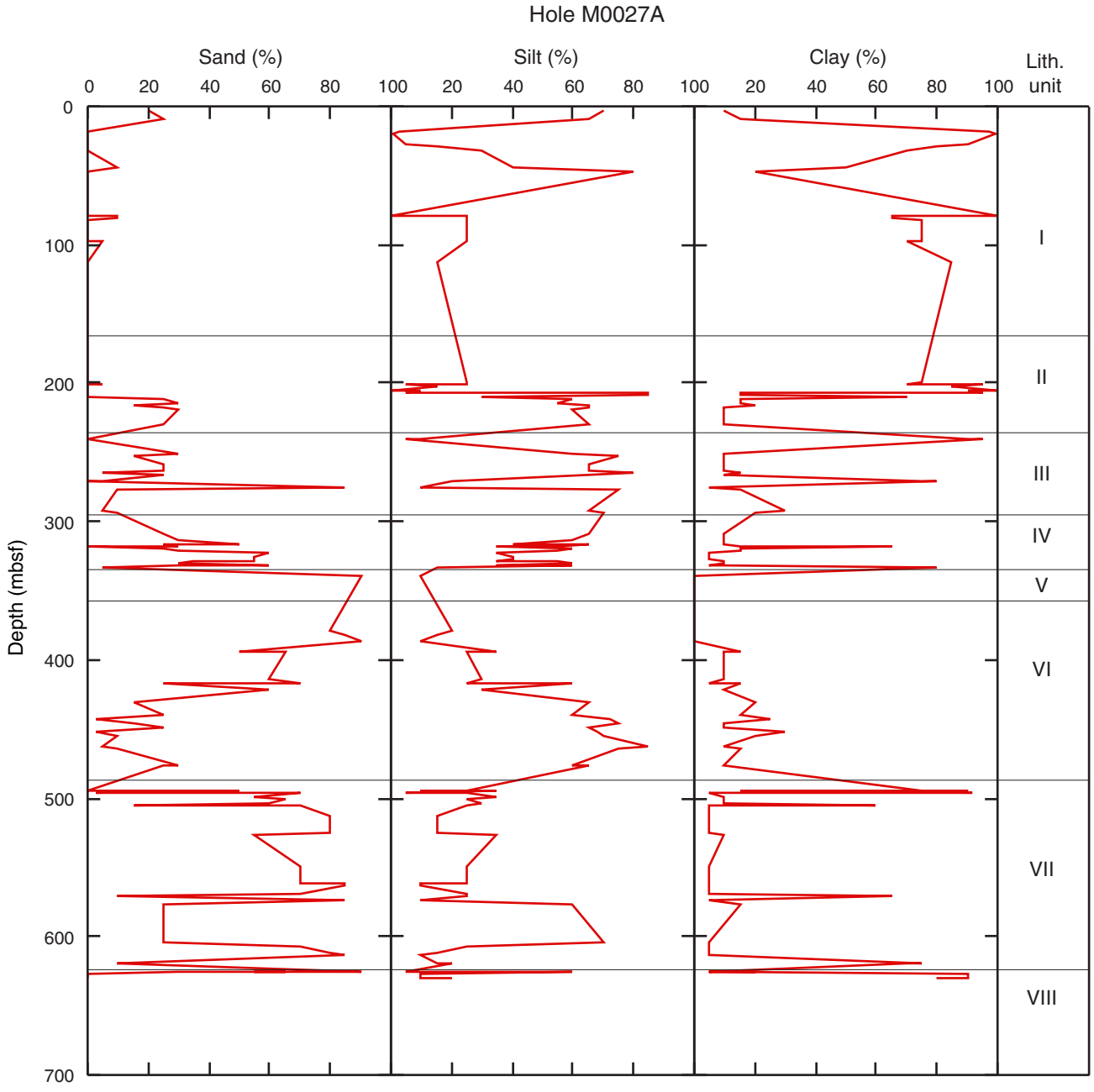

Figure F33. Biostratigraphic summary interpreted from calcareous nannofossils, planktonic foraminifers, and dinocysts, showing Miocene stages in Hole M0027A. See Figure **F12** in the "Methods" chapter for an explanation of the datums used. Zone boundaries are drawn diagonally to indicate uncertainty in zonation between samples because of either the absence of sampling between points or of age-diagnostic taxa. Zonal boundaries are correlated to the geologic timescale. Dashed lines indicate some uncertainty in age assignment. The geologic timescale is that of Berggren et al. (1995), based on the geomagnetic polarity timescale of Cande and Kent (1995). See Figure **F4** in the "Methods" chapter for lithology legend.

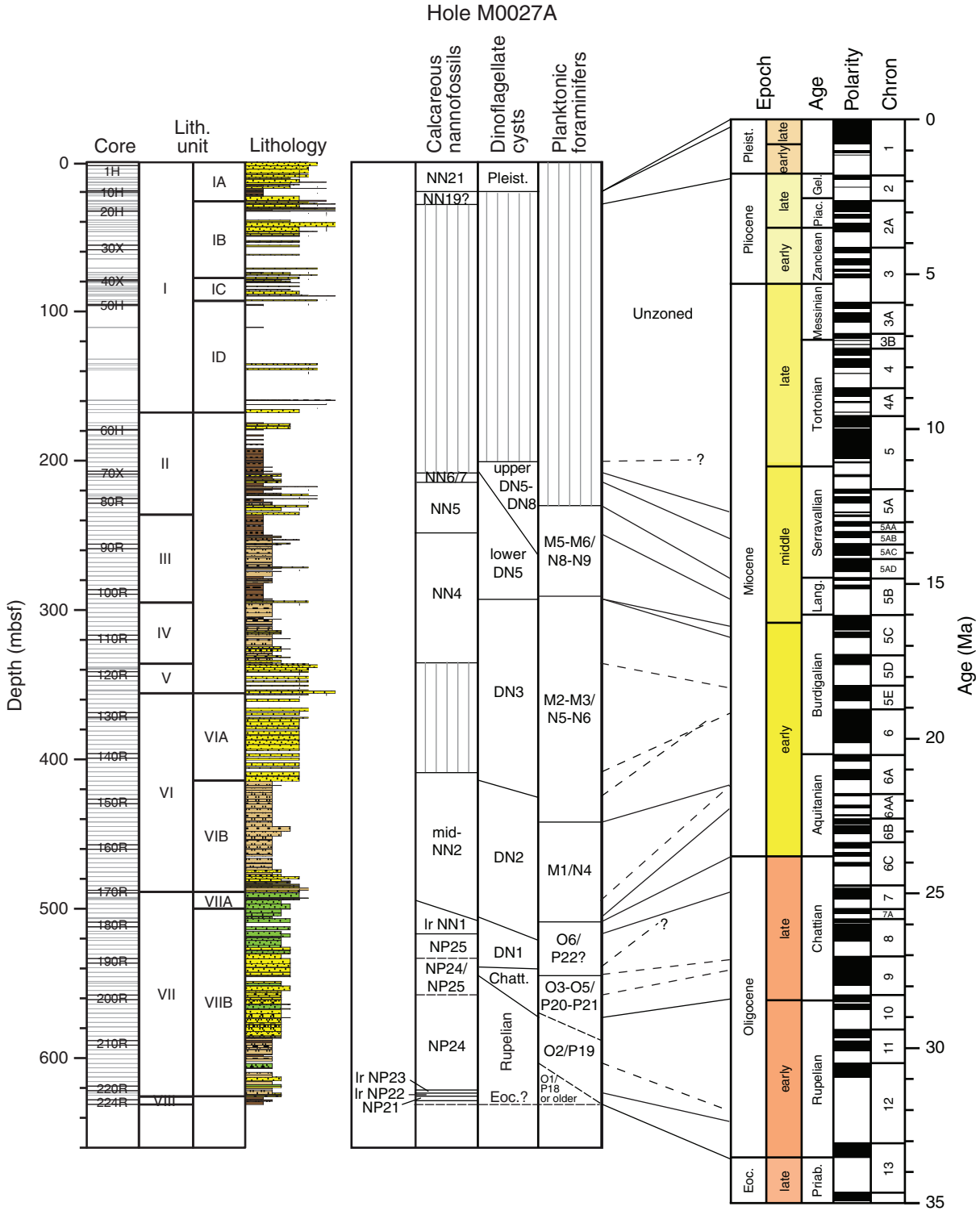

Figure F34. Age-depth plot showing cores (every fifth core shaded) in Hole M0027A, the timescale of Berggren et al. (1995), calcareous nannoplankton zones (light blue bars), planktonic foraminifer zones (dark blue bars), and dinocyst zones (green bars). Sr isotopic ages are shown as circles with errors of ±0.6 m.y. (15.2–34.4 Ma) and ±1.17 m.y. (younger than 15.2 Ma). Horizontal lines for sequence boundaries (red) and tentative sequence boundaries (dashed red) lines are labeled with their corresponding depths. Green lines = flooding surfaces. MFS = maximum flooding surface. TD = total depth. Planktonic foraminifer E and O zones are from Berggren and Pearson (2005); planktonic foraminifer M, PL, and Pt zones are from Berggren et al. (1995); nannofossil zones are from Martini (1971); and dinocyst zones are from de Verteuil and Norris (1996). Geomagnetic polarity timescale is from Cande and Kent (1995). See Figure F85 for detail.

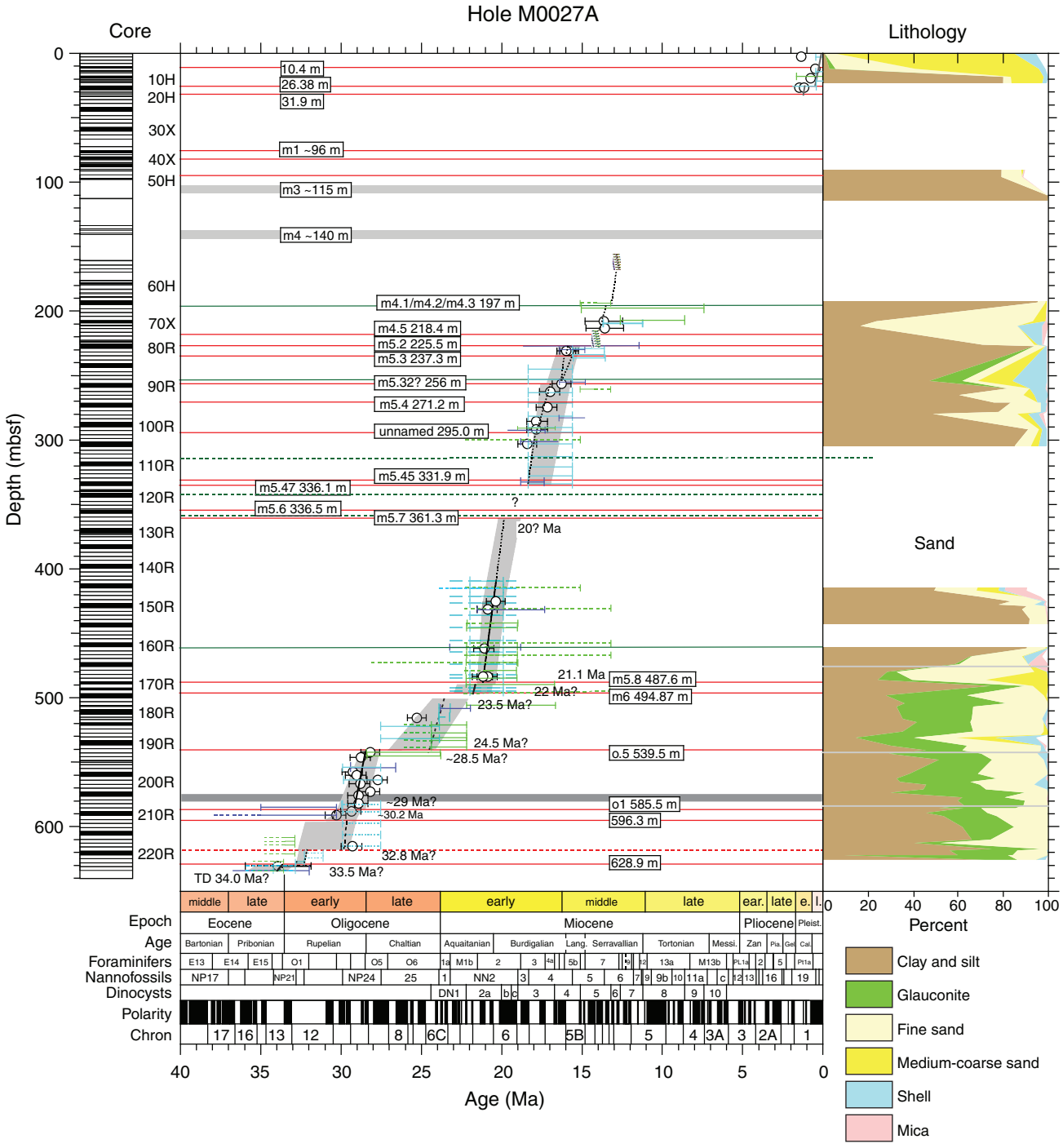

Figure F35. Distribution of biostratigraphically important calcareous nannofossil taxa in Hole M0027A. Thickness of distribution line indicates relative abundance of species. Zonal assignments (Martini, 1971) are given, with approximate age indicated. A > or < in front of the age indicates that part of a zone is presumed to be missing because of an unconformity or nonrecovery of nannofossil-rich facies. Red lines = sequence boundaries, green lines = major flooding surfaces. EOT = Eocene–Oligocene transition. MIC = marine isotope chron. See Figure F4 in the "Methods" chapter for lithology legend.

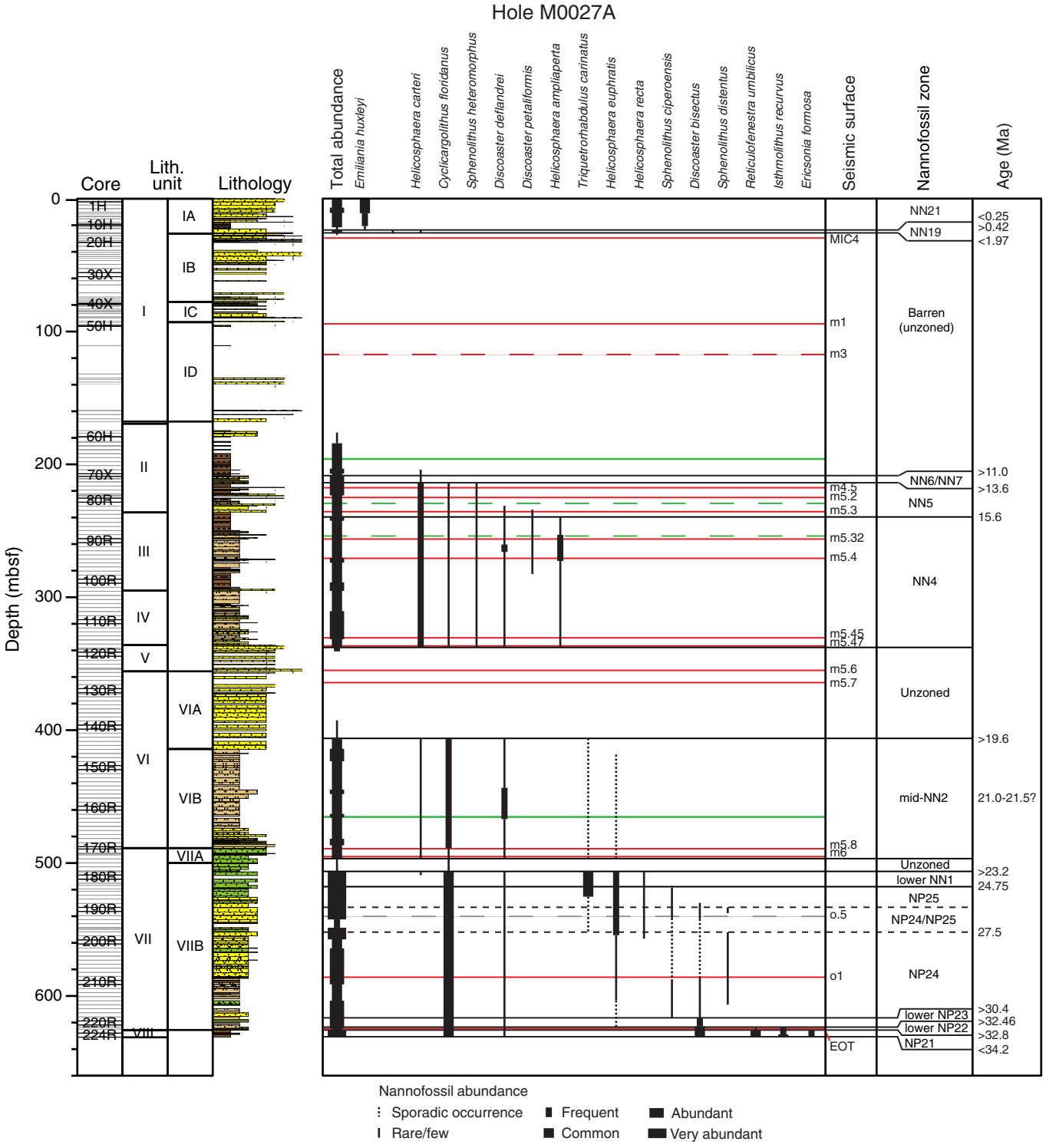

Figure F36. Planktonic foraminifer stratigraphic distributions in Hole M0027A. Red lines = sequence boundaries, green lines = major flooding surfaces. EOT = Eocene–Oligocene transition. MIC = marine isotope chron. See Figure F4 in the "Methods" chapter for lithology legend.

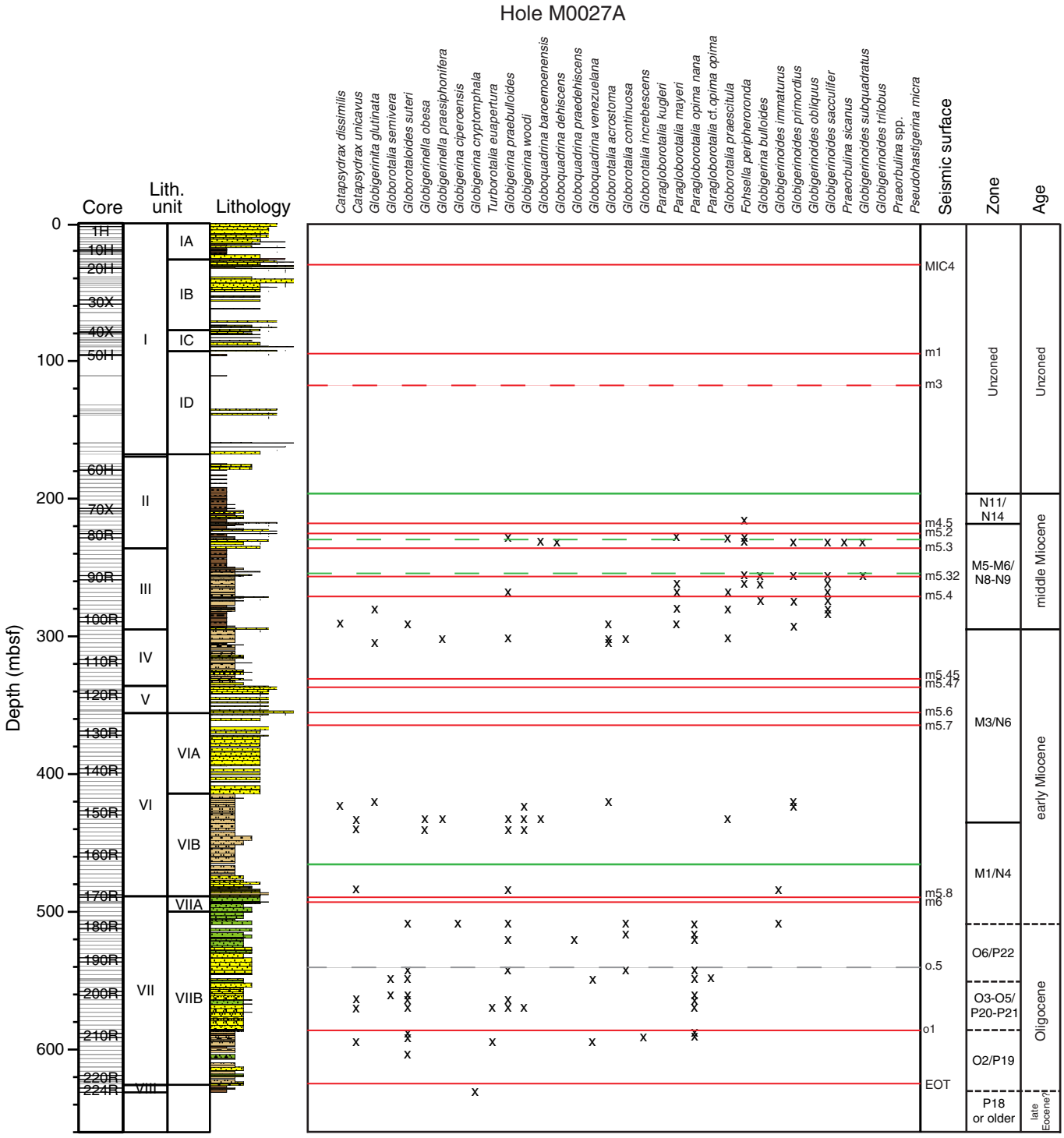

Figure F37. Stratigraphic distribution of age-diagnostic dinocyst taxa in Hole M0027A, with the Miocene zoned following de Verteuil and Norris (1996). Zone boundaries are drawn diagonally to indicate uncertainty in zonation between samples, because of either the absence of sampling between points or of age-diagnostic taxa. Red lines = sequence boundaries, green lines = major flooding surfaces. EOT = Eocene–Oligocene transition. MIC = marine isotope chron. See Figure F4 in the "Methods" chapter for lithology legend.

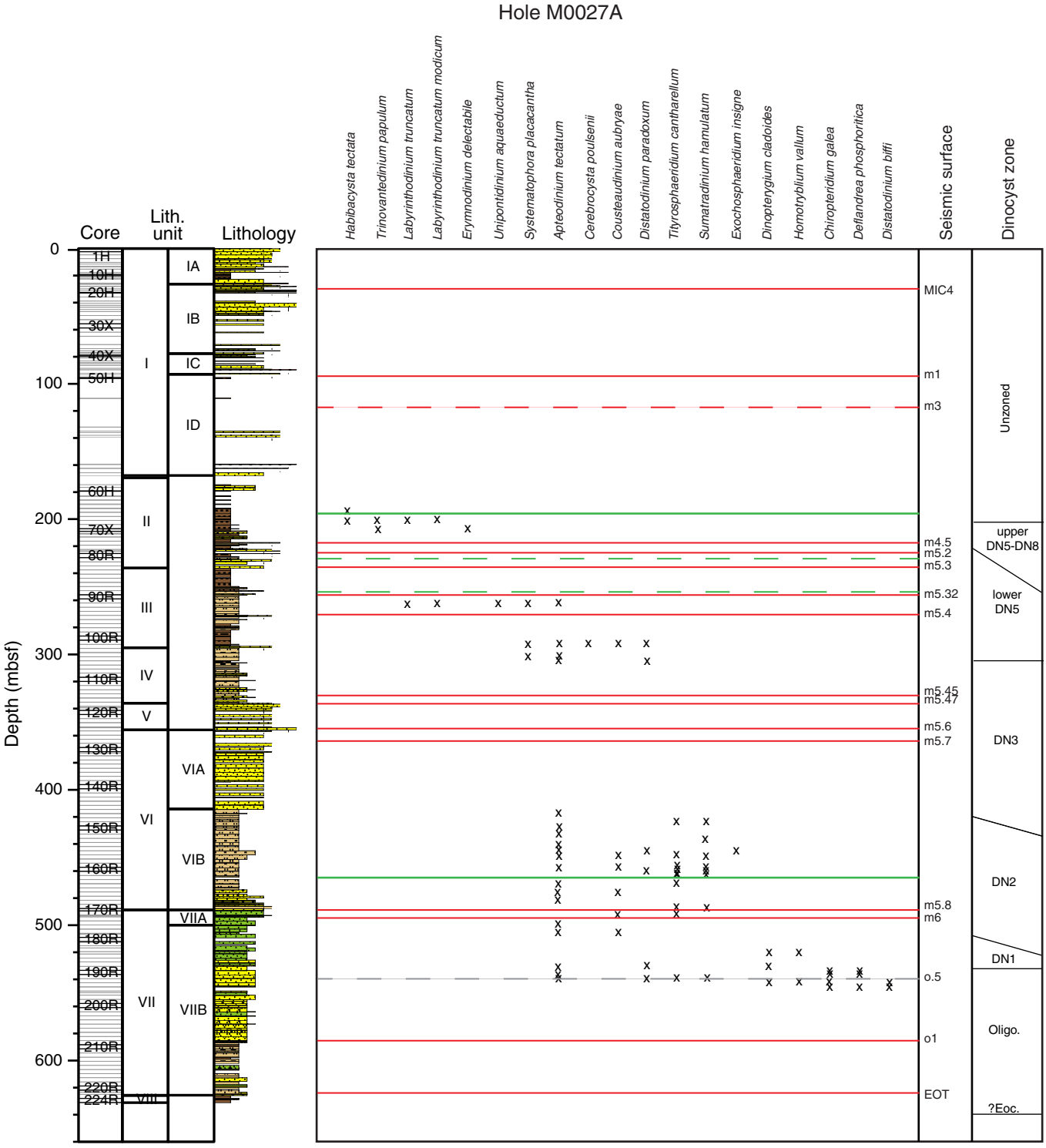

Figure F38. Benthic foraminifer paleobathymetric estimates for Hole M0027A. ? = barren samples or samples with too few specimens to determine a paleodepth. Arrows = depths deeper than 100 m (mostly likely shallower than ~200 m). Red lines = sequence boundaries, green lines = major flooding surfaces. EOT = Eocene–Oligocene transition. MIC = marine isotope chron. See Figure F4 in the "Methods" chapter for lithology legend.

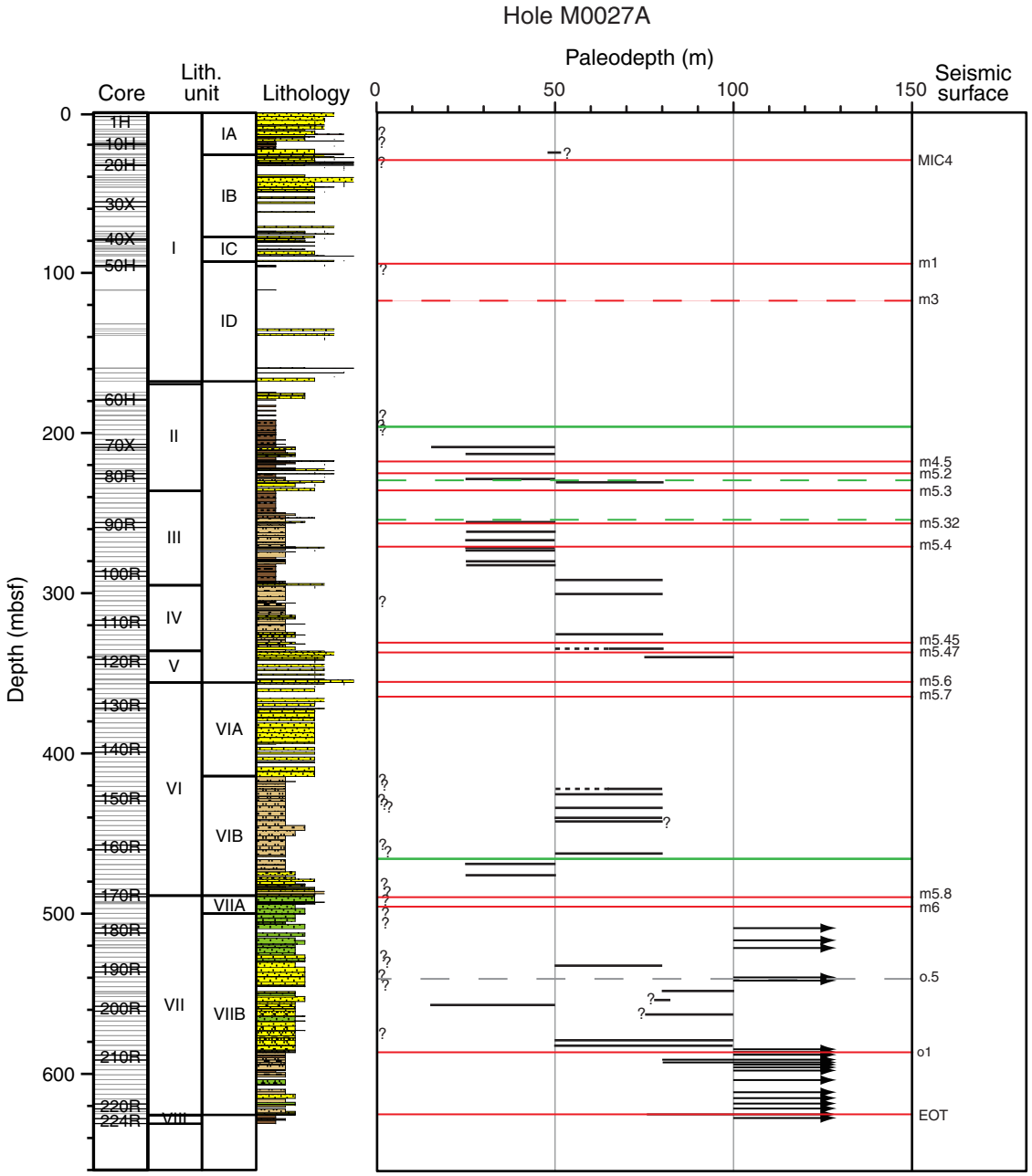

Figure F39. Palynomorph distribution, Hole M0027A. Reference sum for percentages is total amount of nonsaccate pollen (nonsaccate herb, arboreal, sedge, and grass pollen, as well as unidentified nonsaccate pollen).

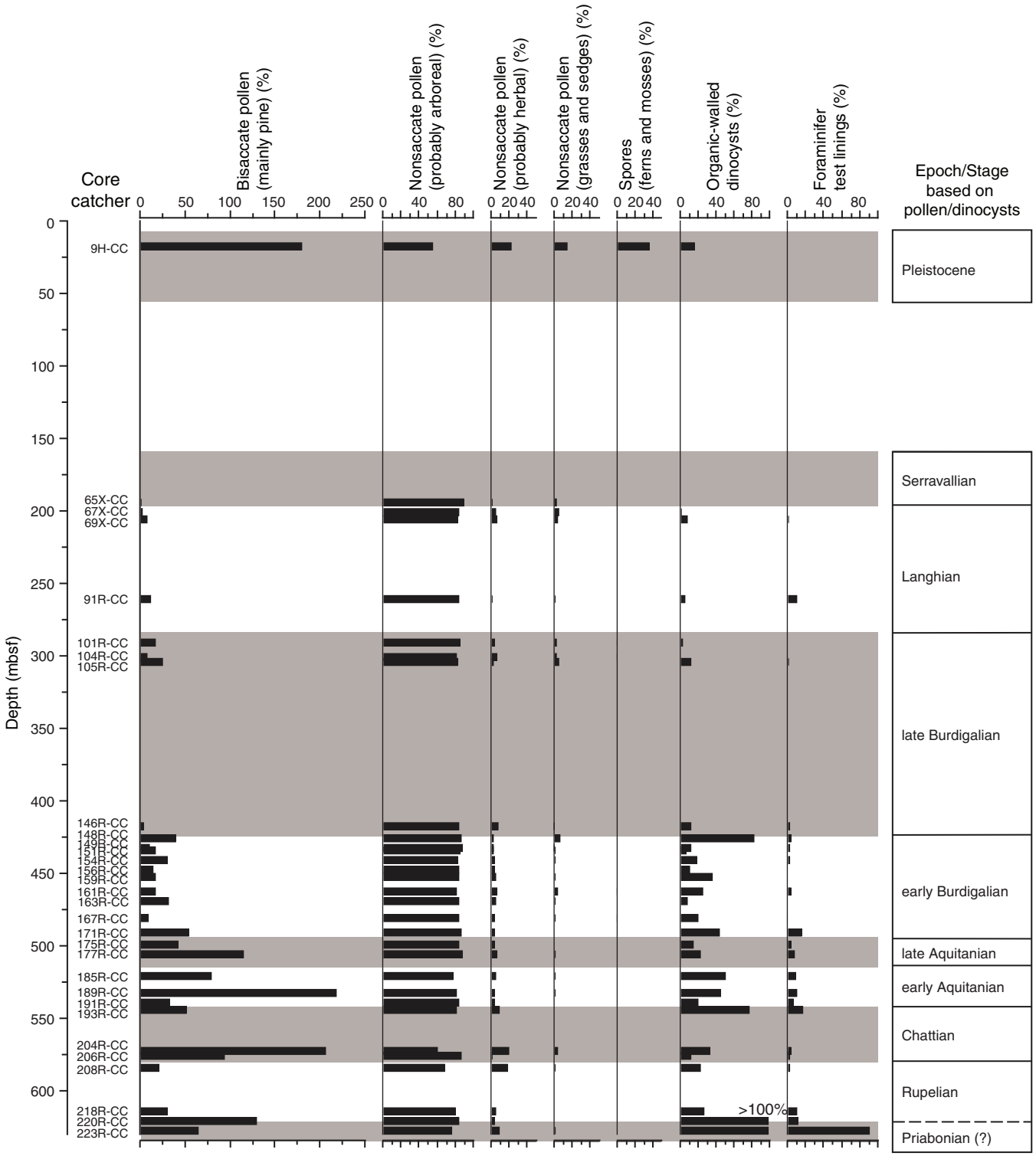

Figure F40. Simplified sketches showing hinterland and coastal ecology based on Hole M0027A sample analysis for the (?)Eocene, Oligocene, lower Miocene, middle Miocene, and Pleistocene. Gray trees = trees producing bisaccate pollen, green trees = trees producing nonsaccate pollen (mainly oaks and hickory during most intervals). Gray triangles = bisaccate pollen transport potential, green triangles = nonsaccate pollen transport potential. Red flowers = herbs producing nonsaccate pollen, excluding monoporate pollen; yellow tussocks = grasses. Spirals = foraminifer test linings, cyan symbols = dinocysts. Size of yellow sun is proportional to estimated temperatures. Percentages of palynomorphs are displayed on the right. Reference sum is the total amount of nonsaccate pollen. Green bars = pollen probably related to broad-leaf trees (mainly oaks in most samples), yellow bars = pollen of grasses (Poacea), red bars = herbal pollen. Gaps between green, red, and yellow bars = nonsaccate pollen that could not be assigned to the three main groups (pollen grains of aquatic plants, pollen filled with pyrite, and pollen of families containing both herbal and arboreal taxa). (**Figure shown on next page.**)

Figure F40 (continued). (Caption shown on previous page.)

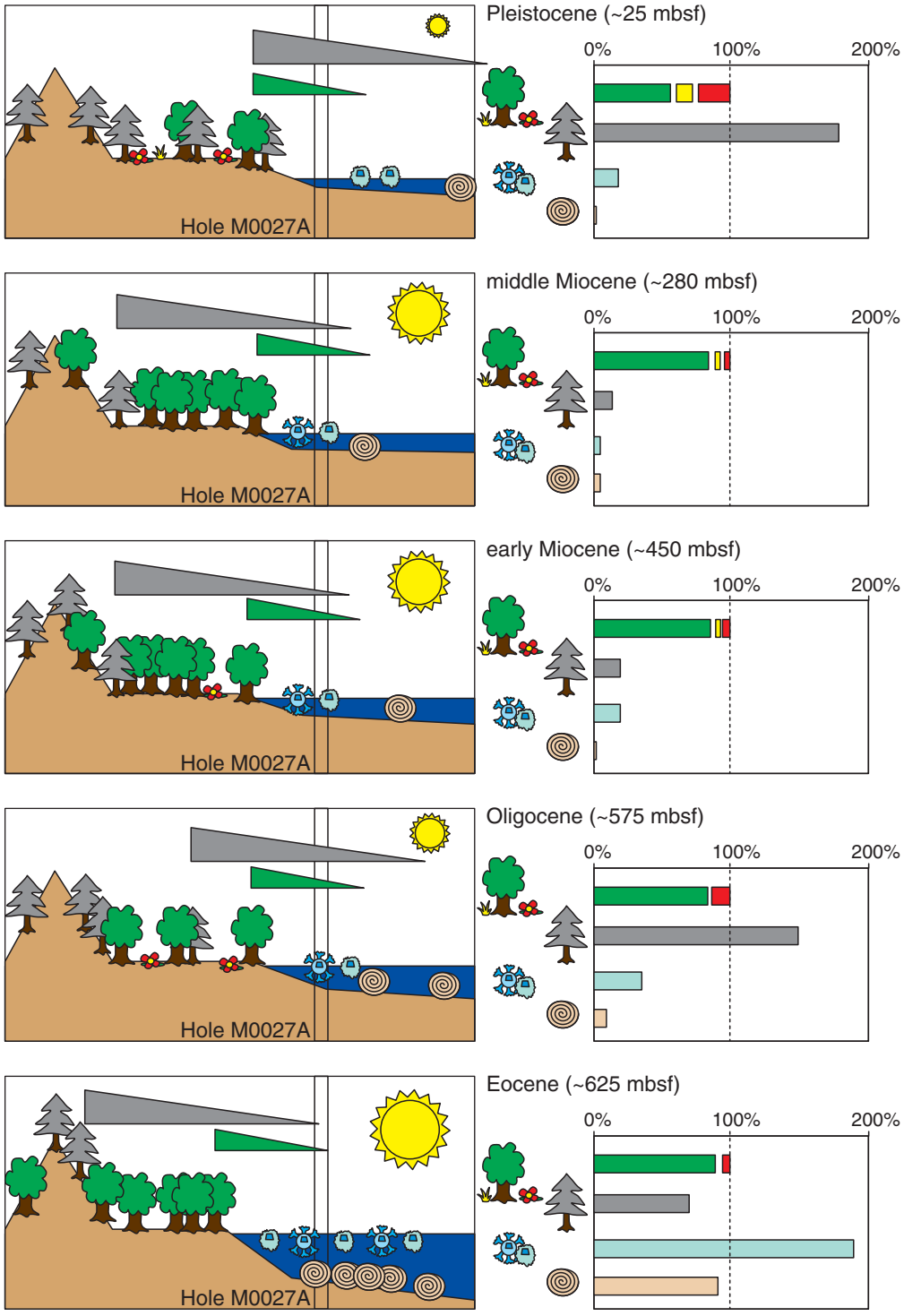

Figure F41. Composition-depth profiles of interstitial water, Hole M0027A. Vertical lines designate value calculated for present-day bottom seawater, which has a chloride concentration of ~524 mM. Horizontal color bands denote discrete freshwater (blue) and salty (pink) layers of interstitial water.

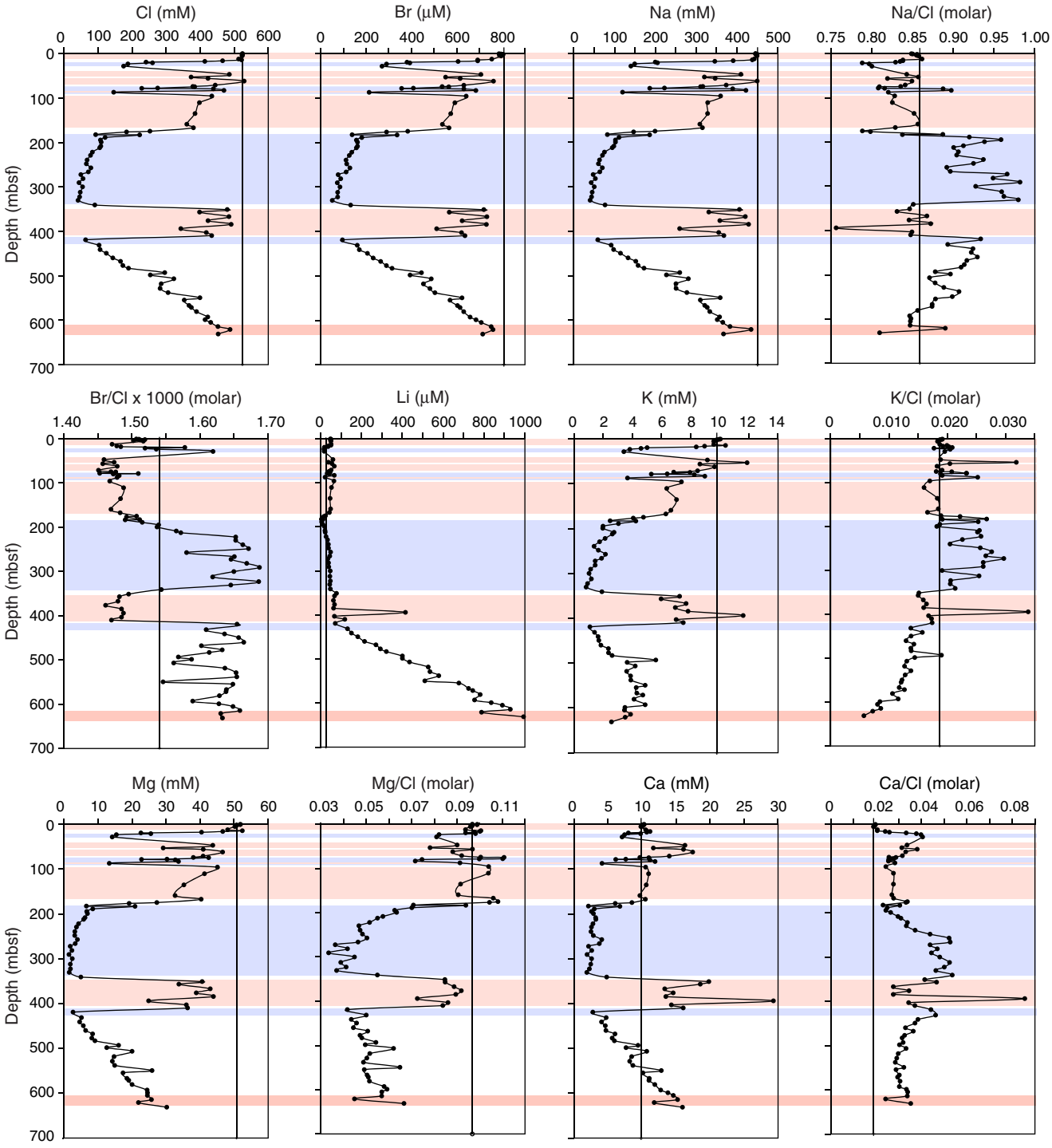

Figure F42. Composition-depth profiles of interstitial water, Hole M0027A. Vertical lines designate value calculated for present-day bottom seawater, which has a chloride concentration of ~524 mM. Horizontal color bands denote discrete freshwater (blue) and salty (pink) layers of interstitial water.

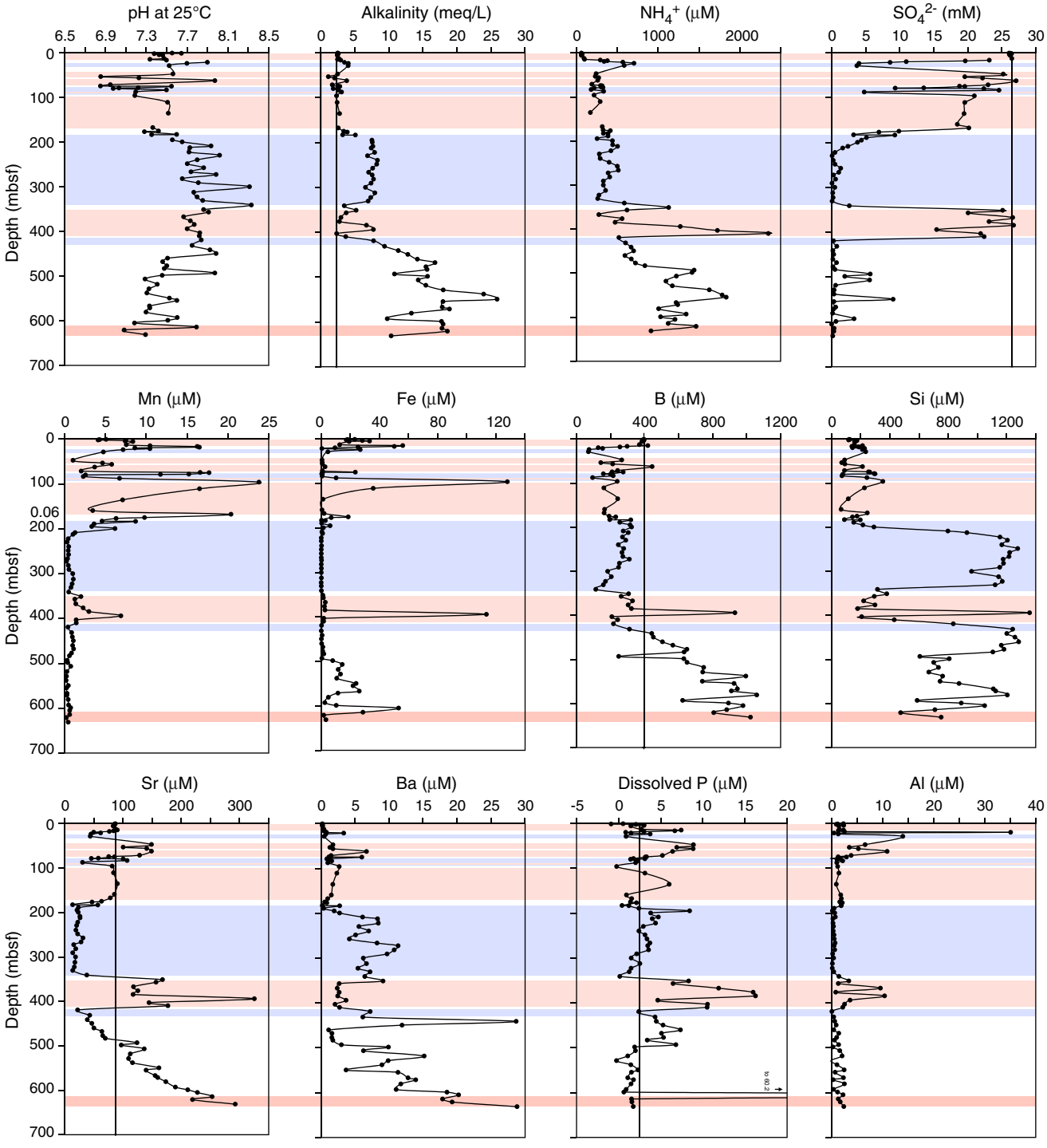

Figure F43. Composition-depth profiles of sediment compared with interstitial water and mineralogy, Hole M0027A. Upper row: total carbon (TC), total organic carbon (TOC), total inorganic (carbonate) carbon (TIC), and total sulphur (TS) concentrations in sediment. Lower row: sulfate/chloride and total phosphorus in interstitial water and concentrations of apatite and pyrite from XRD. Horizontal color bands denote discrete freshwater (blue) and salty (pink) layers of interstitial water.

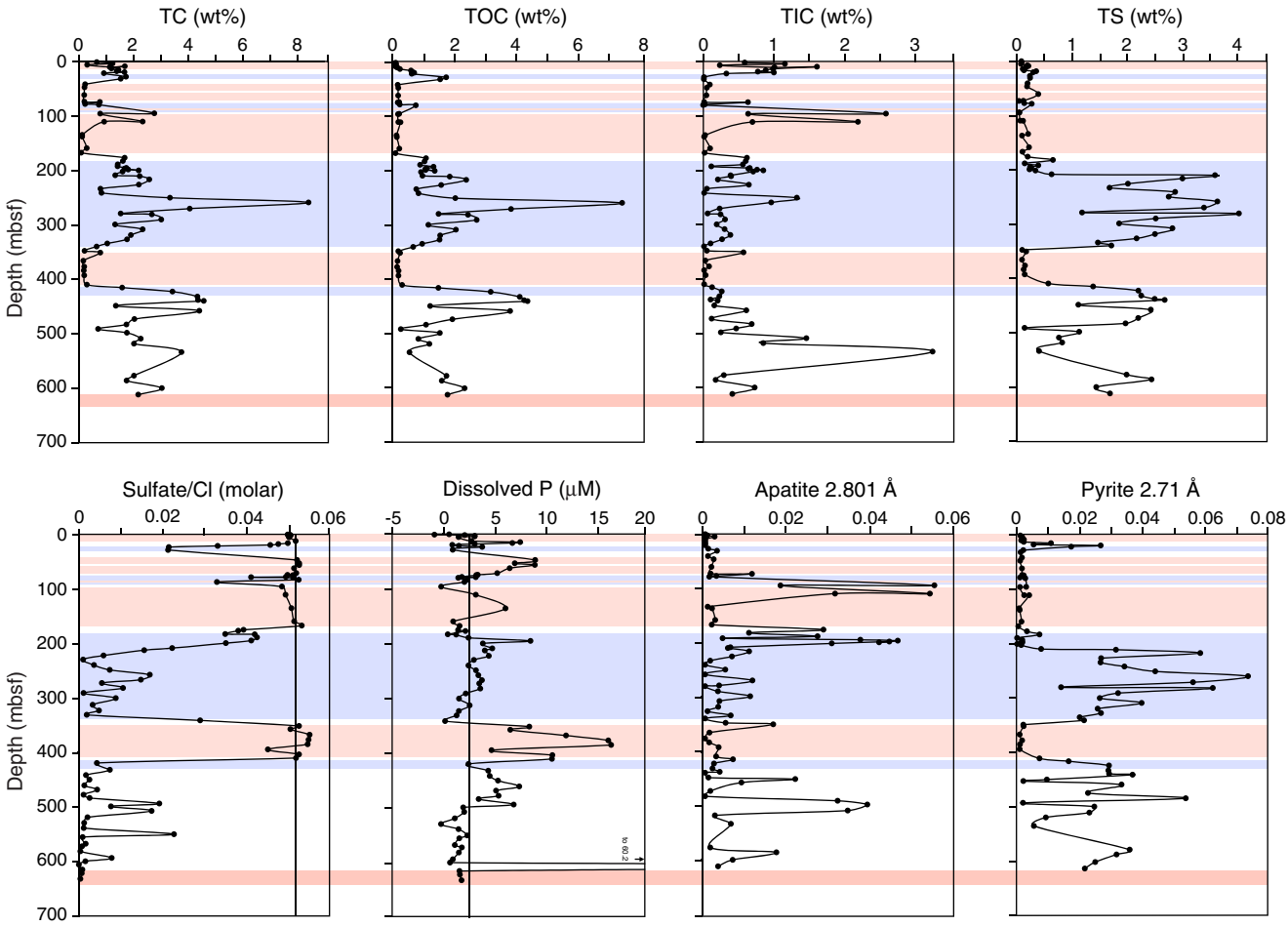

Figure F44. Composition-depth profiles of mineral content in sediment, Hole M0027A, as the ratio of intensity of the specified XRD peak(s) to total intensity of all peaks. Horizontal color bands denote discrete freshwater (blue) and salty (pink) layers of interstitial water.

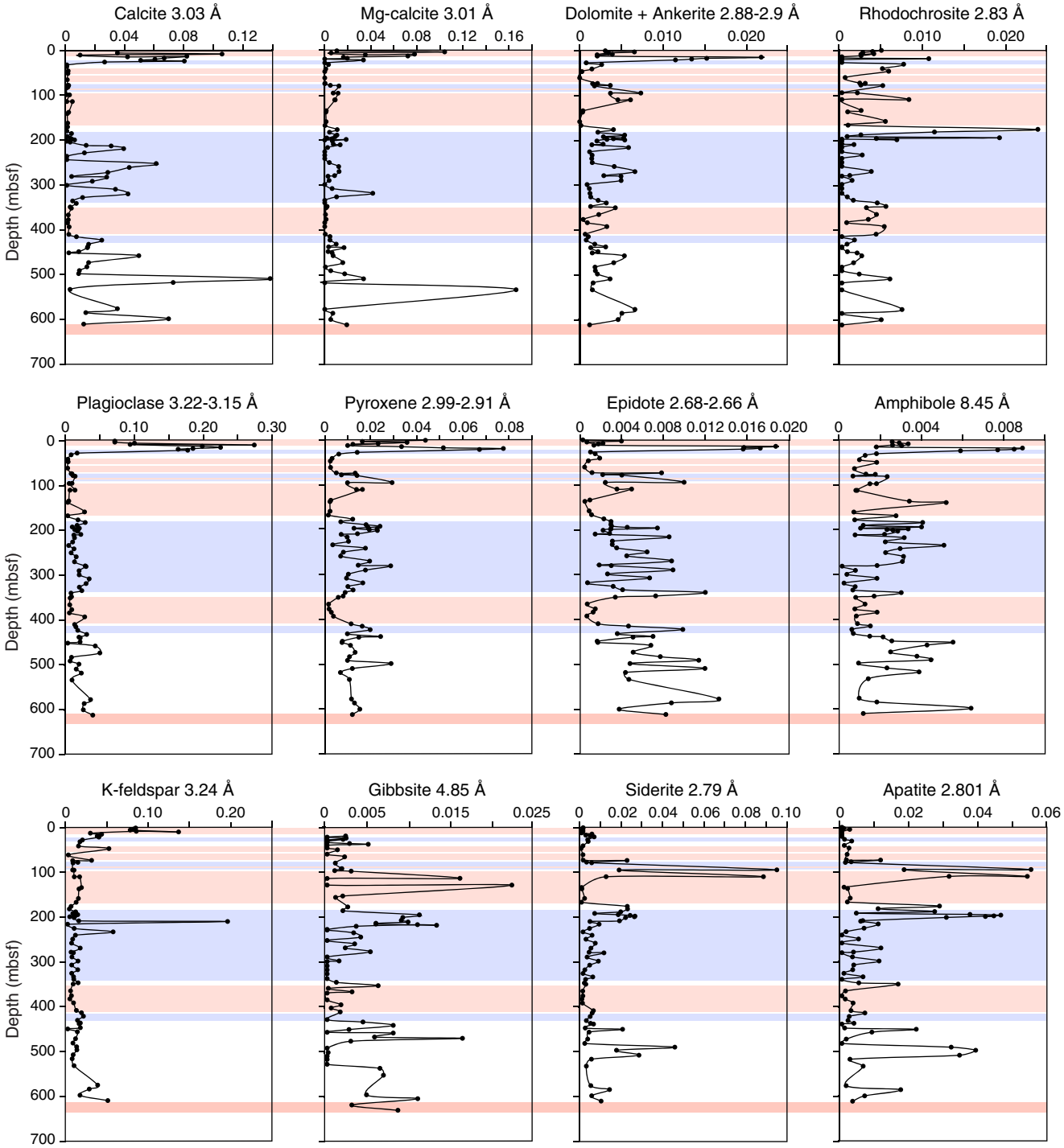

Figure F45. Composition-depth profiles of mineral content in sediment, Hole M0027A, as the ratio of intensity of the specified XRD peak(s) to total intensity of all peaks. Horizontal color bands denote discrete freshwater (blue) and salty (pink) layers of interstitial water.

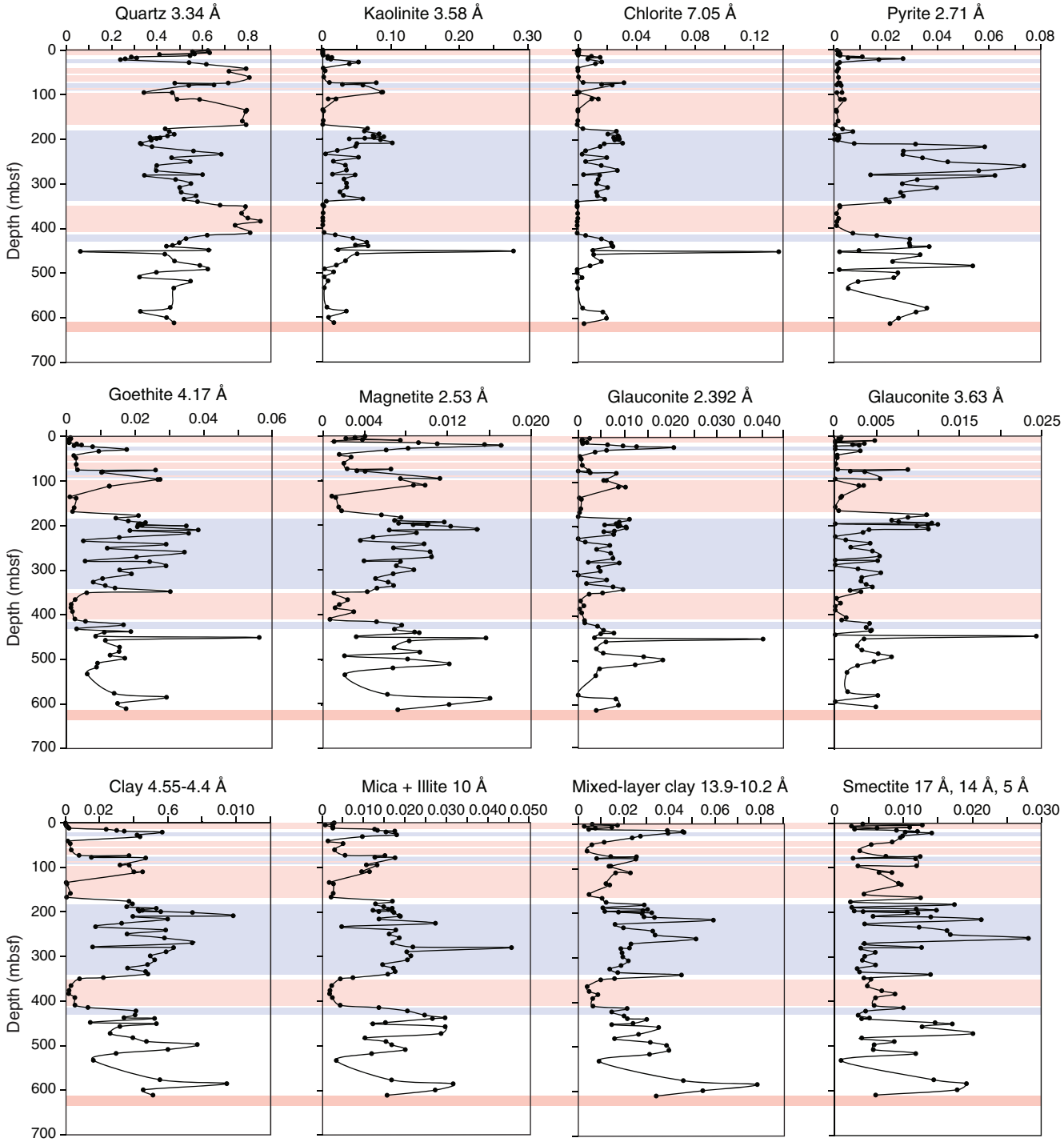

Figure F46. Overview of data acquired from multisensor core logger (MSCL) and sample measurements, Hole M0027A. From MSCL: natural gamma radiation (NGR), *P*-wave velocity, discrete *P*-wave, gamma density, magnetic susceptibility, noncontact electrical resistivity. From sample measurements: water content, wet bulk density, grain density, porosity, void ratio, and thermal conductivity.

Figure F47. Gamma density and wet bulk density, porosity, and resistivity compared with lithology in Hole M0027A. **A.** Gamma density from the MSCL (black line) and wet bulk density from section samples (red crosses). **B.** Porosity from section samples (red crosses) and high-pass filtered porosity (black line). Mean porosity reduction of sands (blue line) and clay (green line) from global averages. Note how sands and muds in the top ~200 mbsf fall outside the trends, possibly because of dewatering during coring and handling. Eight density-porosity units correspond to variation in major lithology. **C.** Electrical resistivity. Back line = original data with section 3s removed (see text), red line = high-pass filtered record, vertical black line at 1.3 Ωm = average clay–silt resistivity with low-chlorinity pore water. Note lower resistivity in the top of the hole and between 344 m and 410 mbsf, bracketed by higher resistivity. Low resistivity corresponds to zones of high chlorinity (see "Geochemistry"). See Figure F4 in the "Methods" chapter for lithology legend.

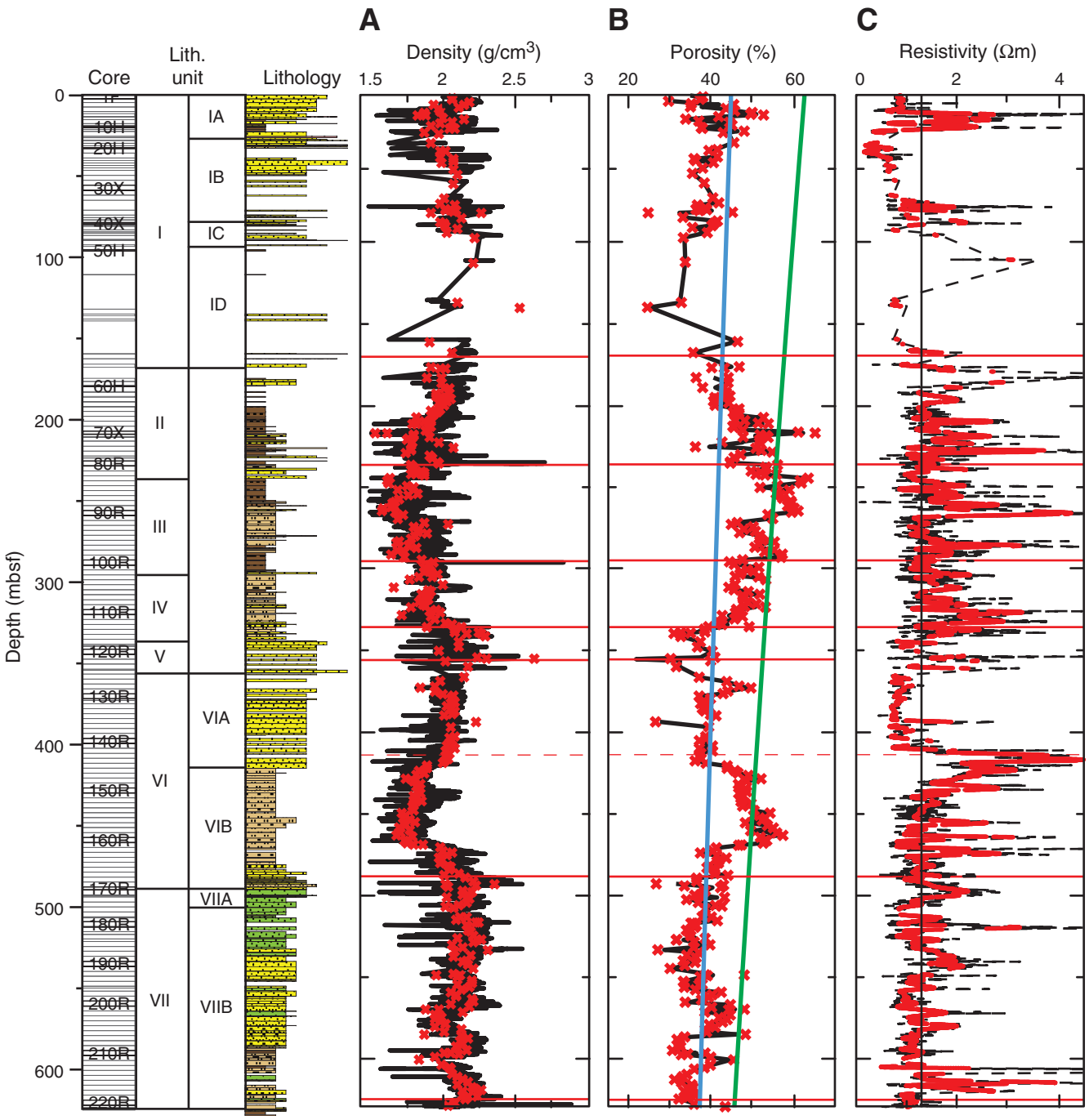

Figure F48. Cross-plot of gamma ray attenuation (GRA) density and wet bulk density, Hole M0027A. At low densities, GRA density is slightly higher than wet bulk density from section samples. MSCL = multisensor core logger.

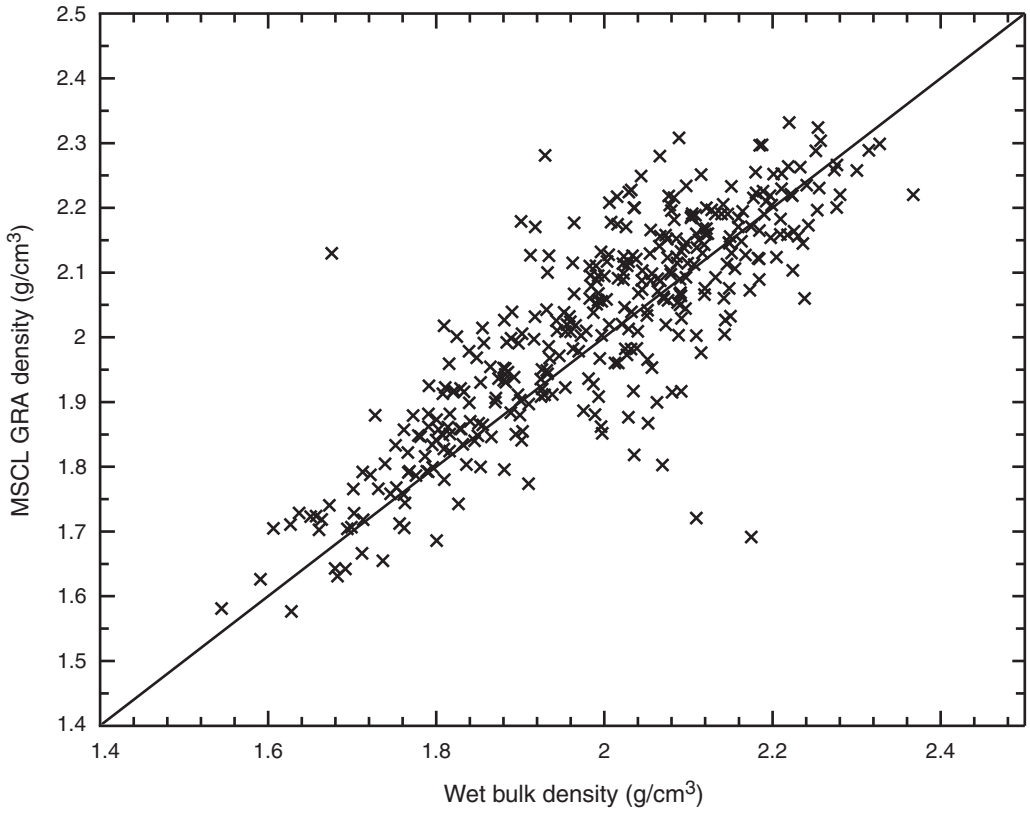

Figure F49. Cross-plot of wet bulk density and porosity from section samples, Hole M0027A. Diagonal line = mixing line between rock (zero porosity and density of 2.7 g/cm^3) and saltwater (100% porosity and density of 1.024 g/cm^3). Clays and silts that plot below the mixing line have lower densities, possibly because of high organic matter content.

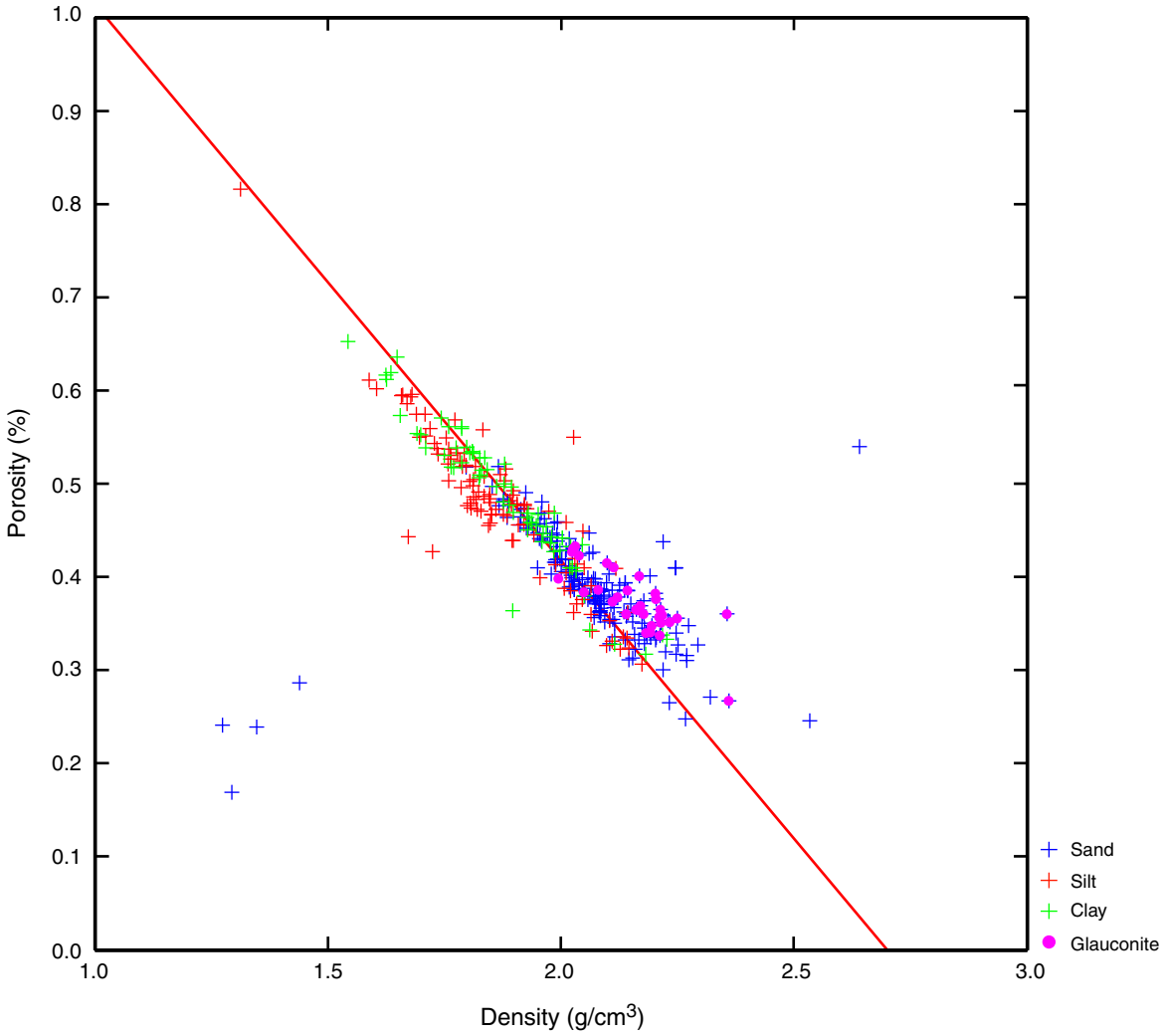

Figure F50. High-pass filtered porosity, density, and resistivity vs. depth compared with lithology in Hole M0027A. Horizontal red lines = lithologic boundaries. Porosity and density: wet bulk density from samples (thick black line) overlain on gamma density (thin black line) and original gamma density (gray). Porosity (red line) increases to left. Resistivity: black line = original data with section 3s removed (see text), red line = high-pass filtered record. Overall packages with increasing density and decreasing porosity (diagonal arrows) have a tendency to culminate with a sharp decrease in density and increase in porosity (horizontal arrows). These sharp shifts to the left correspond to grain size decreases as determined from lithology and may represent flooding surfaces and/or sequence boundaries. High resistivity brackets the sands between 344 and 410 mbsf. See Figure F4 in the "Methods" chapter for lithology legend. **A.** 160 to 290 mbsf. (**Continued on next three pages.**)

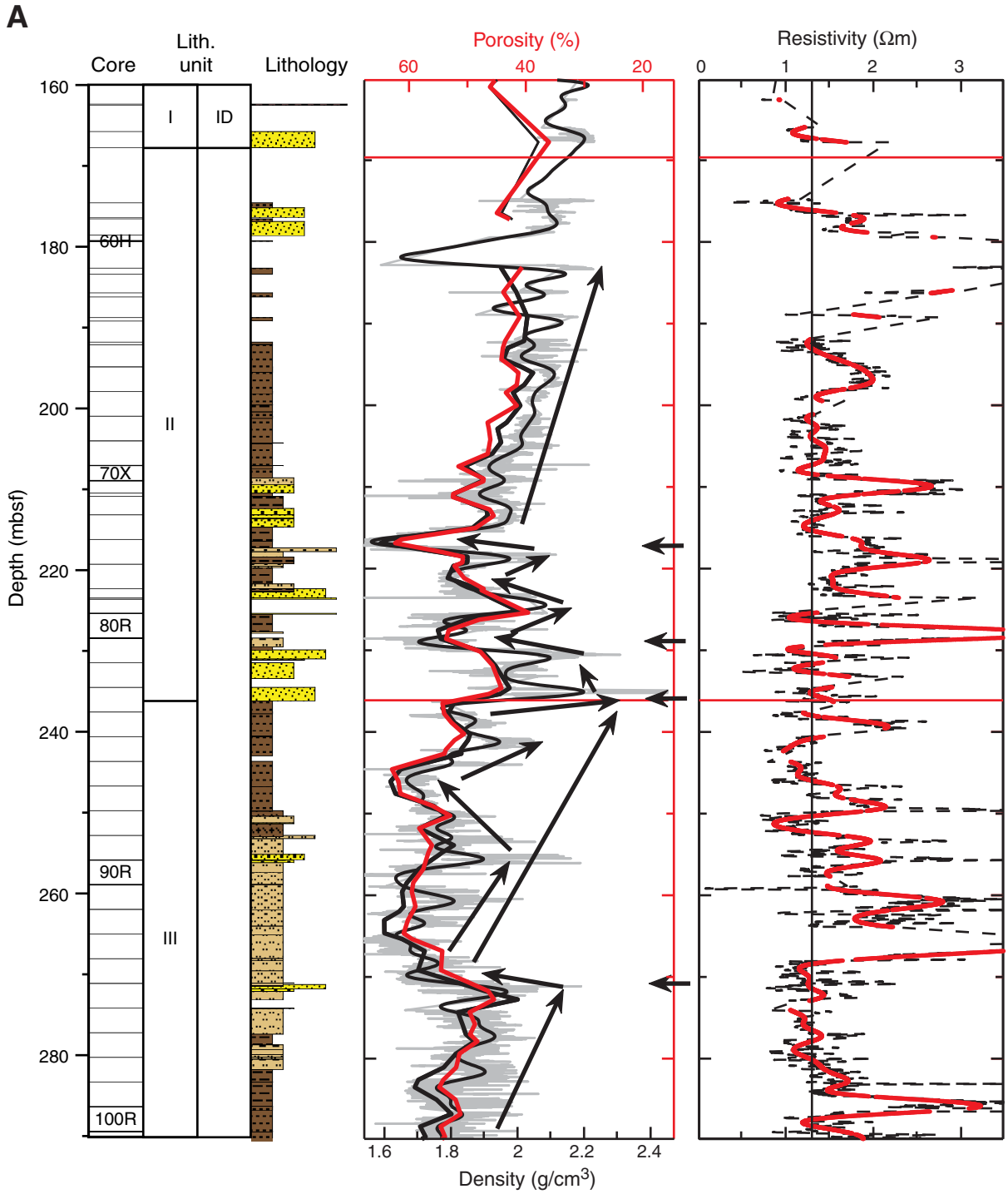

Figure F50 (continued). B. 250 to 380 mbsf. (Continued on next page.)

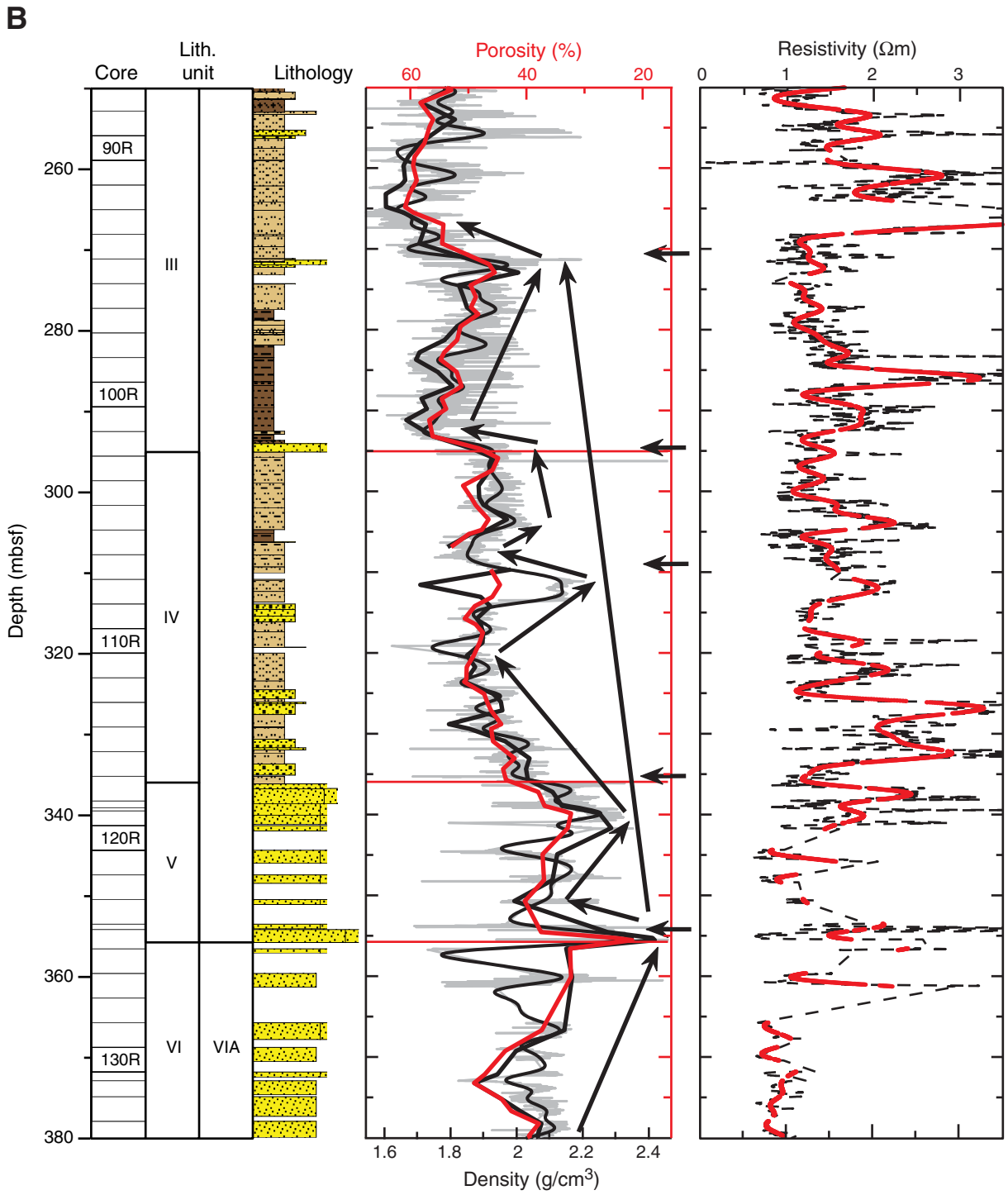

Figure F50 (continued). C. 360 to 510 mbsf. (Continued on next page.)

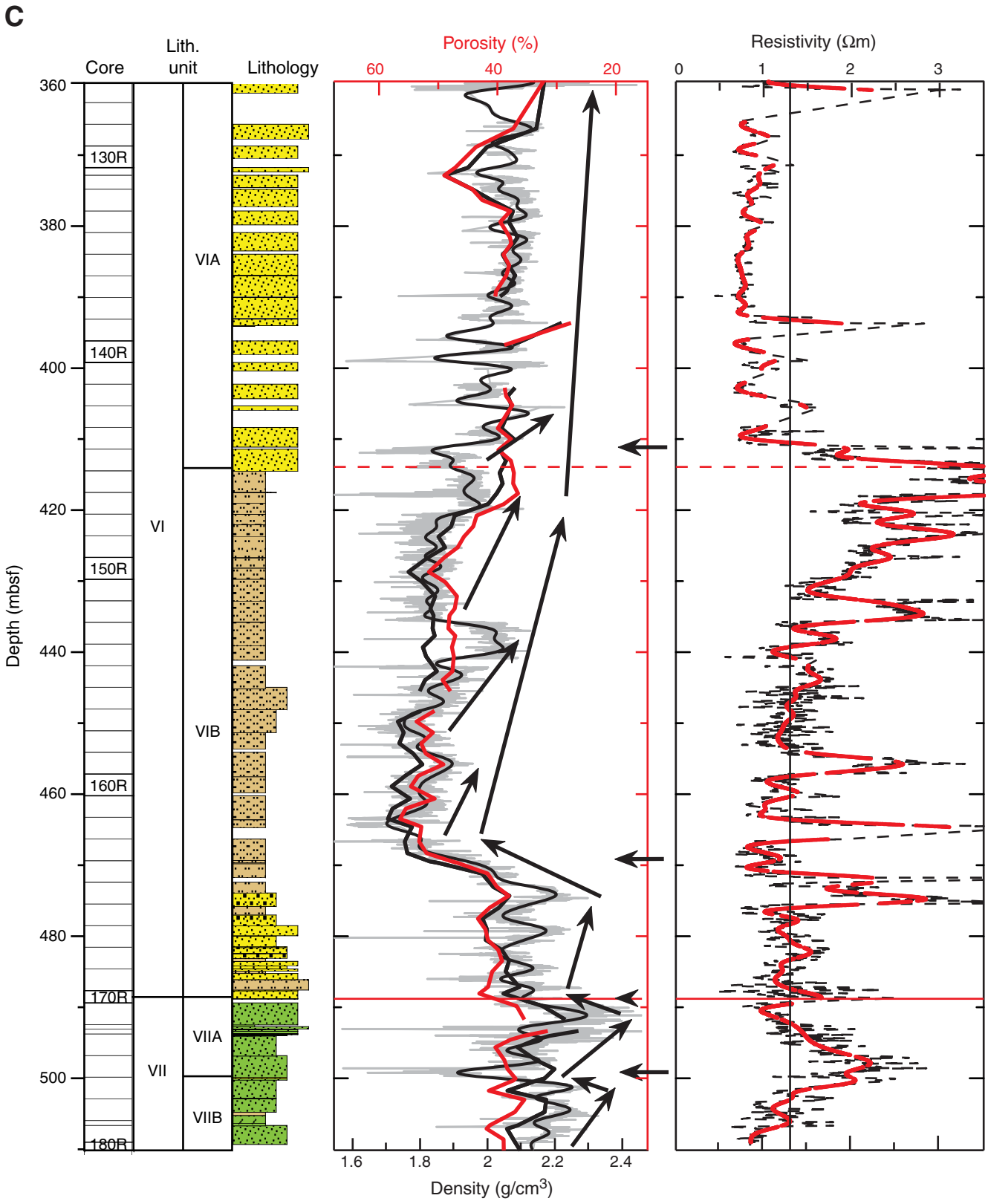

Figure F50 (continued). D. 480 to 630 mbsf.

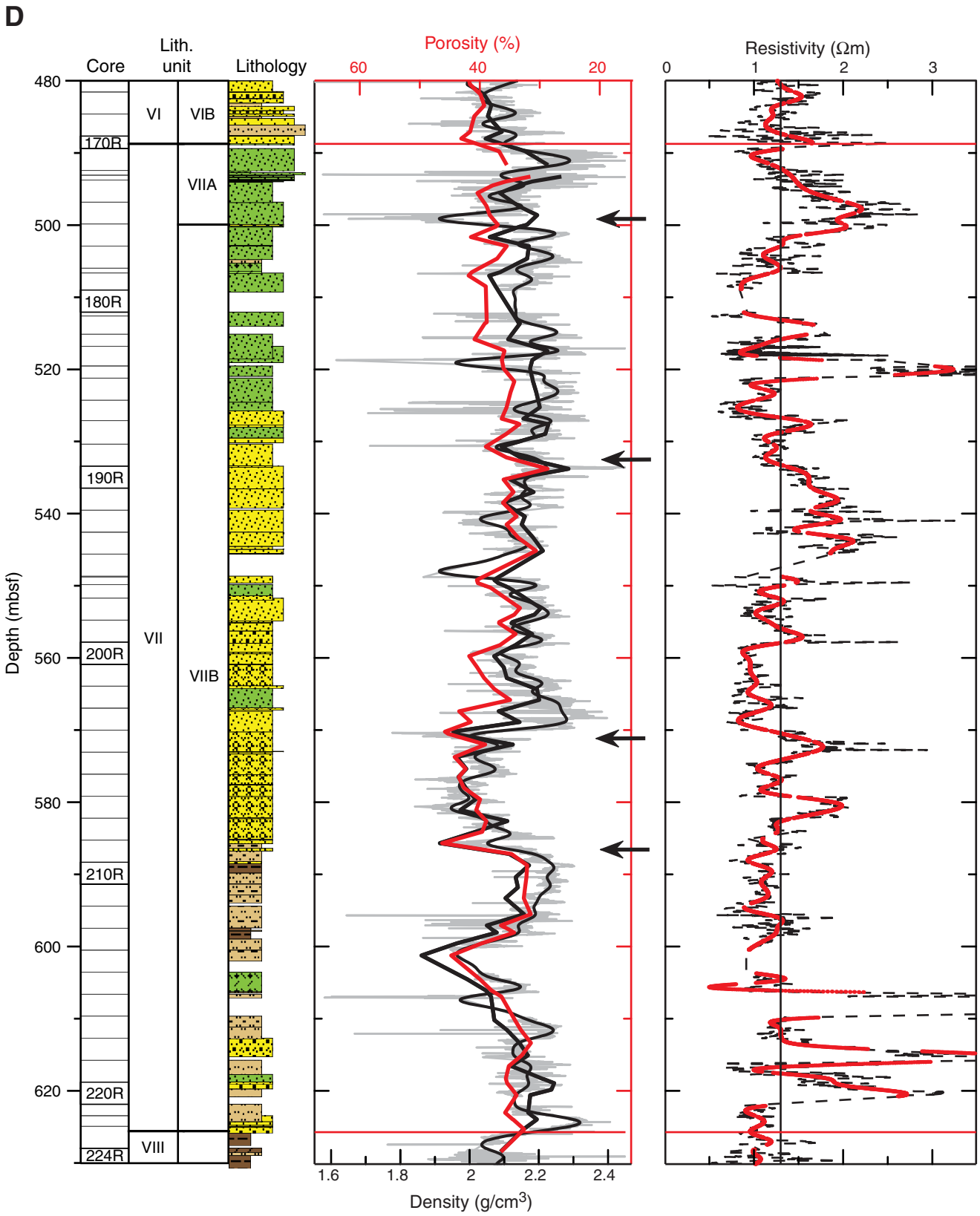

Figure F51. Petrophysical and downhole log data across the m5.3 boundary in Hole M0027A, together with MSCL gamma ray density and *P*-wave velocity. Normalized amplitude and traveltime acoustic images (ABI40 Ampl and ABI40 TT), hole diameter (AcCal), total gamma ray through pipe (ASGRcgs), downhole magnetic susceptibility (EM51), whole-core natural gamma radiation (NGR), and magnetic susceptibility from the multisensor core logger (MagSus MSCL). A composite of line scan images of Sections 313-M0027A-83R-1, 83R-2, and 83R-3 is shown alongside core depth, and whole-core measurements have been shifted down by 0.40 m to match the wireline depth.

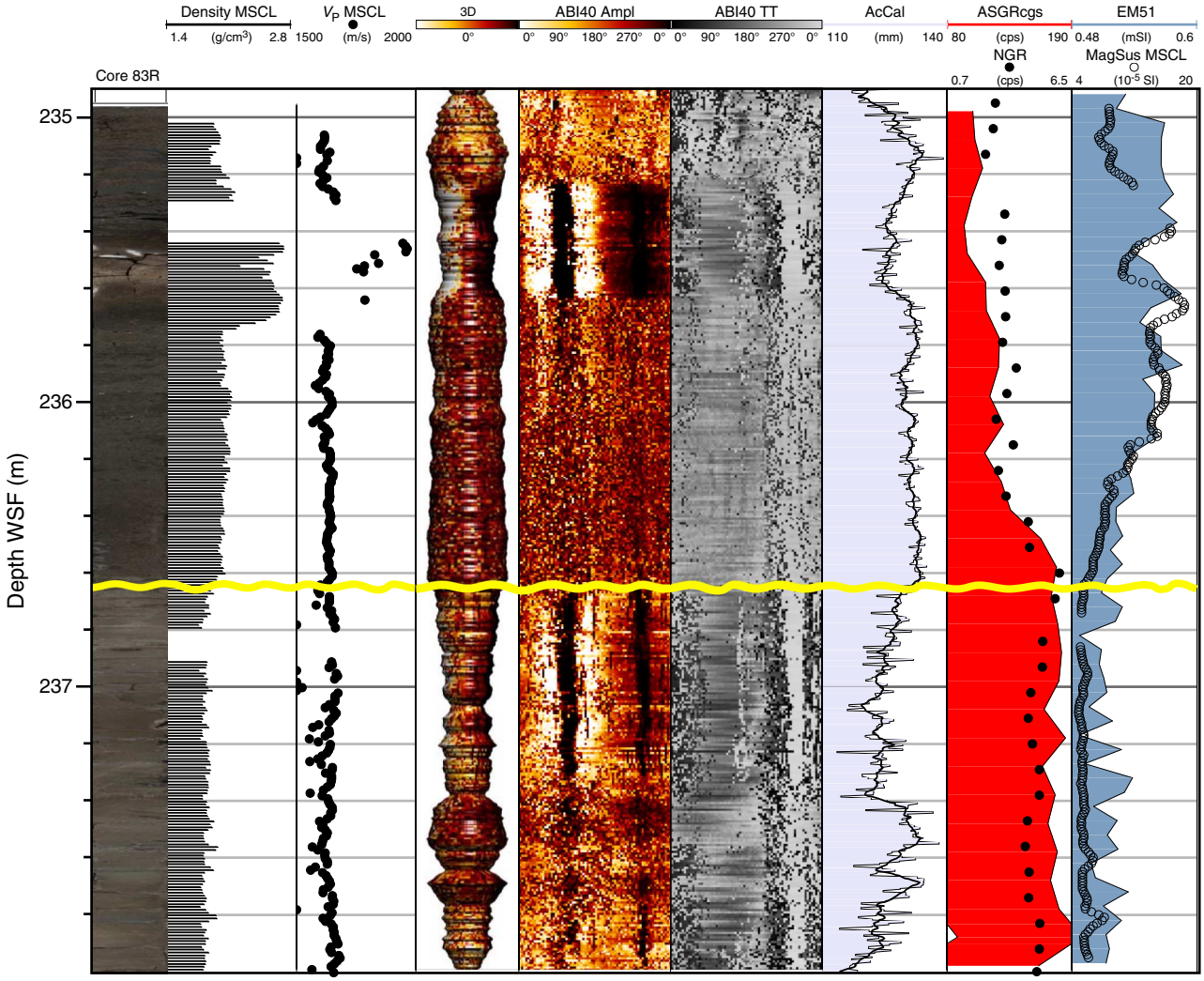

Figure F52. Inclination and magnetic moment data for Hole M0027A for initial natural remanent magnetization (NRM; black) and after 15 (blue) and 30 (red) mT AF demagnetization. MSCL magnetic susceptibility (MS) is also shown for reference.

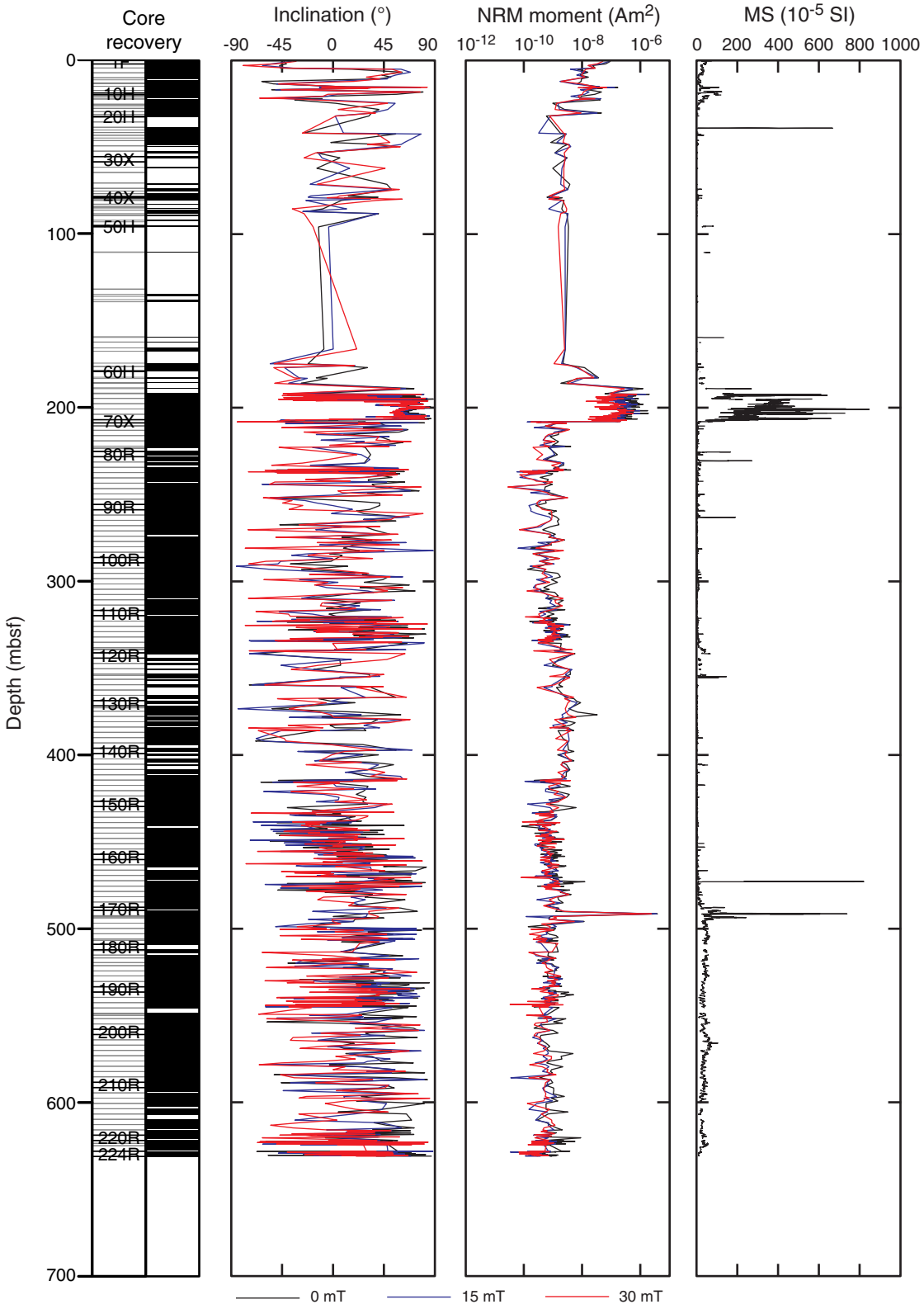

Figure F53. Orthogonal Zijderveld plots obtained from AF demagnetization of the NRM. **A.** Core 313-M0027A-69R, obtained using the antigyroremanent magnetization technique. **B.** Core 313-M0027A-177R, obtained using the antigyroremanent magnetization technique. **C.** Core 313-M0027-68R, obtained without the antigyroremanent magnetization technique. **D.** Core 313-M0027A-68R, obtained using the antigyroremanent magnetization technique. Black = NRM, blue = AF demagnetization at 15 mT, red = AF demagnetization at 30 mT, green = AF demagnetization at 60 mT.

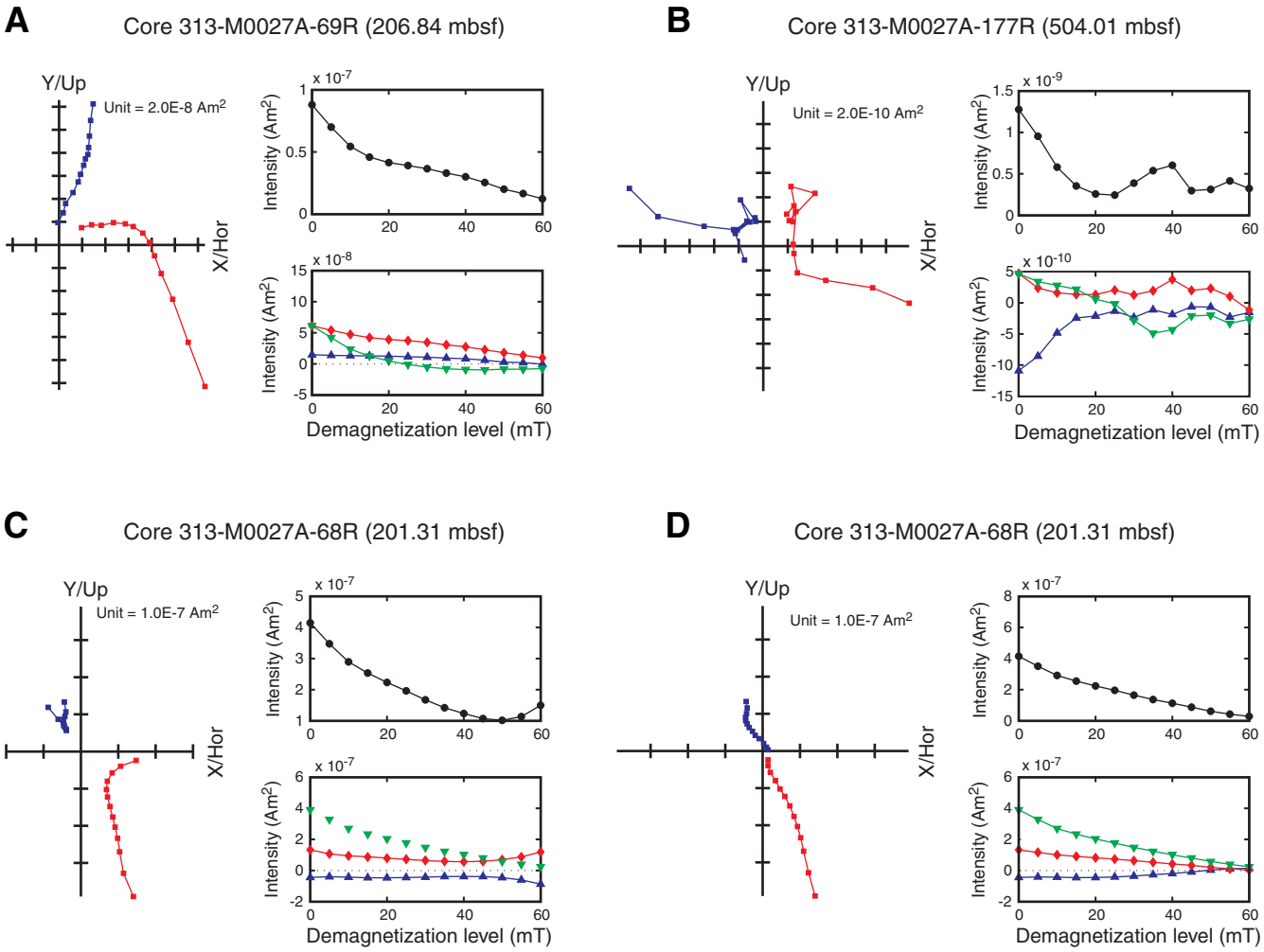

Figure F54. Preliminary magnetostratigraphic interpretation, Hole M0027A. Inclination data of initial NRM (black) and at 30 mT (blue) and of ChRM (red) derived by PCA analyses where applicable. X = depths with no core recovery. Magnetic polarity timescale from Cande and Kent (1995). Preliminary tie points: solid line = interpretation A, dashed line = interpretation B.

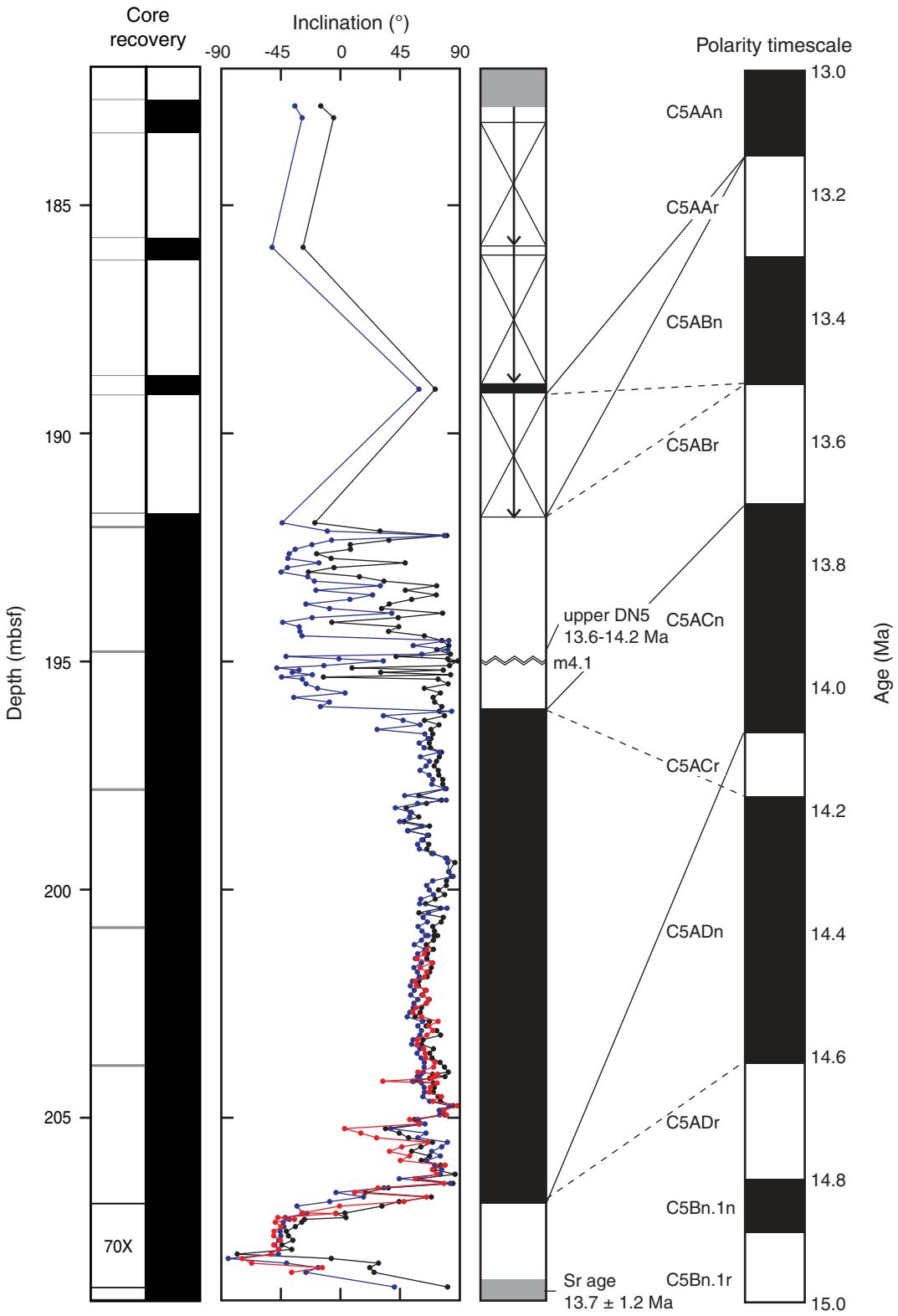

Figure F55. Magnetic susceptibility (MagSus) data for Oligocene sequence o1 (~28.5–29.0 Ma) in Hole M0027A taken on the multisensor core logger (MSCL). Tick marks = magnetic susceptibility peaks that may be astronomically controlled.

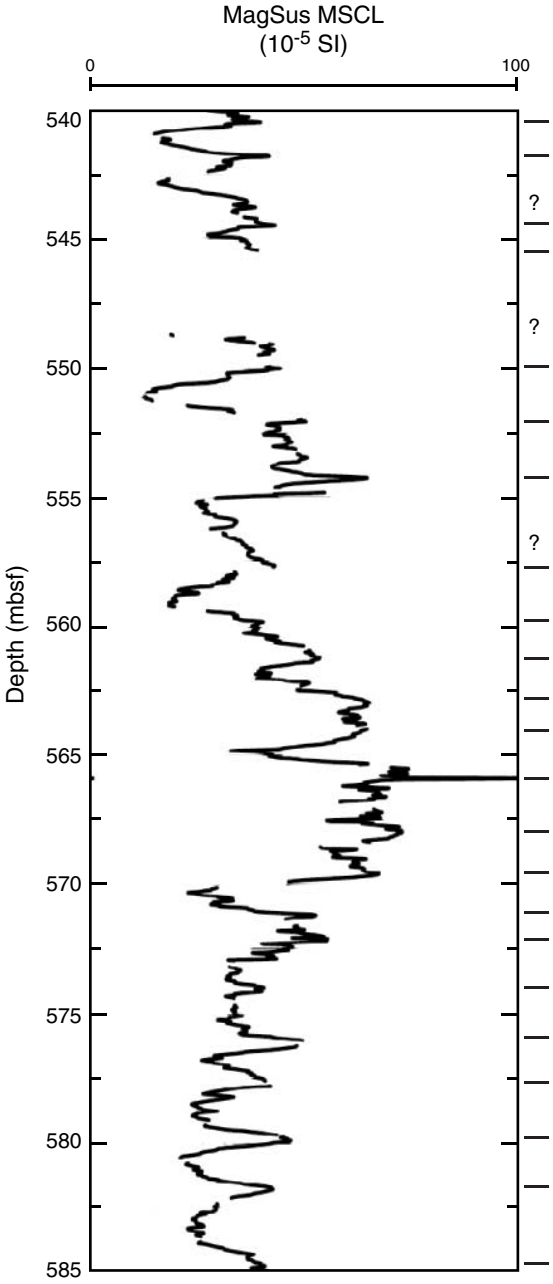

Figure F56. Composite of downhole log data, Hole M0027A. Normalized amplitude and traveltime acoustic images (ABI40 Ampl and ABI40 TT), hole diameter (AcCal), total and spectral gamma ray through pipe (ASGRcgs) and in open hole (ASGR), conductivity (DIL45), *P*-wave sonic (2PSA), and magnetic susceptibility (EM51). See Figure F4 in the "Methods" chapter for lithology legend.

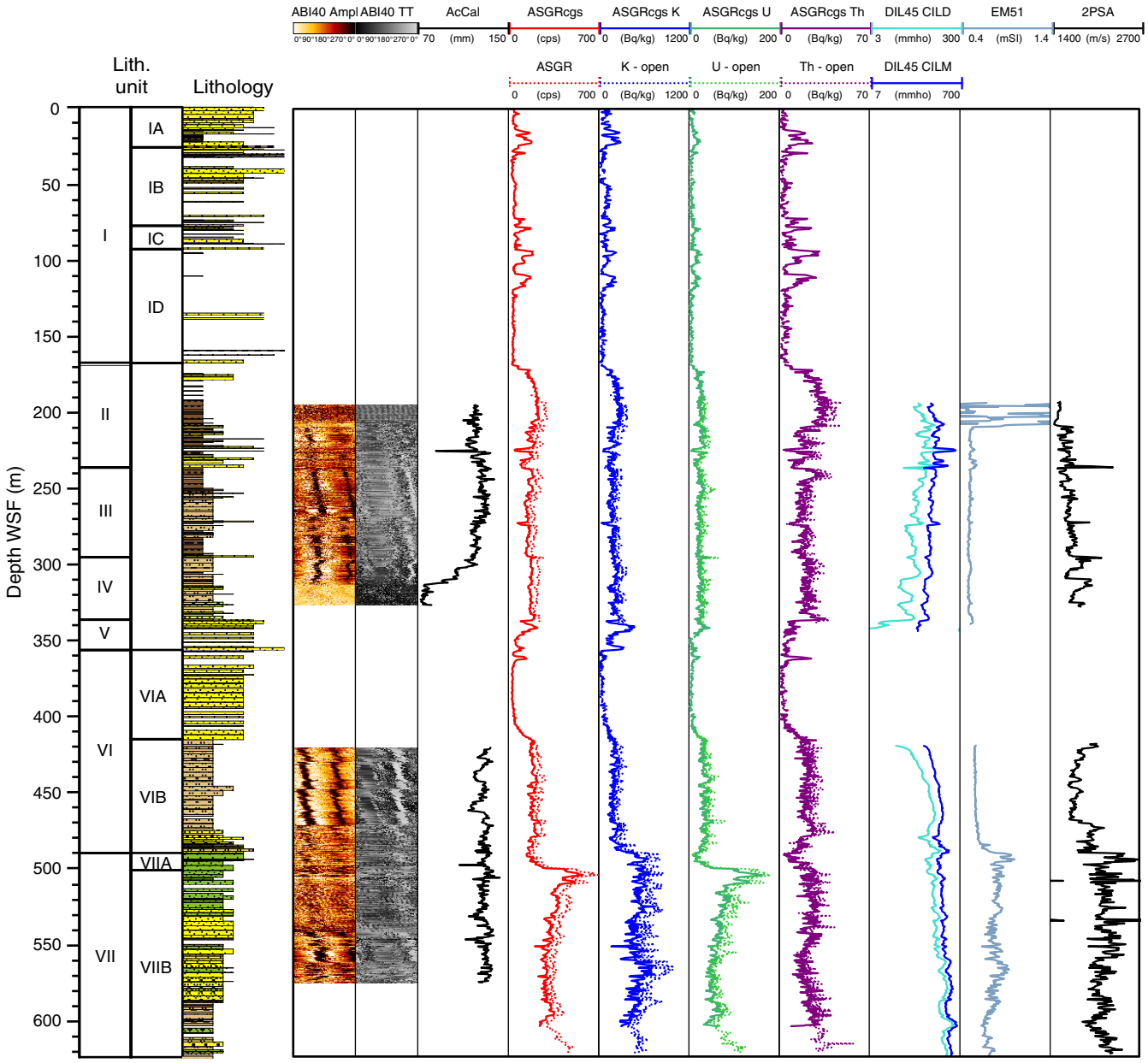

Figure F57. U/K and Th/K ratios on logarithmic scale vs. depth, Hole M0027A. Cemented levels, organic matter, and glauconite-rich levels observed by sedimentologists are indicated.

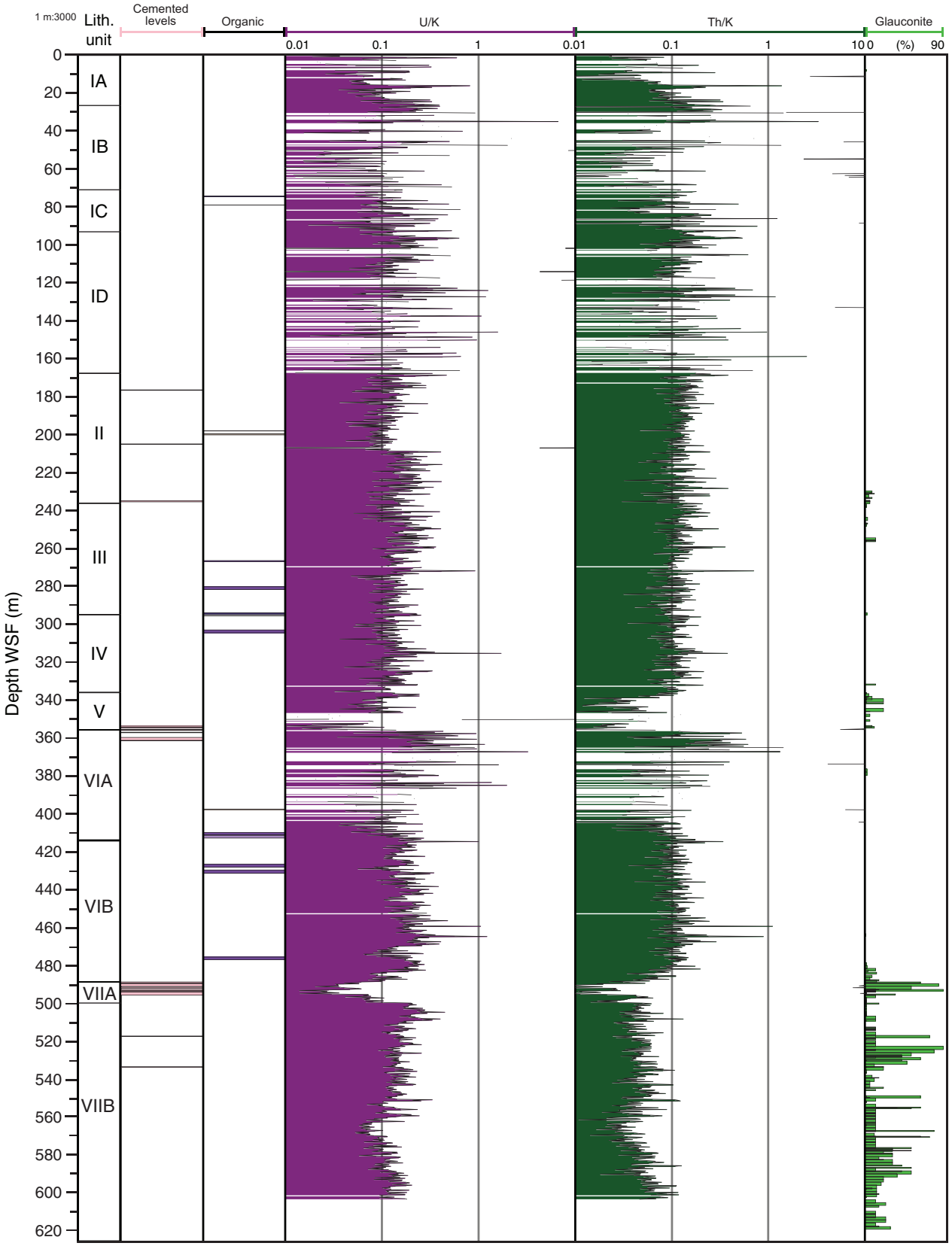

Figure F58. Line scan image of Sections 313-M0027A-69R-1 and 69R-2, along with magnetic susceptibility data from whole-core multisensor core logger (MSCL) measurements and the magnetic susceptibility downhole probe (EM51). Core depth has been shifted up by 0.55 m to match wireline depth.

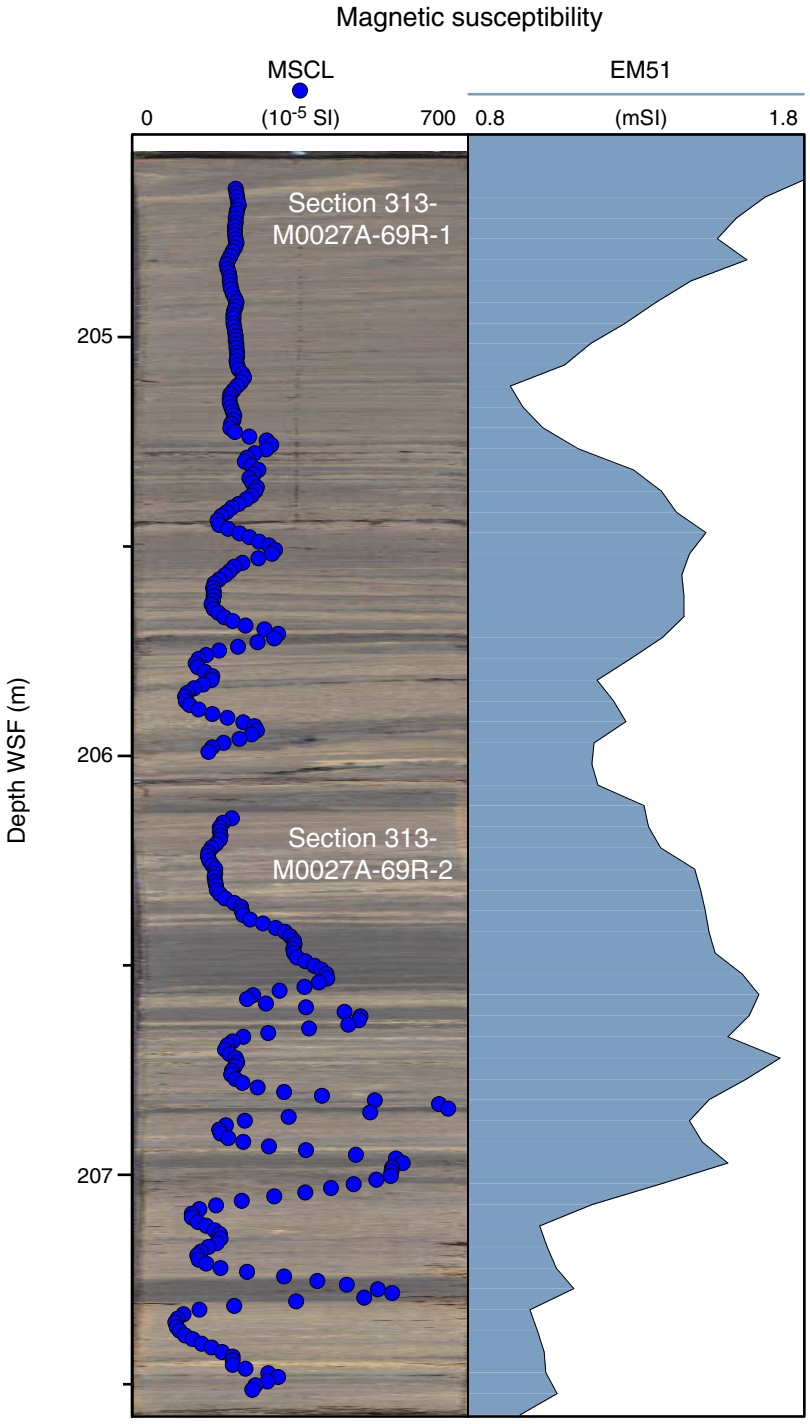

Figure F59. Composite of downhole log data for Hole M0027A illustrating parallel trends of normalized amplitude image (ABI40 Ampl), potassium content (ASGRcgs K), and magnetic susceptibility (EM51). See Figure F4 in the "Methods" chapter for lithology legend.

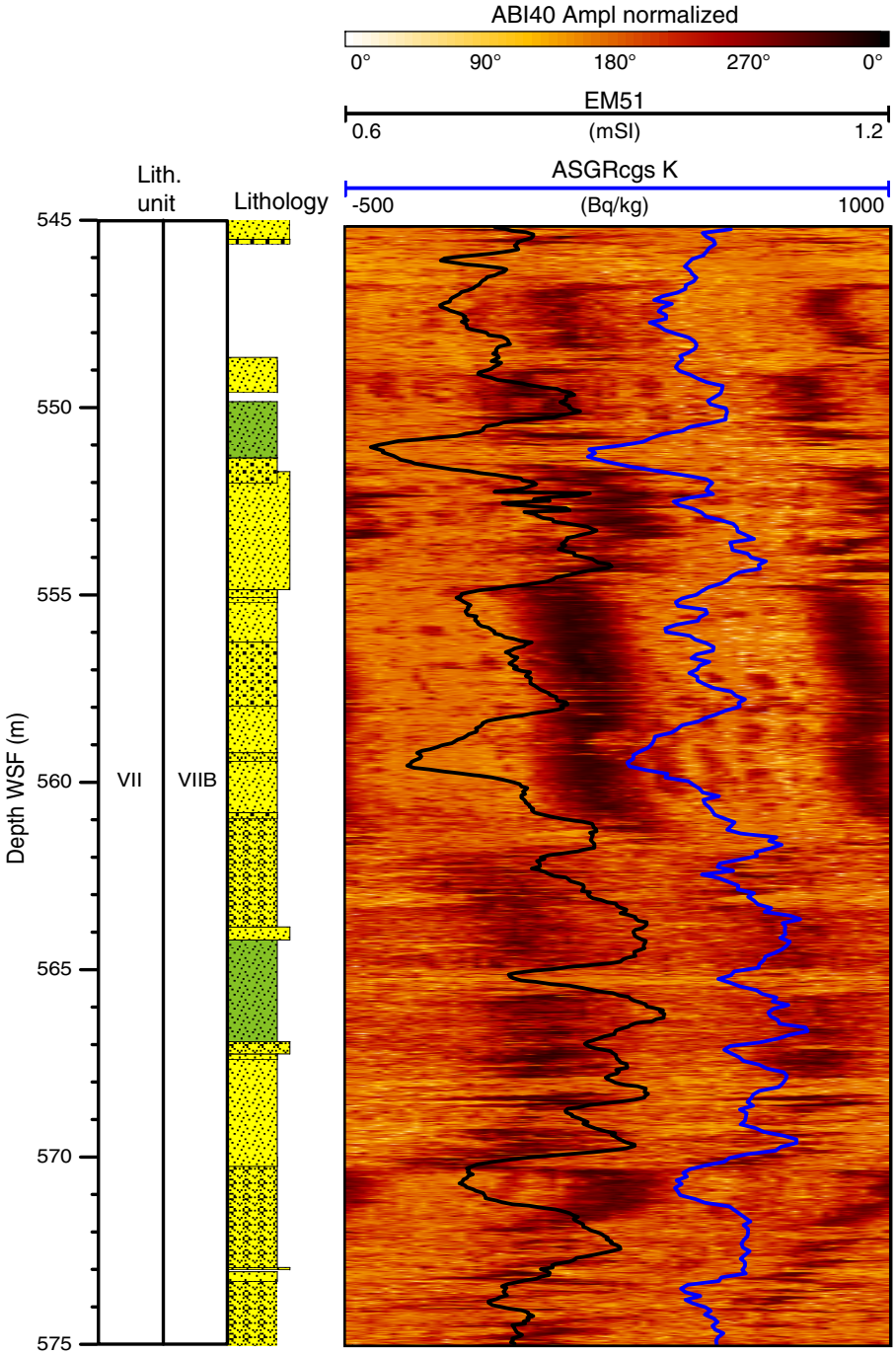

Figure F60. Chlorinity in pore water and thermal conductivity, sonic velocity, total gamma ray, and electrical conductivity measured on cores shown with downhole logging data for Hole M0027A. Conductivity (CILM and CILD), *P*-wave sonic (2PSA), and spectral gamma ray through pipe (ASGRcgs). Cemented levels observed by sedimentologists are plotted as pink lines/bars across the sonic and conductivity logs, which are anticipated to show an increase and decrease, respectively, at most of these horizons. Yellow and blue bars represent intervals of high salinity and freshwater, respectively (see "Geochemistry"). White shading shows transitional areas between "freshwater" and "saltwater" zones. See Figure F1 for lithology legend.

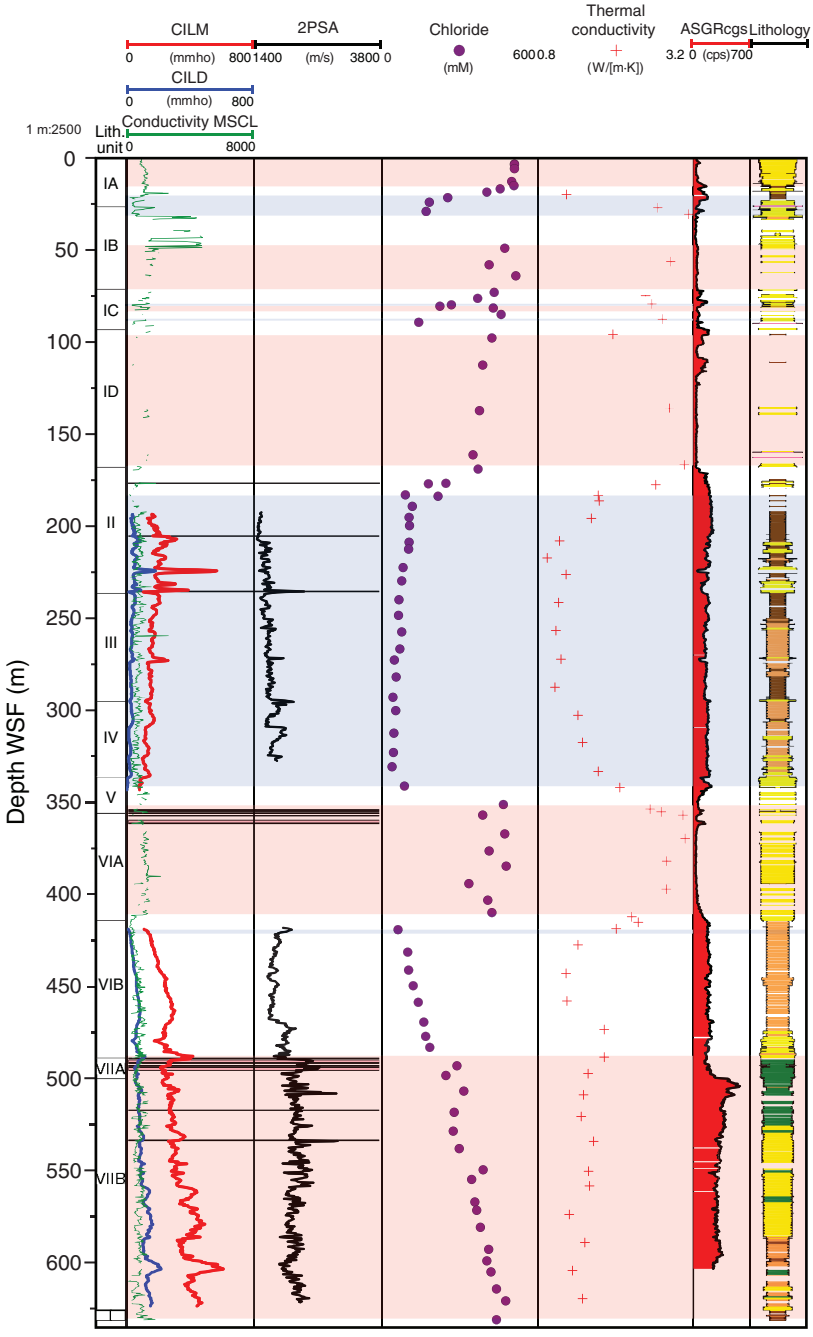

Figure F61. VSP two-way traveltime vs. depth, Hole M0027A.

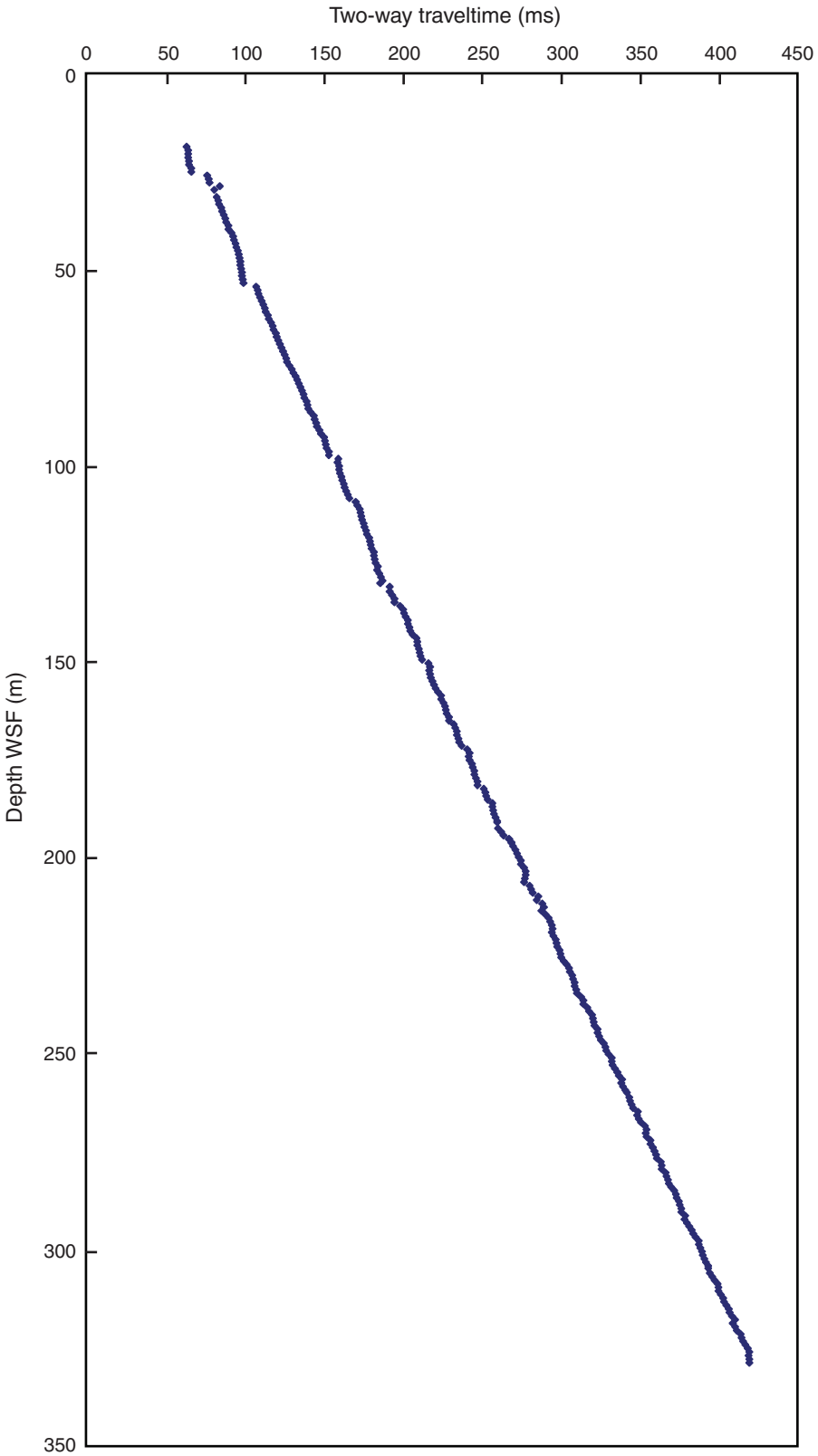

Figure F62. Detailed composite of selected downhole log data, petrophysical measurements, and derived calculations, Hole M0027A. Normalized amplitude acoustic image (ABI40 Ampl); acoustic caliper (AcCal); total gamma ray through pipe (ASGRcgs) and on cores (NGR core); potassium, uranium, and thorium contents (ASGRcgs K, U, and Th, respectively); U-Th/3 ratios; clay volume estimate; magnetic susceptibility from cores on the multisensor core logger (MagSus MSCL) and from downhole logging (EM51); *P*-wave velocities on core (V_P MSCL) and from log (V_P 2PSA); density from whole core (Density MSCL) and filtered signal; porosity from discrete measurements (porosity) and filtered signal; and impedance calculated from MSCL *P*-wave data (impedance MSCL) and sonic *P*-wave log (impedance 2PSA). Stratigraphic surfaces are added to the left: SB = sequence boundary, FS = flooding surface, MFS = maximum flooding surface, TS = transgressive surface. Petrophysical boundaries are shown in pink. EOT = Eocene–Oligocene transition. MIC = marine isotope chron. See text for discussion, Table T13 for boundary descriptions, and Figure F4 in the "Methods" chapter for lithology legend. **A.** 558–626 m WSF. (Continued on next four pages.)

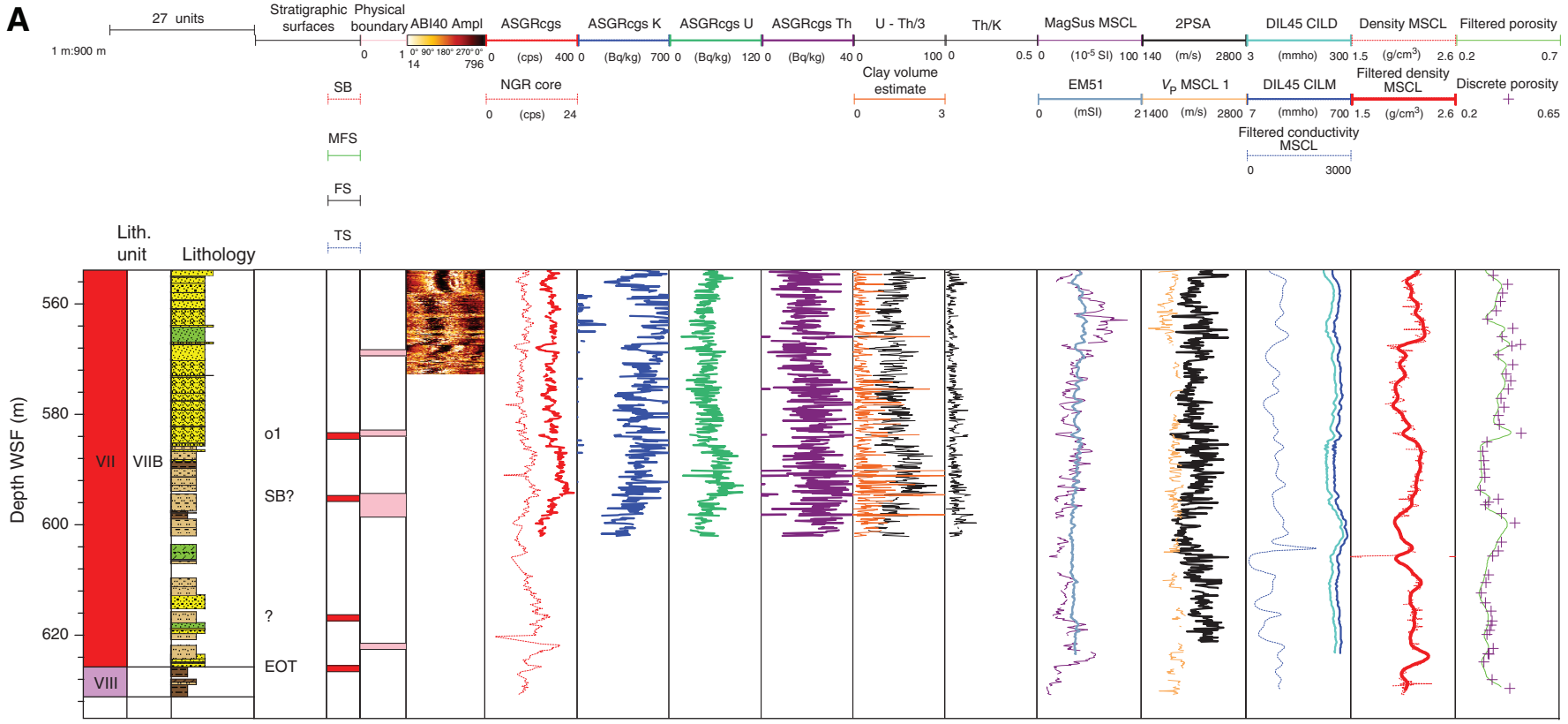

Figure F62 (continued). B. 420–548 m WSF. (Continued on next page.)

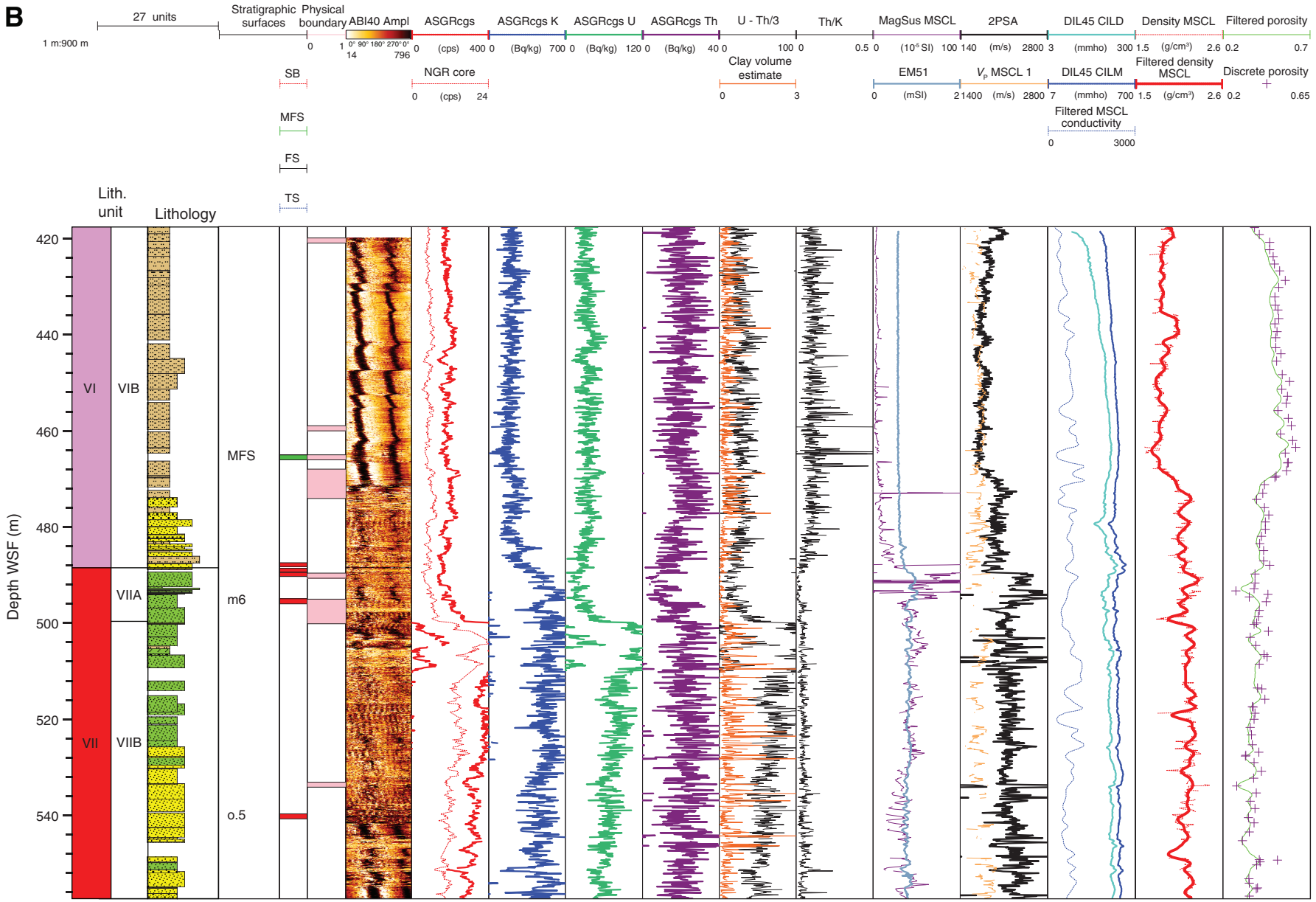

Figure F62 (continued). C. 280–408 m WSF. (Continued on next page.)

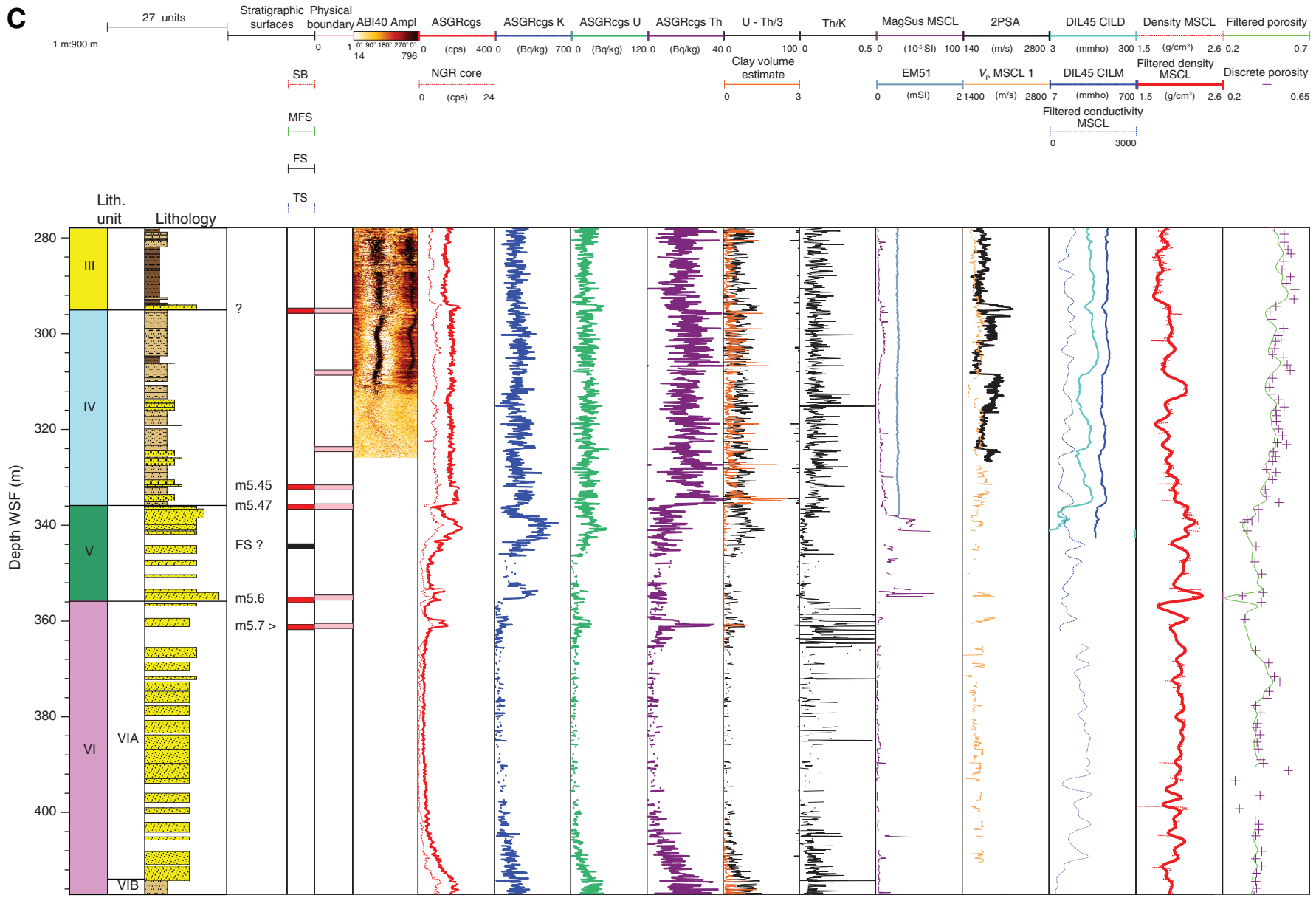

Figure F62 (continued). D. 140–268 m WSF. (Continued on next page.)

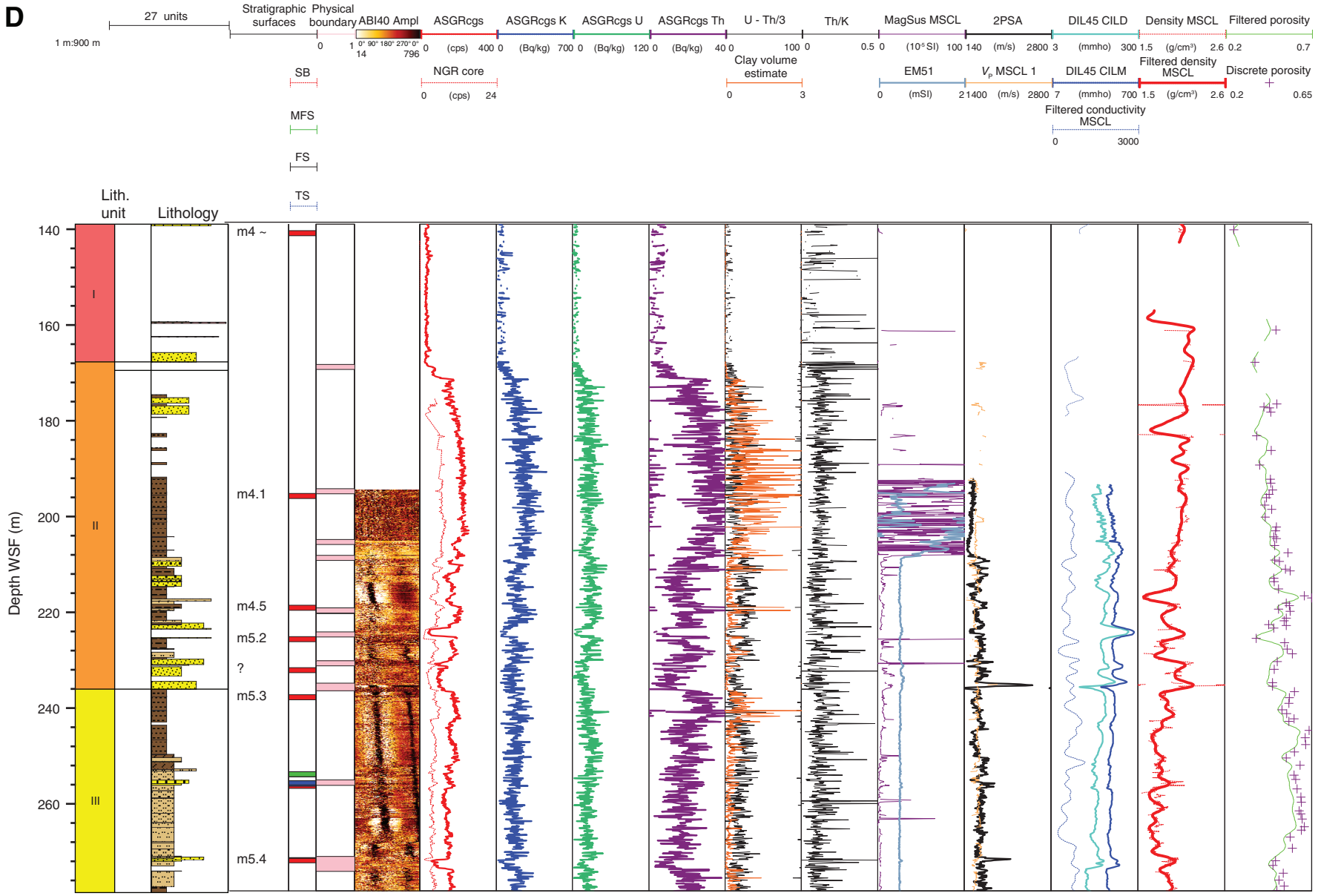

Figure F62 (continued). E. 0–128 m WSF.

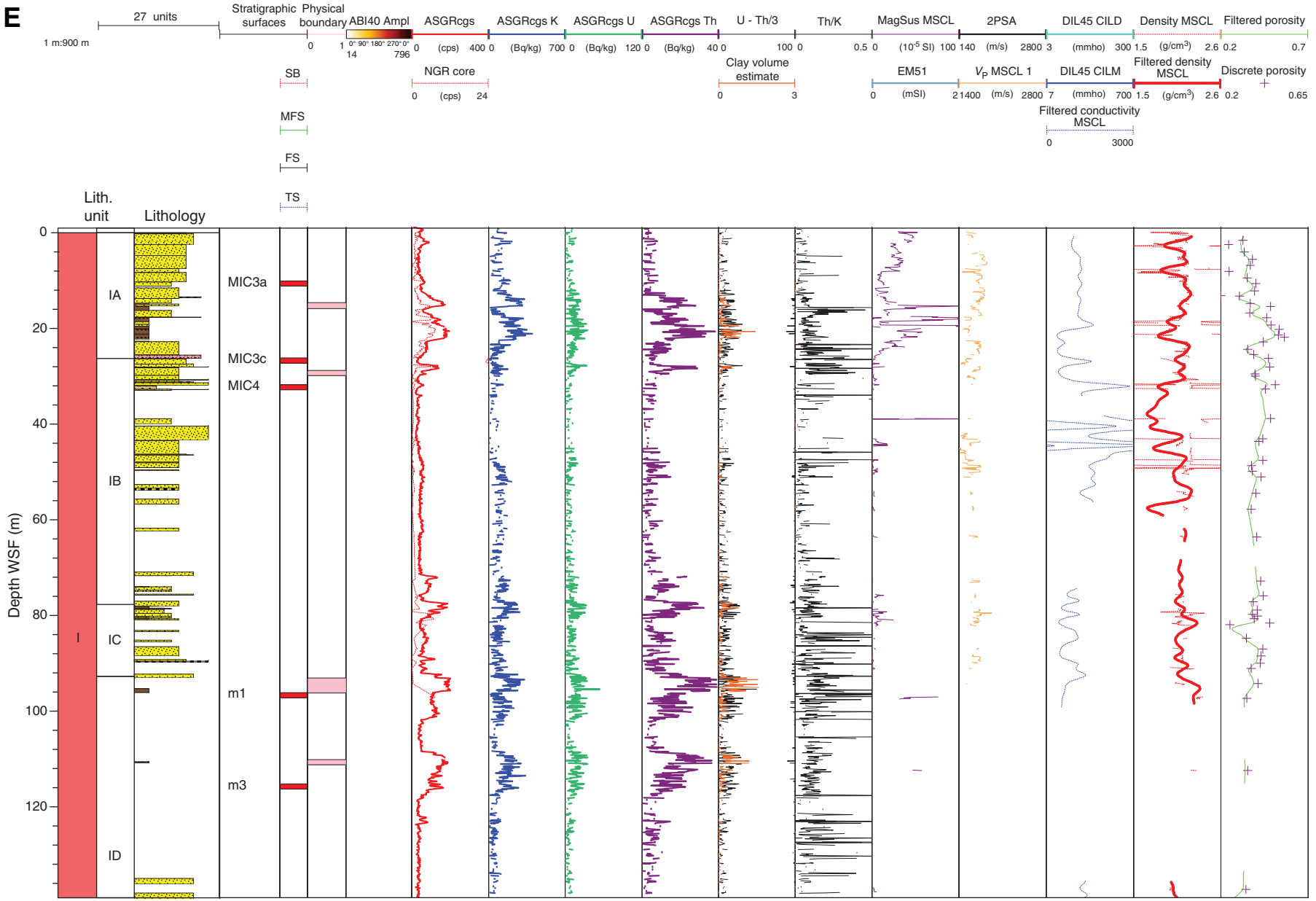

Figure F63. Interpretation of seismic surfaces on dip line Oc270 profile 529, Hole M0027A. Note phase shift in seismic between Oc270 and CH0698 data (Fig. F64). CDP = common depth point.

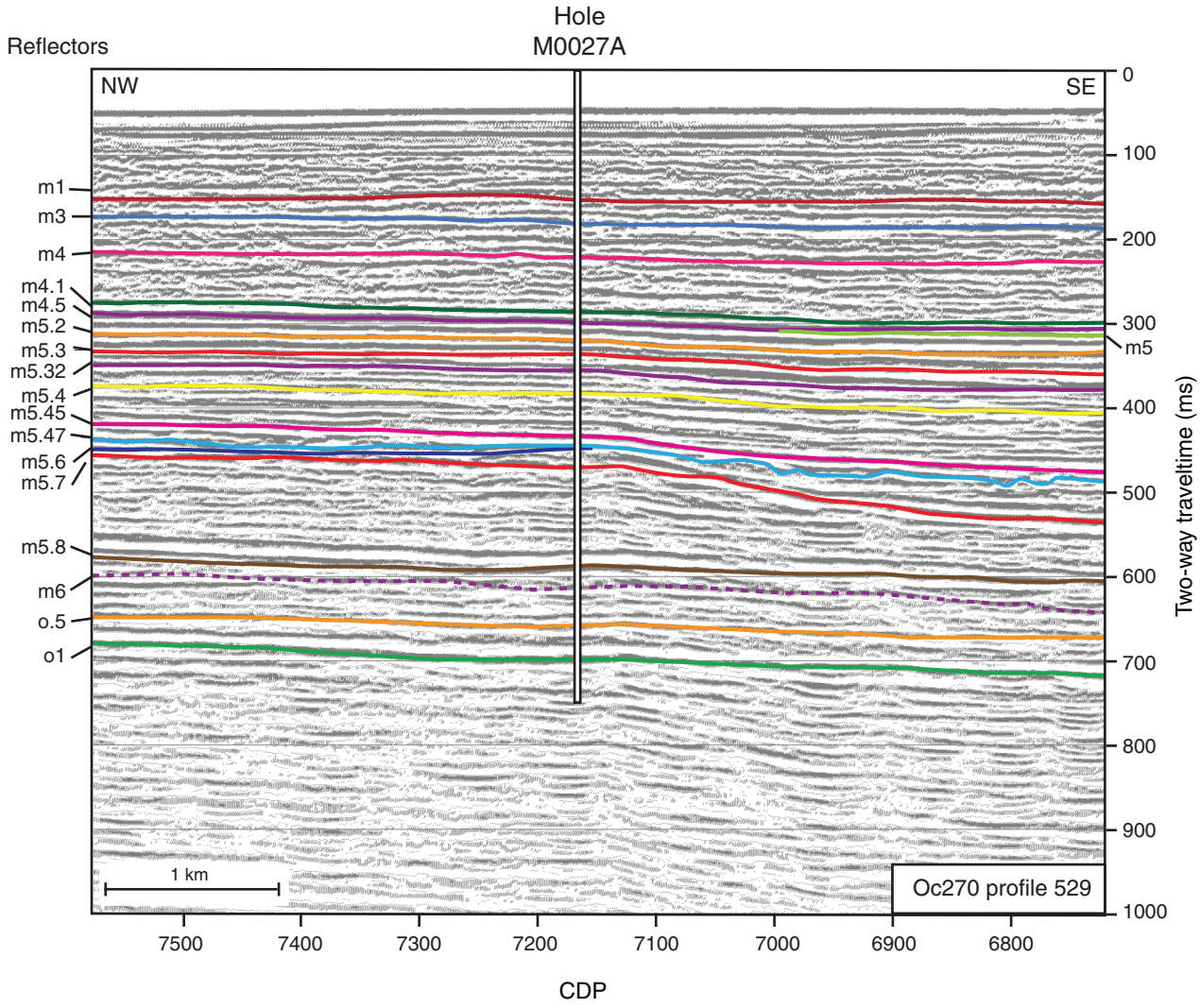

Figure F64. Interpretation of seismic surfaces on strike line CH0698 profile 102, Hole M0027A. Note phase shift in seismic between Oc270 (Fig. F63) and CH0698 data. CDP = common depth point.

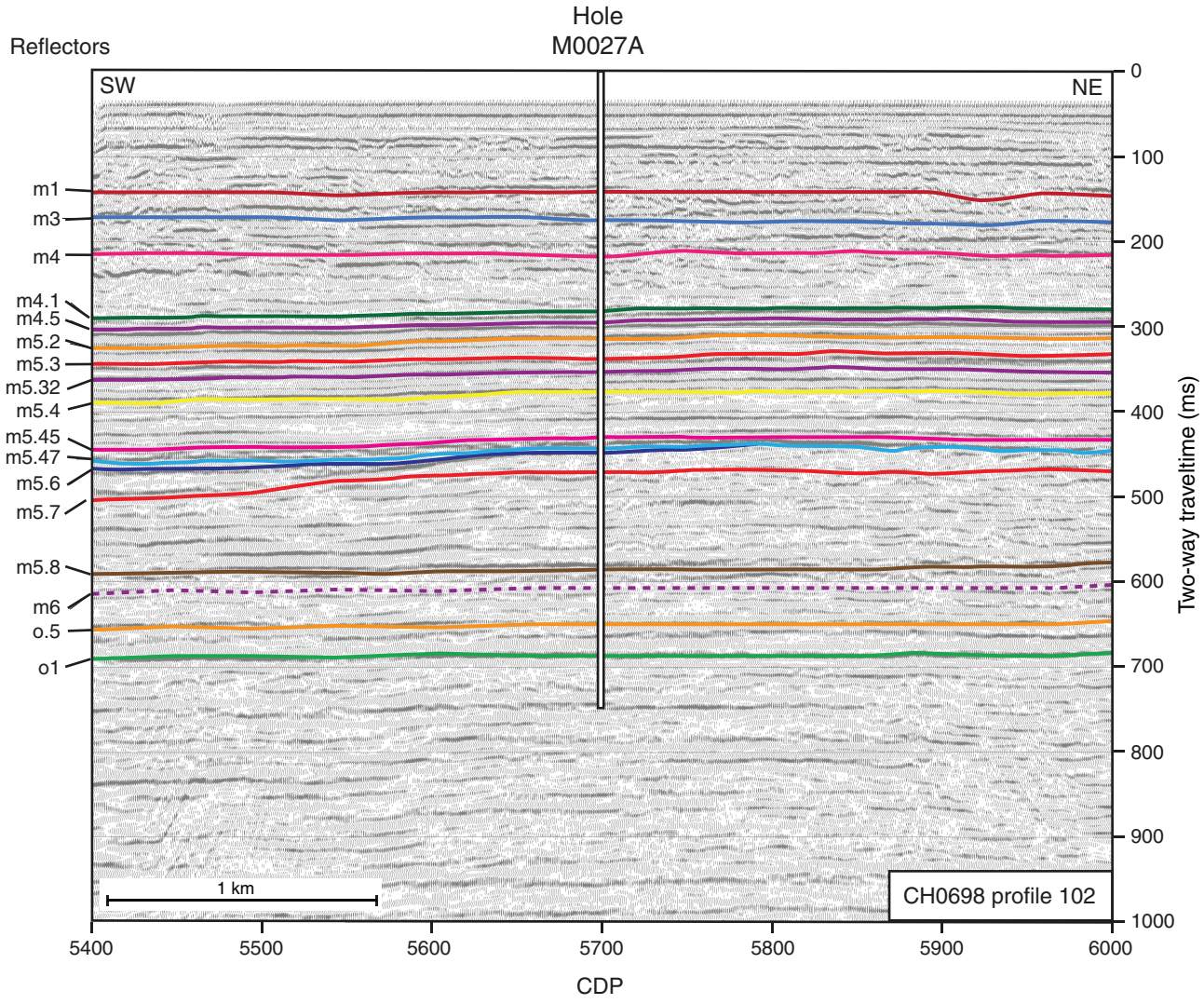

Figure F65. Summary of lithology, lithostratigraphy, well (total gamma ray [TGR], K, U, and Th) and multisensor core logger (MSCL) data (natural gamma radiation [NGR]) and sonic impedance and impedance from V_P MSCL data; depositional environments and correlating core surfaces; and predicted depth ranges based on Hole M0027A velocity between the seafloor and 100 mbsf. SF = shoreface, SOT = shoreface–offshore transition, OFF = offshore. OSP = Onshore Science Party. See Figure F1 for lithology legend.

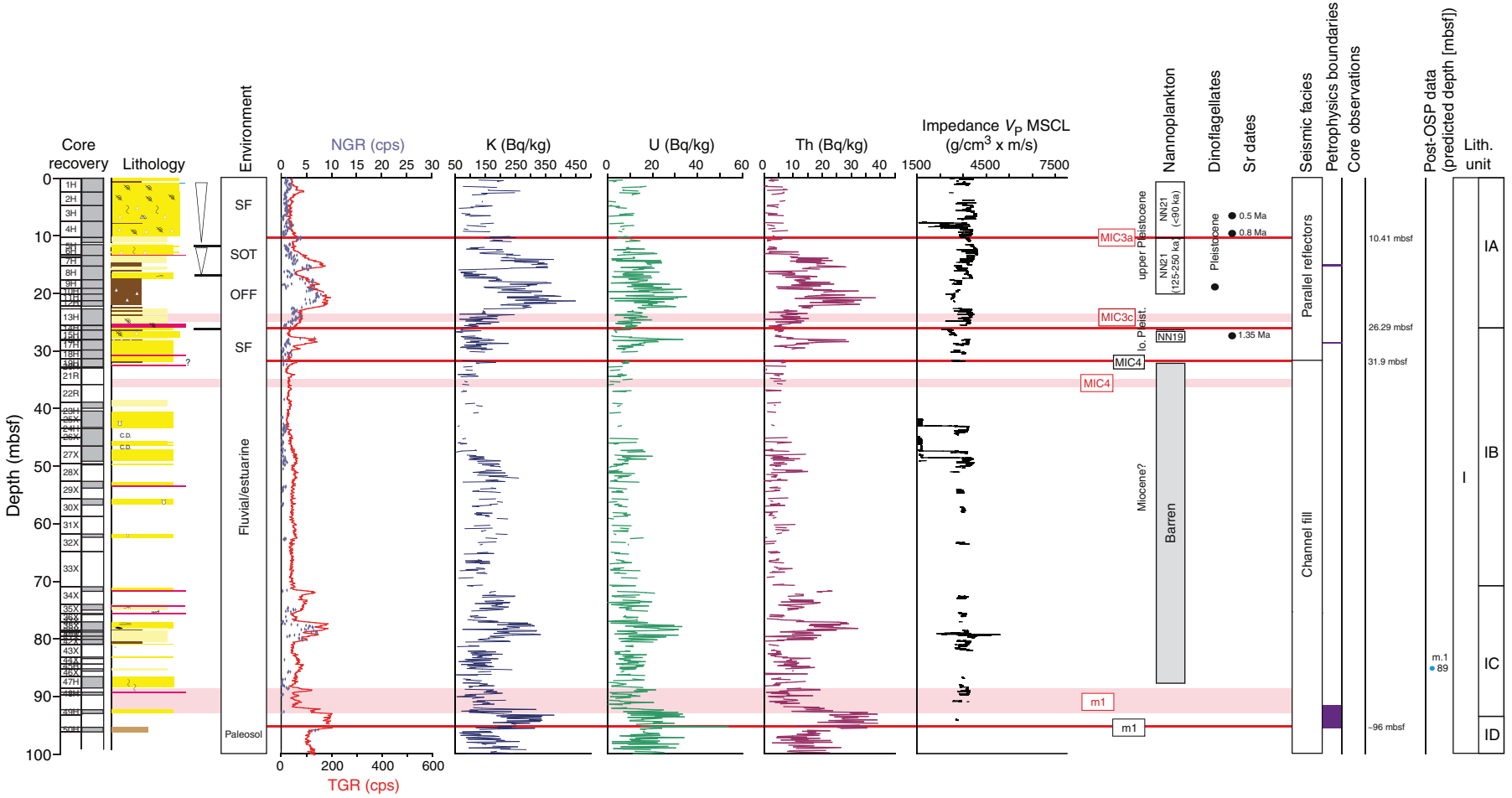

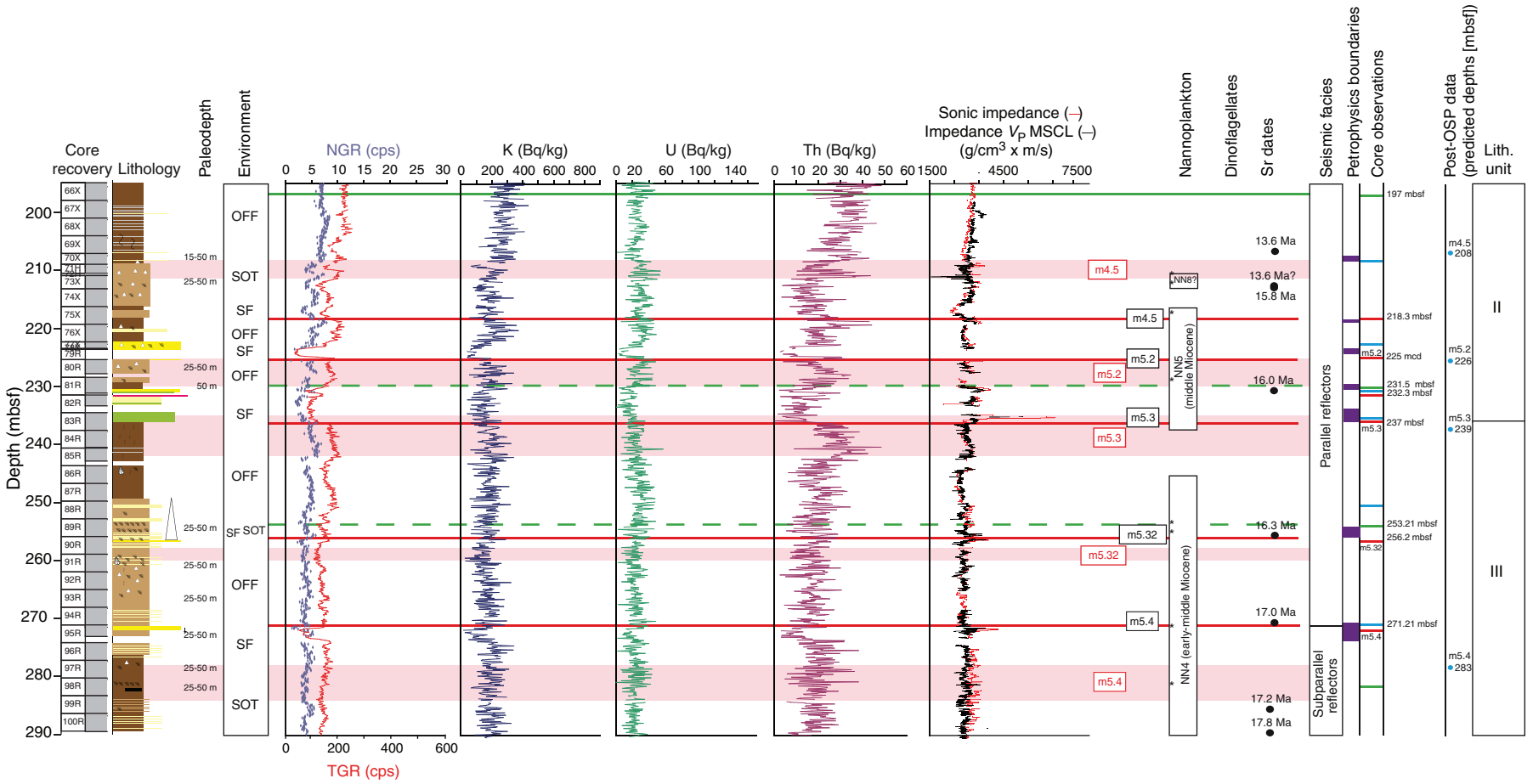

Figure F66. Summary of lithology, lithostratigraphy, well (total gamma ray [TGR], K, U, and Th) and multisensor core logger (MSCL) data (natural gamma radiation [NGR]) and sonic impedance and impedance from V_P MSCL data; depositional environments and correlating core surfaces; and predicted depth ranges based on Hole M0027A velocity between 200 and 290 mbsf. OFF = offshore, SOT = shoreface–offshore transition, SF = shoreface. OSP = Onshore Science Party. See Figure F1 for lithology legend.

Figure F67. Summary of lithology, lithostratigraphy, well (total gamma ray [TGR], K, U, and Th) and multisensor core logger (MSCL) data (natural gamma radiation [NGR]) and sonic impedance and impedance from V_P MSCL data; depositional environments and correlating core surfaces; and predicted depth ranges based on Hole M0027A velocity between 290 and 380 mbsf. SOT = shoreface–offshore transition, OFF = offshore, SF = shoreface. OSP = Onshore Science Party. See Figure F1 for lithology legend.

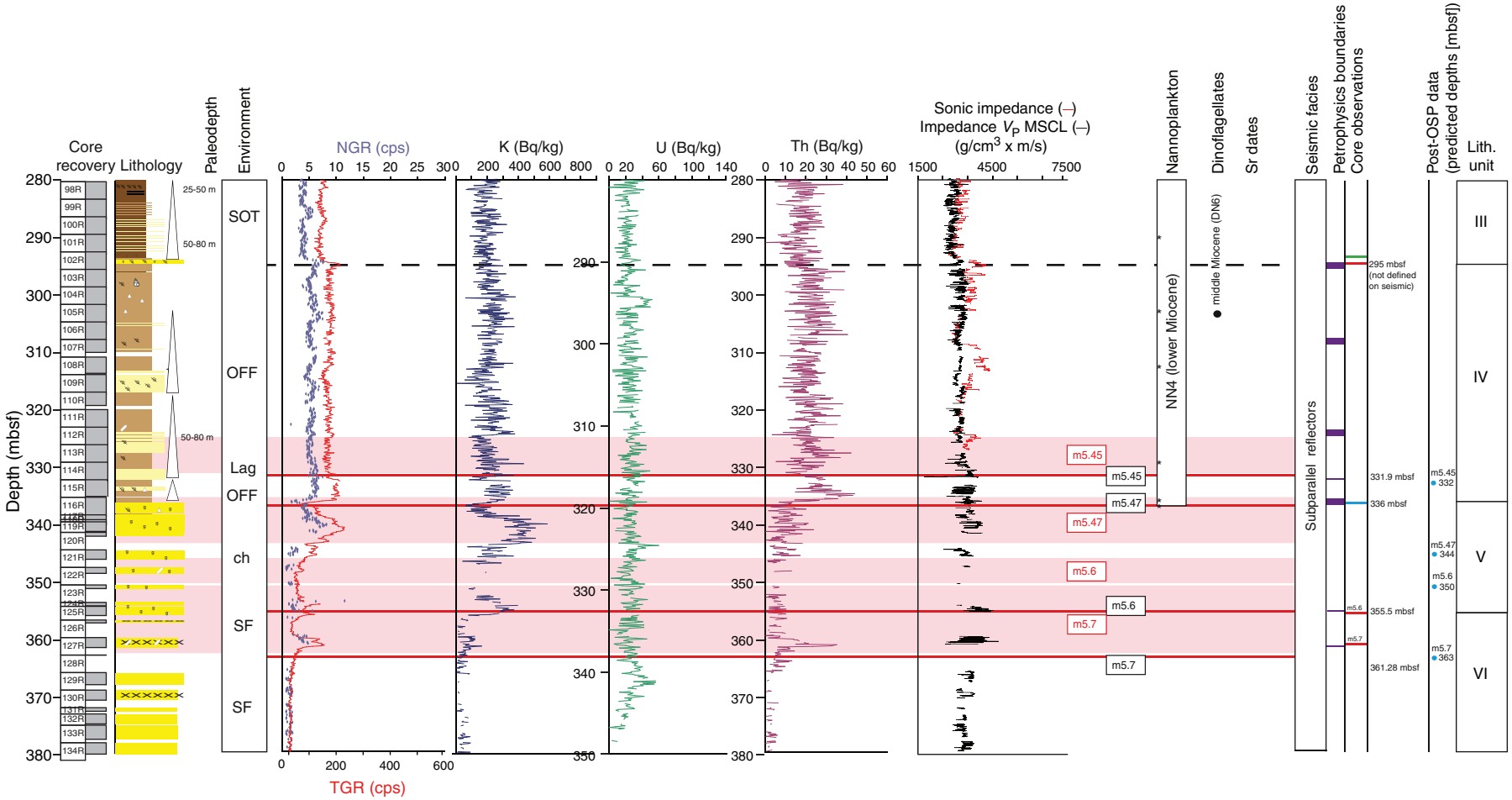

Figure F68. Summary of lithology, lithostratigraphy, well (total gamma ray [TGR], K, U, and Th), and multisensor core logger (MSCL) data (natural gamma radiation [NGR]) and sonic impedance and impedance from V_P MSCL data; depositional environments and correlating core surfaces; and predicted depth ranges based on Hole M0027A velocity between 380 and 490 mbsf. SF = shoreface, SOT = shoreface–offshore transition, OFF = offshore. OSP = Onshore Science Party. See Figure F1 for lithology legend.

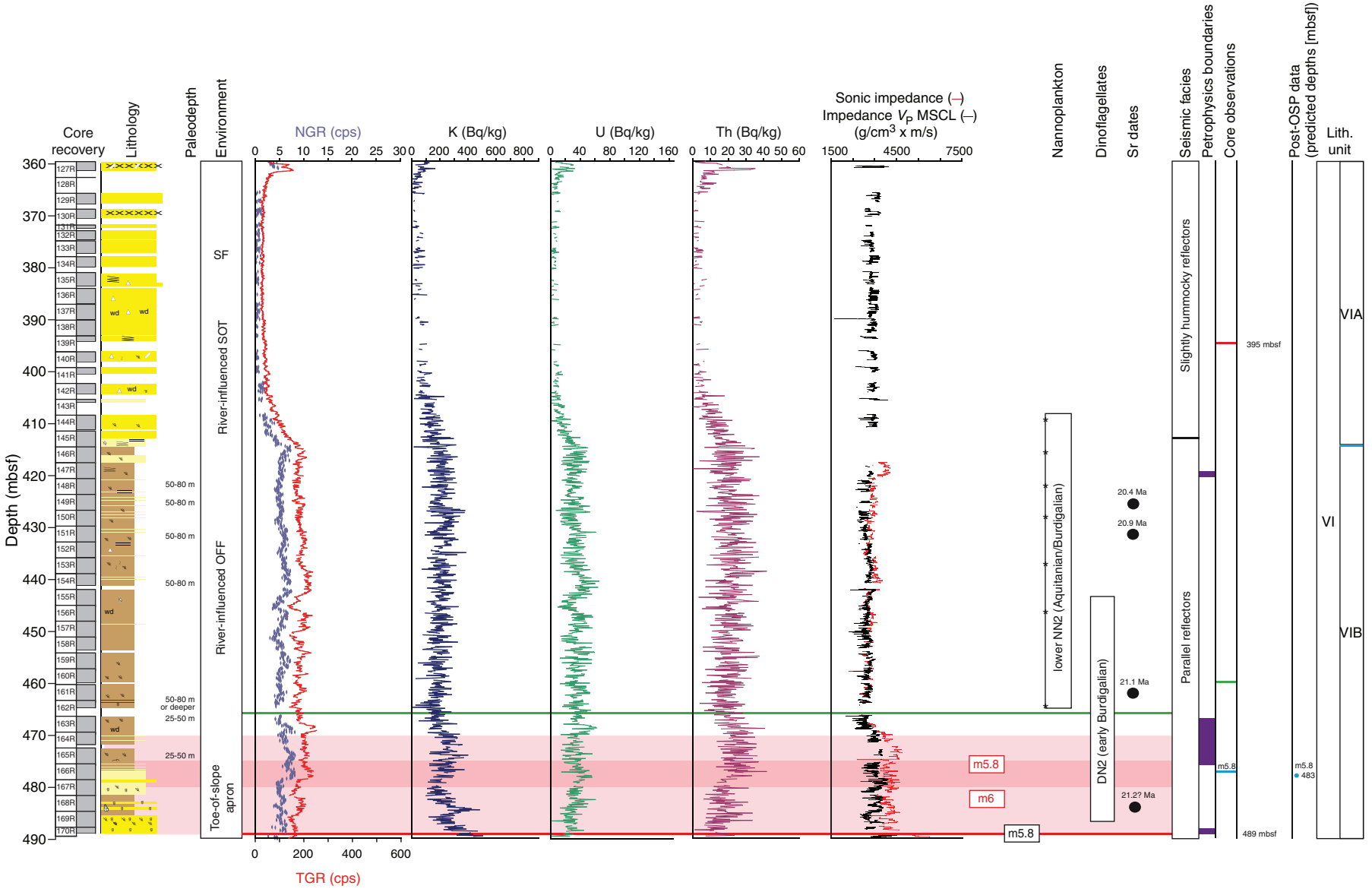

Figure F69. Summary of lithology, lithostratigraphy, well (total gamma ray [TGR], K, U, and Th), and multisensor core logger (MSCL) data (natural gamma radiation [NGR]) and sonic impedance and impedance from V_P MSCL data; depositional environments and correlating core surfaces; and predicted depth ranges based on Hole M0027A velocity between 490 and 600 mbsf. OSP = Onshore Science Party. See Figure **F1** for lithology legend.

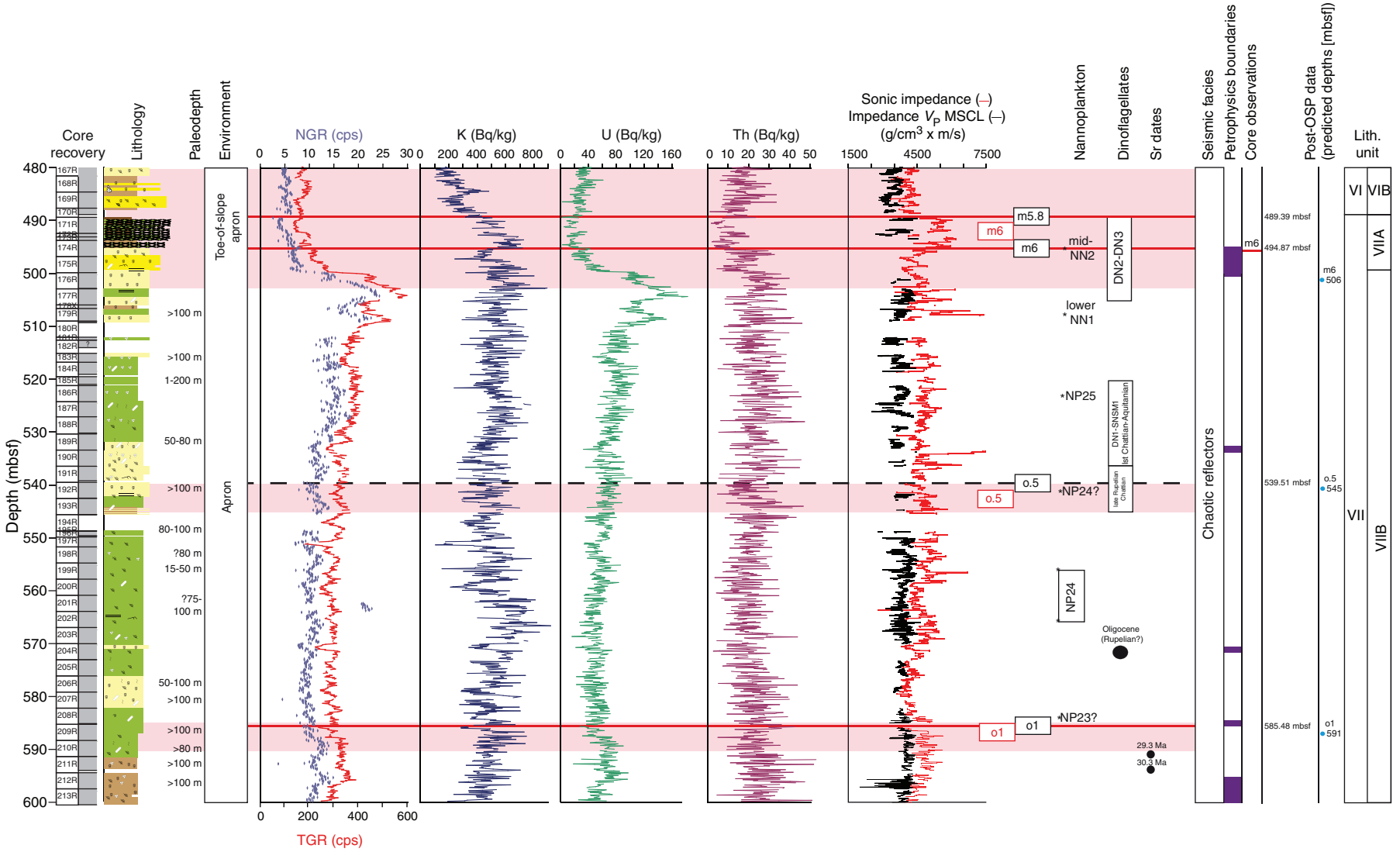

Figure F70. Correlation of core image with interpretation of deposition and age, 10.0–10.9 mbsf, Hole M0027A. USF = upper shoreface, MIC = marine isotope chron, dUSF = distal upper shoreface.

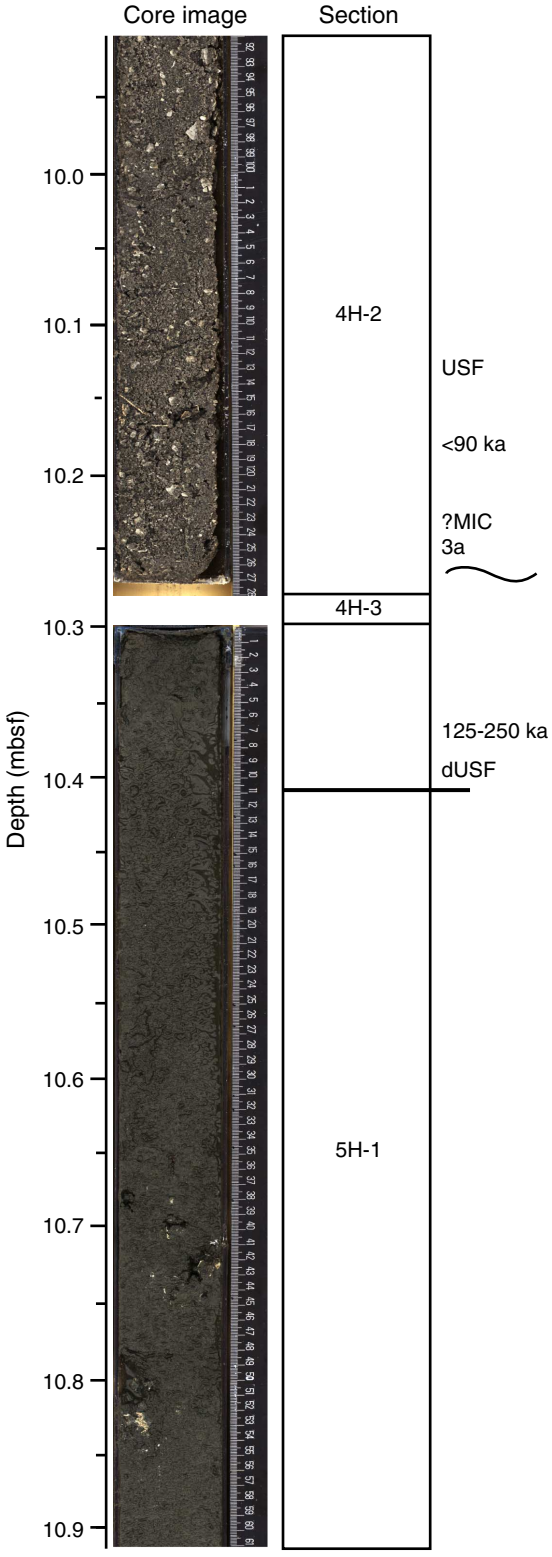

Figure F71. Correlation of core image with interpretation of deposition and age, 25.9–26.8 mbsf, Hole M0027A. MIC = marine isotope chron.

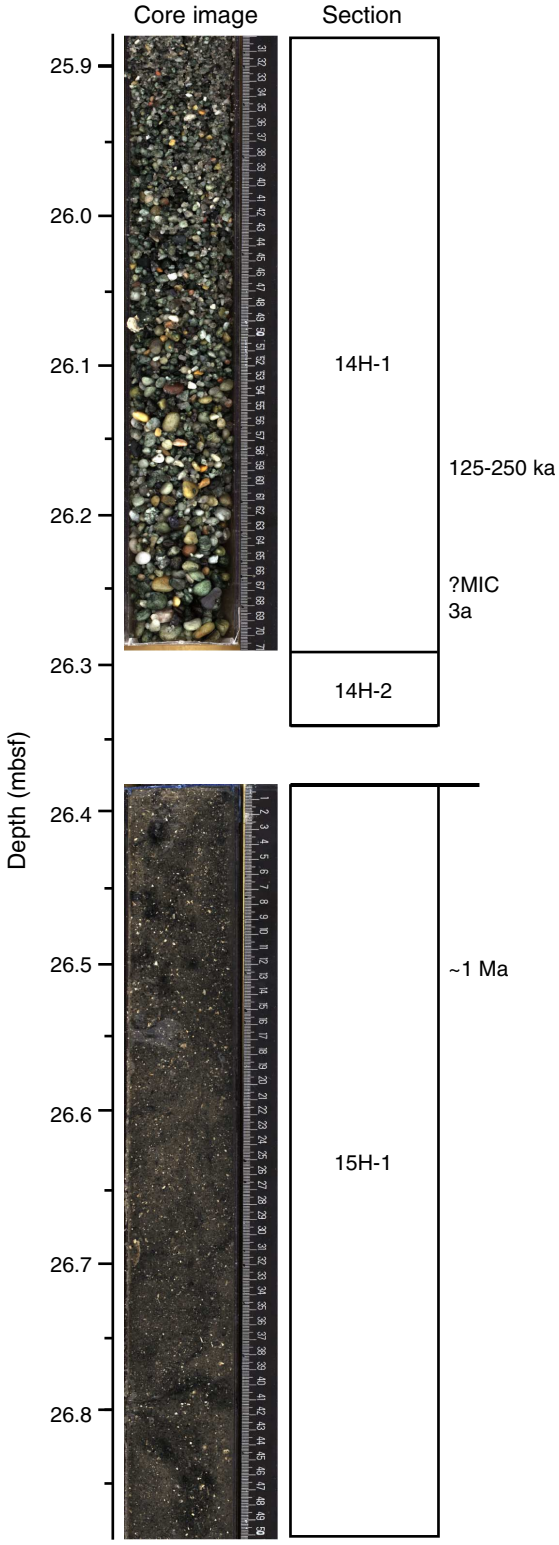

Figure F72. Correlation of core image with interpretation of deposition and age, 95.3–96.1 mbsf, Hole M0027A.

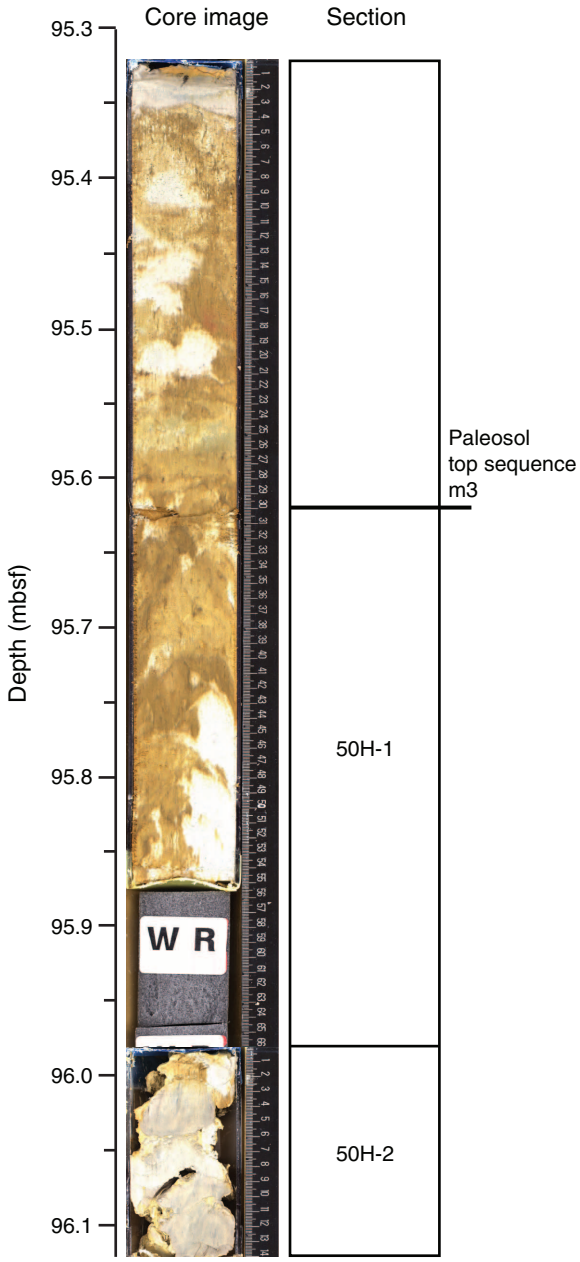

Figure F73. Summary of lithology, lithostratigraphy, well (total gamma ray [TGR], K, U, and Th), and multisensor core logger (MSCL) data (natural gamma radiation [NGR]) and sonic impedance and impedance from V_P MSCL data; depositional environments and correlating core surfaces; and predicted depth ranges based on Hole M0027A velocity between 100 and 200 mbsf. SF = shoreface, SOT = shoreface–offshore transition, OFF = offshore. OSP = Onshore Science Party. See Figure F1 for lithology legend.

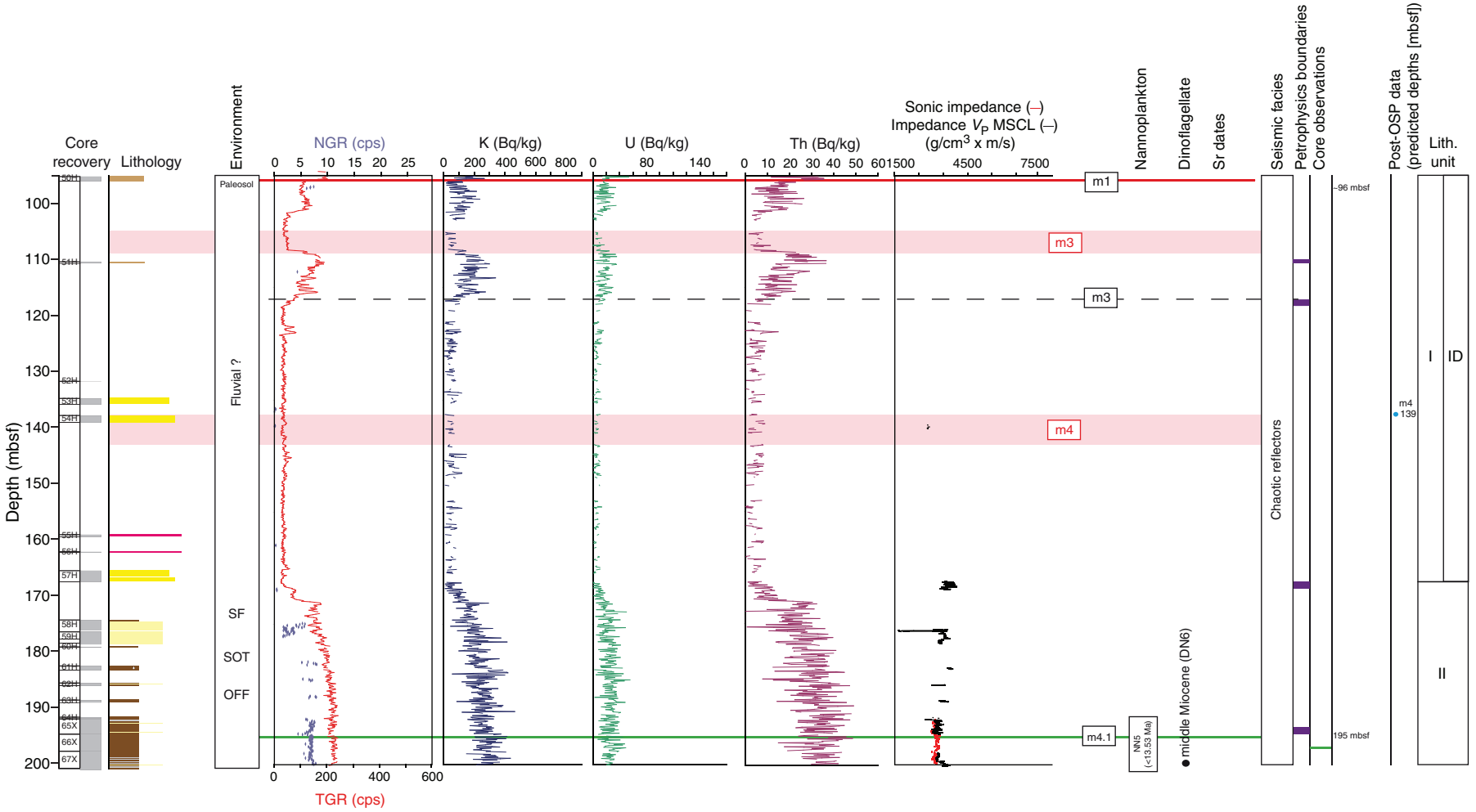

Figure F74. Correlation of core image with interpretation of deposition and age, density, *P*-wave velocity, and resistivity, 217.9–218.8 mbsf, Hole M0027A.

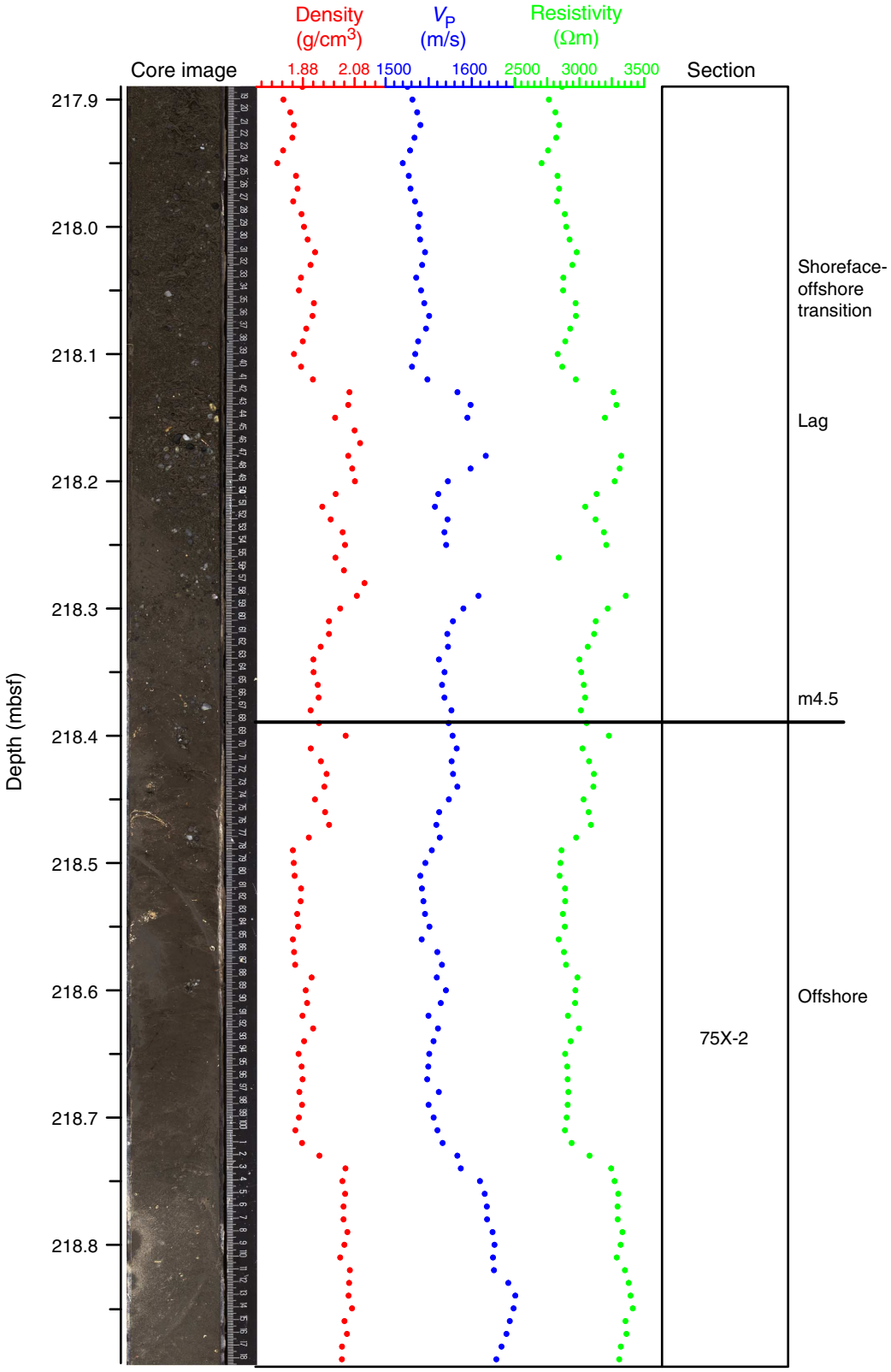

Figure F75. Correlation of core image with interpretation of deposition and age along with density, 235.7–236.6 mbsf, Hole M0027A.

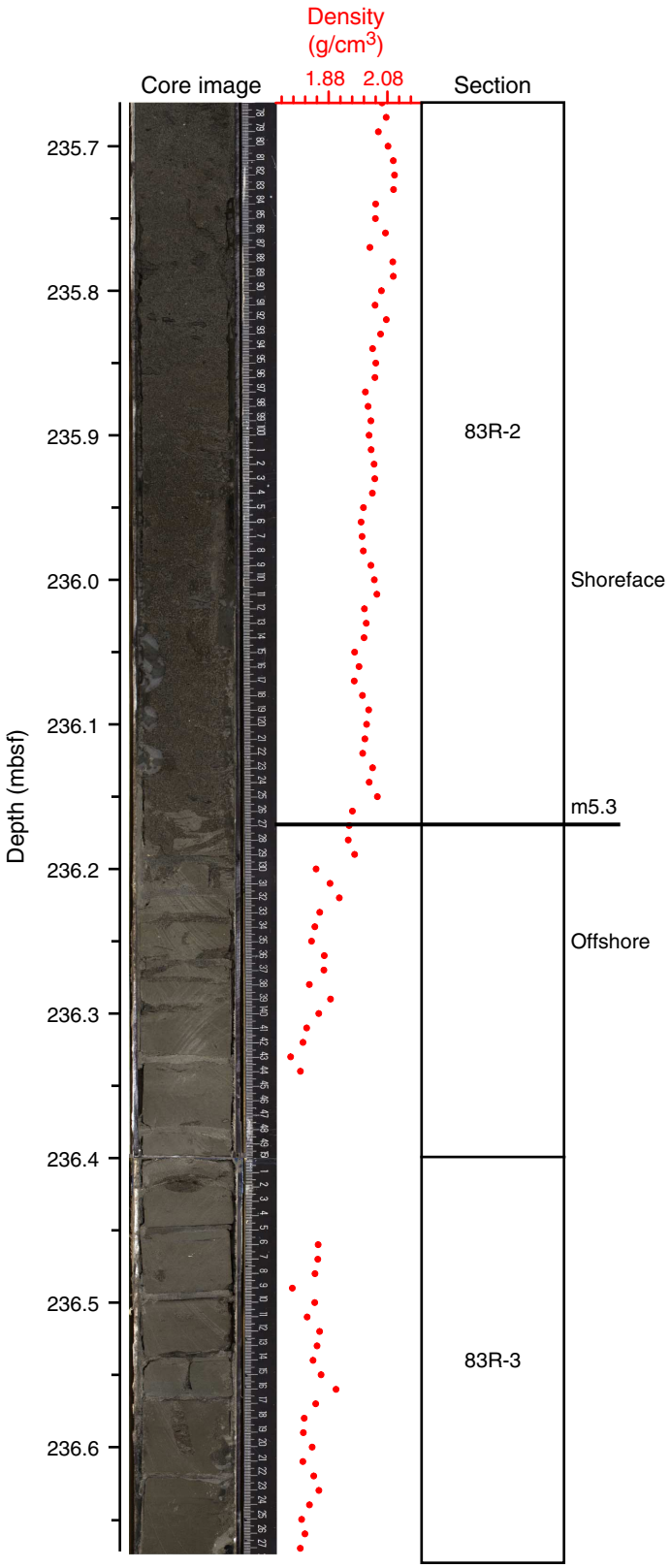

Figure F76. Correlation of core image with interpretation of deposition and age along with density, 255.7–256.6 mbsf, Hole M0027A.

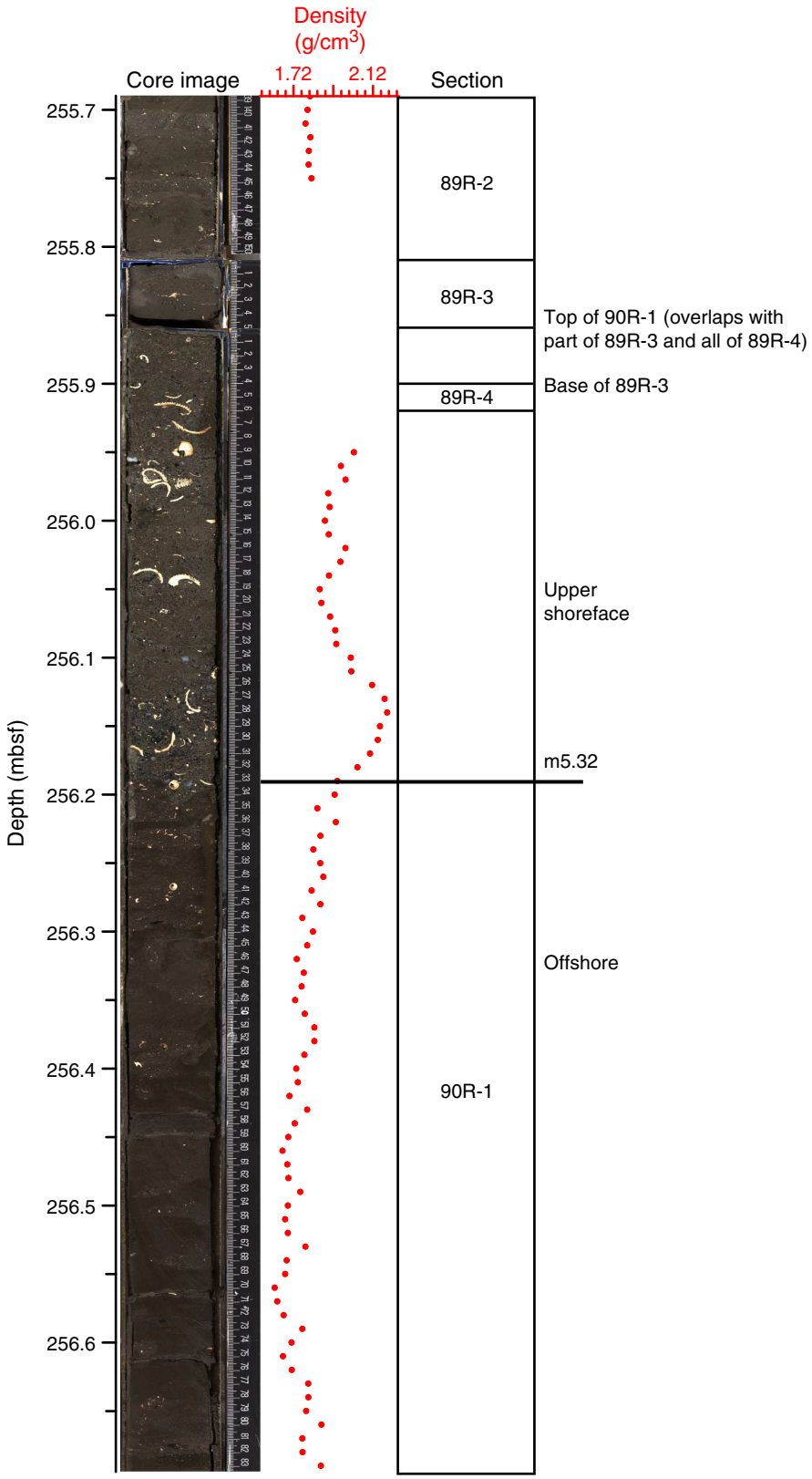

Figure F77. Correlation of core image with interpretation of deposition and age, 270.8–271.7 mbsf, Hole M0027A.

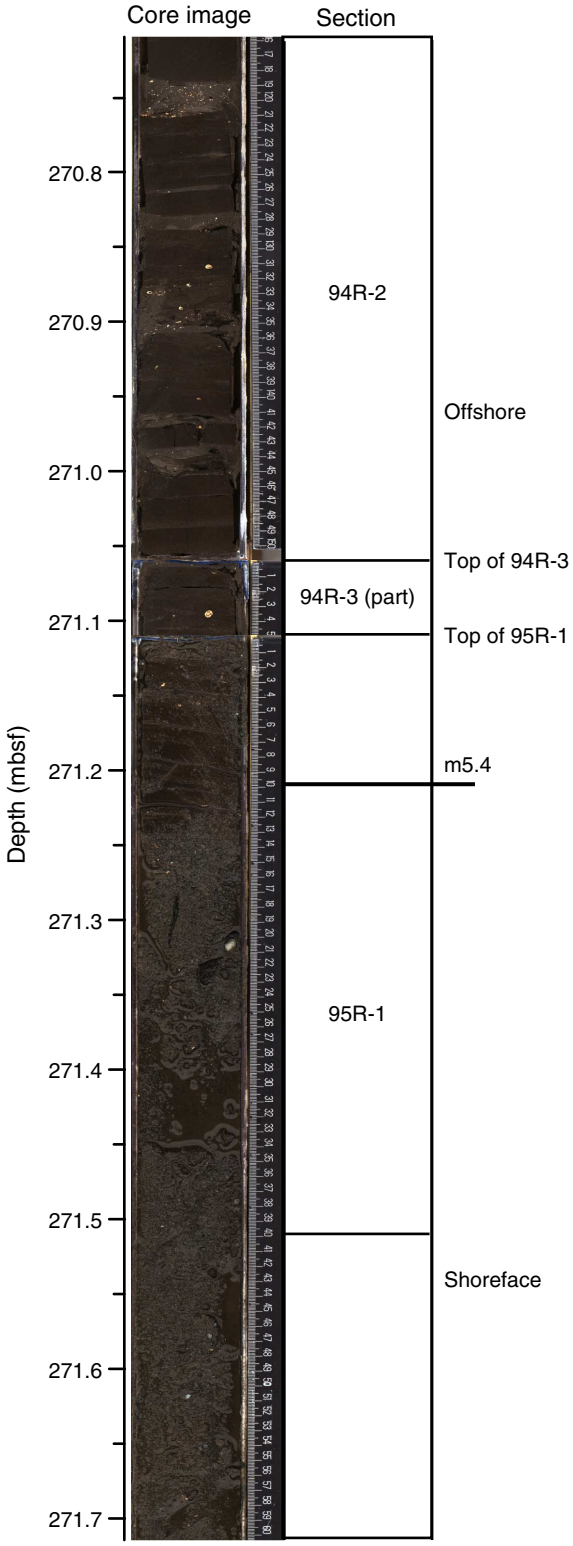

Figure F78. Correlation of core image with interpretation of deposition and age, 294.6–295.5 mbsf, Hole M0027A.

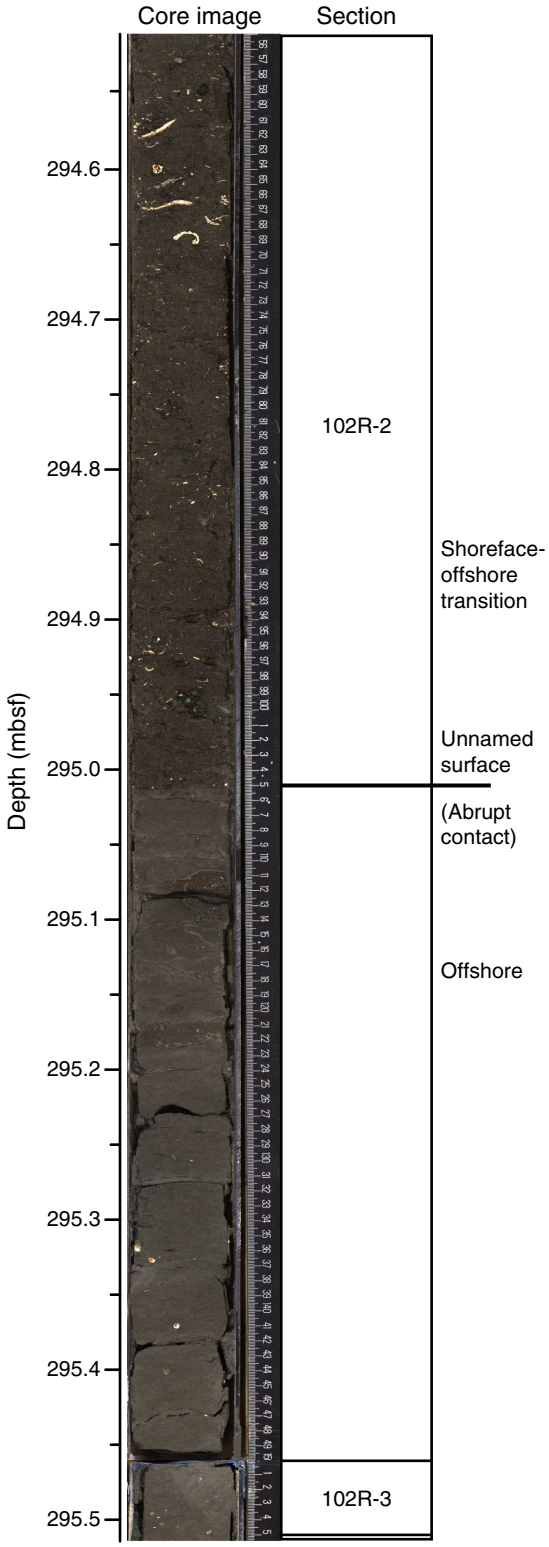

Figure F79. Correlation of core image with interpretation of deposition and age, 331.5–332.4 mbsf, Hole M0027A.

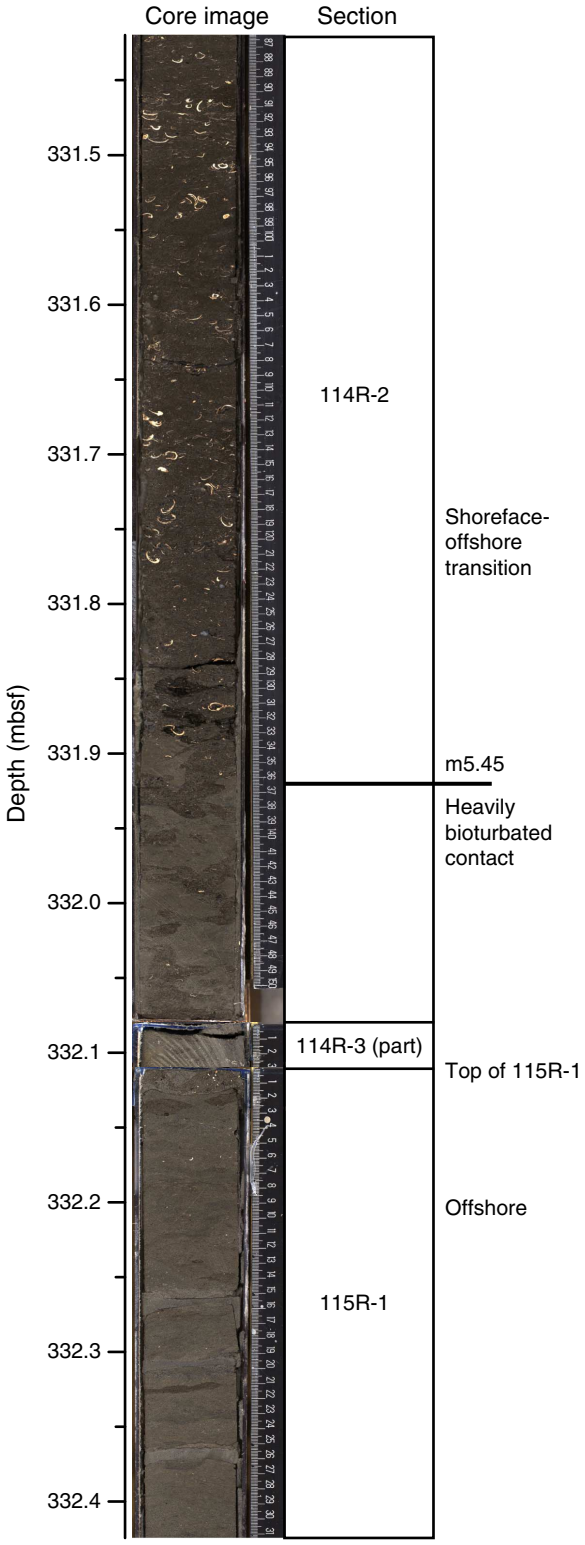

Figure F80. Correlation of core image with interpretation of deposition and age, 355.1–355.7 mbsf, Hole M0027A.

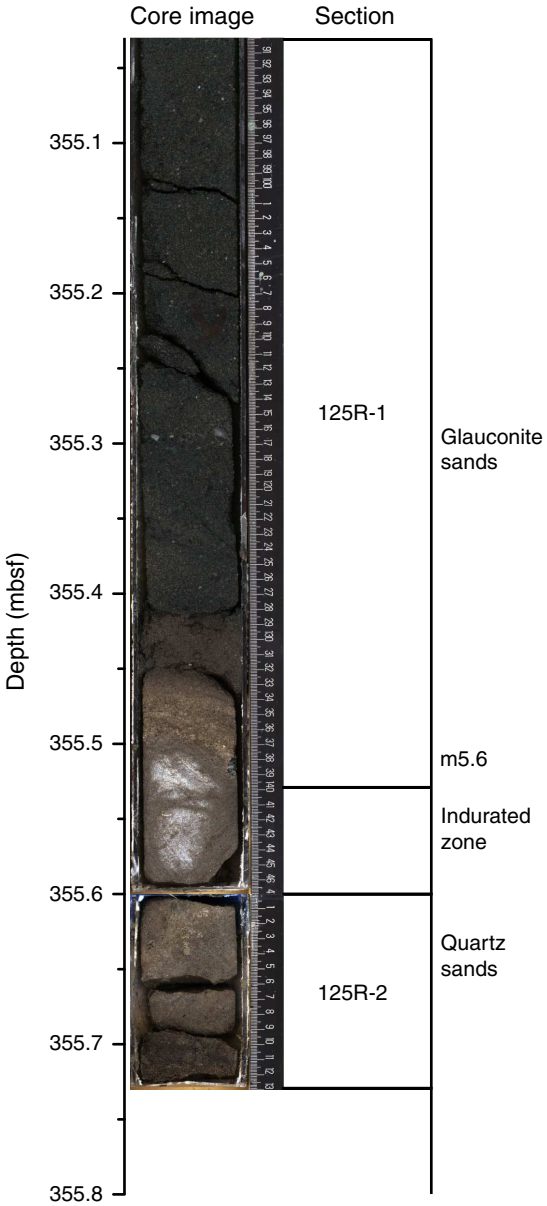

Figure F81. Correlation of core image with interpretation of deposition and age along with density, 585.0–585.9 mbsf, Hole M0027A.

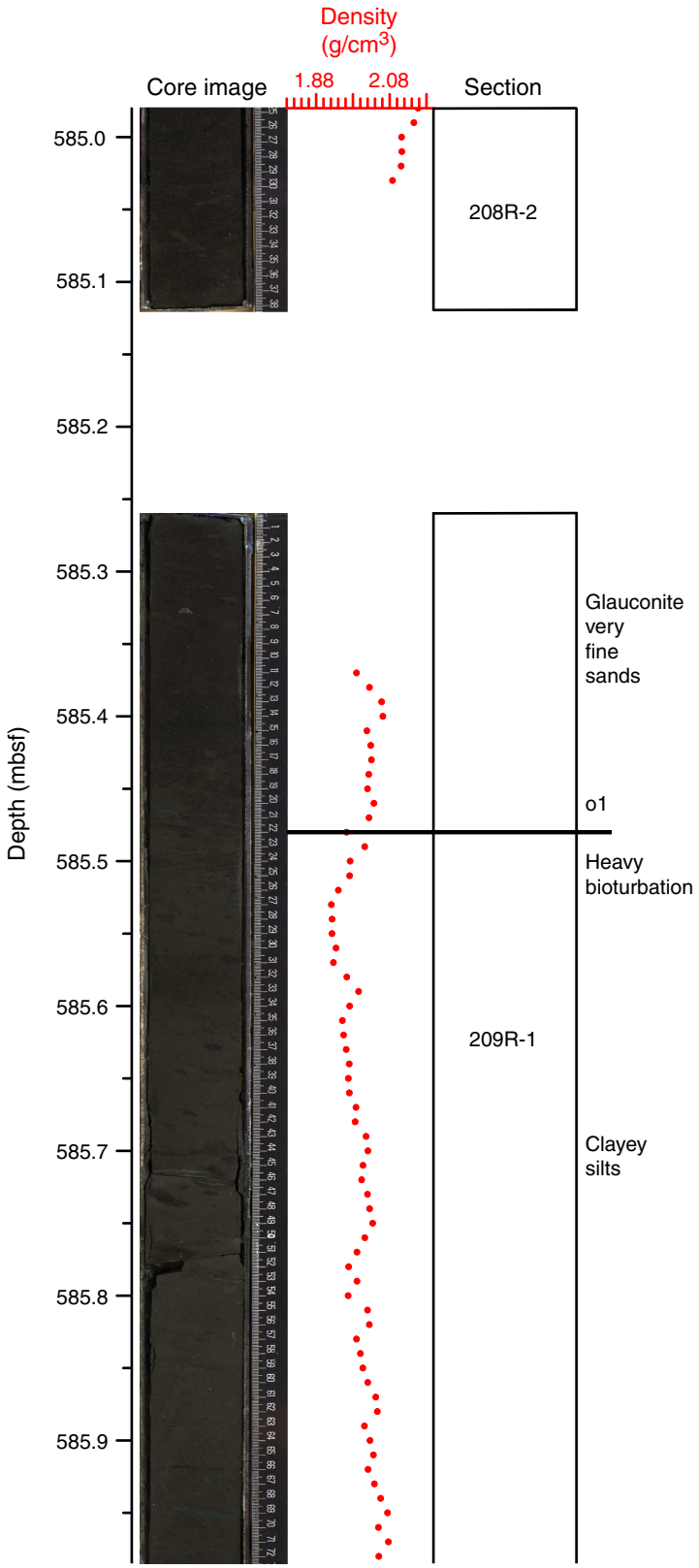

Figure F82. Summary of lithology, lithostratigraphy, well (total gamma ray [TGR], K, U, and Th), and multisensor core logger (MSCL) data (natural gamma radiation [NGR]) and sonic impedance and impedance from V_P MSCL data; depositional environments and correlating core surfaces; and predicted depth ranges based on Hole M0027A velocity between 600 and 631 mbsf. dOFF = distal offshore. EOT = Eocene–Oligocene transition. OSP = Onshore Science Party. See Figure **F1** for lithology legend.

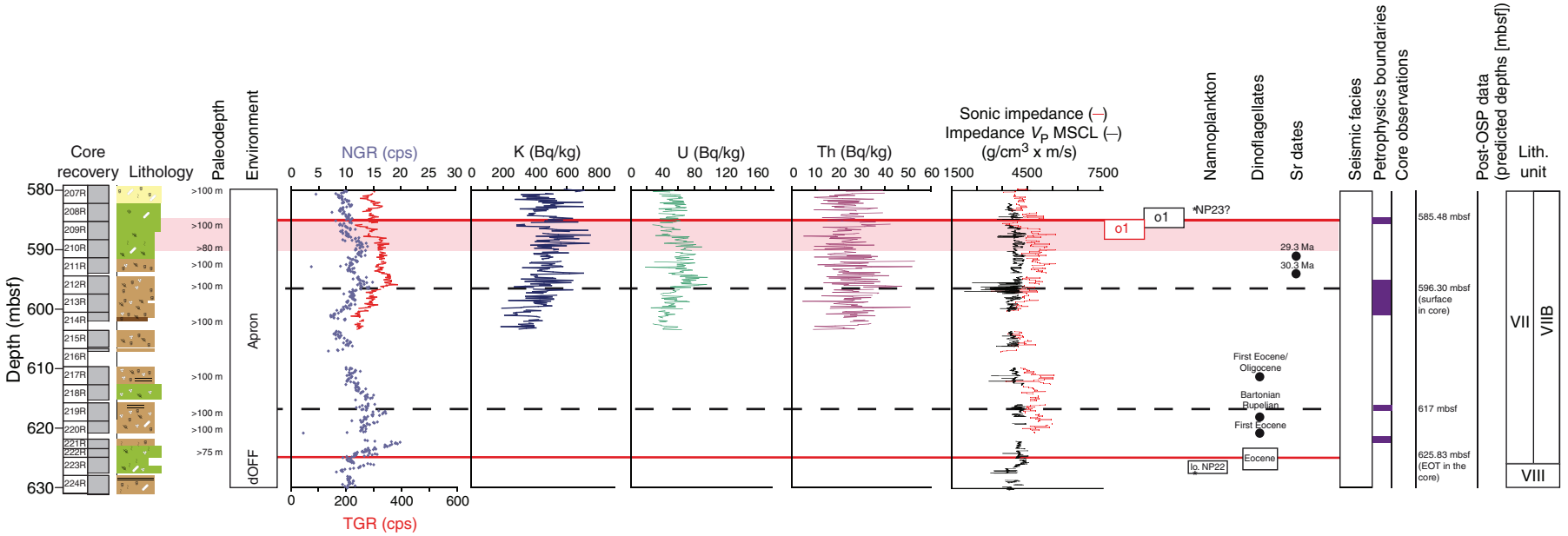

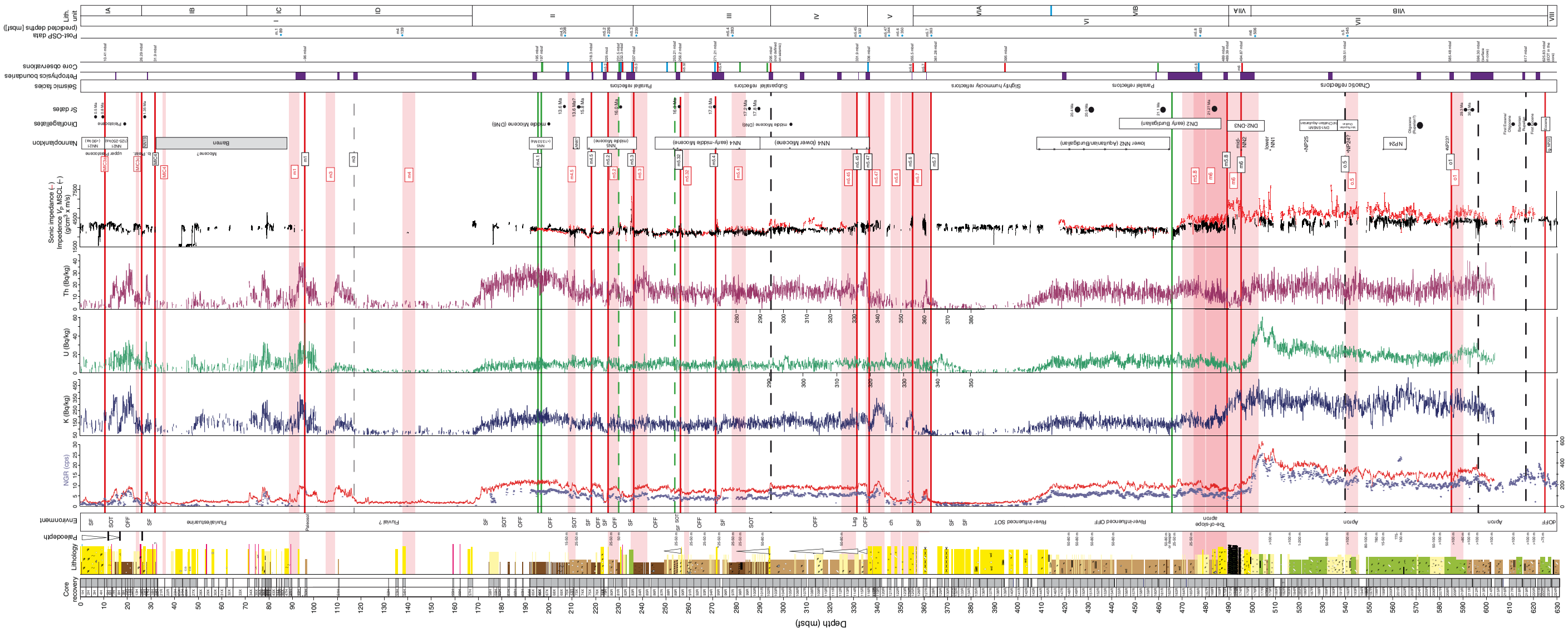

Figure F83. Synthesis of Hole M0027A, including lithology, lithostratigraphy, well (total gamma ray [TGR], K, U, and Th), and multisensor core logger (MSCL) data (natural gamma radiation [NGR]) and sonic impedance from V_P MSCL data; depositional environments and correlating core surfaces; and predicted depth ranges based on velocity. SF = shoreface, SOT = shoreface–offshore transition, OFF = offshore, dOFF = distal offshore. EOT = Eocene–Oligocene transition. OSP = Onshore Science Party. See Figure F1 for lithology legend.

Figure F84. Correlation of core image with interpretation of deposition and age along with density, 335.6–336.5 mbsf, Hole M0027A.

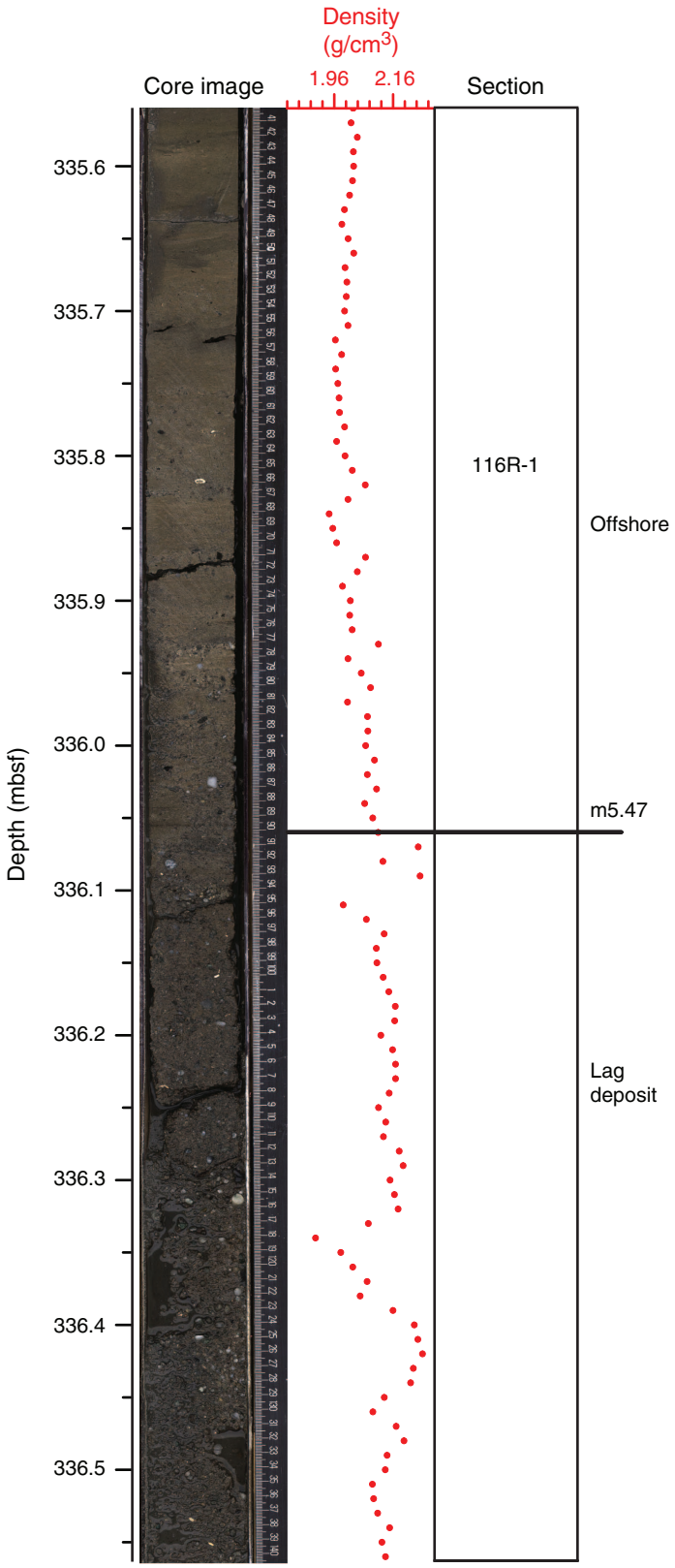

Figure F85. Age-depth plot showing cores (every fifth core shaded) in Hole M0027A, the timescale of Berggren et al. (1995), calcareous nannoplankton zones (light blue bars), planktonic foraminifer zones (dark blue bars), and dinocyst zones (green bars). Sr isotopic ages are shown as circles with errors of ±0.6 m.y. (15.2–34.4 Ma) and ±1.17 m.y. (younger than 15.2 Ma). Horizontal lines for sequence boundaries (red) and tentative sequence boundaries (dashed red) lines are labeled with their corresponding depths. Horizontal green lines = flooding surfaces. MFS = maximum flooding surface. TD = total depth. Planktonic foraminifer E and O zones are from Berggren and Pearson (2005); planktonic foraminifer M, PL, and Pt zones are from Berggren et al. (1995); nannofossil zones are from Martini (1971); and dinocyst zones are from de Verteuil and Norris (1996). Geomagnetic polarity timescale is from Cande and Kent (1995). See Figure F34 for additional information.

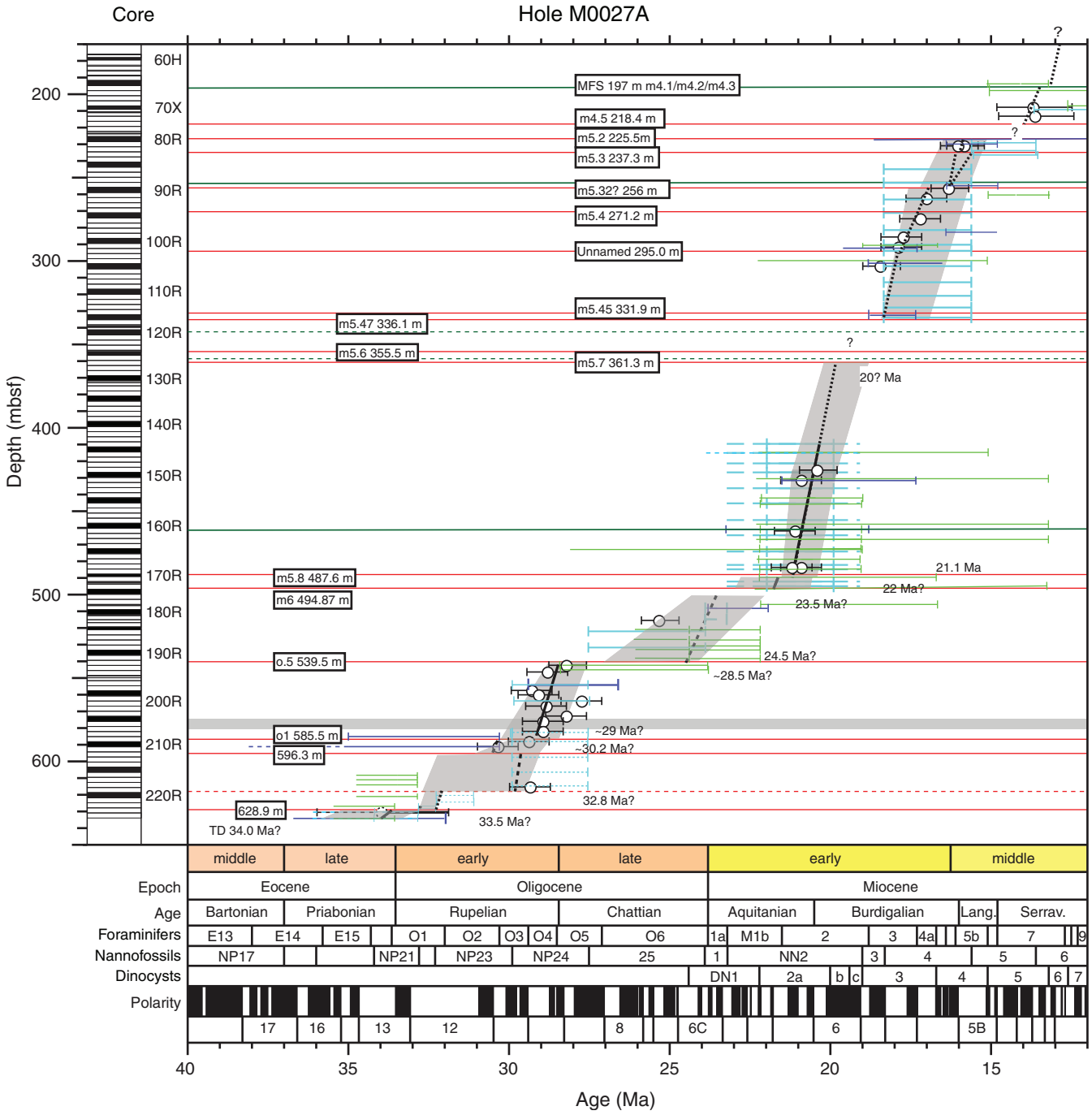

Table T1. Coring summary, Hole M0027A. (See table notes.) (Continued on next three pages.)

Hole M0027A
Latitude: 39°38.046067′N
Longitude: 73°37.301460′W
Seafloor (drill pipe measurement from rig floor, mbrf): 50.55
Distance between rig floor and sea level (m): 17.02
Water depth (drill pipe measurement from sea level, m): 33.53
Total penetration (mbsf): 631.01
Total drilled interval (m): 547.01

Core	Date (May 2009)	Time (UTC)	Depth (mbsf) Top	Depth (mbsf) Bottom	Length (m) Cored	Length (m) Recovered	Recovery (%)	Comments
313-M0027A-								
1H	2	0010	0.00	2.42	2.42	2.42	100.0	
2H	2	0120	2.42	4.76	2.34	2.34	100.0	
3H	2	0230	4.76	7.49	2.73	2.73	100.0	
4H	2	0350	7.49	10.30	2.81	2.81	100.0	
5H	2	0500	10.30	13.26	2.96	0.86	29.1	
6H	2	0735	11.54	13.74	2.20	2.23	101.4	
7H	2	0915	13.41	15.26	1.85	1.85	100.0	
8H	2	1030	15.26	17.64	2.38	2.38	100.0	
9H	2	1230	17.64	19.13	1.49	1.95	130.9	
10H	2	1400	19.13	20.11	0.98	0.98	100.0	
11H	2	1505	20.11	21.27	1.16	1.16	100.0	
12H	2	1620	21.27	22.25	0.98	0.95	96.9	Liner split sample
13H	2	1815	22.68	25.58	2.90	2.85	98.3	
14H	2	1950	25.58	26.38	0.80	0.76	95.0	Gravel in shoes—shoe distorted, casing run to new depth of 17.6 mbsf
15H	3	0350	26.38	27.98	1.60	1.66	103.8	
16H	3	0505	27.98	28.08	0.10	0.10	100.0	
17H	3	0610	28.08	29.93	1.85	1.75	94.6	
18H	3	0944	29.83	31.35	1.52	1.52	100.0	
19H	3	1415	31.35	32.96	1.61	1.61	100.0	Hole caving, bit damaged
20H	3	2245	32.77	32.78	0.01	0.01	100.0	
21R	4	0100	32.77	35.82	3.05	0.00	0.0	
22R	4	0325	35.82	38.87	3.05	0.00	0.0	
23H	4	0415	38.87	41.92	3.05	1.06	34.8	
24H	4	0530	41.92	44.97	3.05	0.01	0.3	
25X	5	0445	40.42	43.47	3.05	2.85	93.4	
26X	5	0540	43.47	46.52	3.05	3.02	99.0	
27X	5	0630	46.52	49.57	3.05	2.61	85.6	
28X	5	0920	49.57	52.62	3.05	0.20	6.6	
29X	5	1020	52.62	55.67	3.05	1.18	38.7	
30X	5	1145	55.67	58.72	3.05	1.07	35.1	
31X	5	1310	58.72	61.77	3.05	0.00	0.0	
32X	5	1415	61.77	64.82	3.05	0.57	18.7	Fluorescent microspheres
33X	5	1600	64.82	70.92	6.10	0.02	0.3	Fluorescent microspheres
34X	5	1710	70.92	73.97	3.05	0.80	26.2	
35X	5	1755	73.97	75.55	1.58	1.00	63.3	Fluorescent microspheres
36X	5	1900	75.55	77.02	1.47	0.22	15.0	
37X	5	1945	77.02	77.03	0.01	0.01	100.0	
38X	5	2020	77.02	78.47	1.45	1.62	111.7	
39X	5	2125	78.47	78.77	0.30	0.40	133.3	
40X	5	2220	78.77	79.51	0.74	0.82	110.8	
41X	5	2310	79.51	80.07	0.56	0.75	133.9	
42X	6	0135	80.07	80.90	0.83	0.83	100.0	Liner jammed in base of core catcher
43X	6	0530	80.90	83.12	2.22	0.00	0.0	
44X	6	1050	83.12	84.34	1.22	0.27	22.1	
45R	6	1200	84.34	85.17	0.83	0.00	0.0	
46X	6	1400	85.17	86.52	1.35	0.40	29.6	
47H	6	1510	86.52	88.49	1.97	1.97	100.0	
			*****Drilled from 88.49 to 89.22 mbsf*****					
48H	6	1750	89.22	89.72	0.50	0.50	100.0	
			*****Drilled from 89.72 to 92.27 mbsf*****					
49H	6	1940	92.27	93.20	0.93	0.66	71.0	
			*****Drilled from 93.2 to 95.32 mbsf*****					
50H	6	2110	95.32	96.12	0.80	0.80	100.0	Fluorescent microspheres
			*****Drilled from 96.12 to 110.57 mbsf*****					
51H	7	0040	110.57	110.83	0.26	0.26	100.0	Fluorescent microspheres
			*****Drilled from 110.83 to 131.92 mbsf*****					
52H	7	0515	131.92	131.92	0.00	0.00	0.0	Fluorescent microspheres
			*****Drilled from 131.92 to 134.97 mbsf*****					

Table T1 (continued). (Continued on next page.)

Core	Date (May 2009)	Time (UTC)	Depth (mbsf) Top	Depth (mbsf) Bottom	Length (m) Cored	Length (m) Recovered	Recovery (%)	Comments
53H	7	0620	134.97	136.07	1.10	1.10	100.0	Fluorescent microspheres
			*****Drilled from 136.07 to 138.02 mbsf*****					
54H	7	0800	138.02	139.24	1.22	1.22	100.0	Fluorescent microspheres
			*****Drilled from 139.24 to 159.32 mbsf*****					
55H	7	1215	159.32	159.67	0.35	0.35	100.0	
			*****Drilled from 159.67 to 162.37 mbsf*****					
56H	7	1415	162.37	162.49	0.12	0.12	100.0	
			*****Drilled from 162.49 to 165.76 mbsf*****					
57H	7	1610	165.76	167.74	1.98	1.98	100.0	
			*****Drilled from 167.74 to 174.57 mbsf*****					
58H	7	2200	174.57	176.37	1.80	1.80	100.0	Fluorescent microspheres, insert bit stuck in BHA
			*****Drilled from 176.37 to 176.56 mbsf*****					
59H	8	1400	176.56	178.57	2.01	2.29	113.9	
			*****Drilled from 178.57 to 179.26 mbsf*****					
60H	8	1530	179.26	179.35	0.09	0.09	100.0	
			*****Drilled from 179.35 to 182.66 mbsf*****					
61H	8	1715	182.66	183.4	0.74	0.74	100.0	
			*****Drilled from 183.4 to 185.71 mbsf*****					
62H	8	1940	185.71	186.21	0.50	0.50	100.0	
			*****Drilled from 186.21 to 188.76 mbsf*****					
63H	8	2115	188.76	189.19	0.43	0.43	100.0	
			*****Drilled from 189.19 to 191.81 mbsf*****					
64H	9	0145	191.81	192.11	0.30	0.28	93.3	Fluorescent microspheres, wireline cut at kink and reconnected
65X	9	0420	192.11	194.86	2.75	3.44	125.1	Fluorescent microspheres
66X	9	0600	194.86	197.91	3.05	3.31	108.5	
67X	9	0815	197.91	200.96	3.05	3.33	109.2	Fluorescent microspheres
68X	9	0930	200.96	204.01	3.05	3.42	112.1	
69X	9	1115	204.01	207.06	3.05	3.44	112.8	
70X	9	1230	207.06	208.92	1.86	2.37	127.4	
71H	9	1315	208.92	210.48	1.56	1.56	100.0	Fluorescent microspheres
72H	9	1530	210.47	210.88	0.41	0.41	100.0	Fluorescent microspheres
73X	9	1715	210.88	213.16	2.28	2.29	100.4	Fluorescent microspheres
74X	9	1910	213.16	216.21	3.05	3.27	107.2	
75X	9	2035	216.21	219.26	3.05	3.48	114.1	
76X	9	2135	219.26	222.31	3.05	3.45	113.1	
77X	9	2220	222.31	223.45	1.14	1.14	100.0	
78X	9	2315	223.45	223.60	0.15	0.15	100.0	
79R	10	0110	223.60	225.36	1.76	0.00	0.0	Backflow and bubbles in string—no H_2S observed
80R	10	0310	225.36	228.41	3.05	2.44	80.0	
81R	10	0440	228.41	231.46	3.05	2.73	89.5	Fluorescent microspheres, H_2S measured
82R	10	0535	231.46	234.51	3.05	1.87	61.3	
83R	10	0640	234.51	237.56	3.05	3.27	107.2	
84R	10	0750	237.56	240.61	3.05	2.95	96.7	
85R	10	0910	240.61	243.66	3.05	2.25	73.8	
86R	10	1015	243.66	246.71	3.05	3.12	102.3	
87R	10	1145	246.71	249.76	3.05	3.12	102.3	Fluorescent microspheres
88R	10	1245	249.76	252.81	3.05	3.19	104.6	
89R	10	1400	252.81	255.86	3.05	3.11	102.0	
90R	10	1500	255.86	258.91	3.05	3.09	101.3	
91R	10	1600	258.91	261.96	3.05	3.15	103.3	
92R	10	1710	261.96	265.01	3.05	3.12	102.3	
93R	10	1750	265.01	268.06	3.05	3.26	106.9	Fluorescent microspheres—bag did not burst
94R	10	1920	268.06	271.11	3.05	3.45	113.1	
95R	10	2005	271.11	274.16	3.05	1.99	65.3	Fluorescent microspheres—bag did not burst
96R	10	2110	274.16	277.21	3.05	3.23	105.9	
97R	10	2200	277.21	280.26	3.05	3.29	107.9	Fluorescent microspheres
98R	10	2240	280.26	283.31	3.05	3.07	100.7	Fluorescent microspheres
99R	10	2345	283.31	286.36	3.05	3.47	113.8	
100R	11	0030	286.36	289.41	3.05	3.13	102.6	
101R	11	0130	289.41	292.46	3.05	3.50	114.8	
102R	11	0205	292.46	295.51	3.05	3.18	104.3	
103R	11	0320	295.51	298.56	3.05	3.31	108.5	
104R	11	0410	298.56	301.61	3.05	3.36	110.2	Fluorescent microspheres
105R	11	0455	301.61	304.66	3.05	3.45	113.1	Fluorescent microspheres
106R	11	0545	304.66	307.71	3.05	3.10	101.6	
107R	11	0715	307.71	310.76	3.05	2.25	73.8	
108R	11	0800	310.76	313.81	3.05	2.83	92.8	
109R	11	0840	313.81	316.86	3.05	3.46	113.4	
110R	11	0930	316.86	319.91	3.05	2.33	76.4	

Table T1 (continued). (Continued on next page.)

Core	Date (May 2009)	Time (UTC)	Depth (mbsf) Top	Depth (mbsf) Bottom	Length (m) Cored	Length (m) Recovered	Recovery (%)	Comments
111R	11	1030	319.91	322.96	3.05	3.45	113.1	Fluorescent microspheres
112R	11	1115	322.96	326.01	3.05	3.22	105.6	
113R	11	1210	326.01	329.06	3.05	3.13	102.6	
114R	11	1310	329.06	332.11	3.05	3.20	104.9	
115R	11	1410	332.11	335.16	3.05	2.90	95.1	
116R	11	1450	335.16	338.21	3.05	3.41	111.8	
117R	11	1550	338.21	339.05	0.84	1.78	211.9	Fluorescent microspheres
118R	11	1750	339.05	339.43	0.38	0.65	171.1	Fluorescent microspheres
119R	11	1850	339.43	341.26	1.83	1.67	91.3	Fluorescent microspheres
120R	11	2020	341.26	344.31	3.05	0.67	22.0	
121R	11	2120	344.31	347.36	3.05	1.63	53.4	
122R	11	2215	347.36	350.41	3.05	1.04	34.1	
123R	12	0040	350.41	353.46	3.05	0.63	20.7	String torquing, undersize core
124R	12	0145	353.46	354.13	0.67	0.58	86.6	
125R	12	0340	354.13	356.51	2.38	1.60	67.2	Fluorescent microspheres
126R	12	0430	356.51	359.56	3.05	0.50	16.4	Fluorescent microspheres
127R	12	0550	359.56	362.61	3.05	1.74	57.1	
128R	12	0705	362.61	365.66	3.05	0.00	0.0	
129R	12	0830	365.66	368.71	3.05	2.10	68.9	
130R	12	0930	368.71	371.76	3.05	1.74	57.1	
131R	12	1035	371.76	372.85	1.09	0.63	57.8	
132R	12	1200	372.85	374.81	1.96	1.74	88.8	
133R	12	1300	374.81	377.86	3.05	2.45	80.3	Main lift wire tangled—cut and fixed
134R	12	2130	377.86	380.91	3.05	1.98	64.9	
135R	12	2220	380.91	383.96	3.05	2.61	85.6	
136R	12	2220	383.96	387.01	3.05	2.97	97.4	
137R	13	0005	387.01	390.06	3.05	2.91	95.4	
138R	13	0100	390.06	393.11	3.05	2.91	95.4	
139R	13	0150	393.11	396.16	3.05	1.03	33.8	Fluorescent microspheres
140R	13	0240	396.16	399.21	3.05	1.91	62.6	
141R	13	0330	399.21	402.26	3.05	1.21	39.7	
142R	13	0415	402.26	405.31	3.05	2.08	68.2	
143R	13	0525	405.31	408.36	3.05	0.62	20.3	
144R	13	0750	408.36	411.41	3.05	2.76	90.5	Fluorescent microspheres
145R	13	0800	411.41	414.46	3.05	3.11	102.0	
146R	13	0920	414.46	417.51	3.05	3.11	102.0	
147R	13	1030	417.51	420.56	3.05	3.07	100.7	
148R	13	1150	420.56	423.61	3.05	3.12	102.3	
149R	13	1255	423.61	426.66	3.05	3.12	102.3	
150R	13	1410	426.66	429.71	3.05	3.08	101.0	
151R	13	1550	429.71	432.76	3.05	3.07	100.7	Fluorescent microspheres
152R	13	1710	432.76	435.81	3.05	3.00	98.4	
153R	13	2000	435.81	438.86	3.05	3.26	106.9	
154R	13	2105	438.86	441.91	3.05	2.28	74.8	
155R	13	2205	441.91	444.96	3.05	3.27	107.2	
156R	13	2305	444.96	448.01	3.05	3.14	103.0	
157R	13	2355	448.01	451.06	3.05	3.32	108.9	Fluorescent microspheres
158R	14	0050	451.06	454.11	3.05	2.55	83.6	Wireline being spliced
159R	14	0155	454.11	457.16	3.05	3.45	113.1	
160R	14	0235	457.16	460.21	3.05	2.65	86.9	
161R	14	0325	460.21	463.26	3.05	3.42	112.1	
162R	14	0420	463.26	466.31	3.05	1.45	47.5	
163R	14	2030	466.31	469.36	3.05	3.50	114.8	Fluorescent microspheres
164R	14	2120	469.36	472.41	3.05	2.41	79.0	
165R	14	2205	472.41	475.46	3.05	3.42	112.1	
166R	14	2310	475.46	478.51	3.05	3.06	100.3	
167R	15	0010	478.51	481.56	3.05	3.11	102.0	
168R	15	0100	481.56	484.61	3.05	3.04	99.7	Fluorescent microspheres
169R	15	0155	484.61	487.66	3.05	3.09	101.3	
170R	15	0300	487.66	489.39	1.73	1.21	69.9	
171R	15	0530	489.39	492.44	3.05	3.09	101.3	
172R	15	0700	492.44	493.09	0.65	0.68	104.6	
173R	15	0810	493.09	493.76	0.67	0.78	116.4	
174R	15	1010	493.76	496.81	3.05	3.12	102.3	
175R	15	1130	496.81	499.86	3.05	3.45	113.1	
176R	15	1300	499.86	502.91	3.05	2.97	97.4	Fluorescent microspheres
177R	15	1500	502.91	505.96	3.05	3.47	113.8	
178X	15	1700	505.96	506.64	0.68	0.76	111.8	
179R	15	1800	506.64	509.01	2.37	2.68	113.1	

Table T1 (continued).

Core	Date (May 2009)	Time (UTC)	Depth (mbsf) Top	Depth (mbsf) Bottom	Length (m) Cored	Length (m) Recovered	Recovery (%)	Comments
180R	15	2035	509.01	512.06	3.05	0.07	2.3	
181R	15	2145	512.06	512.61	0.55	1.98	360.0	
182R	15	2300	512.61	515.11	2.50	0.00	0.0	
183R	16	0035	515.11	516.80	1.69	3.41	201.8	Last 1 cm of liner crumpled
184R	16	0145	516.8	519.52	2.72	2.28	83.8	Fluorescent microspheres, last 10 cm liner intruded and twisted
185R	16	0300	519.52	521.21	1.69	1.46	86.4	
186R	16	0420	521.21	524.26	3.05	3.35	109.8	
187R	16	0540	524.26	527.11	2.85	3.44	120.7	
188R	16	0750	527.11	530.36	3.25	3.07	94.5	
189R	16	0940	530.36	533.41	3.05	3.24	106.2	
190R	16	1145	533.41	536.46	3.05	3.15	103.3	
191R	16	1345	536.46	539.51	3.05	2.75	90.2	Fluorescent microspheres
192R	16	1445	539.51	542.56	3.05	2.98	97.7	
193R	16	1630	542.56	545.61	3.05	3.07	100.7	
194R	16	1800	545.61	548.66	3.05	0.00	0.0	
195R	16	1910	548.66	548.76	0.10	0.94	940.0	
196R	16	2015	548.76	549.84	1.08	0.83	76.9	
197R	16	2120	549.84	551.71	1.87	2.20	117.7	
198R	16	2250	551.71	554.76	3.05	3.50	114.8	Fluorescent microspheres
199R	17	0010	554.76	557.81	3.05	3.21	105.3	
200R	17	0110	557.81	560.86	3.05	3.15	103.3	
201R	17	0215	560.86	563.91	3.05	3.37	110.5	
202R	17	0330	563.91	566.96	3.05	3.49	114.4	
203R	17	0505	566.96	570.01	3.05	3.29	107.9	
204R	17	0650	570.01	573.06	3.05	3.03	99.3	Fluorescent microspheres
205R	17	0820	573.06	576.11	3.05	3.12	102.3	Fluorescent microspheres
206R	17	1000	576.11	579.16	3.05	3.10	101.6	
207R	17	1140	579.16	582.21	3.05	3.12	102.3	
208R	17	1315	582.21	585.26	3.05	2.91	95.4	
209R	17	1515	585.26	588.31	3.05	3.28	107.5	
210R	17	1730	588.31	591.36	3.05	3.03	99.3	Repair made to wireline
211R	17	2015	591.36	594.41	3.05	2.62	85.9	Fluorescent microspheres
212R	17	2215	594.41	597.46	3.05	3.49	114.4	
213R	17	2355	597.46	600.51	3.05	3.01	98.7	
214R	18	0130	600.51	603.56	3.05	1.52	49.8	
215R	18	0310	603.56	606.61	3.05	2.83	92.8	Fluorescent microspheres
216R	18	0510	606.61	609.66	3.05	0.50	16.4	Fluorescent microspheres
217R	18	0810	609.66	612.71	3.05	3.12	102.3	
218R	18	1025	612.71	615.76	3.05	2.56	83.9	Liner crushed
219R	18	1245	615.76	618.81	3.05	3.28	107.5	
220R	18	1450	618.81	621.86	3.05	2.02	66.2	
221R	18	1645	621.86	623.45	1.59	2.93	184.3	Fluorescent microspheres
222R	18	1915	623.45	624.91	1.46	1.53	104.8	
223R	18	2045	624.91	627.96	3.05	2.67	87.5	
224R	18	2210	627.96	631.01	3.05	3.19	104.6	Fluorescent microspheres

Notes: UTC = universal time coordinated. BHA = bottom-hole assembly.

Table T2. Summary of lithostratigraphic units, Hole M0027A. (See table note.)

Unit	Core, section, interval (cm)	Depth DSF (m)	Depositional environment	Age
	313-M0027A-			
Unit I	**1H-1, 0, to 57H-2, 43**	**0.00–167.74**	**Fluvial, estuarine, coastal plain, and marine**	**late Pleistocene–late Miocene**
Subunit IA	1H-1, 0, to 14H-1, 71	0.00–26.29	Shoreface to shoreface–offshore transition	
Subunit IB	14H-1, 71, to 34X-1, 0	26.29–70.92	Littoral to fluvial and coastal plain?	
Subunit IC	34X-1, 0, to 49H-1, 66	70.92–92.93	Estuarine and coastal plain?	
Subunit ID	49H-1, 66, to 57H-2, 43	92.93–167.74	Fluvial (channel and floodplain), minor shoreface	
Unit II	**57H-2, 48, to 83R-2, 126**	**167.74–236.16**	**Channel-fills, transgressive shoreface, shoreface–offshore transition, and offshore**	**middle Miocene (Langhian)**
Unit III	**83R-2, 126, to 102R-2, 105**	**236.16–295.01**	**Shoreface–offshore transition to offshore with strong storm influence, minor shoreface**	**early middle–late early Miocene (early Langhian–late Burdigalian)**
Unit IV	**102R-2, 105, to 116R-1, 77**	**295.01–335.93**	**Offshore, shoreface–offshore transition, and minor shoreface**	**middle early Miocene (mid-Burdigalian)**
Unit V	**116R-1, 77, to 125R-CC, 12**	**335.93–355.72**	**Poorly constrained, rollover**	**middle early Miocene (early–middle Burdigalian)**
Unit VI	**125R-CC, 12, to 170R-1, 109**	**355.72–488.75**	**Clinoform abandonment and outbuilding**	**middle early Miocene (late Aquitanian–early Burdigalian)**
Subunit VIA	125R-CC, 12, to 145-2, 120	355.72–414.11	Shoreface–offshore transition to shoreface to foreshore	
Subunit VIB	145R-2, 120, to 170R-1, 109	414.11–488.75	Deepwater toe-of-slope apron (inferred from seismic context) to offshore	
Unit VII	**170R-1, 109, to 223R-1, 69**	**488.75–625.60**	**Distal and proximal clinoform toe-of-slope aprons**	**early Miocene (early Aquitanian)–late early Oligocene**
Subunit VIIA	170R-1, 109, to 175R-3, 10	488.75–499.91	Debrite and turbidite toe-of-slope apron/channel-fill	
Subunit VIIB	175R-3, 10, to 223R-1, 69	499.91–625.60	Deepwater distal clinoform apron	
Unit VIII	**223R-1, 69, to 224R-3, 19**	**625.60–631.15**	**Offshore**	**late Eocene?**

Note: Bold text indicates generalized features of entire lithostratigraphic unit.

Table T3. Petrographic descriptions of thin sections from select lithified intervals to support macroscopic core descriptions, Hole M0027A.

Core, section, interval (cm)	Thin section	Top depth (mbsf)	Comments	Section ID	Photo
313-M0027A-					
124R-1, 46–52	1	353.92	Slide to aid core description for Unit I. Medium to coarse glauconite-bearing sandstone. Grains of quartz, feldspar, and rock fragments (granitoids) show subangular to rounded shape. Apatite and zircon are also found as accessory minerals. Glauconite pellet (green) is dominant mineral formed by authigenic diagenesis. Flocks of magnetic grains are associated along glauconite boundaries. Significantly altered calcite cement is common.	3131614	250034, 250035, 250036, 250037
125R-1, 139–143	1	355.52	Slide to aid core description for Unit I. Medium grained sandstone. Grains with subangular to subrounded shapes mostly consist of quartz and associated feldspar (perthite, microcline, and plagioclase), rock fragments (granitoids, gneiss, and marble), magnetic grains, zircon, and chlorite. Matrix is filled with clay and organic materials and is partly recrystallized by calcite cement.	3131615	250038, 250039, 250040, 250041
125R-1, 0–4	1	355.6	Slide to aid core description for Unit I. Medium sandstone. Grains are composed mainly of monocrystalline quartz and subordinantly of feldspar (microcline, plagioclase, and perthite), rock fragments (granitoids, schist/gneiss, quartzite, and marble), zircon, muscovite, authigenic glauconite, and fossils (radiolarians, shell, etc.). Some grains are coated by microcrystalline calcite. Matrix is filled with argillaceous mud and clay, organic materials, and opaque minerals. Calcite in matrix is partly recrystallized.	3131616	250030, 250031, 250032, 250033
127R-2, 3–7	1	361.09	Slide to aid core description for Unit I. Fine sandstone. Matrix consists of mud and silt material, unidentified clay mineral flakes, and organic/nonorganic materials. Flakes of chlorite and sericite in matrix are commonly layered. Brown pellets occasionally observed in matrix are considered to be oxidized glauconite formed by diagenesis. Detrital grains are quartz, feldspar, opaque mineral, muscovite, zircon, and fossil carbonate fragments.	3131620	250042, 250043, 250044, 250045
171R-1, 38–42	1	489.77	Slide to aid core description for Unit II. Quartzose glauconite-bearing medium sandstone. Detrital grains consist mainly of quartz and feldspar. Sediment texture is grain supported to matrix supported and rich in authigenic glauconite pellets formed within matrix. Glauconite is aggregated by fine pellets that are pale green in grain margin and green to dark green in grain center. Some glauconite grains are coated by oxidized iron layers. Recrystallized calcite aggregates occupy matrix as relict minerals.	3131750	270058, 270059, 270060, 270061

Table T4. Distribution of calcareous nannofossils, Hole M0027A. This table is available in an **oversized format.**

Table T5. Planktonic foraminifer occurrences and zonations, Hole M0027A. This table is available in an **oversized format.**

Table T6. Dinocyst occurrences and zonations, Hole M0027A. This table is available in an **oversized format.**

Table T7. Benthic foraminifer occurrences and paleobathymetric interpretations, Hole M0027A. (See table notes.) (Continued on next two pages.)

Core, section, interval (cm)	Depth (mbsf)	Benthic foraminifer taxa	Preservation	Comments	Paleodepth estimate (m)
313-M0027A-					
6H-1, 145–150	16.73	Barren	NA		?
9H-CC	19.59	Barren	NA		?
13H-CC	25.51	*Cibicidoides*			? 50??
15H-CC	27.89	None noted			?
50H-CC, 55–60	96.12	Barren	NA	Paleosol, *Sphaerosiderite*	?
64H-CC	192.09	Barren			?
65X-CC, 11–13	195.53	1 *Plectofrondicularia amorneyae*	G		?
66X-3, 30–32	198.15	Barren			?
70X-CC, 0–2	208.92	*Lenticulina–Hanzawaia concentrica–Nonionella pizarrensis*; R: *Buliminella gracilis*	M–G		15–50
73X-CC, 0–3	213.14	A: *Lenticulina–Hanzawaia concentrica–Nonionella pizarrensis*; C: *Buliminella gracilis;* R: *Lagena, Cibicides lobatulus, Fissurina, Pararotalia, Cancris sagra*		All stained	25–50
80R-CC, 0–15	227.65	A: *Lenticulina*–small *Nonionella pizarrensis;* R: *Hanzawaia concentrica, Bulimina mexicana,* polymorhinid, agglutinants, *Rectuvigerina lamelata;* C: *Uvigerina juncea;* F: *Buliminella gracilis*	M–G	Large *Lenticulina*—beat up; small ones are nice	25–50
81R-1, 103–108	229.44	A: *Lenticulina* (and lenticulinids); C–A: *Nonionella pizarrensis, Bulimina mexicana, Buliminella gracilis, Uvigerina juncea* (and others); R: polymorphinid, *Rectuvigerina* cf. *senni, Lagena, Fissurina, Cibicidoides*	VG		50–80
89R-CC, 0–2	255.90	A: *Nonionella pizarrensis, Lenticulina;* C: *Hanzawaia;* F: *Cibicidoides, Bolivina* spp., R: agglutinants, *Bulimina macilenta*	VG		25–50
91R-CC, 9–10	262.05	A: *Nonionella pizarrensis;* R–F: *Buliminella gracilis;* R: *Uvigerina juncea*	VG		25–50
93R-1, 145–150	266.46	A: *Lenticulina–Nonionella pizarrensis;* C: *Hanzawaia concentrica;* F: *Uvigerina juncea, Buliminella gracilis;* R: agglutinants	VG		25–50
95R-1, 139–143	272.50	A: *Nonionella pizarrensis;* C: *Hanzawaia concentrica,* R: agglutinants, *Bolivina, Pararotalia bassleri*	VG		25–50
95R-1, 143–148	272.54	A: *Nonionella pizarrensis;* C: *Hanzawaia concentrica,* R: agglutinants, *Bolivina, Pararotalia bassleri*	VG		25–50
97R-CC, 0–10	280.40	A: *Nonionella pizarrensis, Hanzawaia;* C: *Buliminella gracilis;* R: *Uvigerina juncea*	VG		25–50
98R-1, 144–145	281.70	A: *Nonionella pizarrensis;* C: *Buliminella gracilis, Hanzawaia concentrica;* R: agglutinants, *Cibicidoides*	VG		25–50
101R-3, 34–38	292.76	A: *Nonionella pizarrensis* (24); R: miliolid (1), *Hanzawaia concentrica* (2); F: *Buliminella gracilis* (12); C–A: *Uvigerina juncea* (6)	VG		50–80
104R-1, 62–64	299.18	*Lenticulina* (4); *Nonionella pizarrensis* (33); *Bolivina marginata* var. *multicostata* (4); *Hanzawaia concentrica* (4); *Uvigerina juncea* (7); *Buliminella gracilis* (2);?? (2)	E		50–80
105R-CC, 0–11	304.95	Barren			?
112R-CC	326.11	*Nonionella pizarrensis, Lenticulina, Buliminella gracilis, Bolivina*			50–80
115R-2, 76–78	334.37	*Buliminella gracilis* (17); *Uvigerina juncea* (3); *Nonionella pizarrensis* (4); *Bolivina marginata* var. *multicostata* (4)	G–VG		50–80; probably deeper than 104–1
119R-1, 66–68	340.09	*Lenticulina* (5); *Cibicidoides pachyderma* (3); *Buliminella gracilis* (3); *Hanzawaia concentrica* (12); *Nonionella pizarrensis* (1); *Bulimina mexicana* (1); *Uvigerina auberiana* (1); *Uvigerina juncea* (3)	P–VG		75–100 with downslope transport
146R-1, 73–74	415.19	Barren			?
147R-1, 145–150	418.96	Barren			?
148R-CC	423.68	A: *Buliminella gracilis* (dozens); F: *Nonionella pizarrensis* (6); R: *Lenticulina* (1); *Uvigerina juncea* (1); *Hanzawaia* (3); *Plectofrondicularia morneyae* (1)	VG		50–80 (deep end)
149R-CC, 11–13	426.71	*Dentalina* (1); *Stilostomella* (1); *Nonionella pizarrensis* (2); *Buliminella gracilis* (6)	VG	Rare foraminifers	50–80
150R-CC, 6–8	429.72	Barren			?
151R-1, 155–160	431.26	Barren			?
151R-2, 145–147	432.76	Barren			?
151R-CC	432.78	Foraminifers in pan fraction: *Buliminella, Trifarina, Cibicides, Discorbis*			50–80
154R-1, 141	440.27	*Buliminella, Lenticulina, Sphaeroidina bulloides*			50–80
154R-2, 72–77	441.08	*Buliminella gracilis* (1); R: *Buliminella gracilis* in pan fraction			??50–80

Table T7 (continued). (Continued on next page.)

Core, section, interval (cm)	Depth (mbsf)	Benthic foraminifer taxa	Preservation	Comments	Paleodepth estimate (m)
159R-CC	457.54	Barren (maybe 1 *Buliminella gracilis*)			??50–80
161R-CC, 8–10	463.61	Barren			?
161R-CC(?)	(?)463.63	C: *Buliminella gracilis, Nonionella pizarrensis; Uvigerina juncea*			50–80 or deeper
163R-CC, 13–15	469.79	A: *Nonionella pizarrensis*; C: *Lenticulina*; R: *Buliminella gracilis* (1); *Uvigerina juncea* (1)			25–50
165R-CC, 5–7	475.81	A: *Nonionella pizarrensis*; F: *Cibicidoides* (6); R: *Lenticulina* (1); *Uvigerina juncea* (1); *Fissurina* (1); *Plectofrondicularia* (2); *Stilostomella* (1); *Dentalina* (1); *Buliminella gracilis* (3); *Gyroidinoides* (1); *Hanzawaia* (3)			25–50
167R-CC, 11–13	481.60	Barren			?
169R-CC, 11–13	487.68	Barren			?
171R-CC, 11–13	492.46	Barren			?
175R-CC, 11–13	500.21	Barren			?
177R-CC, 11–13	506.33	Barren			?
179R-CC, 13–15	509.30	A: *Buliminella gracilis, Rectuvigerina lamelata, Rectuvigerina multicostata, Nonionella pizarrensis*; F: *Lenticulina, Uvigerina juncea, Hanzawaia concentrica*; R: *Cibicidoides, Gyroidinoides, Pletofrondicularia*	P–G	Abundant, diverse foraminifers	>100
183R-CC, 6–8	518.50	A: *Uvigerina juncea, Rectuvigerina lamelata, Rectuvigerina multicostata, Buliminella gracilis, Pullenia salisburyi, Nonion, Cibicidoides, Melonis barleeanus, Gyroidinoides, Lenticulina,* polymorph, *Stilostomella, Hanzawaia mantaensis, Cibicidoides pachyerma, Anomalinoides spissiformis*	VG	Abundant (>250), diverse foraminifers	>100
185R-CC, 15–17	520.96	*Siphonina danvellensis, Sphaeroidina bulloides, Pletofrondicularia, Trifarina wilcoxensis, Cibicidoides, Globocassidulina subglobosa, Melonis barleeanus, Gyroidinoides, Alabamina mississippiensis, Hanzawaia mantaensis, Oridorsalis, Cibicidoides pachyderma, Uvigerina auberiana* and several costate *Uvigerina* (continuous across chambers), *Fursenkoina fusiformis, Coryphostoma georgiana, Cibicidoides primulus*	VG		100–200
187R-CC, 8–10	527.68	Barren			?
188R-CC, 8–9	530.17	Barren			?
189R-CC, 6–8	533.58	A: *Globobulimina, Lenticulina, Buliminella gracilis* (A 150–250); C: *Nonionella pizarrensis*; F: costate *Uvigerina;* C: *Pletofrondicularia, Gyroidinoides*	P–G		50–80
191R-CC, 4–6	539.19	Broken Lenticulinids			?
192R-2, 147–148	542.48	>250: A: *Lenticulina, Nonionella pizarrensis,* costate *Uvigerina*; C: polymorph, *Gyroidinoides, Hanzawaia concentrica, Pletofrondicularia* 150–250: *Lenticulina, Nonionella pizarrensis, Buliminella curta, Hanzawaia mantaensis, Cibicidoides pachyderma, Fissurina, Trifarina wilcoxensis, Anomalinoides spissiformis, Marginulina*	P–VG		>100
193R-CC, 10–12	545.61	Barren			?
195R-2, 9–11	549.60	A: *Lenticulina,* polymorph, large costate *Uvigerina*; F-C: *Lenticulina, Nonionella pizarrensis, Gyroidinoides*	P–VG	Abundant, diverse foraminifers	80–100
198R-CC	555.19	*Melonis barleeanus, Nonionella pizarrensis, Cibicidoides, Anomalinoides, Pullenia, Cassidulina, Lenticulina, Buliminella gracilis, Bolivina*			?80
199R-3, 19–21	557.95	*Lenticulina* (1); *Pletofrondicularia* (1); shallow *Hanzawaia* (1); *Nonionella pizarrensis* (1)		Rare benthics, much shallower than above	15–50
201R-CC	564.21	A: *Lenticulina,* polymorph; C: *Cibicidoides, Anomalinoides spissiformis*; R: *Fissurina, Buliminella curta, Globobulimina, Coryphostoma georgiana*	P–G		?75–100
205R-CC	576.15	Fragments			?
206R-CC	579.19	*Lenticulina,* costate *Uvigerina, Nonionella pizarrensis,* polymorph, *Anomalinoides spissiformis*		Rare foraminifers	50–100
207R-3, 10–12	582.26	C: *Lenticulina, Nonionella pizarrensis;* costate *Uvigerina; Nodosaria, Plectofrondicularia morneyae,* polymorph, *Melonis barleeanus*	P–G	Rare foraminifers	50–100
208R-2, 139–141	585.10	A: costate *Uvigerina, Plectofrondicularia morneyae, Anomalinoides spissiformis*; R: *Lenticulina*	M–G	Foraminifers	>100

Table T7 (continued).

Core, section, interval (cm)	Depth (mbsf)	Benthic foraminifer taxa	Preservation	Comments	Paleodepth estimate (m)
209R-3, 33–36	588.51	*Lenticulina, Sphaeroidina bulloides, Nonionella pizarrensis, Gyroidinoides, Melonis barleeanus,* agglutinants, *Oridorsalis, Cibicidoides primulus, Cibicidoides pachyderma, Cibicides* spp., R: costate *Uvigerina*	M–G	Abundant, diverse foraminifers	>100
209R-CC	588.51	*Nonionella pizarrensis, Sphaeroidina bulloides, Oridorsalis, Gyroidinoides, Melonis barleeanus*			>100
210R-CC	591.31	*Melonis pompilioides, Sphaeroidina bulloides, Lenticulina, Gyroidinoides,* large costate *Uvigerina,* polymorph, *Nonionella pizarrensis, Ceratatobulimina, Cassidulinoides,* striate *Plectofrondicularia,* costate and hispid *Stilostomella*	P–M	Foraminifers	>80, perhaps >100
210R-CC, 0–3	591.31	*Nonionella pizarrensis, Pullenia quinqueloba, Melonis barleeanus,* costate *Stilostomella, Stilostomella subspinosa, Sphaeroidina bulloides, Lenticulina, Siphonina,* costate *Uvigerina* (not continuous), polymorph	P–M	Abundant foraminifers	>80, perhaps >100
211R-1, 144–145	592.80	A: *Uvigerina juncea, Melonis barleeanus, Nonionella pizarrensis, Sphaeroidina bulloides,* others			>100
211R-CC, 0–2	593.96	*Dentalina, Lenticulina, Hoeglundina elegans, Melonis pompilioides, Hanzawaia mantaensis,* polymorph, costate *Uvigerina, Plectofrondicularia, Nonionella pizarrensis,* costate *Stilostomella, Stilostomella subspinosa, Lagena,* agglutinants (*~Textularia*), *Cibicidoides pachyderma, Siphonina danvellensis*	P–G	Abundant benthics	>100
212R-CC	597.88	*Sphaeroidina bulloides, Melonis barleeanus, Uvigerina juncea, Oridorsalis, Anomalinoides*			>100
214R-CC, 12–14	602.01	*Nodosaria, Nonionella pizarrensis, Gyroidinoides,* costate *Uvigerina,* costate *Stilostomella, Sphaeroidina bulloides, Oridorsalis,* polymorph, *Lenticulina, Stilostomella subspinosa, Alabamina mississippiensis*	P–G	Abundant benthics	>100
217R-2, 103–106	612.19	A: large costate *Uvigerina, Lenticulina, Siphonina danvellensis, Nonionella pizarrensis, Melonis barleeanus, Cassidulina crassa, Plectofrondicularia, ~Cibicidoides pachyderma*	P–G		>100
218R-2, 103–106	615.24	Barren			?
219R-3, 24–28	619.00	A: costate *Uvigerina* and *Uvigerina* spp., *Oridorsalis, Siphonina danvellensis, Sphaeroidina bulloides, Melonis barleeanus, Hanzawaia* spp., *~Cibicidoides pachyderma, Stilostomella subspinosa, Stilostomella* spp., costate *Stilostomella, Hoeglundina elegans, Gyroidinoides*	P–G		>100
220R-CC	620.83	*Uvigerina juncea, Siphonina, Osangularia, Lenticulina, Sphaeroidina bulloides, Bulimina jacksonensis*			>100
222R-CC	624.97	*Uvigerina juncea*			>75
223R-CC	627.58	A: large costate *Uvigerina;* costate *Stilostomella, Lenticulina, Hoeglundina elegans, Cibicidoides,* polymorph, *Siphonina, Melonis pompilioides, Cibicidoides pachyderma, Pullenia bulloides*	M	Abundant, diverse	>100

Notes: Sample depths to be added. A = abundant, C = common, F = few, R = rare. Preservation: E = excellent, VG = very good, G = good, M = moderate, P = poor. N/A = not available. *Nonionella pizarrensis* includes possible *Nonionella grateloupi. Buliminella gracilis = Caucasina elongata? Gyroidinoides* includes possible *Gyroidinoides nipponica.* Polymorph = *Guttulina austriaca, Guttulina candata,* undifferentiated polymorphinids. *Siphonina danvellensis* = *?Pulsiphonina prima.*

Table T8. Palynomorph data and remarks on dominant tree taxa, Hole M0027A. (See table note.)

Core, section	Depth (mbsf)	Nonsaccate arboreal pollen	Herbal pollen	Cyperaceae and poaceae pollen	Pollen spores	Fungal spores	Dinocysts	Foraminifer combined	All bisaccates including reworked	Nonsaccate arboreal pollen + herbal pollen	Dinocyst + foraminifer test linings	(Dinocysts + foraminifer test linings)/(nonsaccate aboreal pollen + herbal pollen)	Remarks
313-M0027-													
9H-CC	19.59	61	25	17	41	1	19	1.7	195	86	20.7	0.2403	Hickory present but rare; frequent occurrences of hazelnut, birch, alder
65X-CC	195.53	220	6	10	1	7	2	1.0	7	226	3.0	0.0133	Hickory present but not frequent
67X-CC	201.22	126	9	10	0	7	3	0.0	5.5	135	3.0	0.0222	Hickory present but not frequent
69X-CC	207.44	123	12	7	1	11	13	3.0	13.5	135	16.0	0.1185	Hickory present but not frequent
91R-CC	262.05	108	4	3	0	2	8	15.3	16.5	112	23.3	0.2083	Oak and hickory pollen very frequent
101R-CC	292.91	183	11	9	1	3	9	2.0	38.5	194	11.0	0.0567	Hickory present but not frequent
104R-CC	301.86	135	12	6	1	0	2	1.0	16	147	3.0	0.0204	Oak and hickory pollen very frequent, elm extraordinarily frequent
105R-CC	304.95	107	5	8	0	1	17	4.0	34	112	21.0	0.1875	Oak and hickory pollen very frequent, elm extraordinarily frequent, from 105R to 9H frequent occurrences of grasses (Poacea)
146R-CC	417.57	134	15	1	0	2	21	6.3	7.5	149	27.3	0.1834	Hickory present but not frequent
148R-CC	423.68	97	5	8	0	0	93	5.3	44.5	102	98.3	0.9641	Oak and hickory pollen very frequent
149R-CC	426.71	160	7	1	0	2	23	6.3	22.5	167	29.3	0.1756	Oak and hickory pollen very frequent, presence of western hemlock
151R-CC	432.78	135	7	4	0	1	12	2.0	29	142	14.0	0.0986	Oak and hickory pollen very frequent
154R-CC	441.13	112	7	4	0	1	26	5.0	43	119	31.0	0.2605	Oak and hickory pollen very frequent
156R-CC	448.09	133	8	3	0	2	18	0.0	24	141	18.0	0.1277	Oak and hickory pollen very frequent
159R-CC	457.54	128	10	4	0	0	55	1.3	27.5	138	56.3	0.4082	Hickory present but not frequent
161R-CC	463.61	126	11	8	1	2	40	8.0	28	137	48.0	0.3504	Oak and hickory pollen very frequent
163R-CC	469.79	126	9	3	1	0	14	1.3	48.5	135	15.3	0.1136	Oak and hickory pollen very frequent
167R-CC	481.60	129	8	4	1	1	32	0.7	15	137	32.7	0.2384	Oak and hickory pollen very frequent
171R-CC	492.46	104	6	2	2	2	54	20.0	65	110	74.0	0.6727	Oak and hickory pollen very frequent
175R-CC	500.21	102	7	1	0	1	19	5.7	51.5	109	24.7	0.2263	Oak and hickory pollen very frequent
177R-CC	505.33	84	7	3	0	0	23	8.3	110	91	31.3	0.3443	Hickory present but not frequent
185R-CC	520.96	90	8	3	0	0	59	12.7	92	98	71.7	0.7313	Oak and hickory pollen very frequent
189R-CC	533.58	76	5	3	0	0	43	11.0	202	81	54.0	0.6667	Oak, linden, and hickory pollen very frequent
191R-CC	539.19	77	5	1	0	0	19	7.0	31.5	82	26.0	0.3171	Oak, linden, and hickory pollen very frequent
193R-CC	545.61	76	9	1	0	0	72	17.3	48	85	89.3	1.0510	Oak and hickory pollen very frequent
204R-CC	573.01	54	19	5	0	0	31	5.0	182.5	73	36.0	0.4932	Hickory present but not frequent, possibly grass pollen present
206R-CC	579.19	108	3	1	0	0	16	5.3	116.5	111	21.3	0.1922	Oak, linden, and hickory pollen very frequent
208R-CC	585.10	61	17	2	1	0	21	4.0	19.5	78	25.0	0.3205	Hickory present but not frequent
218R-CC	615.24	100	8	2	0	1	35	14.3	39.5	108	49.3	0.4568	Oak, linden, and hickory pollen very frequent
220R-CC	620.83	52	3	1	0	0	157	7.7	80	55	164.7	2.9939	Oak, linden, and hickory pollen very frequent, presence of elm pollen
223R-CC	627.58	37	5	1	0	0	92	44.0	31.5	42	136.0	3.2381	High content of oak and other, probable arboreal, nonsaccate pollen, but no hickory, no elm, and no linden pollen

Note: Remarks concerning nonsaccate pollen, like "frequent" or "rare," are always in relation to the production and transport potential of the different pollen types (e.g., "elm pollen frequent" may refer to 5 or 6 grains, whereas 5 or 6 grains of oak pollen would be regarded as "rare").

Table T9. Composition of interstitial water, Hole M0027A. This table is available in an **oversized format.**

Table T10. Total carbon, total organic carbon, total inorganic carbon, and total sulfur in sediment, Hole M0027A.

Core, section, interval (cm)	Depth (mbsf)	Carbon (wt%)			Total sulfur (wt%)
		Total	Organic	Inorganic	
313-M0027A-					
1R-1, 143.5–144.5	1.44	0.66	0.07	0.59	0.09
2R-1, 145.0–146.0	3.88	1.24	0.08	1.16	0.10
3R-1, 145.0–145.0	6.22	0.31	0.07	0.24	0.08
4R-2, 123.0–124.0	10.24	1.13	0.12	1.01	0.22
4R-1, 145.0–146.0	8.95	1.69	0.08	1.61	0.19
6R-1, 145.0–146.0	13.00	1.20	0.21	0.99	0.17
8H-1, 36.0–37.0	15.63	1.45	0.57	0.89	0.11
9H-1, 49.0–50.0	18.14	1.39	0.61	0.78	0.14
10H-1, 65.0–66.0	19.79	1.67	0.67	1.00	0.36
12H-1, 50.0–51.0	21.78	0.92	0.59	0.33	0.30
17H-1, 10.0–11.0	28.19	1.73	1.71	0.02	0.24
19H-1, 64.0–65.0	32.00	1.53	1.52	0.01	0.24
25R-1, 145.0–146.0	41.88	0.23	0.13	0.10	0.20
27R-1, 117.0–118.0	47.70	0.21	0.15	0.06	0.19
32R-1, 0.0–1.0	61.78	0.20	0.15	0.05	0.39
35X-1, 0.0–1.0	73.98	0.20	0.18	0.02	0.12
35X-1, 49.0–50.0	74.47	0.77	0.13	0.64	0.04
38X-1, 138.0–139.0	78.41	0.23	0.20	0.03	0.14
41X-1, 14.0–16.0	79.66	0.73	0.73	0.01	0.28
50H-1, 7.0–8.0	95.40	2.77	0.18	2.58	0.05
50H-1, 47.0–48.0	95.80	0.78	0.14	0.64	0.05
51H-1, 8.0–9.0	110.66	2.34	0.16	2.19	0.07
51R-1, 17.5–18.5	110.75	0.93	0.23	0.70	0.12
53R-1, 0.5–1.5	134.98	0.13	0.10	0.03	0.21
54R-1, 0.0–1.0	138.03	0.12	0.11	0.02	0.10
55R-1, 0.0–1.0	159.33	0.29	0.19	0.10	0.23
57R-2, 42.0–43.0	167.69	0.09	0.06	0.02	0.11
59H-1, 28.0–29.0	176.85	1.68	1.06	0.62	0.20
61H-1, 8.0–11.0	182.76	1.61	1.01	0.61	0.66
63H-1, 35.0–36.0	189.12	1.43	0.86	0.56	0.15
65X-1, 50.0–51.0	192.62	1.42	1.30	0.12	0.39
66X-1, 71.0–72.0	195.58	1.74	1.08	0.66	0.25
66X-2, 71.0–72.0	197.08	1.67	1.03	0.64	0.27
67X-3, 48.0–49.0	200.07	2.19	1.34	0.85	0.24
67X-2, 60.0–61.0	198.69	1.81	1.04	0.77	0.25
68X-1, 130.0–131.0	202.27	1.60	0.89	0.71	0.34
70X-2, 66.0–67.0	209.23	1.33	0.94	0.39	0.63
72H-1, 22.0–23.0	210.70	2.23	1.83	0.40	3.59
75X-1, 48.0–49.0	216.70	2.58	2.37	0.21	3.00
80R-1, 88.0–89.0	226.25	2.20	1.55	0.65	2.01
82R-2, 90.0–91.0	233.87	0.80	0.74	0.06	1.68
85R-1, 74.0–75.0	241.36	0.83	0.81	0.02	2.87
88R-1, 62.0–63.0	250.39	3.34	2.01	1.33	2.75
91R-1, 13.0–14.0	259.05	8.41	7.45	0.96	3.63
94R-2, 72.0–73.0	270.29	4.06	3.83	0.24	3.39
97R-2, 62.0–64.0	279.34	1.53	1.47	0.07	1.18
98R-1, 60.0–61.0	280.87	2.67	2.42	0.25	4.02
101R-1, 89.0–90.0	290.31	3.02	2.71	0.31	2.52
104R-1, 68.0–69.0	299.25	1.33	1.13	0.19	1.86
107R-1, 52.0–53.0	308.24	2.34	2.03	0.31	2.82
110R-2, 40.0–41.0	318.77	1.90	1.52	0.39	2.50
113R-1, 81.0–82.0	326.83	1.77	1.50	0.27	2.17
115R-2, 75.0–76.0	334.37	1.04	0.93	0.11	1.47
119R-1, 65.0–66.0	340.09	0.65	0.64	0.02	1.72
122R-1, 60.0–61.0	347.97	0.21	0.16	0.06	0.10
123R-1, 54.0–55.0	350.96	0.79	0.21	0.57	0.18
129R-1, 30.0–31.0	365.97	0.17	0.13	0.04	0.10
133R-2, 50.0–51.0	376.82	0.20	0.11	0.09	0.15
136R-1, 0.0–1.0	383.97	0.18	0.17	0.02	0.13
138R-2, 127.0–128.0	392.84	0.20	0.16	0.04	0.15
144R-1, 139.0–140.0	409.76	0.30	0.28	0.02	0.57
146R-1, 72.0–73.0	415.19	1.59	1.46	0.13	1.39
148R-2, 67.0–68.0	422.74	3.43	3.16	0.27	2.20
151R-2, 55.0–56.5	431.87	4.34	4.11	0.23	2.26
153R-2, 75.0–76.0	438.07	4.36	4.25	0.11	2.50
154R-1, 91.0–92.0	439.78	4.58	4.37	0.21	2.68
157R-1, 66.0–67.0	448.68	1.35	1.19	0.16	1.12
160R-1, 56.0–57.0	457.73	4.41	3.80	0.61	2.43
165R-1, 69.0–70.0	473.11	2.04	1.91	0.12	2.20
168R-1, 144.0–145.0	483.01	1.74	1.06	0.69	1.97
171R-2, 21.0–22.0	491.11	0.71	0.23	0.47	0.15
175R-1, 139.0–140.0	498.21	1.76	1.51	0.25	1.14
179R-2, 96.0–97.0	509.11	2.27	0.81	1.46	0.77
183R-2, 149.0–150.0	518.11	2.02	1.17	0.85	0.83
190R-1, 22.0–23.5	533.64	3.76	0.52	3.24	0.41
206R-1, 85.0–86.0	576.97	2.02	1.73	0.30	1.99
209R-1, 60.0–61.0	585.87	1.75	1.57	0.18	2.44
213R-2, 82.0–83.0	599.79	3.04	2.31	0.73	1.44
217R-2, 40.0–41.0	611.57	2.18	1.76	0.42	1.69

Table T11. Summary of sediment mineralogy from X-ray diffraction, Hole M0027A. (See table notes.)

Intensity ratios	Mean	Max
Clay minerals	12.2	59.2
Kaolinite	5.7	40.3
Micas and Illite	2.7	8.2
Mixed layered clays	2.7	7.9
Smectite	1.0	2.8
Carbonates	6.5	47.6
Mg-rich calcite	1.4	16.6
Calcite	2.2	13.9
Siderite	1.1	9.5
Rhodochrosite	0.5	3.4
Dolomite and ankerite	0.4	2.2
Aragonite	1.0	2.0
Detrital minerals	74.6	170.6
Quartz	61.5	85.6
Plagioclase	4.0	27.4
Chlorite	2.7	22.9
K-Feldspar	2.7	19.7
Pyroxene	1.7	7.7
Zeolites	0.7	2.3
Gibbsite	0.4	2.2
Epidote	0.6	1.9
Amphibole	0.3	0.9
Authigenic minerals	6.7	27.8
Pyrite	1.7	7.3
Glauconite	1.1	6.5
Goethite	1.6	5.6
Apatite	1.1	5.5
Magnetite	0.8	1.7
Barite	0.4	1.1
Total	100.0	305.1

Notes: The original sum for the mean of all measured peak intensity ratios was 90.5%. After elimination of all clay minerals (4.55–4.4 Å, 3.4%), gypsum (0.9%), and halite (0.7%), this sum became 85.5%, which was then renormalized to 100% above.

Table T12. Preliminary magnetostratigraphic age-depth tie points, Hole M0027A. (See table note.)

Depth (mbsf)	Interpretation A	Age (Ma)	Interpretation B	Age (Ma)
191.96–189.03	C5AAr–C5AAn	13.139	C5ABr–C5ABn	13.510
196.09–195.79	C5ACn–C5ABr	13.703	C5ADn–C5ACr	14.178
206.94–206.74	C5ACr–C5ACn	14.076	C5ADr–C5ADn	14.612

Note: All ages according to Cande and Kent (1995).

Table T13. Downhole surfaces and trends from petrophysical and downhole measurements, Hole M0027A. (See table notes.)

Depth (mbsf)	Depth Top	Depth Bottom	Total gamma ray	Th/K	U	Th	Conductivity	Sonic	V_P	Density	Resistivity	Magnetic susceptibility	Surface correspondence	Comments/Interpretation
15.0	—	—	Increase										MIC3A surface pick 5 m above	
29.0	—	—				Increase							MIC3C and subunit boundary 3 m above	
—	93	96	Peak										m1 surface at base	
—	110	111				Peak							m3 surface 4 m below	
118.0	—	—	Decrease										m3 surface 3 m above	
168.0	—	—	Increase										Unit I/II boundary	
194.0	—	—										Increase	m4.1 surface 1 m below	
205.04	—	—	Small Low				Small Low					Decrease	No corresponding surface	Very clear in acoustic image; massive clays change to banded clays
208.0	—	—										Decrease	No corresponding surface	Base of high magnetic susceptibility
219.0	—	—				Small Peak		Peak					m4.5 surface 1 m above	
224.0	—	—	Hole				Peak						m5.2 surface 1 m below	
230.0	—	—						Increase					Unnamed surface 1 m below	
—	234.7	236.2	Increase	Increase			Peak	Peak					m5.3 surface 1 m below	Log picks out sand to clay lithology change
—	255	256	Fluctuations					Fluctuations				Fluctuations	MFS/TS/m5.32 surface in this interval	
271.0	272	274	Hole				Peak	Peak		Increase			m5.4 surface at top of interval	
295.0	—	—			Increase			Increase					Unit III/IV boundary and unnamed surface	
308.0	—	—						Increase		Increase			No corresponding surface	
324.0	—	—						Increase		Increase			No corresponding surface	
332.5	—	—				Peak							m5.45 surface 0.5 m above	
336.0	—	—	Hole							Increase			Unit IV/V boundary and m5.47 surface	
355.0	—	—		Increase									m5.6	Cemented horizon
361.0	—	—				Peak			High V_P discrete sample				m5.7	Cemented horizon
420.0	—	—						Decrease					No corresponding surface	
459.0	—	—		Peak									No corresponding surface	
465.0	—	—		Peak									MFS	
474.0	468	474	Increase		Increase			Increase		Increase			No corresponding surface	
489.6	—	—					Decrease	Increase				Increase	Bottom pick of three for m5.8	Cemented horizon
—	495	500	Increase							Hole			m6 surface at top of interval	
533.0	533	534						Peak		Peak			o.5 6 m below	Cemented horizon
571.0	—	—	Hole							Hole			No corresponding surface	
585.0	—	—								Hole			o1 surface	
—	596	600	Decrease				Increase			Decrease			Surface in core at top of interval	
—	621	622	Peak (core)										In between two surfaces EOT 3 m below	

Notes: — = not applicable. All descriptions indicate increase/decrease downhole. No petrophysical picks have been made using gamma ray in the top 200 m of the hole with no core recovery; refer to text and Fig. F3 for discussion of this interval. Hole = sharp confined low in measurement, peak = sharp confined high in measurement. MIC = marine isotope chron. MFS = maximum flooding surface, TS = transgressive surface. EOT = Eocene–Oligocene transition.

Table T14. Correlations of seismic sequence boundaries to core surfaces, Hole M0027A. (See table notes.)

GTS 2008	Predicted age BKSA95	Seismic sequence boundaries	Monteverde seismic picks ms	Monteverde seismic picks mbsf	Predicted depth (mbsf) Monteverde seismic range	Predicted depth (mbsf) Seismic	Predicted core	Actual depth (mbsf)	Actual core, section, interval (cm)	Notes	Age derived from age-depth plot BKSA95	Age derived from age-depth plot GTS 2004 (Ma)	Age derived from age-depth plot Error (Ma)
							313-M0027A-		313-M0027A-				
—	35 ka	MIC3a	—	—	12	12	5H	10.41	5H-1, 11	Base coarsening up	<90 ka	—	—
—	55 ka	MIC3c	—	—	—	24	13H	26.38	Base of 14H	Gravel	125–250 ka	—	—
—	70 ka	MIC4	—	—	24	36	22R	31.90	19H-1, 56	Based on core	LO Pleistocene?~1 Ma MIC30	—	—
11.58	11.5 Ma	m1	118	95	91–95	89–91	47H–48H	96	Top of ?50H-1	Based on log	No data	—	—
12.85	12.8 Ma	m2	—	—	91–94	NR	—	—			—	—	—
13.66	13.6 Ma	m3	—	—	NR	105–109	Not cored	115	Not cored	Based on log	No data	—	—
14.11	?14.1 Ma	m4	178	143	140–143	138–142	53H–54H	~140	Not cored		No data	—	—
—	—	m4.1	—	—	—	—	—	—	66X-2	Based on core	?13.5 Ma	?13.6	Poorly constrained
14.8–15.8	14.8–15.8 Ma	m4.5	256	210	208–211	210–215	72H–73X	218.39	75X-2, 68	Granulated sand/silty clay	?14.2–14.8 Ma	?14.0–15.0	Poorly constrained
—	—	m5	—	—	—	—	—	—		Merged with m4.5	—	—	—
16.0–16.5	16.0–16.5 Ma	m5.2	276	227	226–228	225–230	80R–81R	225	80R-1, 10	Pebbly lag, gamma core minimum; mcd shift	?15.6–16.0 Ma	?15.6–16.0	14.5–15.5
—	—	?Unnamed	—	—	—	—	—	231.46	Top of 82R-1	Pebbly lag	?15.6–16.0 Ma	<15.6	14.5–15.5
17.2	17.2 Ma	m5.3	291	240	239–242	235–240	83R–84R	237.17	83R-2, 127	Sand/tight clay	~16.0 Ma	15.7	15.0–15.7
—	—	MFS/SB	—	—	—	—	—	253.21	89R-1, 40		—	—	—
—	—	TS	—	—	—	—	—	255.16	89R-2, 85		—	—	—
—	—	SB ?m5.32	—	259	258–260	—	—	256.19	90R-1, 33	Lag, USF over offshore	~16.3 Ma	~16.3	15.8–16.3
17.6–17.7	17.8–18.2 Ma	m5.4	338	282	281–284	278–282	97R–98R	271.21	95R-1, 10	SOT over offshore	~17.3 Ma	~17.3	16.3–17.8
—	—	?Unnamed	—	—	—	—	—	295.01	102R-2, 105	Erosion surface	~17.8 Ma	~17.6	17.2–18.2
19.2	19.5 Ma	m5.45	390	329	328–331	325–330	112R–113R	331.90	114R-2, 133.5	Sharp contact; SOT over offshore	~18.3 Ma	~18.1	17.3–18.5
19.3	19.7 Ma	m5.47	403	342	340–343	335–340	116R–117R	336.06	116R-1, 90	Erosion surface, top glauconite	~18.4 Ma	~18.2	17.5–18.5
19.7	20.1 Ma	m5.5	—	—	—	NR	—	—			—	—	—
—	—	?FS	—	—	—	—	—	—	Top of 121R-1		—	—	—
19.8	20.2 Ma	m5.6	403	347	346–349	345–350	121R–122R	355.53	125R-1, 140	Cemented zone	?20.0–19.0 Ma	19.6–18.7	20.0–18.5
19.9	20.4 Ma	m5.7	423	360	359–362	350–360	123R–126R	>361.28	Below 127R-2, 22	Core gap, gamma log kick	?20.0–19.0 Ma	19.6–18.7	20.0–18.5
—	—	mFS	—	—	—	450–460	158R–160R	465.00	162R	Benthic foraminifers: shallowing	—	—	—
20.9–21.4	21.5–22.0 Ma	m5.8	546	478	476–480	470–480	164R–166R	487.66/488.87/489.39	Top of 169R-CC/170R-CC, 2/top of 172R	Indurated zone	21.1 Ma	20.5	20.5–21.5
—	—	m6	569	501	499–503	475–80	166R–167R	494.87	174R-1, 111	Either base indurated or facies changes/gamma peak pull up	22.0 Ma	21.3	21.0–23.0
–	23.5–24.0 Ma	o.5	608	540	540–545	540–545	191R–192R	539.51	Top of ?192R	No core surface	24.5 Ma	23.8	24.0–27.5
33.2–34.2	33.0–34.0 Ma	o1	654	587	585–590	585–590	207R–208R	585.48	209R-1, 22	Core pick	29.0 Ma	29.0	28.5–30.0
—	—	Surface in core	—	—	—	—	—	?596.3	?212R-2, 39	Core pick	30.2 Ma	30.3	29.0–31.0
—	—		—	—	—	—	—	617.00	?219R-1, 124	Core pick	?	—	—
—	—	Surface EOT	—	—	—	—	—	625.83	223R-1, 93	Core pick	32.8 Ma	33.0	32.2–32.8

Notes: GTS = geologic timescale. GTS 2008 = Ogg et al. (2008). Predicted age for BKSA95 (Cande and Kent, 1995) from Monteverde et al. (2008) and Miller et al. (1998). Seismic sequence boundaries from Monteverde et al. (2008), Miller et al. (1998), and Sheridan et al. (2000). Predicted depths based on seismic velocity function. Predicted depth and ages for seismic sequence boundaries MIC3a to o1 from Monteverde et al. (2008) for the pre-Pleistocene and Sheridan et al. (2000) for the Pleistocene. Two predicted depths in two way travel time (TWT) and depth (mbsf) are given, the first from Monteverde et al. (2008) and the second from Mountain et al. (2009). Actual depth and actual core are the best fit to surfaces or other contacts noted in the cores. Preliminary age is derived from "Chronology." MIC = marine isotope chron, MFS = maximum flooding surface, SB = sequence boundary GTS2008 (Ogg et al., 2008), TS = transgressive surface, FS = flooding surface, EOT = Eocene–Oligocene transition. NR = none recovered. USF = upper shoreface, SOT = shoreface–offshore transition.